Sylwin Pawlowski

Mestre em Engenharia Química e Bioquímica

Experimental and modeling studies on reverse electrodialysis for sustainable power generation

Dissertação para obtenção do Grau de Doutor em
Engenharia Química e Bioquímica,
Especialidade em Engenharia Química

Orientador: Svetlozar Velizarov, Investigador Auxiliar, FCT-UNL

Co-orientador: João Goulão Crespo, Professor Catedrático, FCT-UNL

Júri:

Presidente:	Prof. Doutor José Paulo Barbosa Mota
Arguentes:	Prof. Doutor Bart Van der Bruggen Prof. Doutor Adélio Miguel Magalhães Mendes
Vogais:	Prof. Doutor João Paulo Serejo Goulão Crespo Prof. Doutor Vítor Manuel Geraldes Fernandes Prof. Doutor Carlos Manuel Santos da Silva Doutor Svetlozar Gueorguiev Velizarov

FACULDADE DE CIÊNCIAS E TECNOLOGIA
UNIVERSIDADE NOVA DE LISBOA

Maio, 2015

Experimental and Modeling Studies on Reverse Electrodialysis for Sustainable Power Generation

AGRADECIMENTOS

Em primeiro lugar gostaria de agradecer ao Svetlozar (Zarko) Velizarov por me ter proposto o presente trabalho, de inegável interesse científico, quase sem me conhecer e ao João Paulo Crespo por prontamente concordar. Agradeço aos dois todo o apoio, a dedicação, o rigor, as perguntas, os desafios, as ideias e a partilha de conhecimento prestada durante a orientação do meu doutoramento. Foi um privilégio e um prazer trabalhar com vocês. Agradeço também por terem-me proporcionado as oportunidades de intercâmbio científico dentro do nosso e com outros grupos de investigação, que seguramente possibilitaram a conclusão desta tese.

Agradeço ao Philippe Sistat, ao Vítor Geraldes e à Cláudia Galinha, com quem trabalhei durante estes anos, não só a valiosa ajuda e as contribuições nos respectivos trabalhos mas sobretudo o seu interesse pelo todo o conjunto da minha tese. Foram muitas as discussões e as sugestões dadas que me fizeram pensar, procurar e investigar mais. Claramente alargaram os meus horizontes.

Aos meus colegas do BPEG, os que estão e os que estiveram, agradeço a boa disposição, o interesse e o espírito de entreajuda ao longo destes anos. Quando precisei, as minhas vizinhas sempre me mostraram como olhar para todas as dificuldades de uma maneira mais positiva. Mesmo quando podia trabalhar em casa, sempre preferi vir à faculdade para poder dar aqueles dois dedos de conversa no gabinete. Por fim, não me posso esquecer da Alice;). Além de ter sido paciente, foi a pessoa que me mais motivou para acabar rapidamente a preparação dos últimos artigos! Obviamente (a escolha da palavra foi intencional…), a menção prévia é um indirecto, talvez um bocado desajeitado, porém um profundo agradecimento à Cláudia, sempre tão conscienciosa, preocupada e disponível para ajudar, ouvir e falar, sobre seja o que for.

Finalmente, e em especial, queria agradecer aos meus pais pelo enorme apoio, interesse, amor e incentivo que sempre me deram.

À Fundação para a Ciência e Tecnologia agradeço o financiamento através de minha bolsa de doutoramento SFRH/BD/68649/2010.

Dla mojej Babci

ABSTRACT

A potentially renewable and sustainable source of energy is the chemical energy associated with solvation of salts. Mixing of two aqueous streams with different saline concentrations is spontaneous and releases energy. The global theoretically obtainable power from salinity gradient energy due to World's rivers discharge into the oceans has been estimated to be within the range of 1.4-2.6 TW. Reverse electrodialysis (RED) is one of the emerging, membrane-based, technologies for harvesting the salinity gradient energy.

A common RED stack is composed by alternately-arranged cation- and anion-exchange membranes, stacked between two electrodes. The compartments between the membranes are alternately fed with concentrated (*e.g.*, sea water) and dilute (*e.g.*, river water) saline solutions. Migration of the respective counter-ions through the membranes leads to ionic current between the electrodes, where an appropriate redox pair converts the chemical salinity gradient energy into electrical energy. Given the importance of the need for new sources of energy for power generation, the present study aims at better understanding and solving current challenges, associated with the RED stack design, fluid dynamics, ionic mass transfer and long-term RED stack performance with natural saline solutions as feedwaters.

Chronopotentiometry was used to determinate diffusion boundary layer (DBL) thickness from diffusion relaxation data and the flow entrance effects on mass transfer were found to avail a power generation increase in RED stacks. Increasing the linear flow velocity also leads to a decrease of DBL thickness but on the cost of a higher pressure drop. Pressure drop inside RED stacks was successfully simulated by the developed mathematical model, in which contribution of several pressure drops, that until now have not been considered, was included. The effect of each pressure drop on the RED stack performance was identified and rationalized and guidelines for planning and/or optimization of RED stacks were derived. The design of new profiled membranes, with a chevron corrugation structure, was proposed using computational fluid dynamics (CFD) modeling. The performance of the suggested corrugation geometry was compared with the already existing ones, as well as with the use of conductive and non-conductive spacers. According to the estimations, use of chevron structures grants the highest net power density values, at the best compromise between the mass transfer coefficient and the pressure drop values.

Finally, long-term experiments with natural waters were performed, during which fouling was experienced. For the first time, 2D fluorescence spectroscopy was used to monitor RED stack performance, with a dedicated focus on following fouling on ion-exchange membrane surfaces.

To extract relevant information from fluorescence spectra, parallel factor analysis (PARAFAC) was performed. Moreover, the information obtained was then used to predict net power density, stack electric resistance and pressure drop by multivariate statistical models based on projection to latent structures (PLS) modeling. The use in such models of 2D fluorescence data, containing hidden, but extractable by PARAFAC, information about fouling on membrane surfaces, considerably improved the models fitting to the experimental data.

Keywords: Reverse electrodialysis, Salinity gradient energy, Mass transfer, Pressure drop, Fouling, Net power density, Profiled membranes, Chronopotentiometry, 2D fluorescence spectroscopy, Computational fluid dynamics, Multivariate statistical modeling

RESUMO

A energia química associada a solvatação de sais poderá tornar-se numa fonte de energia renovável e sustentável. Quando duas correntes aquosas, com diferentes salinidades, se misturam, é libertada energia pois o referido processo é espontâneo. Teóricamente, se se considerar o desaguar de todos os rios para os Oceanos, é possível obter entre 1.4 e 2.6 TW de potência a partir da energia do gradiente de salinidade. Para captar este tipo de energia, tem sido proposta a utilização de electrodiálise inversa (RED, "reverse electrodialysis"), que é um dos processos electro membranares emergentes.

Um módulo de RED é composto, em regra, por dois eléctrodos, entre os quais estão empilhadas, alternadamente, as membranas de permuta de catiões e de aniões. Entre as membranas, nos compartimentos formados por espaçadores, fluem alternadamente as soluções salinas diluída (por exemplo água do rio) e concentrada (por exemplo água do mar). Devido à diferença de concentração, os respectivos contra-iões passam através das membranas, da solução concentrada para a diluída, e consequentemente gera-se uma corrente de iões entre os dois eléctrodos, onde um par redox converte a energia química em energia eléctrica. Dada a importância da necessidade de novas fontes de energia, pretendeu-se no presente trabalho estudar e solucionar os desafios associados à geometria e estrutura de um módulo de RED, à dinâmica de fluidos, à transferência de massa e ao desempenho de um módulo de RED quando alimentado com soluções salinas naturais.

A cronopotenciometria foi utilizada para determinar, a partir dos dados do relaxamento da difusão, a espessura da camada limite de difusão (DBL, "difussion boundary layer") em condições da operação de um módulo de RED. Adicionalmente, foi sugerido aproveitar os efeitos da entrada de fluxo na transferência de massa para aumentar a geração de energia em tais módulos. O aumento da velocidade linear do fluido conduz a uma diminuição da espessura de DBL, no entanto provoca também o aumento da perda de carga no módulo. A perda de carga num módulo de RED foi simulada com sucesso usando um modelo matemático desenvolvido, no qual foi incluída a previsão de várias perdas de carga parciais até agora não consideradas. A influência de cada perda de carga no desempenho do módulo de RED foi discutida e foram dadas sugestões para a optimização dos módulos de RED. Foi proposta uma nova estrutura em forma de "V" para as membranas corrugadas usando a dinâmica de fluidos computacional (CFD, "computational fluid dynamics"). O desempenho de um módulo de RED com tais membranas foi comparado com o desempenho de módulos de RED com espaçadores (conductivos e não conductivos) e com outras membranas corrugadas já existentes. De acordo

com os cálculos realizados, a utilização das estruturas propostas permite a obtenção de valores mais altos de potência, além de proporcionar o melhor compromisso entre o coeficiente de transferência de massa e a perda de carga.

Finalmente, durante um mês, as águas naturais de um rio e do mar foram usadas como correntes salinas num módulo de RED e a colmatação das membranas (fouling) foi observada durante o período da experiência. Para monitorizar o desempenho de um módulo de RED, e sobretudo o processo de "fouling" na superfície das membranas, foi usada fluorescência bidimensional, pela primeira vez para tal efeito. Devido à complexidade da informação contida nos espectros de fluorescência, usaram-se técnicas de estatística multivariada, tal como a análise de componentes principais (PCA, "principal componente analysis"), para extrair a informação relevante dos espectros. Adicionalmente, a informação extraída sob a forma de componentes principais foi usada nos modelos baseados na projecção de estruturas latentes (PLS, "projection to latent structures") para prever a potência, a resistência eléctrica e a perda de carga. A utilização em tais modelos dos dados obtidos através da fluorescência bidimensional melhorou consideravelmente o ajuste de modelos aos dados experimentais.

Palavras-chave: Electrodiálise inversa, Energia do gradiente de salinidade, Transferência de massa, Perda de carga, Colmatação das membranas, Densidade de potência, Membranas corrugadas, Cronopotenciometria, Fluorescência bidimensional, Dinâmica dos fluidos computacionais, Modelação estatística multivariada

CONTENTS

LIST OF FIGURES

LIST OF TABLES

ABBREVIATIONS

2DFS	2D fluorescence spectroscopy
AEM	Anion-exchange membrane
CAPMIX	Capacitive mixing
CEM	Cation-exchange membrane
CFD	Computational fluid dynamics
DBL	Diffusion boundary layer
ED	Electrodialysis
EEM	Excitation-emission matrix
EU	European Union
HPLC	High pressure liquid chromatography
LCD	Limiting current density
LCOE	Levelised cost of electricity
LV	Latent variables
MBR	Membrane bioreactor
OCV	Open circuit voltage
PARAFAC	Parallel factor analysis
PC	Principal component
PCA	Principal component analysis
PLS	Projection to latent structures
PRO	Pressure retarded osmosis
Re	Reynolds number
RED	Reverse electrodialysis
RMSECV	Root mean square error of cross-validation
RMSEP	Root mean square error of prediction
Sc	Schmidt number
SGE	Salinity gradient energy
Sh	Sherwood number
SWRO	Sea water reverse osmosis
TOC	Total organic carbon

Chapter

1

MOTIVATION AND RESEARCH STRATEGY

1.1. INTRODUCTION

1.1.1. Background

Sustainable development cannot be achieved without a sustainable power generation. Energy represents from 1 % to 10 % of industrial cost production (excluding personnel costs) [1] and has been responsible, in 2011, for almost 80 % of the greenhouse gas emissions in EU-28 [2]. Moreover, the power generation is pointed out as a key factor which may solve other worldwide problems, such as education or health care as well as water and food availability [3]. For example, cooling for electricity production dominates the water use in industry [4]. The EU 2050 roadmap assumes that the power sector has the biggest potential for cutting greenhouse gas emissions, as electricity generated by renewable sources could partially replace fossil fuels used in transport and for heating [5]. In 2011, the World gross electricity generation was approximately 2.5 TW, but only 20.6 % was generated from renewable sources [2]. Therefore decarbonizing our energy sources, which must be affordable, accessible and sustainable, is essential [6].

1.1.2. Salinity gradient energy

When water streams with different salt concentrations mix, energy is released due to a chemical potential difference between the two water bodies. The process is spontaneous, irreversible and leads to an increase in the system entropy, which offers an opportunity to capture a renewable energy [7-11]. During the mixing process no CO_2 or other greenhouse gases, which may interfere with the global climate are released, no salts are "consumed" and, virtually (unless the water must be pre-treated and transported [8]), this "fuel" has no cost [11-13]. Salinity gradient energy can therefore be considered as a completely renewable and sustainable source of energy.

The salinity gradient energy can be transformed into electric power only when appropriately harvested since, in a random mixing, the system quickly reaches chemical equilibrium, without giving the time to capture the released energy [13]. The first concept of extracting electrical energy from such systems has been developed by Pattle in 1954 [14] and is very similar to the process currently known as Reverse Electrodialysis (RED).

1.1.3. Reverse electrodialysis (RED)

RED is a membrane-based technology for controlled mixing of saline solutions. A RED stack is composed by an array of, alternately arranged, cation- and anion-exchange membranes (CEM and AEM), stacked between two electrodes. A basic unit of the stack is a cell pair formed by one cation-exchange membrane, one anion-exchange membrane, one dilute stream compartment and one concentrated stream compartment. In order to close the stack, an additional cation-exchange membrane is added facing the cathode. Figure 1.1 shows a schematic representation of the RED principle.

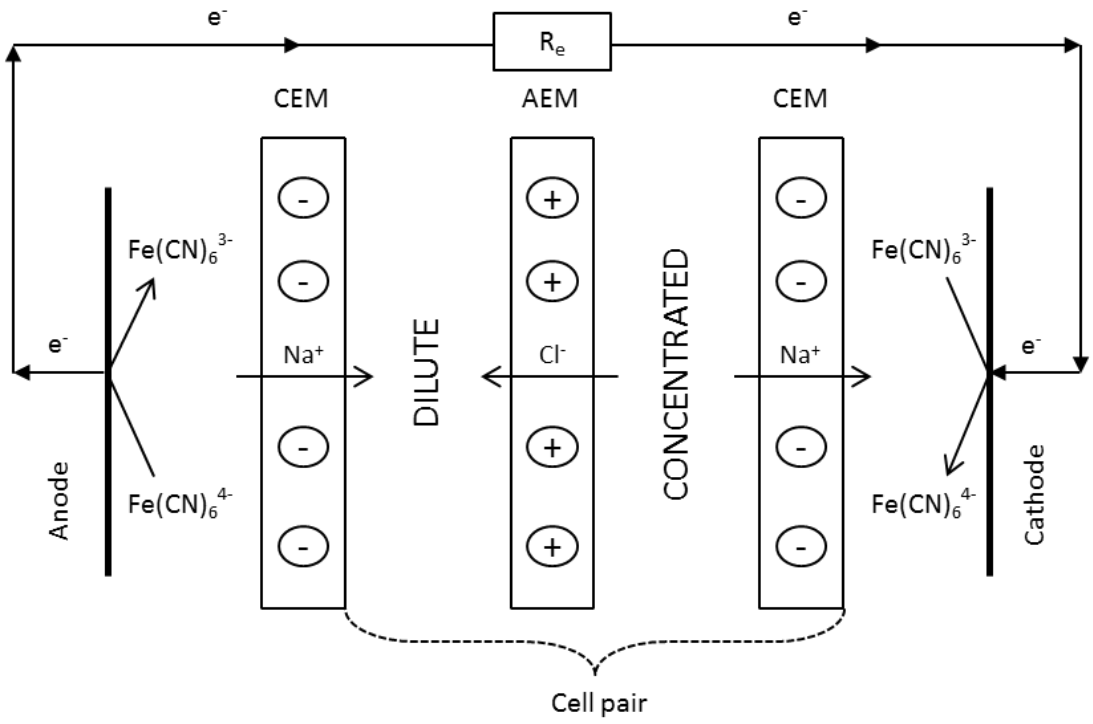

Figure 1.1. Schematic representation of the RED principle (CEM – cation-exchange membrane, AEM – anion-exchange membrane, R_e – external load resistance).

In the classical RED design, the gap between the membranes is assured by spacers, which maintain the intermembrane distance constant. The so formed compartments are alternately fed with concentrated and dilute saline solutions, with the exception of the electrode compartments, where cation-exchange membranes separate a dilute or a concentrated saline stream from a

solution containing a redox pair which is recirculated between the two terminal electrode compartments.

Since the membranes are semipermeable barriers which, in ideal conditions, allow only the passage of anions (through anion-exchange membranes) or cations (through cation-exchange membranes), while blocking transport of co-ions and water, only the respective counter-ions should migrate from a concentrated to a dilute saline stream. Due to the alternate arrangement of anion- and cation-exchange membranes, the cations and anions migrate in opposite directions. This movement leads to the establishment of an electric potential difference between the two electrodes. Therefore, the chemical salinity gradient energy is converted, by an appropriate redox couple, into electrical energy, i.e. an electron flux from the anode to the cathode through an external circuit, resulting from the need of maintaining electro-neutrality in the solution recirculated through the electrode compartments.

So far, the maximal gross power density obtained for an artificial river-sea interface (model NaCl solutions of 0.017 and 0.5 M as river and sea water, respectively) is close to 2.2 W/m^2 in a RED stack with 0.1 mm spacers and special, low resistant (< 1 Ωcm^2), homogeneous, ion exchange membranes [15]. Utilization of such conditions is, however, not feasible due to the high cost of such membranes and high pressure drop in thin channels.

Therefore, more affordable ion exchange membranes should be developed (membrane cost must be below 4.3 $€/m^2$ in order to assure a cost of electricity generation by RED, at power density near 2.7 W/m^2, competitive (around 0.16 €/kWh) with other energy sources [16]). Otherwise, further improvements of the RED process are required.

1.2. CHALLENGES

This PhD project thesis was dedicated to understanding and solving challenging issues associated to stack design, fluid dynamics and long-term RED stack performance when natural saline solutions are used as feedwaters:

1.2.1. Mass transfer

The RED process consists in ion transport from a concentrated to a dilute saline stream. However, due to the presence of selective barriers (ion-exchange membranes), concentration polarization commonly affects the process leading to a decrease in potential difference over the membranes and, therefore, to a decreased obtainable power [17-18]. Therefore, development of the mass transfer limitations across the liquid diffusion boundary layers (DBL) must be carefully taken into consideration.

The diffusion boundary layer thickness, in classical electrodialysis, where the potential difference is externally imposed between the electrodes, can be determined by the Cowan-Brown method from current-voltage curves when the limiting current density is achieved [19-20]. In RED, however, the ionic current is due to the internally established potential difference (due to the salinity gradient between the two aqueous saline streams), thus the current density values reached are much lower than the limiting current density value. Therefore, it is essential to determine the DBL thickness in under-limiting current density conditions.

The DBL thickness can be decreased by intensifying the hydrodynamic conditions, such as through an increase of the linear flow velocity or by introducing turbulence promoters inside the channels [15, 17, 20-22]. However, both measures lead also to an increase of the pressure drop inside the stack [15, 22-24] and, consequently, may result in even negative values of the net power density, since more power is spent for pumping the solutions than the one generated by the RED stack itself. Moreover, turbulence promoters are usually non-conductive spacers, which partially cover the ion-exchange membranes surface (the so-called spacer "shadow" effect) and, consequently, increase the electric resistance of the stack [17, 22-23, 25-26].

1.2.2. Pressure drop

The power spent for solutions pumping may consume up to 25 % of the generated power [23]. Minimization of the pressure drop in a RED stack is therefore one of the most important and challenging issues for optimizing the RED stack performance.

Considering a RED stack as being composed by a repeating single cell pair with equal performance does not take into account the possible non-uniform fluid distribution due to pressure variation inside the stack [27]. Therefore, the pressure drop estimation by the Hagen-Poiseuille or Darcy-Weisbach equations, which assumes a fully developed and uniform flow [15, 18, 28-29] and, therefore, equal pressure drop in all compartments, can result in pressure drop value predictions up to 20 times lower than the experimentally determined pressure drop [15, 18]. Moreover, since, for example, in a 50 cell-pair RED stack, pressure drop in manifolds constitutes 80 % of the total pressure drop [27], only when all partial pressure drops are considered, the total pressure drop is expected to be accurately predicted.

1.2.3. Stack design – Profiled membranes

The RED performance depends significantly on the stack design and on the hydrodynamic conditions inside its flow channels. As mentioned in section 1.2.1, introduction of turbulence

promoters inside the channels can reduce the diffusion boundary layer thickness, but it also increases the ohmic electric resistance and the pressure drop.

An explored possibility for overcoming this limitation is the use of conductive spacers, which promote solutions mixing without covering a part of the membrane surface for counter-ion transport [25]. However, since the pressure drop remains relatively high in such a design, a more viable alternative seems to be the utilization of profiled membranes [18, 22, 30].

Profiled membranes, also known as corrugated membranes, provide channels for the feed streams, while the relief formed on their surfaces keeps the membranes separated [18, 31-32]. In such a way, the intermembrane distance is still maintained constant even without spacers. The use of profiled membranes is very promising since, if used, the obtainable net power density can be almost two times higher than that obtained in a RED stack with spacers, due to both the increase of available membrane area and a pressure drop reduction in the channels [22]. However, there is still a need for designing optimal corrugation forms, since the actual ones do not grant the same reduction of the diffusion boundary layer resistance as spacers do [18, 22, 30].

1.2.4. Fouling

When natural waters are used as saline streams, fouling (mainly organic [33]) may cause a significant decrease in the obtained power density in a RED stack [33-34]. The current anti-fouling strategies such as periodical feedwater switch and air sparging [34], have significant energy costs associated and, therefore, must be applied with precaution.

Fouling presence in a RED stack can be manifested by an increase of the non-ohmic overpotential in chronopotentiometric measurements [35] or when a pronounced increase in the pressure drop is registered [33-34]. However, both alterations depend also on factors such as stack design, solutions flow rate and position in the stack, which impact on the obtainable power density. Moreover, fouling effects are not accounted for by the so far proposed RED mechanistic models [24, 28-29, 32] and this could hardly be done in a straightforward and simple manner through a mechanistically based approach since it requires an extensive knowledge of the system behavior.

Therefore, more accurate analytical tools for fouling detection and monitoring, with metrics which can be easily incorporated in mathematical models capable of predicting the relevant RED stack performance parameters, are needed.

1.3. OUTLINE

This thesis is divided into eight chapters.

Chapter 1 describes the motivation, challenges and the goals of this PhD project and the Chapter 2 presents the current state-of-the-art of sustainable power generation from salinity gradient energy (SGE) by reverse electrodialysis (RED). These two chapters, partially, resulted in an invited book chapter to be published in "Electrokinetics across disciplines and continents: New strategies for sustainable development" (Springer Group), currently under editorial work.

Chapters 3-7 deal with specific issues outlined in sections 1.2.1 – 1.2.4 and have resulted in five scientific articles. The contents of Chapters 3 and 4 are already published in Journal of Membrane Science ((2014) 471: 72–83 and (2014) 462: 96–111, respectively), while the contents of Chapters 5, 6 and 7 have been submitted for publication.

Chapter 3 presents and discusses the use of diffusion relaxation data, obtained through chronopotentiometry, for an accurate determination of diffusion boundary layer thickness under RED operating conditions. Moreover, the fluid flow entrance effects on mass transfer are discussed in terms of their impact on power generation in RED stacks. The content of this chapter was presented by the author of this Thesis at the international conference – "Membrane and Electromembrane Processes (MELPRO)", May 18-21, 2014, Prague, Czech Republic, where a Student Oral Presentation Award was to him attributed by European Membrane Society.

In Chapter 4, a mathematical model for pressure drop simulation inside RED stacks is proposed. Several partial pressure drops, which contributions have not been so far considered for estimation of the total pressure drop, are included in the model. In such a way, a very good prediction of the pressure drop in the investigated RED stack is obtained. The effect of each partial pressure drop on the RED stack performance is discussed and guidelines for planning and/or optimization of RED stacks design and operation are proposed.

Chapter 5 is based on computational fluid dynamics (CFD) modeling and on findings described in Chapters 3 and 4. Based in this study a new type of profiled membranes with chevron corrugation structure is proposed. The suggested corrugation geometry is compared with existing ones, as well as with the use of conductive and non-conductive spacers, in terms of their performance.

In Chapter 6, the use of 2D fluorescence spectroscopy, combined with parallel factor analysis (PARAFAC), is presented for the first time as a monitoring tool for RED. Procedures for monitoring fouling deposition on ion-exchange membrane surfaces, evaluating the membrane cleaning strategy efficiency and detecting transport of humic compounds from river to sea water by using 2D fluorescence spectroscopy are developed and discussed in detail.

In Chapter 7, multivariate statistical models, based on projection to latent structures (PLS) approach, are used for predicting net power density, stack electric resistance and pressure drop in RED stacks. The successful utilization of 2D fluorescence data in such models, containing hidden information about fouling on membrane surfaces, is validated.

In Chapter 8, the main results obtained during this PhD project are summarized, and the major conclusions drawn and outlined. Remaining challenges and suggestions for future research are finally presented and discussed.

REFERENCES

[1] European Commission, Background on energy in Europe, Information prepared for the European Council, 4 February 2011.

[2] Eurostat, The EU in the world 2014, A statistical portrait, Publications Office of the European Union, 2014.

[3] R.E. Smalley, Future global energy prosperity: The terawatt challenge, Mater. Res. Soc. Bull. 30 (2005) 412–417.

[4] J. Forster, Environment and energy - Water use in industry, Eurostat – Statistics in focus 14/2014.

[5] http://ec.europa.eu/clima/policies/roadmap/perspective/index_en.htm, consulted in 10/11/2014.

[6] S. Chu, A. Majumdar, Opportunities and challenges for a sustainable energy future, Nature 488 (2012) 294-303.

[7] J. Kuleszo, C. Kroeze, J.W. Post, B.M. Fekete, The potential of blue energy for reducing emissions of CO_2 and non-CO_2 greenhouse gases, J. Integr. Environ. Sci. 7 (S1) (2010) 89–96.

[8] J.W. Post, H.V.M. Hamelers, C.J.N. Buisman, Energy recovery from controlled mixing salt and fresh water with a reverse electrodialysis system, Environ. Sci. Technol. 42 (2008) 5785–5790.

[9] D.A. Vermaas, J. Veerman, N.Y. Yip, M. Elimelech, M. Saakes, K. Nijmeijer, High efficiency in energy generation from salinity gradients with reverse electrodialysis, Sustain. Chem. Eng. 1(10) (2013) 1295-1302.

[10] G.Z. Ramon, B.J. Feinberg, E.M.V. Hoek, Membrane-based production of salinity-gradient power, Energy Environ. Sci. 4 (2011) 4423–4434.

[11] C. Murray, J. Blackledge, D. Kearney, The feasibility of salinity gradient technology for Ireland: An initial case study by the river Suir, J. Dev. Appl. Ocean. Eng. (2013) 1-11.

[12] A.T. Jones, W. Finley, Recent developments in salinity gradient power, OCEANS 2003 Proceedings 4 (2003) 2284 – 2287.

[13] C.R. Merz, W.A. Moreno, M. Barger, S.M. Lipka, Salinity gradient power (SGP): A developmental roadmap covering existing generation technologies and recent investigative results into the feasibility of bipolar membrane-based salinity gradient power generation, Technol. Innov. 14 (2012) 249–275.

[14] R.E. Pattle, Production of electric power by mixing fresh and salt water in the hydroelectric pile, Nature 174 (1954) 660.

[15] D.A. Vermaas, M. Saakes, K. Nijmeijer, Doubled power density from salinity gradients at reduced intermembrane distance, Environ. Sci. Technol. 45 (2011) 7089–7095.

[16] A. Daniilidis, R. Herber, D.A. Vermaas, Upscale potential and financial feasibility of a reverse electrodialysis power plant, Appl. Energy 119 (2014) 257–265.

[17] P. Dlugolecki, A. Gambier, K. Nijmeijer, M. Wessling, Practical potential of reverse electrodialysis as process for sustainable energy generation, Environ. Sci. Technol. 43 (2009) 6888–6894.

[18] D.A. Vermaas, M. Saakes, K. Nijmeijer, Power generation using profiled membranes in reverse electrodialysis, J. Membr. Sci. 385–386 (2011) 234–242.

[19] V. Geraldes, M.D. Afonso, Limiting current density in the electrodialysis of multi-ionic solutions, J. Membr. Sci. 360 (2010) 499–508.

[20] P. Dlugolecki, B. Anet, S.J. Metz, K. Nijmeijer, M. Wessling, Transport limitations in ion exchange membranes at low salt concentrations, J. Membr. Sci. 346 (2010) 163–171.

[21] P. Dlugolecki, P. Ogonowski, S.J. Metz, M. Saakes, K. Nijmeijer, M. Wessling, On the resistances of membrane, diffusion boundary layer and double layer in ion exchange membrane transport, J. Membr. Sci. 349 (2010) 369–379.

[22] D.A. Vermaas, M. Saakes, K. Nijmeijer, Enhanced mixing in the diffusive boundary layer for energy generation in reverse electrodialysis, J. Membr. Sci. 453 (2014) 312–319.

[23] J. Veerman, M. Saakes, S.J. Metz, G.J. Harmsen, Reverse electrodialysis: Performance of a stack with 50 cells on the mixing of sea and river water, J. Membr. Sci. 327 (2009) 136–144.

[24] M. Tedesco, A. Cipollina, A. Tamburini, W. Baak, G. Micale, Modelling the reverse electrodialysis process with seawater and concentrated brines, Desalin. Water Treat. 49 (2012) 404–424.

[25] P. Dlugolecki, J. Dabrowska, K. Nijmeijer, M. Wessling, Ion conductive spacers for increased power generation in reverse electrodialysis, J. Membr. Sci. 347 (2010) 101–107.

[26] J. Balster, D.F. Stamatialis, M. Wessling, Membrane with integrated spacer, J. Membr. Sci. 360 (2010) 185–189.

[27] R. Kodym, P. Panek, D. Snita, D. Tvrznık, K. Bouzek, Macrohomogeneous approach to a two-dimensional mathematical model of an industrial-scale electrodialysis unit, J. Appl. Electrochem. 42 (2012) 645–666.

[28] D.A. Vermaas, E. Guler, M. Saakes, K. Nijmeijer, Theoretical power density from salinity gradients using reverse electrodialysis, Energy Proc. 20 (2012) 170 – 184.

[29] J. Veerman, M. Saakes, S.J. Metz, G.J. Harmsen, Reverse electrodialysis: a validated process model for design and optimization, Chem. Eng. J. 166 (2011) 256–268.

[30] E. Guler, R. Elizen, M. Saakes, K. Nijmeijer, Micro-structured membranes for electricity generation by reverse electrodialysis, J. Membr. Sci. 458 (2014) 136–148.

[31] H. Strathmann, Electrodialysis, a mature technology with a multitude of new applications, Desalination 264 (2010) 268–288.

[32] E. Brauns, Salinity gradient power by reverse electrodialysis: Effect of model parameters on electrical power output, Desalination 237 (2009) 378–391.

[33] D.A. Vermaas, D. Kunteng, M. Saakes, K. Nijmeijer, Fouling in reverse electrodialysis under natural conditions, Water Res. 47 (2013) 1289-1298.

[34] D.A. Vermaas, D. Kunteng, J. Veerman, M. Saakes, K. Nijmeijer, Periodic feedwater reversal and air sparging as antifouling strategies in reverse electrodialysis, Environ. Sci. Technol. 48 (2014) 3065−3073.

[35] D.A. Vermaas, M. Saakes, K. Nijmeijer, Early detection of preferential channeling in reverse electrodialysis, Electrochim. Acta 117 (2014) 9– 17.

Chapter

2

LITERATURE REVIEW

2.1. SALINITY GRADIENT ENERGY (SGE)

As mentioned in Chapter 1, the salinity gradient energy, known also as a "blue energy", is a renewable source of energy that can be harvested and converted to electricity [1].

2.1.1. SGE thermodynamic / Available work

The theoretically available energy (i.e., exergy), which is released due to mixing of two streams with different salinity can be estimated in terms of Gibbs free energy [2-3]:

$$\Delta G_{mix} = G_b - (G_c + G_d) \quad (2.1),$$

where ΔG_{mix} is the change in Gibbs energy upon solutions mixing, G_b, G_c and G_d are the Gibbs energies of the brackish (outlet stream from the stack), concentrated and dilute solutions, respectively. The Gibbs energy of an ideal solution is equal to:

$$G = \sum_i \mu_i \cdot n_i \quad (2.2),$$

where μ is the chemical potential and n is the number of moles of a component i in the solution. Therefore, the amount of released energy corresponds to the chemical potential difference between the brackish solution and the initial dilute and concentrated solutions. For ideal dilute solutions (i.e. with no change in the enthalpy, ΔH_{mix}=0), eq. 2.1 can be also rewritten in terms of the entropy change (ΔS) [3-6]:

$$\frac{\Delta G_{mix}}{n_b} = -T \cdot [\Delta S_b - f \cdot \Delta S_c - (1 - f) \cdot \Delta S_d] \quad (2.3),$$

with ΔS given by:

$$\Delta S = -R \cdot \sum_i x_i \cdot \ln(x_i) \quad (2.4),$$

where n_b is nº of moles of salts in brackish water, T is temperature, f is the fraction of seawater, and R is the universal gas constant. The power which can be generated by harvesting the released energy ($P_{\Delta Gmix}$) depends therefore on the salinity difference between the two initial streams as well as on the solutions flow rate (Q) and molar volume (V_{mol}) [6]:

$$P_{\Delta Gmix} = -T \cdot [\Delta S_b - f \cdot \Delta S_c - (1-f) \cdot \Delta S_d] \cdot \frac{Q_b}{V_{mol,b}} \quad (2.5).$$

2.1.2. River – Sea interface

A naturally occurring interface between water streams of differing salinities exists when, *e.g.* a river flows into a sea. The chemical potential difference between sea and river water is equivalent to 175-270 m of hydraulic head [2, 6-11], which has inspired the name "silent waterfalls" for rivers' mouths [8]. Mixing of equal volumes (1 m^3) of" river" (~0.01 M of NaCl) and "sea" (~0.50 M of NaCl) waters, releases approximately 1.4 MJ of energy at 293 K [6-7, 12]. If we consider, instead of $1m^3$, an infinite amount of sea water, 2.3 MJ would be released [3]. Moreover, unlike wind or solar energies, the salinity gradient energy source is non-periodic due to the Earth's continuous evaporation/precipitation hydrological cycle [2, 10] as schematically illustrated in Figure 2.1.

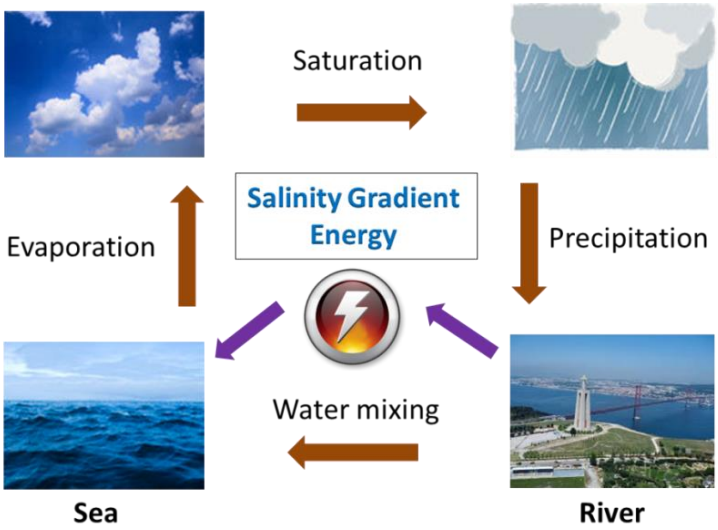

Figure 2.1. Schematic illustration of Earth's water cycle, with identification of a possible source of salinity gradient energy (The photo of the "river" is the Tagus river under the 25th of April Bridge in Lisbon). Adapted from P.Dlugolecki, PhD thesis, Mass transport in reverse electrodialysis for sustainable energy generation, University of Twente, 2009.

The worldwide potential of all rivers discharge into seas/oceans has been estimated to be within the range of 1.4-2.6 TW [4, 8-9]. However, a feasible electricity amount that can be generated depends, besides river and sea salinities, on temperature and flow rate, streams salt composition, salinity gradient steepness and environmental impacts [4, 7-8].

For example, rivers with very high flow rates, such as Amazon and Congo, have a diluting effect on the Atlantic Ocean salinity, which decreases the salinity gradient in their mouths [4, 13]. Another study has shown that in Colombia, the site specific potential is 31 % of the theoretical potential, mainly due to salinity gradient variations [5]. In such a way, the expected realizable global salinity gradient potential, due to rivers discharge, is close to 1 TW [4, 8] (Table 2.1). This power, if fully used, may lead to a significant reduction of greenhouse gas emissions by around 8 Gt CO_2-eq /year, which corresponds to 24 % of the total amount of greenhouse gas emissions related with the energy sector [4].

Table 2.1. Theoretical and technical potential of salinity gradient energy due to rivers discharge throughout the World (Adapted from [4]).

Region	Nº of rivers	Discharge (m^3/s)	Theoretical potential (GW)	Technical potential (GW)
Africa	391	170294	311	190
Asia	1243	236769	374	206
Europe	779	74569	94	56
North America	1878	191434	321	189
Oceania	791	165566	308	195
South America	390	320078	316	148
World	5472	1158709	1724	983

2.1.3. Alternative salinity gradient interfaces

The amount of power obtainable from salinity gradient energy can be increased if hybrid applications, away from seas/oceans, are also considered. Inland highly saline (hypersaline) lakes, underground salt reserves/aquifers and wastewaters (industrial, mining solutions, desalination plants' brines) [7, 10-11, 14, 15] can be alternative sources of concentrated saline streams. Figure 2.2 shows the osmotic pressure of some concentrated saline solutions based on literature data, summarized in [16]:

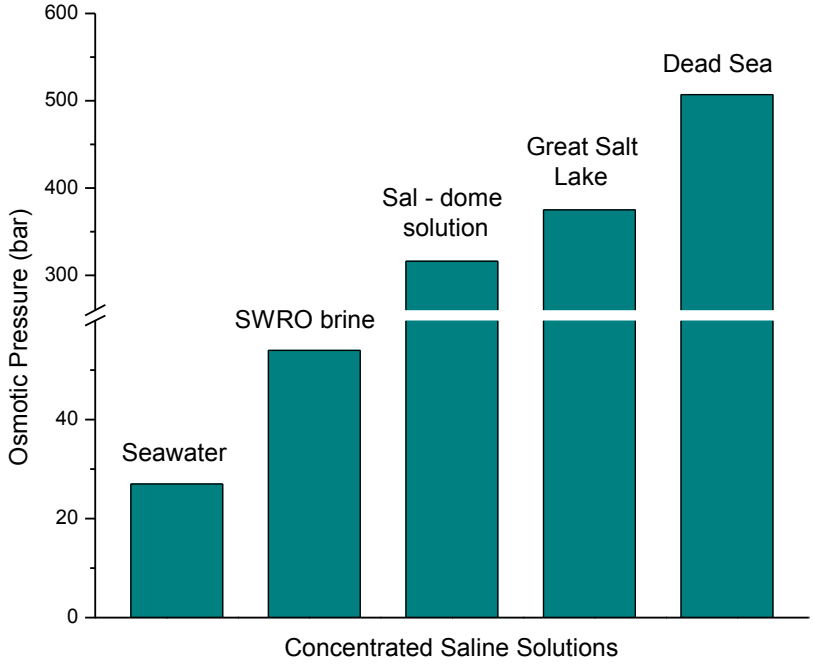

Figure 2.2. The osmotic pressure of possible five sources of concentrated saline streams (SWRO brine – brine from Sea Water Reverse Osmosis).

Worldwide municipal wastewaters plants' effluents, when drawn into seas, offer a possible potential of 18.5 GW [8, 16]. Mixture of equal volumes ($1m^3$) of brine (~5M of NaCl) and river (~0.01M of NaCl) waters can release around 16 MJ of energy [7, 12], besides providing inherent ecological benefits of diluting saline wastewater streams before disposal. The mentioned sources, despite of offering higher saline concentration differences, have limited overall potential compared to river-sea systems because of their smaller volumes, but still may found rather interesting site specific applications, *e.g.* as energy recovery systems. Highly saline waters may be also stored in ponds for being used when necessary [7, 15]. Another opportunity of creating a salinity gradient interface could pass through utilization of thermolytic solutions (e.g. containing ammonium bicarbonate) in the osmotic heat engines used to capture energy from waste heat [14, 16-17].

2.2. REVERSE ELECTRODIALYSIS (RED)

As mentioned in Chapter 1, RED is a process that allows for harvesting the salinity gradient energy released when two aqueous streams of different salinity mix.

2.2.1. RED metrics

The main parameter determining a RED stack performance is the provided net power density ($P_{net\ density}$), which consists in a trade-off between the gross power density ($P_{gross\ density}$) obtained in the stack and the power spent for pumping the solutions ($P_{pumping}$):

$$P_{net\ density} = P_{gross\ density} - \frac{P_{pumping}}{2 \cdot N \cdot A_m} \quad (2.6),$$

where A_m is the area of one membrane and N is the number of cell pairs [18-19]. For the same hydrodynamic conditions, in the dilute and concentrated compartments, the power spent for pumping can be obtained as follows [18-19]:

$$P_{pumping} = 2 \cdot (\Delta p_t \cdot Q) \quad (2.7),$$

where Q is feed solutions flow rate and Δp_t is the total pressure drop between the stack inlet and outlet. The factor 2 appears because there are two saline solutions which are pumped, the diluted and the concentrated one. The total pressure drop is the sum of partial pressure drops along the solutions pathway inside the RED stack. The power required for pumping the redox couple solution recirculated between the electrode compartments, especially for stacks with a high number of pairs, can be neglected [20].

The gross power generated by a RED stack depends on the potential difference established between the electrodes (OCV – open circuit voltage), the stack internal resistance (R_i) and the external load resistance. The maximal value of gross power density is achieved when the external load resistance has the same value as the internal resistance [21-23]. For such a case:

$$P_{gross\ density} = \frac{OCV^2}{4 \cdot R_i} \quad (2.8).$$

The open circuit voltage is the driving force of the RED process and represents the sum of potential differences over each membrane, which mainly depends on the activities ($\gamma \cdot C$) ratio between the concentrated (c) and the diluted (d) saline solutions [19, 24]:

$$OCV = 2N \cdot \alpha \cdot \frac{R \cdot T}{F} \cdot \ln\left(\frac{\gamma_c \cdot C_c}{\gamma_d \cdot C_d}\right) \quad (2.9).$$

In eq. 2.9, α is the membrane permselectivity, R is the universal gas constant, T is the absolute temperature, F is the Faraday constant, γ is the activity coefficient and C is the saline solution concentration at the membrane surface.

The stack internal resistance (R_i) is the sum of cation- and anion-exchange membranes (*CEM* and *AEM*) resistances, solutions resistances in the compartments, where h is the compartment thickness (intermembrane distance) and κ is the solution conductivity, diffusion boundary layers resistance (R_{DBL}) and electrode compartments resistance (R_{el}) [18-19, 24-27]:

$$R_i = N \cdot \left(R_{CEM} + R_{AEM} + \frac{h_c}{\kappa_c} + \frac{h_d}{\kappa_d} + R_{DBL}\right) + R_{el} \quad (2.10).$$

The diffusion boundary layer resistance is considered as a non-ohmic resistance, while all other resistances are of ohmic nature [18, 19, 25]. In a large-scale stack, the resistance of the electrodes' compartments is insignificant, compared to the other resistances [18, 26], and could be neglected.

2.2.2 Ion transport and concentration polarization

In a RED stack, the potential difference established across the membranes due to the difference in salinity of the two aqueous streams leads to transport of ions. The amount of current transported by an ion is characterized by its effective transport number [28-32]. In the membrane, the current is preferentially due to the respective counter-ion and, if the external solutions are sufficiently diluted, the transport numbers of a counter-ion and co-ion in the membrane are close to 1 and 0, respectively. In the solution, both ions transport the current, and each ion transport number in the solution depends from its mobility. For example for 1 g/L NaCl solution, the transport numbers in the solution are 0.392 and 0.608 for Na^+ and Cl^-, respectively [33]. Due to this ion transport numbers difference in the solution and in the membrane, the salt concentration in the concentrated stream is lower close to the membranes than in the bulk, while in the dilute stream compartments an opposite situation occurs [8, 27, 34-35]. Development of a solute concentration gradient across the liquid diffusion boundary layer (DBL) close to a membrane is a phenomenon known as polarization of concentration, which in RED leads to a decrease in the potential difference over the membranes (eq. 2.9) and, as a consequence, to a decrease in the obtainable gross power density [8].

Figure 2.3 shows a schematic representation of concentration profiles in a RED cell pair.

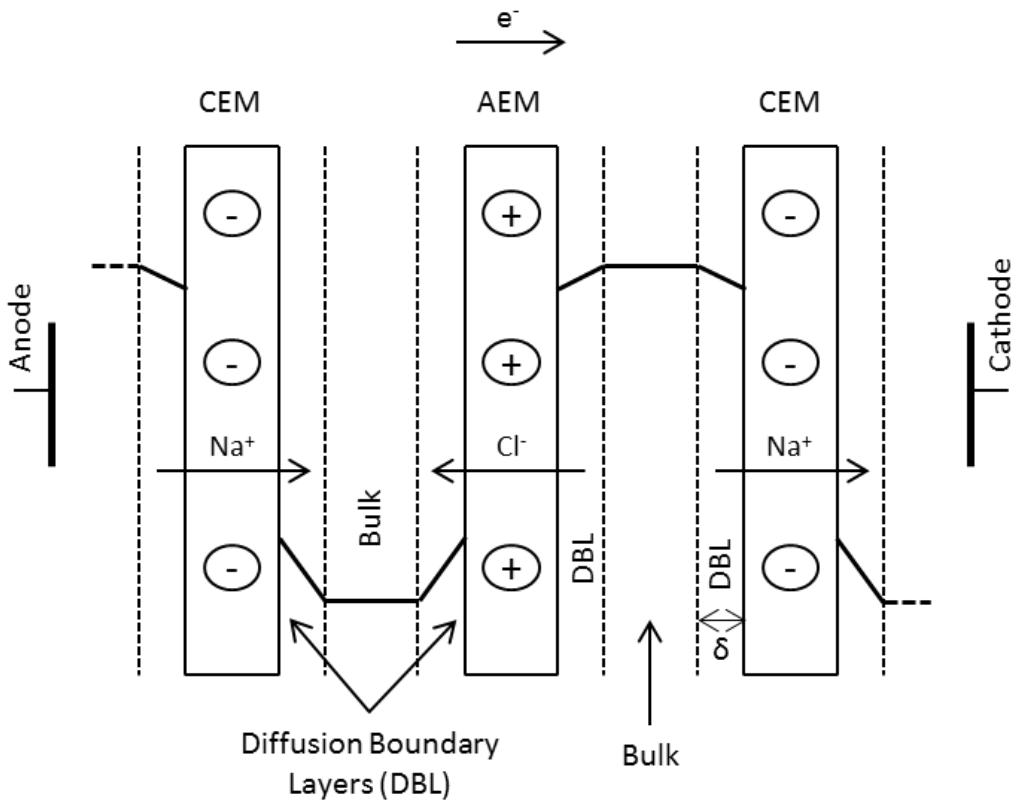

Figure 2.3. Schematic representation of electrical potential and concentration profiles in a RED cell pair (CEM – cation-exchange membrane, AEM – anion-exchange membrane).

In practice, the concentration gradient at the solution bulk-DBL interface is continuous but, by assuming the Nernst film model, the DBL thickness (δ) can be estimated from the tangents intersection of the two concentration profiles (across the DBL and in the bulk). Such an approximation allows for a reasonable description of the diffusion phenomena in electromembrane processes [27-28, 31-32, 36-39]. Furthermore, it is commonly assumed that the transport of a target counter-ion (J_m) in the membrane takes place predominantly by migration, *i.e.* due to electric field:

$$J_m = \frac{iT}{zF} \tag{2.11},$$

while in the diffusion boundary layer the same counter-ion moves (J_{DBL}) due to both migration and diffusion caused by its concentration difference across the boundary layer:

$$J_{DBL} = \frac{it}{zF} + D\left(\frac{\partial C}{\partial x}\right)_x \tag{2.12},$$

where i is the current density, T is the counter-ion transport number in the membrane, z is its valence, F is the Faraday constant, t is the counter-ion transport number in solution, D is salt diffusivity, C is salt concentration and x is the direction perpendicular to the membrane surface

[28, 31-32, 36-38]. Integration of equations 2.11 and 2.12 across the diffusion liquid boundary layer in the concentrated stream compartment gives for the current density:

$$i = \frac{zF(C_b - C_m)D}{\delta(T-t)} \quad (2.13),$$

where C_b is salt concentration in the bulk, C_m is salt concentration at the membrane surface and δ is the DBL thickness.

2.2.3. Ion-exchange membranes

An efficient ion transport in electromembrane processes, such as reverse electrodialysis, firstly depends on the ion-exchange membranes' performance. Besides, the price of the membranes is the main cost in terms of Levelised Cost of Electricity (LCOE) generated by RED [40]. Ion-exchange membranes are capable of selective transport of the respective counter-ions from one phase to another due to the high concentration of oppositely charged functional groups, fixed to the polymer matrix. Most common negatively charged fixed groups for cation-exchange membranes are sulfonic acid groups ($-SO_3^-$), while as positively charged groups of anion-exchange membranes, quaternary amine groups ($-N^+(CH_3)_3$) are usually chosen [29, 41-42].

The main properties of some commercially available ion-exchange membranes [26, 30, 41, 43-46], which can be used in RED are summarized in Table 2.2.

Table 2.2. Main properties of some commercially available ion-exchange membranes.

Membrane	Area resistance (Ωcm^2)	Perm-selectivity (%)	Wet thickness (μm)	Ion Exchange Capacity (meq/g)	Swelling Degree (%)
Cation-exchange membranes					
Fuji [46]	> 2.0	95.0	140		
Fumasep FKD [30, 41, 43]	2.14	89.5	113	1.14	29
Fumasep FKE [41]	2.46	98.6	34	1.36	12
Fumasep FKS [43]	1.50	94.2	40	1.54	13.5
Neosepta CM-1 [41]	1.67	97.2	133	2.30	20
Neosepta CMX [30, 41, 43-44]	2.91-3.00	95.0-99.0	158-164	1.62	18
Qianqiu CEM [43]	1.97	82.0	205	1.21	33
Ralex CMH-PES [26, 41, 43]	11.33-7.0	94.7-97.0	764-650	2.34	31
Selemion CMV [41, 43]	2.29	98.8	101	2.01	20

Membrane	Area resistance (Ωcm^2)	Perm-selectivity (%)	Wet thickness (μm)	Ion Exchange Capacity (meq/g)	Swelling Degree (%)
Anion-exchange membranes					
Fuji [45-46]	0.93	89.0-91.0	123-140		
Fumasep FAD [30, 41, 43]	0.89	86.0	74	0.13-1.42	34
Fumasep FAS [43]	1.03	89.4	33	1.12	8
Neosepta AFN [41]	0.70	88.9	163	3.02	43
Neosepta AM-1 [41]	1.84	91.8	126	1.77	19
Neosepta AMX [30, 41, 43-44]	2.35	90.0-90.7	134	1.25-1.40	16-26
Qianqiu AEM [43]	2.85	86.3	294	1.33	35
Ralex AMH-PES [26, 41, 43]	7.3-7.66	89.0-89.3	670-714	1.97	56
Selemion AMV [43]	3.15	87.3	124	1.78	17

The resistance values in Table 2.2 have been measured in 0.5 M NaCl solutions at 25ºC, while the permselectivity has been obtained from membrane potential measured across the membranes separating 0.5 M and 0.1 M NaCl solutions. In a given RED application, however, these values will depend on the actual saline solutions used, as the electrical resistance of an ion-exchange membrane strongly depends on the solution concentration, especially for salt concentrations <0.1M NaCl, in which range the electrical resistance of the membrane strongly increases with the decrease in salt concentration in the solution [30, 42, 47-48]. The membrane resistance could be decreased significantly by increasing temperature [47] and it is mainly determined by the compartment with the lowest external salt concentration [42]. Contrarily, the membrane permselectivity decreases when the salt concentration in the solution increases, due to a weakened Donnan exclusion of co-ions [30]. The nature of co-ions also influences the membrane permselectivity; co-ions that are charge dense and have low polarizability tend to provide a higher membrane permselectivity [49].

It has been found that a high ion-exchange capacity and a low swelling degree lead to an increased membrane selectivity, but do not have a clear effect on the membrane area resistance [43-44]. In order to decrease the membrane resistance, a more appropriate step passes through decreasing membrane thickness as the counter-ion transport becomes faster for thinner membranes [43-44]. The gross power density of a RED stack with membranes following the mentioned indications was found to be the highest one in comparison with stacks equipped with commercial membranes [43-44].

2.2.4. Monovalent *versus* Multivalent ions

During the development of the RED technology, in order to investigate and model the process performance, NaCl electrolyte solutions of different concentrations have been considered. However, in natural seawater and river water a number of other ions, including multivalent such as Mg^{2+} and SO_4^{2-} can be present in both feed solutions [45, 50-51].

Contrarily to monovalent ions, such as Na^+ and Cl^-, which are the major contributors for water salinity [51], multivalent ions could be transported from the dilute to the concentrated stream compartments [45, 50-51]. This is caused by the Donnan equilibrium condition, which requires a valence-interdependent-redistribution of counter-ions, which, for a monovalent "i" and divalent counter-ions "j" in the concentrated (*c*) and dilute (*d*) saline solutions is written as follows:

$$\Delta\varphi_D = \frac{RT}{F}\ln\left(\frac{a_{i,c}}{a_{i,d}}\right)^{1/1} = \frac{RT}{F}\ln\left(\frac{a_{j,c}}{a_{j,d}}\right)^{1/2} \quad (2.14).$$

Until the Donnan equilibrium is not achieved, multivalent ions might continue to be transported, even against their own concentration gradient (uphill transport), from the dilute to the concentrated saline compartment [45, 50-51]. To confirm this behavior for the Ralex-type ion-exchange membranes used during this PhD project, an experiment with an artificial saline stream was performed and in Figure 2.4, the results relative to the anions concentrations in the dilute stream can be seen.

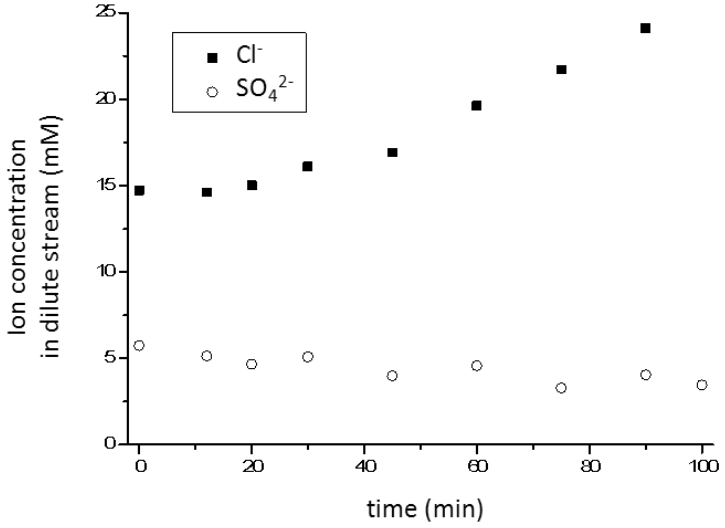

Figure 2.4. Cl^- and SO_4^{2-} concentrations evolvement in the dilute stream in a 10-cell pair RED stack, with Ralex ion-exchange membranes. The initial solutions compositions were: dilute stream (4mM $MgSO_4$, 13 mM NaCl) and concentrated stream (50 mM $MgSO_4$, 460 mM NaCl). The solutions volume was 1 dm^3 and they were fed at a 72 l/h flow rate. The anions' concentrations were followed by HPLC measurements using an AS9 column (Dionex) connected to a Dionex conductivity detector.

Depending on the initial ionic compositions, membrane properties and other process parameters, such as temperature, hydrodynamic conditions, etc., such uphill ion transport may occur in the time scale of tens of minutes up to several hours [51], thus causing a decrease in the salinity gradient across the membranes, lowering the stack voltage and, consequently, reducing the obtainable power density in RED [45, 50].

The use of ion-exchange membranes with selectivity for monovalent counter-ions may overcome this limitation as they offer steric hindering and/or charged repulsion of multivalent counter-ions [45, 50-51]. This would be beneficial especially if the dilute water composition is rich in multivalent ions [50]. As an example, the power density was reduced by 63 % when artificial multi-ionic solutions mimicking real brackish water and an exhausted brine were used instead of NaCl solutions [52]. In river – sea systems, the presence of multivalent ions in the feed solutions has led to a 9–20 % lower power density than when sodium chloride was used as a single ions' source [53], nevertheless utilization of monovalent membranes did not significantly improve the obtainable power [45, 50].

2.2.5 Redox couples

In RED, the ionic current is converted into electron current by an appropriate redox couple contained between the solution recirculated in the electrode compartments [54]. Since the conversion is mainly controlled by mass transfer in the electrolyte rather than by the electrocatalytic properties of the electrode material [55], an inexpensive graphite carbon material can be used as electrodes [54-56]. As redox couples, homogeneous redox systems, such as those based on iron compounds, are preferable, because they do not cause net chemical reactions and the potential difference needed for reduction on the cathode is counterbalanced by oxidation on the anode [56]. To choose the most appropriate redox couple to be used throughout this PhD project, some preliminary experiments were performed using different redox couples in the recirculated electrodes compartments solution. The results obtained are summarized in Table 2.3.

Table 2.3. Redox couple influence on the performance of a 10-cell pair RED stack, with Ralex ion-exchange membranes, fed with 0.5 M and 0.017 M NaCl solutions at a 72 l/h flow rate. The redox solution is 0.015 M electrolyte in 0.26 M bulk of NaCl, recirculated at 280 ml/min.

Redox couple electrolytes	OCV (V)	I (mA)	P_{gross} (mW)
Na_2SO_4	1.31	12.5	4.1
$K_3Fe(CN)_6$ and $K_4Fe(CN)_6$	1.33	38.4	12.8
$KMnO_4$ and K_2MnO_4	1.38	39.0	13.4

Since the hexacyanoferrate(III)/hexacyanoferrate(II) system has a relatively low toxicity except for the case when it is in contact with strong acids (when a toxic gas is released) and already has been proven to be rather stable in the absence of light and oxygen [54], it has been selected as a redox pair to be used throughout this PhD project.

In any case, power generation by RED does not have to be necessarily the only objective of the process. Simultaneous power generation and treatment of recalcitrant water contaminants (Cr(VI)) [57] or organic pollutant resistant to conventional biological processes (Acid Orange 7) [58], has been suggested to be done in the electrode compartments by redox reactions. Also, as mentioned in section 2.1.3, biological wastes can be converted into electricity, hydrogen gas, methane and other chemicals by coupling microbial electrochemical technologies with RED [59-62]. In such systems, appropriate microorganisms may oxidize and reduce the organics at the anode and the cathode, respectively [62].

An alternative to the use of redox couples could be utilization of capacitive electrodes, which eliminates redox reactions at the electrodes and avoids possible small leakages of redox couple solution to the feed water compartments, which may pollute the environment via the brackish effluent [63]. Furthermore, in case of internal leakages, hexacyanoferrate anions may poison the anion-exchange membranes in the RED stack through irreversible binding, thus leading to its decreased performance [64].

However, since the feed waters (dilute and concentrated saline streams) must be periodically switched when using capacitive electrodes, the obtainable gross power density is lower in a RED stack with capacitive electrodes in comparison with a stack equipped with conventional Ti/Pt electrodes and using a hexacyanoferrate system as the redox couple [63].

2.3. MONITORING OF FOULING

Fouling, mainly organic, which occurs in the RED stacks when natural water streams are used, causes a significant decrease in the obtainable power density [65-66]. Therefore, it should be accurately monitored and its causes identified in order to select the most appropriate antifouling strategies. Nevertheless, there are only few reported studies regarding this issue in RED [65-67], as described in Chapter 1, section 1.2.4.

2.3.1 2D fluorescence spectroscopy as a fouling monitoring tool

Fluorescence spectroscopy explores the natural fluorescence of a large variety of compounds for their detection. A fluorophore compound when excited emits light, which can be recorded by

fluorescence spectroscopy. In complex media, since many different fluorophore compounds can be present, to access them all, simultaneous scanning of excitation and emission light in an adequate wavelength range is needed (2D fluorescence spectroscopy). 2D fluorescence spectroscopy can therefore be used as a "fingerprint" tool for characterization of complex media such as for example honey [68], natural aquatic environments [69] or bacterial cultures [70]. What is even more relevant in the context of this PhD project is the ability of 2D fluorescence spectroscopy to characterize dissolved organic matter [71-72], especially in membrane bioreactors (MBR), a technology applied in wastewater treatment plants where organic and biofouling can be severe [73].

2.3.2 Multivariate statistical tools

Since 2D fluorescence spectroscopy captures diverse types of information, adequate modeling strategies must be used to extract the relevant data [73-74]. Statistic modeling tools, such as principal component analysis (PCA) and projection to latent structures (PLS) can be used to integrate, analyze and correlate different types of information. For the case of fluorescence spectra data treatment, a parallel factor analysis (PARAFAC), which is a generalization of PCA, is the tool usually used [75].

The objective of PCA is to substitute the initial representation of objects into a new Principal Component coordinate space with a reduced noise and lower dimensionality through decomposition of the data matrix, into a "structure" part (CP^T) plus a "noise" part (E):

$$X = CP^T + E \qquad (2.15).$$

C is the scores matrix, and can be seen as the representation of the initial data in the new and reduced co-ordinate system, composed by the new components (Principal Components, PC). P^T is the loadings matrix that describes the 'distance' between the initial co-ordinate system and the PC system. The E matrix contains unexplained data variance, such as co-linearity and noise. Therefore what PCA does is to extract the most relevant information from original data, but with reduced dimension [76].

As a number of organic foulants are natural fluorophores, which variance in complex media can be scanned by 2D fluorescence spectroscopy, this technique could be therefore a monitoring tool for fouling detection after data compression by PARAFAC [74]. The compressed fluorescence data can be further incorporated as one of the inputs in multivariate statistical

models, based on PLS modeling, and fouling parameters could successfully be predicted as, for example, for an MBR process [77].

PLS is a linear regression method that maximizes the covariance between the matrix with input and the matrix with output performance parameters. This technique combines features from PCA and multiple linear regression by decomposing iteratively both the input and output matrices into reduced orthogonal factors (latent variables). PLS models can therefore handle well with co-linearity between variables, data noise and missing data [76]. The output in PLS model is described by linear correlations of the multiple inputs:

$$y = a \cdot x_1 + b \cdot x_2 + c \cdot x_3 + \ldots \quad (2.16),$$

where *a*, *b*, and *c* are the regression coefficients and x_1, x_2, and x_3 are the useful predictors to describe the modeled output. There is also a possibility to make the models more complex, if the simple linear model fitting proves unsatisfactory, by making the inputs quadratic or by multiplying different inputs [78].

REFERENCES

[1] Z. Jia, B. Wang, S. Song, Y. Fan, Blue energy: Current technologies for sustainable power generation from water salinity gradient, Renew. Sustain. Energy Rev. 31 (2014) 91–100.

[2] C. Murray, J. Blackledge, D. Kearney, The feasibility of salinity gradient technology for Ireland: An initial case study by the river Suir, J. Dev. Appl. Ocean. Eng. (2013) 1-11.

[3] J.W. Post, H.V.M. Hamelers, C.J.N. Buisman, Energy recovery from controlled mixing salt and fresh water with a reverse electrodialysis system, Environ. Sci. Technol. 42 (2008) 5785–5790.

[4] J. Kuleszo, C. Kroeze, J.W. Post, B.M. Fekete, The potential of blue energy for reducing emissions of CO_2 and non-CO_2 greenhouse gases, J. Integr. Environ. Sci. 7 (S1) (2010) 89–96.

[5] O. Alvarez-Silva, A.F. Osorio, Salinity gradient energy potential in Colombia considering site specific constraints, Renew. Energy 74 (2015) 737-748.

[6] D.A. Vermaas, J. Veerman, N.Y. Yip, M. Elimelech, M. Saakes, K. Nijmeijer, High efficiency in energy generation from salinity gradients with reverse electrodialysis, Sustain. Chem. Eng. 1(10) (2013) 1295-1302.

[7] R. Kempener, F. Neumann, Salinity gradient energy - Technology brief, IRENA Ocean Energy Technology 2014.

[8] G.Z. Ramon, B.J. Feinberg, E.M.V. Hoek, Membrane-based production of salinity-gradient power, Energy Environ. Sci. 4 (2011) 4423–4434.

[9] Y. Emami, S. Mehrangiz, A. Etemadi, A. Mostafazadeh, S. Darvishi, A brief review about salinity gradient energy, Int. J. Smart Grid Clean Energy 2 (2013) 295-300.

[10] C.R. Merz, W.A. Moreno, M. Barger, S.M. Lipka, Salinity gradient power (SGP): A developmental roadmap covering existing generation technologies and recent investigative results into the feasibility of bipolar membrane-based salinity gradient power generation, Technol. Innov. 14 (2012) 249–275.

[11] A.T. Jones, W. Finley, Recent developments in salinity gradient power, OCEANS 2003 Proceedings 4 (2003) 2284 – 2287.

[12] J.W. Post, J. Veerman, H.V.M. Hamelers, G.J.W. Euverink, S.J. Metz, K. Nymeijer, C.J.N. Buisman, Salinity-gradient power: Evaluation of pressure-retarded osmosis and reverse electrodialysis, J. Membr. Sci. 288 (2007) 218–230.

[13] J. Huckerby, H. Jeffrey, J. Sedgwick, B. Jay, L. Finlay, An international vision for Ocean energy–Version II, Ocean Energy Systems (2012).

[14] F. Neuman, B. Hamelers, R. Siebers, J. Helsen, R. Schroeder, P. Stenzel, Report of the meeting on salinity gradient power generation, INES, Brussels 20 of June 2012.

[15] F. Helfer, O. Sahin, C.J. Lemckert, Y.G. Anissimov, Salinity gradient energy: a new source of renewable energy in Australia, Water Utility J. 5 (2013) 3-13.

[16] B.E. Logan, M. Elimelech, Membrane-based processes for sustainable power generation using water, Nature 488 (2012) 313-319.

[17] X. Luo, X. Cao, Y. Mo, K. Xiao, X. Zhang, P. Liang, X. Huang, Power generation by coupling reverse electrodialysis and ammonium bicarbonate: Implication for recovery of waste heat, Electrochem. Commun. 19 (2012) 25–28.

[18] D.A. Vermaas, M. Saakes, K. Nijmeijer, Doubled power density from salinity gradients at reduced intermembrane distance, Environ. Sci. Technol. 45 (2011) 7089–7095.

[19] D.A. Vermaas, E. Guler, M. Saakes, K. Nijmeijer, Theoretical power density from salinity gradients using reverse electrodialysis, Energy Proc. 20 (2012) 170 – 184.

[20] H. Strathmann, Electrodialysis, a mature technology with a multitude of new applications, Desalination 264 (2010) 268–288.

[21] J. Veerman, M. Saakes, S.J. Metz, G.J. Harmsen, Electrical power from sea and river water by reverse electrodialysis: A first step from the laboratory to a real power plant, Environ. Sci. Technol. 44 (2010) 9207–9212.

[22] J. Veerman, M. Saakes, S.J. Metz, G.J. Harmsen, Reverse electrodialysis: Performance of a stack with 50 cells on the mixing of sea and river water, J. Membr. Sci. 327 (2009) 136–144.

[23] J. Veerman, J.W. Post, M. Saakes, S.J. Metz, G.J. Harmsen, Reducing power losses caused by ionic shortcut currents in reverse electrodialysis stacks by a validated model, J. Membr. Sci. 310 (2008) 418–430.

[24] P. Dlugolecki, A. Gambier, K. Nijmeijer, M. Wessling, Practical potential of reverse electrodialysis as process for sustainable energy generation, Environ. Sci. Technol. 43 (2009) 6888–6894.

[25] D.A. Vermaas, M. Saakes, K. Nijmeijer, Enhanced mixing in the diffusive boundary layer for energy generation in reverse electrodialysis, J. Membr. Sci. 453 (2014) 312–319.

[26] D.A. Vermaas, M. Saakes, K. Nijmeijer, Power generation using profiled membranes in reverse electrodialysis, J. Membr. Sci. 385–386 (2011) 234–242.

[27] E. Brauns, Salinity gradient power by reverse electrodialysis: Effect of model parameters on electrical power output, Desalination 237 (2009) 378–391.

[28] A. Kozmai, V. Nikonenko, N. Pismenskaya, O. Pryakhina, P. Sistat, G. Pourcelly, Diffusion layer thickness in a membrane system as determined from voltammetric and chronopotentiometric data, Russ. J. Electrochem. 46 (2010) 1383–1389.

[29] H. Strathmann, A. Grabowski, G. Eigenberger, Ion-exchange membranes in the chemical process industry, Ind. Eng. Chem. Res. 52 (2013) 10364−10379.

[30] P. Dlugolecki, B. Anet, S.J. Metz, K. Nijmeijer, M. Wessling, Transport limitations in ion exchange membranes at low salt concentrations, J. Membr. Sci. 346 (2010) 163–171.

[31] V.V. Nikonenko, A.V. Kovalenko, M.K. Urtenov, N.D. Pismenskaya, J. Han, P. Sistat, G. Pourcelly, Desalination at overlimiting currents: State-of-the-art and perspectives, Desalination 342 (2014) 85–106.

[32] V.V. Nikonenko, N.D. Pismenskaya, E.I. Belova, P. Sistat, P. Huguet, G. Pourcelly, C. Larchet, Intensive current transfer in membrane systems: Modelling, mechanisms and application in electrodialysis, Adv. Colloid Interface Sci. 160 (2010) 101–123.

[33] C. Larchet, S. Nouri, B. Auclair, L. Dammak, V. Nikonenko, Application of chronopotentiometry to determine the thickness of diffusion layer adjacent to an ion-exchange membrane under natural convection, Adv. Colloid Interface Sci. 139 (2008) 45–61.

[34] K. Kim, W. Ryoo, M. Chun, G. Chung, S. Lee, Transport analysis in reverse electrodialysis with pulsatile flows for enhanced power generation, Korean J. Chem. Eng. 29(2) (2012) 162-168.

[35] M. Tedesco, A. Cipollina, A. Tamburini, I.D.L. Bogle, G. Micale, A simulation tool for analysis and design of reverse electrodialysis using concentrated brines, Chem. Eng. Res. Des. 93 (2015) 441-456.

[36] A.H. Galama, J.W. Post, M.A. Cohen Stuart, P.M. Biesheuvel, Validity of the Boltzmann equation to describe Donnan equilibrium at the membrane-solution interface, J. Membr. Sci., 442 (2013) 131–139.

[37] A.H. Galama, G. Daubaras, O.S. Burheim, H.H.M. Rijnaarts, J.W. Post, Seawater electrodialysis with preferential removal of divalent ions, J. Membr. Sci. 452 (2014) 219–228.

[38] V. Geraldes, M.D. Afonso, Limiting current density in the electrodialysis of multi-ionic solutions, J. Membr. Sci. 360 (2010) 499–508.

[39] P. Sistat, G. Pourcelly, Chronopotentiometric response of an ion-exchange membrane in the underlimiting current-range. Transport phenomena within the diffusion layers, J. Membr. Sci. 123 (1997) 121-131.

[40] A. Daniilidis, R. Herber, D.A. Vermaas, Upscale potential and financial feasibility of a reverse electrodialysis power plant, Appl. Energy 119 (2014) 257–265.

[41] P. Dlugolecki, K. Nymeijer, S.J. Metz, M. Wessling, Current status of ion exchange membranes for power generation from salinity gradients, J. Membr. Sci. 319 (2008) 214–222.

[42] A.H. Galama, D.A. Vermaas, J. Veerman, M. Saakes, H.H.M. Rijnaarts, J.W. Post, K. Nijmeijer, Membrane resistance: The effect of salinity gradients over a cation exchange membrane, J. Membr. Sci. 467 (2014) 279–291.

[43] E. Guler, R. Elizen, D.A. Vermaas, M. Saakes, K. Nijmeijer, Performance-determining membrane properties in reverse electrodialysis, J. Membr. Sci. 446 (2013) 266–276.

[44] E. Guler, Y. Zhang, M. Saakes, K. Nijmeijer, Tailor-made anion-exchange membranes for salinity gradient power generation using reverse electrodialysis, Chem. Sus. Chem. 5 (2012) 2262 – 2270.

[45] E. Guler, W. Baak, M. Saakes, K. Nijmeijer, Monovalent-ion-selective membranes for reverse electrodialysis, J. Membr. Sci. 455 (2014) 254–270.

[46] M. Slagt, Blue Energy: Current status and progress of RED, 3rd Osmosis membrane Summit Barcelona April 26-27 2012.

[47] P. Dlugolecki, P. Ogonowski, S.J. Metz, M. Saakes, K. Nijmeijer, M. Wessling, On the resistances of membrane, diffusion boundary layer and double layer in ion exchange membrane transport, J. Membr. Sci. 349 (2010) 369–379.

[48] G.M. Geise, A.J. Curtis, M.C. Hatzell, M.A. Hickner, B.E. Logan, Salt concentration differences alter membrane resistance in reverse electrodialysis stacks, Environ. Sci. Technol. Lett. 1 (2014) 36-39.

[49] G.M. Geise, H.J. Cassady, D.R. Paul, B.E. Logan, M.A. Hickner, Specific ion effects on membrane potential and the permselectivity of ion exchange membranes, Phys. Chem. Chem. Phys. 16 (2014) 21673-21681.

[50] J.W. Post, H.V.M. Hamelers, C.J.N. Buisman, Influence of multivalent ions on power production from mixing salt and fresh water with a reverse electrodialysis system, J. Membr. Sci. 330 (2009) 65–72.

[51] D.A. Vermaas, J. Veerman, M. Saakes, K. Nijmeijer, Influence of multivalent ions on renewable energy generation in reverse electrodialysis, Energy Environ. Sci. 7 (2014) 1434-1445.

[52] R. Tufa, E. Curcio, W. Baak, J. Veerman, S. Grasman, E. Fontananova, G. Profio, Potential of brackish water and brine for energy generation by salinity gradient power-reverse electrodialysis (SGP-RE), RSC Adv. 4 (2014) 42617-42623.

[53] J. Hong, W. Zhang, J. Luo, Y. Chen, Modeling of power generation from the mixing of simulated saline and freshwater with a reverse electrodialysis system: The effect of monovalent and multivalent ions, Appl. Energy 110 (2013) 244–251.

[54] O. Scialdone, C. Guarisco, S. Grispo, A. Angelo, A. Galia, Investigation of electrode material – Redox couple systems for reverse electrodialysis processes. Part I: Iron redox couples, J. Electroanal. Chem. 681 (2012) 66–75.

[55] O.S. Burheim, F. Seland, J.G. Pharoah, S. Kjelstrup, Improved electrode systems for reverse electro-dialysis and electro-dialysis, Desalination 285 (2012) 147–152.

[56] J. Veerman, M. Saakes, S.J. Metz, G.J. Harmsen, Reverse electrodialysis: evaluation of suitable electrode systems, J Appl Electrochem 40 (2010) 1461–1474.

[57] O. Scialdone, A. Angelo, E. Lume, A. Galia, Cathodic reduction of hexavalent chromium coupled with electricitygeneration achieved by reverse-electrodialysis processes usingsalinity gradients, Electrochim. Acta 137 (2014) 258–265.

[58] O. Scialdone, A. Angelo, A. Galia, Energy generation and abatement of Acid Orange 7 in reverse electrodialysis cells using salinity gradients, J. Electroanal. Chem. 738 (2015) 61–68.

[59] J. Nam, R.D. Cusick, Y. Kim, B.E. Logan, Hydrogen generation in microbial reverse-electrodialysis electrolysis cells using a heat-regenerated salt solution, Environ. Sci. Technol. 46 (2012) 5240-5246.

[60] M. Hatzell, X. Zhu, B.E. Logan, Simultaneous hydrogen generation and waste acid neutralization in a reverse electrodialysis system, Sustain. Chem. Eng. 2(9) (2014) 2211-2216.

[61] X. Luo, F. Zhang, J. Liu, X. Zhang, X. Huang, B.E. Logan, Methane production in microbial reverse-electrodialysis methanogenesis cells (MRMCs) using thermolytic solutions, Environ. Sci. Technol.

[62] B.E. Logan, K. Rabaey, Conversion of wastes into bioelectricity and chemicals by using microbial electrochemical technologies, Science 337 (2012) 686-690.

[63] D.A. Vermaas, S. Bajracharya, B. Sales, M. Saakes, B. Hamelers, K. Nijmeijer, Clean energy generation using capacitive electrodes in reverse electrodialysis, Energy Environ. Sci. 6 (2013) 643-651.

[64] R.E. Lacey, Energy by reverse electrodialysis. Ocean Eng. 7 (1980) 1-47.

[65] D.A. Vermaas, D. Kunteng, M. Saakes, K. Nijmeijer, Fouling in reverse electrodialysis under natural conditions, Water Res. 47 (2013) 1289-1298.

[66] D.A. Vermaas, D. Kunteng, J. Veerman, M. Saakes, K. Nijmeijer, Periodic feedwater reversal and air sparging as antifouling strategies in reverse electrodialysis, Environ. Sci. Technol. 48 (2014) 3065−3073.

[67] D.A. Vermaas, M. Saakes, K. Nijmeijer, Early detection of preferential channeling in reverse electrodialysis, Electrochim. Acta 117 (2014) 9– 17.

[68] L. Lenhardt, R. Bro, I. Zekovic, T. Dramicanin, M.D. Dramicanin, Fluorescence spectroscopy coupled with PARAFAC and PLS DA for characterization and classification of honey, Food Chem. 175 (2015) 284–291.

[69] C.A. Stedmon, S. Markager, R. Bro, Tracing dissolved organic matter in aquatic environments using a new approach to fluorescence spectroscopy, Mar. Chem. 82 (2003) 239–254.

[70] A. Surribas, J.M. Amigo, J. Coello, J.L. Montesinos, F. Valero, S. Maspoch, Parallel factor analysis combined with PLS regression applied to the on-line monitoring of Pichia pastoris cultures, Anal. Bioanal. Chem. 385 (2006) 1281–1288.

[71] C.A. Stedmon, R. Bro, Characterizing dissolved organic matter fluorescence with parallel factor analysis: a tutorial, Limnol. Oceanogr.: Methods 6 (2008) 572–579.

[72] A. Huguet, H. Roux-de Balmann, E. Parlanti, Fluorescence spectroscopy applied to the optimisation of a desalting step by electrodialysis for the characterisation of marine organic matter, J. Membr. Sci. 326 (2009) 186–196.

[73] C.F. Galinha, G. Carvalho, C.A.M. Portugal, G. Guglielmi, M.A.M. Reis, J.G. Crespo, Two-dimensional fluorescence as a fingerprinting tool for monitoring wastewater treatment systems, J. Chem. Technol. Biotechnol. 86 (2011) 985–992.

[74] C.F. Galinha, G. Carvalho, C.A.M. Portugal, G. Guglielmi, R. Oliveira, J.G. Crespo, M.A.M. Reis, Real-time monitoring of membrane bioreactors with 2D-fluorescence data and statistically based models, Water Sci. Technol. 63 (2011) 1381-1388.

[75] R. Bro, PARAFAC. Tutorial and applications. Chemometr. Intell. Lab. Syst. 38 (1997) 149-171.

[76] C.F. Galinha, PhD thesis, Monitoring and modelling of membrane bioreactors for wastewater treatment incorporating 2D fluorescence spectroscopy, FCT-UNL, March 2012, pp. 22-24.

[77] C.F. Galinha, G. Carvalho, C.A.M. Portugal, G. Guglielmi, M.A.M. Reis, J.G. Crespo, Multivariate statistically-based modelling of a membrane bioreactor for wastewater treatment using 2D fluorescence monitoring data, Water Res. 46 (2012) 3623-3636.

[78] C.F. Galinha, G. Guglielmi, G. Carvalho, C.A.M. Portugal, J.G. Crespo, M.A.M. Reis, Development of a hybrid model strategy for monitoring membrane bioreactors, J. Biotechnol. 164 (2013) 386– 395.

Chapter

3

MASS TRANSFER IN REVERSE ELECTRODIALYSIS: FLOW ENTRANCE EFFECTS AND DIFFUSION BOUNDARY LAYER THICKNESS

SUMMARY

Power generation by reverse electrodialysis (RED) depends on ionic mass transfer through alternately arranged cation- and anion-exchange membranes. Chronopotentiometric measurements were carried out in an EDR-Z Mini stack (MEGA a.s.), equipped with Ralex heterogeneous membranes, separated by either sheet flow spacers or mesh-free gaskets. Various concentrations of model NaCl solutions were used to study the ohmic and non-ohmic resistances in the stack under different hydrodynamic conditions. In order to eliminate the uncertainties associated with a non-uniform distribution of the applied current over the membrane surface, the relaxation zone of the obtained chronopotentiograms was used to estimate the diffusion boundary layer thickness. It was found that this approach provide more accurate data under RED operating conditions, which are strongly influenced by entrance effects on mass transfer, especially for a spacer-free channel configuration. For shorter flow channels, since the salt concentration profile across the diffusion boundary layer is not yet fully developed, more power can be obtained than in the case of longer channels. The presence of spacers was found to reduce the boundary layer thickness, but also increased the ohmic resistance, due to their shadow effect over the membrane surface. The description of the impact of flow entrance effects on mass transfer, and therefore on diffusion boundary layer thickness, can be useful for characterization and further design and/or optimization of RED stacks performance.

Published as: S. Pawlowski, P. Sistat, J.G. Crespo, S. Velizarov, Mass transfer in reverse electrodialysis: flow entrance effects and diffusion boundary layer thickness, Journal of Membrane Science 471 (2014) 72-83.[1]

Graphical abstract:

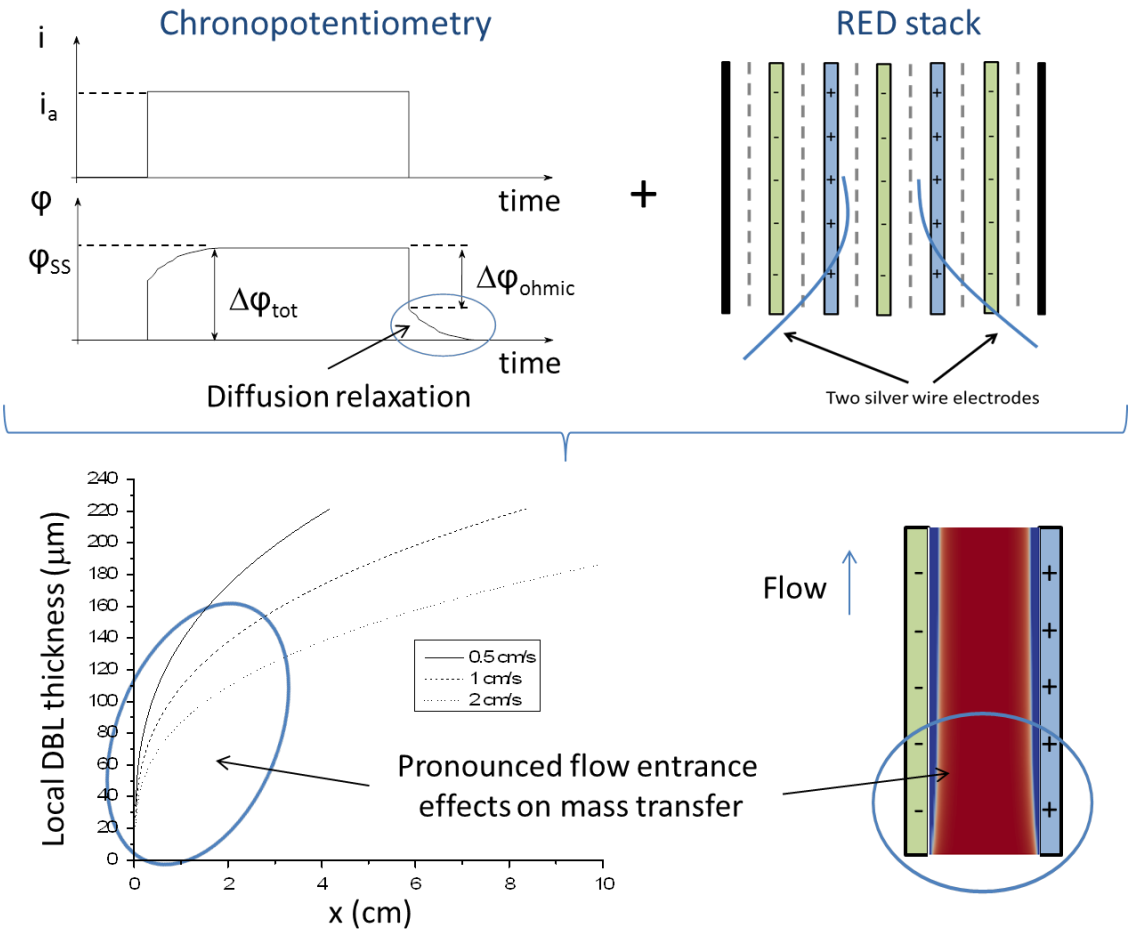

Highlights

- The diffusion boundary layer (DBL) thickness has been accessed under RED operating conditions.
- Diffusion relaxation zone of chronopotentiogram allows for accurate estimation of DBL thickness.
- In a RED stack with spacer-free channels, the Leveque equation adjusted well to experimental data.
- Flow entrance effects on mass transfer could strongly favor power generation in RED stacks.

Keywords: Chronopotentiometry, Diffusion boundary layer (DBL) thickness, Flow entrance effects

3.1. INTRODUCTION

Reverse electrodialysis (RED) is one of the emerging sustainable technologies for renewable power generation, which is based on harvesting salinity gradient energy [1-4], released when two aqueous streams of different salinity are mixed. In a RED stack, composed by alternately-arranged cation- and anion-exchange membranes, stacked between two electrodes, the chemical energy associated with solvation of salts can be directly converted into electrical energy. The global theoretically obtainable power from salinity gradient energy due to World's rivers discharge into the oceans has been estimated to be within the range of 1.4-2.6 TW [4-5].

The power output of a RED stack depends on its internal resistance (ohmic and non-ohmic) and on the total potential difference established between the electrodes [6-11]. The main ohmic resistance is commonly located in the compartments of the dilute (salinity usually below 0.1 M NaCl) stream [12-14]. This resistance can be reduced by decreasing the intermembrane distance [2, 6, 15-17]; however, in such situations, most probably due to small changes in the spacers structure, an increase of concentration polarization (non-ohmic resistance) in the diffusion boundary layers (DBLs) adjacent to the membranes forming the stack compartments [2, 6, 16-17] has been reported. In result, at a sufficiently low linear fluid flow velocity, the total resistance in a narrow stack compartment has become even higher than that in a thicker one [17]. Also, as a consequence of concentration polarization, the potential difference established between the electrodes drops, since the salt concentration gradient across the membranes becomes lower [7, 17].

Promoting fluid mixing, through an increase in the linear flow velocity and/or introducing spacers, can reduce the thickness of the diffusion boundary layer (DBL) [6, 11, 13-14, 17-18]. However, in both cases, this also increases the pressure drop, which negatively affects the obtainable net power density [6, 11-12, 19-20]. Furthermore, the "shadow" effect imposed over the membranes by non-conductive spacers tends to additionally reduce the ionic mass transport and increase the ohmic resistance [11-12, 17, 21].

In systems with ion-exchange membranes, the chronopotentiometry has been proven to be a very useful tool to perform the process analysis, since it allows for a direct access of the voltage contributions in polarized and non-polarized solution-membrane systems [22-24]. The respective electrochemical measurements are usually performed in dedicated lab-scale cells with electrodes (normally Haber-Luggin capillaries) located close to the two sides of a very small ion-exchange membrane area available for counter-ion transport [23-28]. The electrolyte solutions on both sides of the membrane are usually dilute in order to guarantee an efficient

Donnan exclusion of the co-ions and therefore preferential transport of counter-ions in the membrane [23, 25, 29]. Moreover, in a RED stack the salt concentration profile within the DBL gradually develops from the channels entrance to a certain channel length before becoming fully developed [30-31]. Therefore, only an approximate agreement could be expected between data obtained in dedicated electrochemical cells and in an operating RED stack.

There are experimental evidences that the obtainable power density in shorter channels is higher than in longer channels, as the measured non-ohmic resistance was lower in such cases [32]. However, the effect of decreasing the channels' length on the net power density had been only considered in terms of lower pressure drop and/or smaller decrease in potential difference, due to solutions mixing, along the channel [8, 33-35]. The possible impact on power generation of flow entrance effects, which extend to a longer channel length as the fluid linear flow velocity increases [30-31], has not yet been reported. The models [8-9, 19, 33] which have so far been proposed to simulate and/or predict the performance of a RED stack either do not consider concentration polarization effects [19, 33], or the non-ohmic resistance has been estimated by an empirical equation obtained under the studied conditions [8], or it has been considered that the resistance is dependent from a previously assumed DBL thickness value [9].

In this study, different methodologies were tested and compared in order to allow for more accurate DBL thickness estimation in a RED stack. Utilization of diffusion relaxation chronopotentiometry data is proposed for the first time in order to access the diffusion boundary layer thickness under RED operating hydrodynamic conditions. It has been found that this approach is the most accurate one within the linear flow velocity range relevant for RED, if the estimations are based on electric potential values. Also, a comparison of experimental results with the Leveque equation predictions for spacer-free channels was performed in order to allow for evaluating the impact of flow entrance effects on mass transfer. Finally, the influence of the streams' salinity on the ohmic and non-ohmic stack resistances was evaluated.

3.2. THEORY

3.2.1. Linear sweep voltammetry

The DBL thickness (δ) is usually calculated from experimental data of the limiting current density (i_{lim}) obtained for a cation-exchange membrane by linear sweep voltammetry [23, 25-27, 29, 36-37]:

$$i_{lim} = \frac{z_+ DFC_b}{(T_+ - t_+)\delta} \quad (3.1),$$

where F is the Faraday constant and z_+, T_+, t_+ are respectively the cation valence, effective transport number in the membrane and transport number in the solution, with known salt diffusivity (D) for a given salt concentration in the bulk (C_b).

For relatively short ($L < 0.02\ u\ h^2 / D$) rectangular channels without mixing promoters and, therefore, under conditions of a not fully developed salt concentration profile across the DBL [30], the limiting current density can be estimated by the Leveque equation [25-27, 29, 37-39]:

$$i_{lim} = \frac{1.47FDC_b}{h(T_+ - t_+)} \left(\frac{h^2 u}{LD}\right)^{1/3} \quad (3.2),$$

where u is the fluid linear flow velocity inside a channel with a known length (L) and intermembrane distance (h). The Leveque equation considers the existence of electroconvection, which may be suppressed in case of competitive transfer through the membrane of H^+/OH^- ions, as they carry the charge without bringing any liquid volume into motion [27, 37, 40].This is a semi-empirical correlation which, for the case of natural convection, is compatible with Levich-kind of equations based on the physical deduction for a channel formed between two plane parallel electrodes, in which a steady state laminar solution flow is established [28].

The limiting current density, and therefore the DBL thickness, can be also estimated by empirical correlations. In such cases, the working flow channel geometry, the fluid properties, as well as the hydrodynamic conditions are considered. When mixing promoters are present, correlations in the form of $Sh = aRe^bSc^c$ are widely used [41-42].

The Sherwood number (Sh) is correlated with the Reynolds number (Re), which depends on the hydrodynamic conditions and the channel hydraulic diameter (d_{ch}). The value of the exponent of the Reynolds number are usually 0.33 for a laminar regime, 0.5 if mixing promoters are present and 0.7-1.0 for a fully developed turbulent regime [42]. The Schmidt number (Sc) exponent is commonly set as 0.33 [31, 41-44]. For a bench-scale ED stack, with a geometry similar to that of the investigated RED stack, the proposed correlation is [43]:

$$Sh = 0.29Re^{0.5}Sc^{0.33} \quad (3.3).$$

Since the Sherwood number (Sh) depends of the mass transfer coefficient ($k=D/\delta$):

$$Sh = \frac{k \cdot d_{ch}}{D} \quad (3.4),$$

and the limiting current density also depends on the ratio D/δ (eq. 3.1), its estimation becomes possible by using the Sherwood number:

$$i_{lim} = \frac{z_+ F C_b}{(T_+ - t_+)} \cdot \frac{Sh \cdot D}{d_{ch}} \quad (3.5),$$

where the channel hydraulic diameter for channels with spacers is [8]:

$$d_{ch} = \frac{4 \cdot \varepsilon}{\frac{2}{h} + (1-\varepsilon) \cdot \frac{S_{sp}}{V_{sp}}} \quad (3.6),$$

where ε is the spacer porosity from the flow direction perspective and S_{sp}/V_{sp} is the ratio between the surface and volume of the spacer filaments.

3.2.2. Chronopotentiometry

To calculate the DBL thickness within the under-limiting current density range, chronopotentiometric measurements could be performed as illustrated in Figure 3.1.

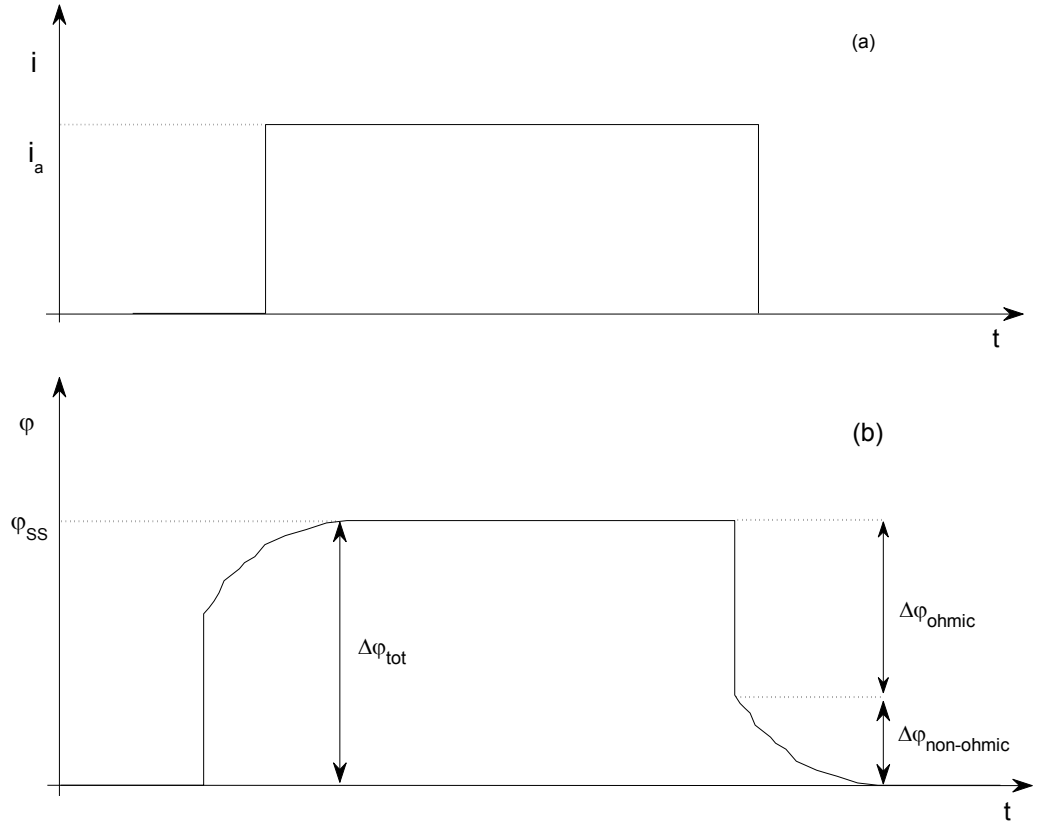

Figure 3.1. Shape of galvanostatic current density-voltage curves. (a) Current density-time curve; (b) Resulting V-time curve with different overvoltages. Adapted from [23].

A unidimensional counter-ion transport, described through the Nernst-Planck formalism within the two DBLs adjacent to the membrane is considered in a system composed by a single cation-exchange membrane that separates two 1:1 electrolyte (*e.g.* NaCl) solutions. The following equations can be written for the resulting electric potential drops in the steady state, if co-ion transport is neglected and the electrolyte concentration is the same on both sides of the membrane ($C_b = C_{bL} = C_{bR}$) [25-27]:

$$\Delta\varphi_{DBL}^{L} = -\frac{RT}{F}\ln\frac{C_L}{C_b} \quad (3.7),$$

$$\Delta\varphi_{DBL}^{R} = \frac{RT}{F}\ln\frac{C_R}{C_b} \quad (3.8),$$

$$\sum\Delta\varphi_{Don} = \frac{RT}{F}\ln\frac{C_R}{C_L} \quad (3.9),$$

where $\Delta\varphi_{DBL}{}^{L}$, $\Delta\varphi_{DBL}{}^{R}$ are the potential differences across the left (depleted) and right (enriched) diffusion boundary layers, respectively, C_L and C_R are the electrolyte concentrations at the two membrane surfaces contacting the corresponding DBLs and $\sum\Delta\varphi_{Don}$ is the sum of the Donnan potential differences at the two membrane solution interphases.

The total potential difference between the electrodes thus becomes [25-27]:

$$\Delta\varphi_{tot} = \Delta\varphi_{DBL}^{L} + \Delta\varphi_{DBL}^{R} + \sum\Delta\varphi_{Don} + \Delta\varphi_{m+sol} \quad (3.10),$$

where $\Delta\varphi_{m+sol}$ accounts for the potential differences across the membrane and the bulk solutions situated between the electrodes. Since the electroosmotic and diffusion potential differences in a dense and highly charged ion-exchange membrane could be neglected [23, 25], the resistance of the membrane and the two stirred bulk solutions can be considered purely ohmic and therefore $iR_{m+sol} = \Delta\varphi_{m+sol}$ and the transmembrane potential becomes:

$$\Delta\varphi_{tot} = 2\frac{RT}{F}\ln\left(\frac{C_R}{C_L}\right) + iR_{m+sol} \quad (3.11).$$

At steady state, for an exposed current density, $i \ll i_{lim}$, the membrane system becomes polarized and a linear electrolyte concentration profile is developed across the two equal (thus, there is an equality of the concentration gradients at the left and at the right-hand sides of the membrane) DBLs [25-27, 42]:

$$C_L = C_{bL}(1 - {}^{i}/_{i_{lim}}) \quad (3.12)$$

$$C_R = C_{bR}(1 + {}^{i}/_{i_{lim}}) \quad (3.13),$$

and for the same solutions concentration on both sides of the membrane ($C_b = C_{bL} = C_{bR}$), the transmembrane potential measured at the steady state ($\Delta\varphi_{SS}$) becomes:

$$\Delta\varphi_{tot} = 2\frac{RT}{F}\ln\left(\frac{1+\frac{i}{i_{lim}}}{1-\frac{i}{i_{lim}}}\right) + iR_{m+sol} \approx 4\frac{RT}{F}\frac{i}{i_{lim}} + iR_{m+sol} = \Delta\varphi_{SS} \quad (3.14).$$

As the ohmic contribution for the part of the potential loss is proportional to the current and to the resistivity of the media (iR_{m+sol}), the remaining part is non-ohmic. When the applied current is interrupted, a process of diffusion relaxation starts [24, 26] and the measured potential difference, at that instance ($\Delta\varphi_{SS} - \Delta\varphi_{ohmic}$), is only due to concentration polarization ($4\frac{RT}{F}\frac{i}{i_{lim}}$) developed during the current application time period. Therefore, with i_{lim} defined by Eq. 3.1, the DBL thickness becomes:

$$\delta = \frac{C_b F^2 \mathrm{D}(\Delta\varphi_{SS} - \Delta\varphi_{ohmic})}{4RTi(T_+ - t_+)} \quad (3.15)$$

Another possibility to calculate the DBL thickness, also by chronopotentiometry, involves determination of the boundary layer resistance (R_{DBL}). The non-ohmic resistance is reported to be the sum of the DBL resistance (R_{DBL}) and resistance due to concentration gradient in the bulk along the channel length ($R_{\Delta C}$) [6, 8]:

$$R_{non-ohmic} = R_{DBL} + R_{\Delta C} \quad (3.16)$$

However, when the solutions at both sides of the membrane have equal electrolyte concentrations, the latter:

$$R_{\Delta C} = \frac{N_m}{2} \cdot \alpha \cdot \frac{RT}{zFi} \cdot \ln\left(\frac{1+\frac{i \cdot t_{res}}{F \cdot \varepsilon \cdot h \cdot C_b}}{1-\frac{i \cdot t_{res}}{F \cdot \varepsilon \cdot h \cdot C_b}}\right) \quad (3.17)$$

becomes minimal (N_m is the number of membranes, t_{res} is the residence time of the saline solution in the stack and α is the membrane permselectivity) and therefore the non-ohmic resistance ($R_{non\text{-}ohmic}$) is only due to the boundary layer resistance (R_{DBL}). For a non-polarized membrane system the equation therefore becomes [25]:

$$R_{non-ohmic} = \frac{\Delta\varphi_{tot}}{\Delta i} - \frac{\Delta\varphi_{ohmic}}{\Delta i} \approx R_{DBL} = \frac{2\delta}{\kappa_{sol}} \quad (3.18),$$

where κ_{sol} corresponds to the solution conductivity, which may be obtained experimentally or, for dilute solutions, by the Debye–Huckel–Onsager theory derived from Kohlrausch's law [19, 33].

3.3. MATERIALS AND METHODS

3.3.1. Experimental installation

An electrodialysis EDR-Z-Mini unit (MEGA - Czech Republic), constituted by 2 cell pairs (2 AMH-PES and 3 CMH-PES membranes of the Ralex type) stacked between two titan electrodes with a platinum layer, was used to perform the studies.

The stack channels were defined by 0.8 mm thick gaskets with two different configurations (with or without a spacer mesh) and fed with model solutions of NaCl at three different concentrations of 0.017, 0.085 and 0.511 M, respectively. In order to provide laminar flow hydrodynamic conditions, the upper value of the linear fluid flow velocity did not exceed 4 cm/s, at which the corresponding Re number values were equal to 62.0 in a spacer-free stack configuration (gaskets without mesh) and 25.3 for spacer-filled channels (gaskets with mesh).

In the spacer-free stack configuration, the intermembrane distance is maintained, since the total area of a membrane is 115.36 cm^2 (5.6 x 20.6 cm), while an exposed area for ionic transport between the channels has 64 cm^2 (4x16 cm). Therefore 44.5 % of the membrane area is still compressed and fixed between the gaskets. Moreover, the used membranes have thickness of about 0.7 mm and therefore remain rather rigid. Besides, the co-current streams pattern and equal flow rates at both sides of the membranes ensure similar hydrostatic pressures.

In the middle of the stack length, two silver (purity 99.99 %) wires (Goodfellow, England) with a diameter of 0.125 mm were clamped between the gaskets and anion-exchange membranes located on both sides of the central cation-exchange membrane [27], as illustrated in Figure 3.2. In such a way, the distance between the silver wire electrodes corresponds to the sum of two compartment channels heights (0.8 mm each) and thickness of one cation-exchange membrane (0.7 mm). An AUTOLAB potentiostat / galvanostat (Eco Chemie, The Netherlands), coupled with a 10 A current booster, was then connected to the RED stack electrodes and to the two clamped, measuring, silver wires.

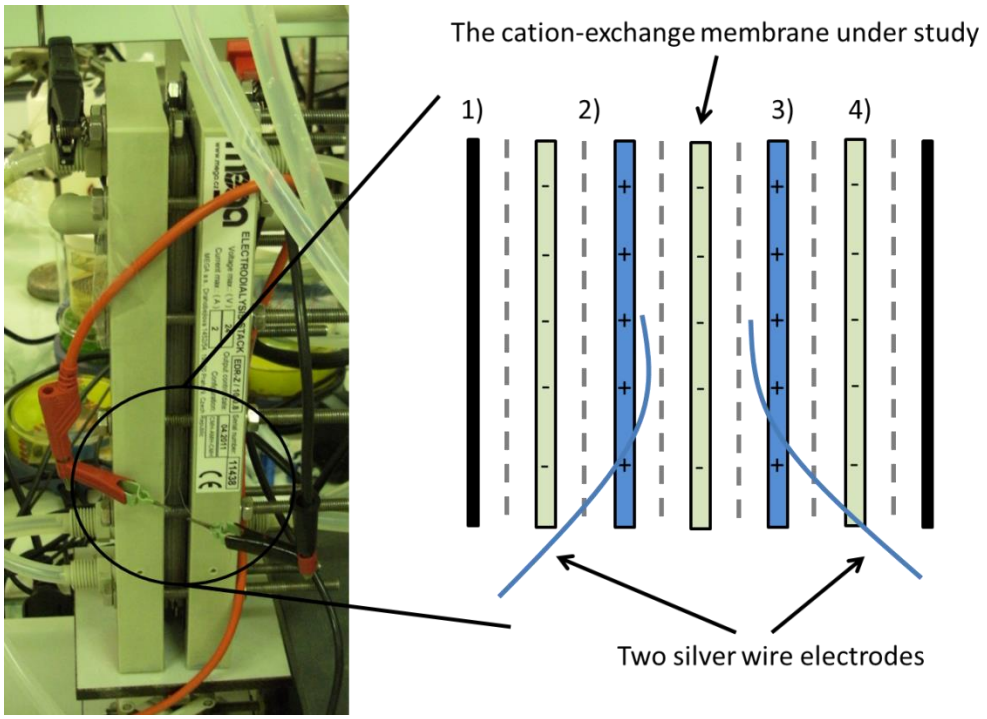

Figure 3.2. Illustration and scheme of the RED stack installation used during the electrochemical measurements: 1) Ti/Pt electrode, 2) gasket, 3) anion-exchange membrane, 4) cation-exchange membrane.

3.3.2 Analytical methods

Two electrochemical techniques were applied: linear sweep voltammetry and chronopotentiometry.

3.3.2.1 Linear sweep voltammetry

The current-voltage curves were obtained through linear sweep voltammetry measurements with 0.016(7) V/s scan rate during 480 s. In each case, the limiting current density was obtained directly from the respective current-voltage curve by intersecting the tangents to the ohmic and plateau regions data [18, 45]. Additionally, the method of Cowan and Brown was applied to confirm the obtained value. Knowledge of the limiting current density is required for selecting appropriate current densities to be applied in the chronopotentiometric measurements. The obtained limiting current density values in function of the linear flow velocity and solutions concentration, as well the respective theoretical predictions, are presented in Appendix 3A.

3.3.2.2 Chronopotentiometry

Under galvanostatic operating conditions, chronopotentiograms were obtained for the under- and over-limiting current density ranges with an interval of data collection equal to 0.01 s.

3.3.2.2.1 Under-limiting current density range

In the under-limiting range, three different current density steps (i_a) (Table 3.1) were applied during 300 s. This time period largely exceeds the 45 s, which were estimated as the lag-time (τ_l) for NaCl diffusion across a 0.4 mm (the half-channel height) thick DBL formed at steady state [46]:

$$\tau_l = 0.42 \frac{\mathrm{DBL}_{\mathrm{thickness}}^2}{D_{\mathrm{NaCl}}} \quad (3.19).$$

Table 3.1. Values of under limiting current densities (i_a) applied in the chronopotentiometric measurements.

Stack	NaCl concentration	1st i_a (A/m^2)	2nd i_a (A/m^2)	3rd i_a (A/m^2)
With spacers	1 g/L	11.6	14.4	17.7
	5 g/L	17.8	33.5	49.2
	30 g/L	50.5	66.2	81.8
Spacer-free	1 g/L	8.8	12.5	16.6
	5 g/L	17.7	32.8	48.2
	30 g/L	40.1	55.6	71.3

After the mentioned 300 s time period, the current was switched off and data was acquired during additional 200 s, as shown in Figure 3.1.

Chronopotentiometry in the under-limiting current density range can be used to estimate the DBL thickness (as described in Section 3.2.2), and to calculate the ohmic and non-ohmic resistances as follows [6, 10, 23]:

$$R_{i(Total)} = \frac{\Delta\varphi_{tot}}{\Delta i} = R_{ohmic} + R_{non-ohmic} \quad (3.20)$$

$$R_{ohmic} = \frac{\Delta\varphi_{ohmic}}{\Delta i} \quad (3.21)$$

$$R_{non-ohmic} = R_{i(Total)} - R_{ohmic} \quad (3.22).$$

3.3.2.2.2 Over-limiting current density range

Chronopotentiometric measurements were performed under over-limiting current density conditions to obtain experimentally the transition times (τ) required to calculate (through the

Sand equation) the effective Na^+ transport number in the cation-exchange membrane (T_+) [22, 24, 26, 29]:

$$\tau = \frac{\pi D}{4} \cdot \left(\frac{C_b z_+ F}{T_+ - t_+}\right)^2 \cdot \frac{1}{i^2} \quad (3.23).$$

As the Sand equation has been derived for a semi-infinite diffusion process, the DBL next to the membrane should grow unlimitedly (without any forced convection). However, even for a system with forced convection, the concentration in the DBL would not change for $\sqrt{2D\tau} < \delta$ [22]. Having this in mind, in each case, at least 3 different over-limiting current densities were chosen and applied during 50 s or until the potential difference of 10V (the maximum value allowed by the used potentiostat) was achieved. Appendix 3B presents figures of experimentally obtained chronopotentiograms.

The counter-ion transport number is an effective transport number and corresponds to the fraction of the current carried by the sodium ion, since the transport mechanism is not differentiated [46-48].

3.3.3 Transport parameters of NaCl solutions

The NaCl diffusion coefficient (D_{NaCl}) and Na^+ transport number in the solution (t_{Na^+}) were accounted for by the Nernst-Hartley equations [28]:

$$D_{\mathrm{NaCl}} = D_o g \quad (3.24)$$

$$g = 0.1213\, C^2 - 0.4331\, C^{3/2} + 0.7666\, C - 0.4494\, C^{1/2} + 0.9946 \quad (3.25)$$

$$t_{Na^+} = -0.0334\, C^{1/2} + 0.396 \quad (3.26),$$

where D_0 ($1.61 \cdot 10^{-9}$ m^2/s) is the NaCl diffusion coefficient in water at infinite dilution at 25ºC and C is the NaCl concentration [mol/dm^3]. The effective Na^+ transport number (T_{Na^+}) in the CMH-PES membrane was calculated through the Sand equation (Eq. 3.23) for each used NaCl concentration from chronopotentiometry measurements performed in the over-limiting current density regime. A conductivity meter Lab-910 (Schott Instruments, Germany) was used to measure solution' conductivity. All parameters' values related with ion transport used in the study are summarized in Table 3.2.

Table 3.2. Transport parameters used in the study. The values were obtained from experimental results (T_{Na^+}, κ) and by Nernst-Hartley equations (D_{NaCl}, t_{Na^+}).

Parameter	1 g/L NaCl	5 g/L NaCl	30 g/L NaCl
D_{NaCl} (m^2/s)	$1.526 \cdot 10^{-9}$	$1.479 \cdot 10^{-9}$	$1.511 \cdot 10^{-9}$
T_{Na^+}	0.97	0.91	0.83
t_{Na^+}	0.392	0.386	0.372
κ(S/m)	0.196	0.859	4.56

3.4. RESULTS AND DISCUSSION

3.4.1 Diffusion boundary layer thickness (by LCD) / flow entrance effects on mass transfer

The DBL thickness can be calculated through Eq. 3.1 from experimental values of limiting current density (LCD) shown in Appendix 3A. The calculated DBL values are presented in Figure 3.3. Since the prediction of the limiting current density values by the Leveque equation and the Sherwood correlation was accurate, in the same way the DBL thickness was therefore well predicted.

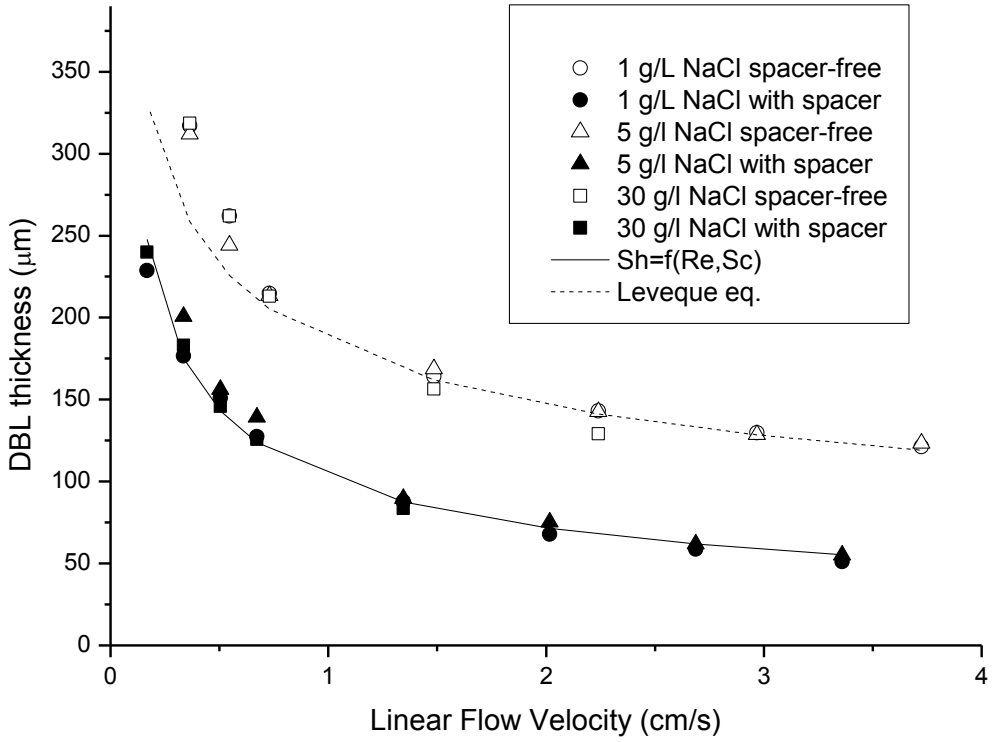

Figure 3.3. Variation of DBL thickness with linear flow velocity in a stack with spacers and in a spacer-free stack at NaCl concentrations of 1, 5 and 30 g/L.

As it can be observed, the DBL thickness did not depend on the NaCl concentration within the investigated range, when it is obtained from limiting current density values. Also, as expected,

the presence of spacers reduced the DBL thickness compared to the case without spacers in the channels. Since the shapes of DBL thickness curves in the stack with and without spacers are similar (Figure 3.3), an increase in the linear flow velocity did not cause an increase in the spacers' efficiency. Such an increase is possible due to formation of steady vortices near the spacers' yarn and/or unsteady vortices above the critical Reynolds number [49-50]. The latter, however seems unlikely to have developed in our case due to the relatively low range of linear flow velocities studied.

In such a way, at the lowest studied linear flow velocity, the DBL thickness was reduced by 25 % while, for the highest one, the DBL thickness reduction reached 60 % for both stacks. Therefore it becomes clearly important to consider the impact of flow entrance effects on mass transfer as a function of the linear flow velocity.

Since the concentration profile formation is not affected by the velocity profile formation, as the latter becomes developed almost immediately for a laminar flow [51], the Leveque equation may be used to calculate the local Sherwood numbers along a valid empty (spacer-free) channel length for a given linear flow velocity.

In order to do it, for each linear flow velocity, a maximum channel length (L_{max}) was estimated, for which the Leveque equation is valid. The calculated maximum channel lengths were then divided into J small parts with length of ΔL. The lower the chosen value of ΔL, the more accurate becomes the prediction of the local Sherwood number, which may be calculated from two adjacent Sherwood numbers obtained by Leveque equation ($\overline{Sh}$):

$$Sh_{L=j\cdot\Delta L-\Delta L/2} = j\cdot \overline{Sh_{L=j\cdot\Delta L}} - (j-1)\cdot \overline{Sh_{L=(j-1)\cdot\Delta L}}\,, \text{for } j = 1, 2, \dots, J \qquad (3.27)$$

The estimated local Sherwood number values along the channel, for ΔL = 0.5 mm, are presented in Figure 3.4.

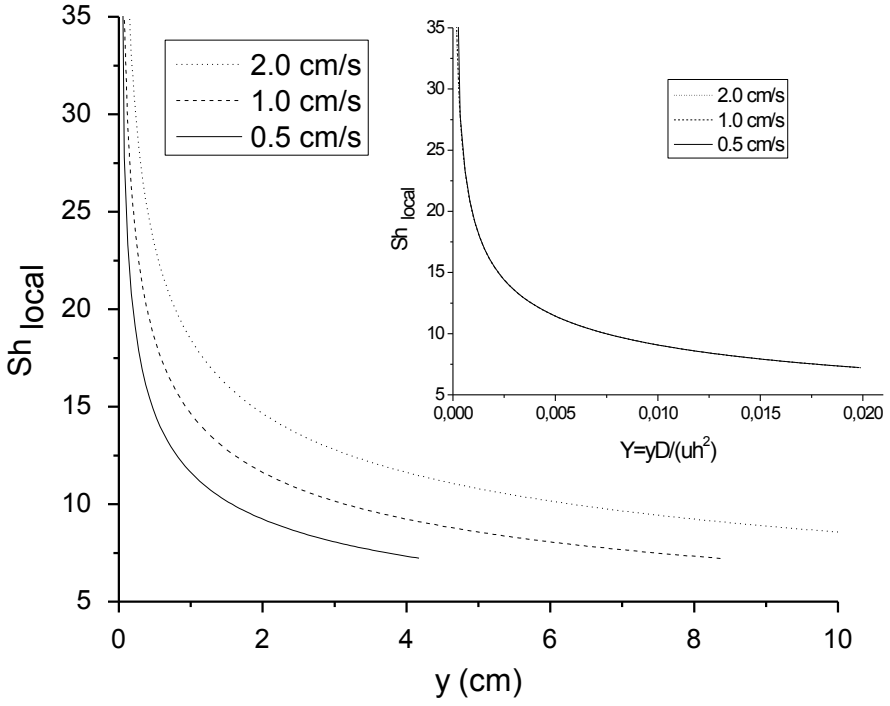

Figure 3.4. Variation of local Sherwood number (Eq. 3.27) along a rectangular channel, without mixing promoters, at different linear flow velocities.

As the linear flow velocity increases (Figure 3.4), the impact of flow entrance effects on mass transfer extends to a longer channel length. Therefore the non-ohmic resistance for short channels is strongly influenced by the linear flow velocity. When the channel length increases, the concentration profile across the DBL eventually becomes fully developed and, at such a distance from the channel entrance, the influence of the linear flow velocity on the obtained power is minimal. In other words, the Sherwood number becomes constant and independent of the linear flow velocity. The expected constant Sherwood number value is approximately equal to 6 (the DBL thickness is about h/3) [31]. An easier way to visualize this effect is by representing the local Sherwood number as a function of the dimensionless parameter (length) $Y= y \cdot D/(u \cdot h^2)$, where y is the distance from the channel entrance (see the inset in Figure 3.4). The linear velocities and the distance between the membranes applied in our study allowed calculation of the local Sherwood number until Y of 0.02. It is known however that for Y > 0.05, the local Sh number (DBL thickness) should not change anymore with increasing Y [31].

The shape of the curves presented in Figure 3.3 could therefore be rationalized as follows: The beneficial influence of increasing the linear flow velocity becomes stronger than the beneficial aspect of spacers' presence, which consists in enhancing the convective transfer [37]. This influence was stronger up to 1 cm/s, in which velocity range, the DBL thickness dropped significantly. When the linear flow velocity was increased above 1 cm/s, the DBL thickness

continued to decrease; however, at a significantly lower rate. The impact of flow entrance effects on mass transfer is more pronounced when linear flow velocity increase at linear flow velocity range below 1 cm/s, since the length of the channel for which the salt concentration profile is fully developed decreases and, therefore, the mean salt mass transfer coefficient significantly increases. At linear flow velocities above 1 cm/s, the salt concentration profile is not yet fully developed in the middle of the studied 16 cm-long flow channel, and the Sherwood number (*i.e.*, the salt mass transfer coefficient) continues to decrease as it can be seen in Figure 3.4. Therefore, the differences between the mean mass transfer coefficient values are less significant for linear flow velocities higher than 1 cm/s.

In such a way the non-ohmic resistance, which depends on the DBL thickness, is strongly reduced when the linear flow velocity increases in the lower range, as this leads to a decrease of the channel length for which the concentration profile is fully developed. Hence, it becomes possible to explain quantitatively the documented significant reductions of the non-ohmic resistance with increase of the linear flow velocity in its lower range [6, 7, 11, 17, 21]. Since the pumping power cost increases with increase of linear flow velocity [20, 52], the necessity of operating at an optimal linear flow velocity becomes even more evident. Consequently, the power generation in RED could be even strongly favored by entrance effects on mass transfer, for stacks with short flow channels. For example for a linear flow velocity of 1 cm/s, the average Sherwood number in an 0.5 cm-long empty channel (Sh = 27.6) is two times higher than the Sherwood number in a 5 cm-long empty channel (Sh = 12.85), meaning that, in the given example, the DBL resistance in the longer channel is twice larger than that in the shorter channel.

For longer channels, it has been proposed to use segmented electrodes [33-35] in which case the load resistance is adjusted in function of the local stack resistance, which DBL non-ohmic contribution, as already discussed, depends on the channels length due to flow entrance effects on mass transfer.

3.4.2 Under-limiting current density chronopotentiometry

Under-limiting current density chronopotentiometry has been used as a technique for determination of ohmic and non-ohmic resistances [6-7, 10-11, 23, 27], as well DBL thickness [23, 25-26], in solution-membrane-solution systems. For DBL thickness, the methodology is based on determination of the resistances at the initial stage of current-voltage curves and at the instant when the current is starting to be applied in the chronopotentiometric essays performed in the under-limiting current density range [25-27]. However, as mentioned in the introduction,

the electrochemical measurements are commonly performed in dedicated cells (Guillou's cells), which geometry and dimensions differ from those of RED stack channels.

Figures 3.5a and 3.5b present chronopotentiometric curves obtained in under-limiting current density regime in the spacer-free RED stack, for NaCl solutions of 1 and 30 g/L, respectively. It can be seen that when the current is switched on the voltage jump is not constant, and that the inflection point is not clearly identifiable, making an extrapolation of the resistance value in this region uncertain. Also, for the initial instant, the values measured may not represent steady conditions. For instance, for the case of 30 g/L NaCl solutions (Figure 3.5b) at low flow rates, the measured voltage decreased after reaching an initial peak. At steady state, the observed voltage oscillation is most likely due to pressure pulses of the used peristaltic pump.

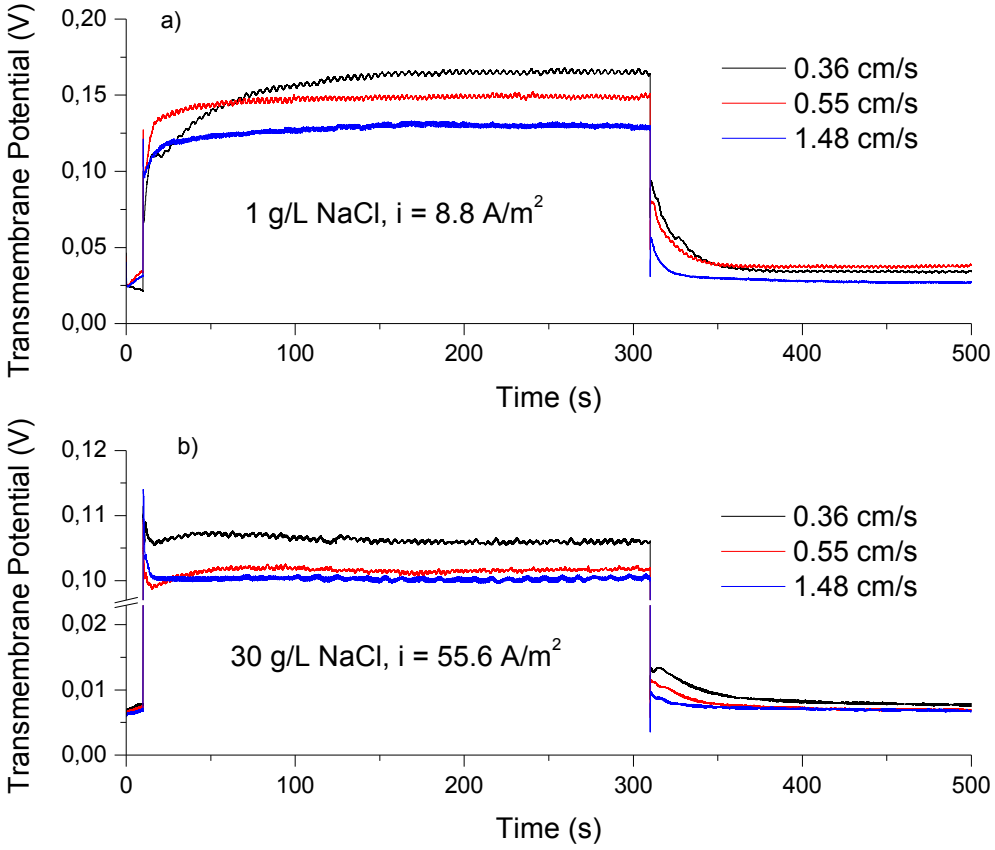

Figure 3.5. Chronopotentiograms obtained in the under-limiting current density regime, for different linear flow velocities, over the central cation-exchange membrane in a two-cell pair, spacer-free RED stack, with a) 1 g/L NaCl solution and b) 30 g/L NaCl solution.

In such a way, in the studied lab-scale RED stack, the methodology used for estimation of DBL thickness at Guillou's cells [25-27] gave values higher than 0.4 mm, in all linear flow velocity range, which is physically impossible. The relatively large membrane area available for counter-ion transport, as well as heterogeneity of the used membrane (such as cavities between the matrix and the ion-exchange particles [53]), could have led to a non-uniform current distribution

over the membrane surface [24, 27, 29, 45, 54]. As a result of such phenomena, the concentration gradient formation may suffer a delay due to tangential diffusion along the existing non-conducting regions [24, 54] which is equivalent to an increase in the DBL thickness [24, 29]. Moreover, the two DBLs may not be immediately charged ($C_{L\text{-}DBL}$=$C_{R\text{-}DBL}$=C_b) when the current is switched on [26].

Therefore, it appears more adequate to use the final part of the chronopotentiograms when the current has been switched off, *i.e.*, after a steady state has being achieved and the membrane system is fully polarized, as it has been done in a recent study on the chronoamperometric response of a cation-exchange membrane [55]. Also, for the same change in concentration, the potential response was proved to be more sensitive if the final instead of the initial part of the chronopotentiogram is used [10].

3.4.2.1 Ohmic and non-ohmic resistances

The ohmic and non-ohmic resistance values obtained through the chronopotentiogram analysis are presented in Figure 3.6.

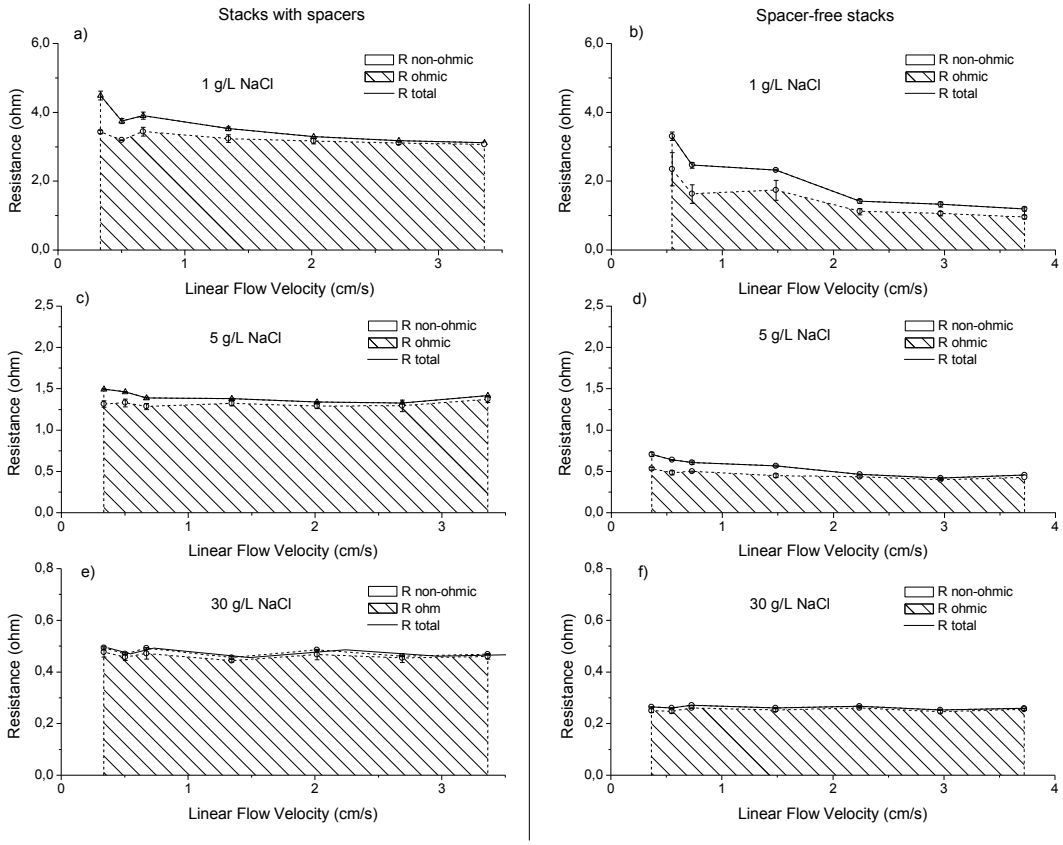

Figure 3.6. Ohmic and non-ohmic (DBL) resistances calculated from chronopotentiograms obtained in the under-limiting current density regime over the central cation-exchange membrane in a two-cell pair RED stack with and without spacers at NaCl concentrations of 1, 5 and 30 g/L.

As it can be observed (Figure 3.6), the presence of spacers reduced the non-ohmic resistance from 30 % to 70 % in case of a 1g/L NaCl solution for the applied linear flow velocity range, which is similar to the degree of reduction of the DBL thickness. For higher NaCl concentrations, the presence of spacers did not have any significant effect on the non-ohmic resistance, as the solution conductivity became sufficiently high. However, in all cases the presence of a spacer caused a significant increase in the ohmic resistance, due to the "shadow" effect of its non-conductive material on the membrane surface.

The additional ohmic resistance caused by the spacers slightly increased at low linear flow velocities (Figure 3.6). It has been found that for the same applied current density the membrane resistance increases as the solution conductivity decreases [56]. Thus, for the same initial solution concentration on both sides of the membrane and constant applied current density, the concentration/conductivity on the depleted side will decrease more for lower linear flow velocities as the residence time will be higher. Therefore the membrane resistance is higher at lower linear flow velocities as the membrane is in contact with a more dilute solution.

Also, as expected, the ohmic resistance strongly increased (7-8 times) with dilution of the NaCl solution from 30 g/L to 1 g/L. Therefore the RED operation could be directed to the use of a mixture of river water and sea water or just sea water as the dilute solution, if sufficiently high salinity gradients could be maintained (i.e., if more concentrated saline brines are available, close to the sea water, in order to serve as the concentrated solution stream), and if the membranes have a chemical structure capable of assuring a high counter-ion transport number and low water osmotic flux when in contact with a highly concentrated saline solution [19, 57-58].

3.4.2.2 DBL thickness (by chronopotentiometry)

When the DBL thickness is calculated from the values of the limiting current density (Figure 3A.1), phenomena such as electroconvection may occur, especially in dilute solutions and, therefore, the DBL thickness is reduced [24, 26-27, 37, 40]. A low-frequency fluctuation was indeed observed on chronopotentiograms obtained at over-limiting current densities (Figure 3B.1a) which indicates the presence of electroconvection in such cases. Therefore, it is more appropriate to determine the DBL thickness under RED operating conditions, where no electroconvection phenomena exist.

Considering this, the estimation of DBL thickness in under-limiting current densities range and based on two distinct sets of measured data related to the concentration polarization process:

DBL (non-ohmic) resistances (Figure 3.7a) and electric potential values obtained at different process stages (Figure 3.7b), was compared.

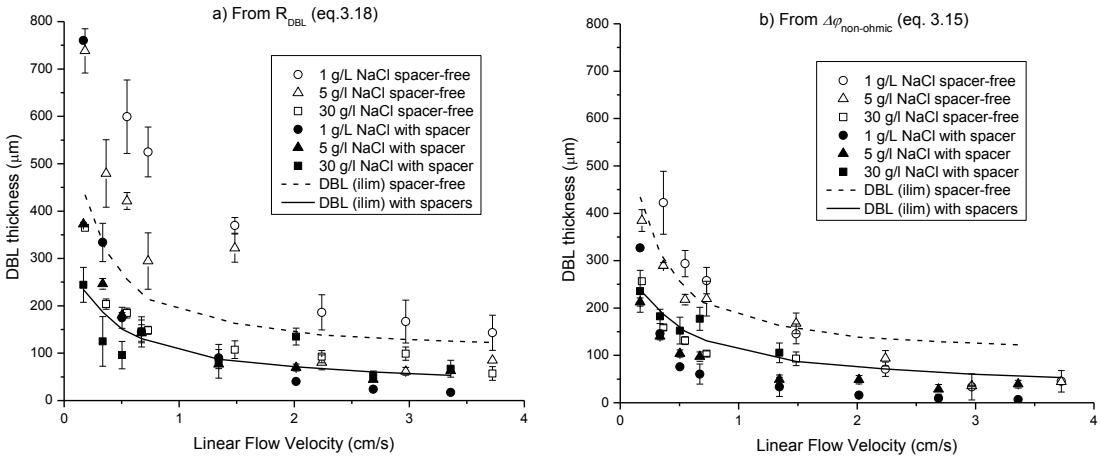

Figure 3.7. Variation of DBL thickness, with linear flow velocity, calculated from a) DBL resistances and b) potential drop due to diffusion relaxation, both obtained at under-limiting current density, in a stack with spacers and in a spacer-free stack at NaCl concentrations of 1, 5 and 30 g/L.

3.4.2.2.1 DBL resistance

As expected, at higher salt concentrations, both, ohmic and non-ohmic, electric resistances decreased (Figure 3.6). Thus, Eq. 3.18, which correlates the resistance of the DBL resistance with its thickness and with the solution conductivity, can be used for calculating the DBL thickness in under-limiting current density conditions. A possible limitation of using this approach is that Eq. 3.18 does not contain explicitly the linear flow velocity, which is included in the DBL resistance value that must be obtained experimentally.

The results obtained are presented in Figure 3.7a. As can been seen, for the stack without spacers inside the channels, the curves appears to be grouped by salt concentration, since the higher it is, the lower is the DBL thickness. All DBL thickness predictions are more coherent for higher linear velocities, at which the DBL thickness becomes smaller. The resistance due to salt concentration gradient along the channel length decreases with increasing linear flow velocity; however, in this case this is not the main reason as its estimated maximum contribution (Eq. 3.17) does not represent more than 0.08 % of the total measured electric resistance (Figure 3.6).

The main reason for the behavior observed is possibly that the solution conductivity in the bulk was used to calculate the DBL thickness. In theory, as at one of the membrane sides the solution becomes enriched and at the other it is salt depleted, use of average bulk solution conductivity

as the conductivity in the diffusion boundary layers seems correct. However, when the DBL thickness was reduced by the presence of spacers for 5 and 30 g/L NaCl solutions, the non-ohmic resistance was not affected significantly (Figures 3.6c and 3.6e). Since the DBL resistance is more influenced by the DBL thickness in case of a dilute solution, the resistance in the salt depleted DBL has a higher contribution to the total resistance than the resistance inside the salt enriched DBL. This could explain why some of the obtained DBL thickness values are higher than they could be physically (> 0.4 mm), as the average conductivity in the DBL is, in fact, lower than the considered conductivity in the bulk solution. The behavior observed is more pronounced in the lower linear flow velocities range (Figure 3.7a), as therein the DBL is thicker and the concentration polarization is stronger, which affects more the average conductivity value. As expected, this is also more evident for the data obtained in spacer-free channels since, if the spacers are present, the concentration polarization should be reduced due to additional fluid mixing provided by them.

3.4.2.2.2 Concentration polarization

The second approach to determine the DBL thickness, from the chronopotentiometry data, was based on following the process of concentration polarization development at the membrane surfaces, as described by the respective potential drops (Eqs. 3.7-3.11 and 3.14). Since on both sides of the membrane, solutions with identical NaCl concentrations were applied, when the imposed current was switched off, the measured potential difference was only due to the two DBLs meanwhile formed. Therefore, it becomes possible to estimate their thickness through Eq. 15. The obtained results are presented in Figure 3.7b. As can be seen, a good agreement exists between these values and those of the DBL thickness curve (Figure 3.3) obtained by the LCD method, especially in the low linear flow velocity range, which is the one that is more indicated for power generation by RED.

The DBL thickness data for a NaCl concentration of 30 g/L in spacer-free channel geometry demonstrate slightly lower values, since the potential difference (due to the two DBLs and due to the Donnan potentials (Eqs. 3.7-3.9)) is calculated considering a zero co-ion current. However, the co-ion (Cl^-) exclusion was less efficient at this NaCl concentration (effective transport number of Na^+ in the studied membrane lower than 1; see Table 3.2). For similar heterogeneous cation-exchange membranes, it has been found that the co-ion transport is not negligible, if the difference between the salt concentration at the salt enriched and depleted membrane interfaces is higher than 0.1 M (i.e., 5.8 g/L of NaCl) [37]. According to Eqs. 3.12 and 3.13, such a concentration difference exists for linear velocities below 0.54 cm/s for the studied case of 30 g/L of NaCl, which could explain the deviations observed.

In any case, the DBL thickness calculated from concentration polarization shows similar values to those obtained from the LCD data. The estimated values in under-limiting current density conditions were expected to be a bit higher, since phenomena such as electroconvection are not present [24, 26-27, 37, 40] and, therefore, the DBL thickness should not become reduced as it can happen at over-limiting current densities. However, although the electric potential values had been acquired just 0.01 s after switching off the current, since the two solutions were still flowing, the salt concentration in the DBLs could have been already partially affected [24]. Such behavior is expected to be favored at higher linear flow velocities, and in the presence of spacers, which it is indeed in accordance with the experimental results (Figure 3.7b).

3.5. CONCLUSIONS

Utilization of chronopotentiometry for DBL thickness determination in RED stacks proved to be a simple, fast (does not require more than 300 s) and accurate electrochemical tool. It can be applied for different saline concentrations in the under-limiting current density range.

Use of chronopotentiogram data relative to the diffusion relaxation process was found to be preferable, most probably because avoiding problems associated with the relatively large membrane area and its surface inhomogeneity in the investigated RED stack. At low linear flow velocities, up to 1.5 cm/s, utilization of potential drop values was preferable, while at higher ones, utilization of non-ohmic resistance data gave more accurate predictions of the DBL thickness. A possible reason for this behavior could be a not fully developed mass transfer conditions along the stack channels length at higher solutions flow rates.

It can be therefore concluded that flow entrance effects on mass transfer could be a key factor for enhancing the obtainable gross power density in RED. The channels should be as short as possible, and not exceeding the length of the flow entrance effect zone. An exact analysis of the concentration boundary layer profile along the channels is therefore necessary for an accurate RED stack optimization. Moreover, the herein presented findings: a 50 % lower ohmic resistance for spacer-free stacks than in the stacks with spacers and a more pronounced impact of the flow entrance effects on mass transfer in such stacks, as well as the observed decrease (especially for the dilute solution side) of the non-ohmic resistance when the spacers are present, suggests that utilization of profiled membranes [59] could be advantageous for power generation in RED stacks.

Due to the complexity of the mathematical solution, optimization in the case of profiled membranes requires the use of mathematical tools as computational fluid dynamics (CFD), in

which the film model could be used for local mass transfer coefficient calculation and mass continuity and Navier-Stokes equations should be solved in order to model the fluid motion inside the channels [60-62].

APPENDIX 3A

Linear Sweep Voltammetry / Limiting Current Density

The experimental limiting current density values for 1 and 30 g/L of NaCl are presented by points in Figures 3A.1a and 3A.1b, respectively. In order to predict the values of limiting current density, Eqs. 3.1-3.3 were used.

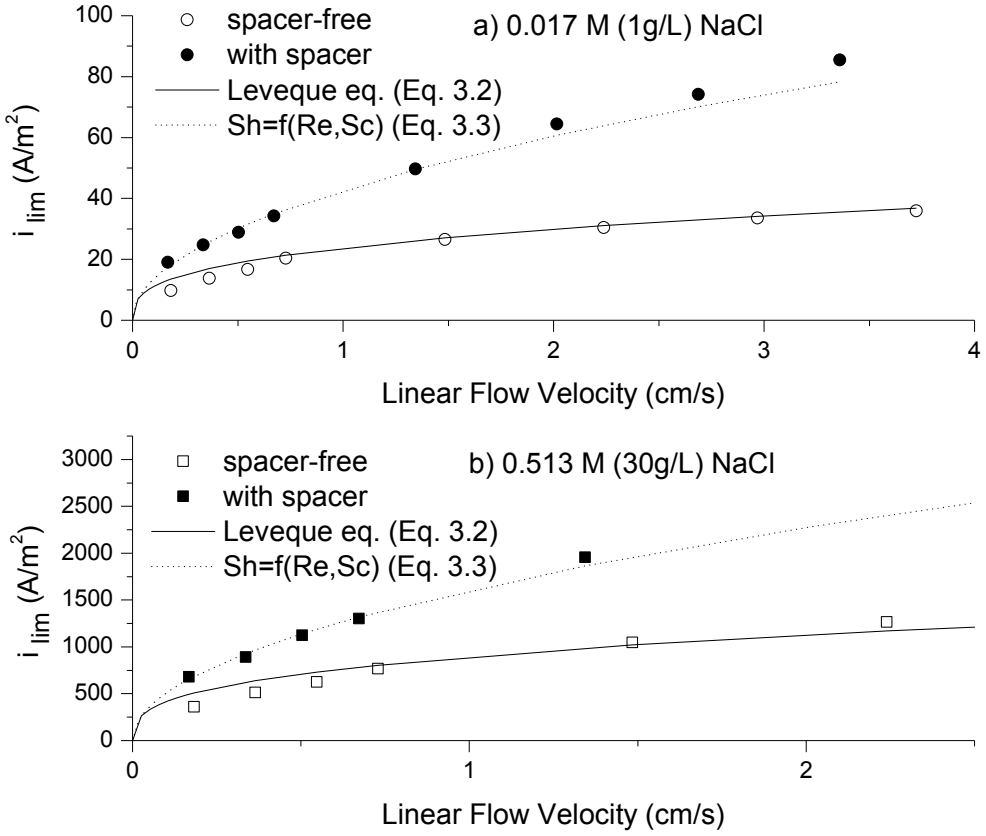

Figure 3A.1. Limiting current density results obtained by linear sweep voltammetry, over the central cation-exchange membrane in a two-cell pair RED stack configuration, with a) 1 g/L NaCl solution and b) 30 g/L NaCl solution. The adjustment of Leveque's equation and a Sherwood correlation is shown for a spacer-free stack and a stack with spacers, respectively.

Utilization of transport parameters, such as those in Table 3.2, instead of making approximations to transport numbers for infinitely dilute solutions, resulted in a correct prediction of the limiting current density for the NaCl concentrations investigated. For example, for a NaCl concentration of 0.511 M, the corresponding effective Na^+ transport number in the cation-exchange membrane was equal to 0.83, which means that 83 % of the current was

conducted by the Na^+ counter-ions. In such a way the Leveque equation (Eq. 3.2) and the Sherwood correlation (Eq. 3.3) allowed for an accurate prediction of the experimentally determined limiting current densities for a spacer-free design at sufficiently high linear flow velocities and for channels with spacers at lower linear flow velocities, respectively.

For a RED stack with spacers, the Sherwood correlation predictions of limiting current density (Figure 3A.1) adjust very well to the data obtained for linear flow velocities up to 2 cm/s, and above this value the predictions are slightly lower than the experimental values. The Sherwood type correlation predicts the same limiting current density value independently of the channel length, since it is proposed for conditions of a fully developed DBL. In a stack with spacers, it is considered that the DBL thickness is constant along the channel length due to periodic mixing granted by the forced convection [22, 43]. However, since flow entrance effects on mass transfer extend along the channel length as the linear flow velocity increases [30-31], at sufficiently high linear flow velocities the values estimated by the Sherwood type correlation become lower than the experimental ones.

For a spacer-free RED stack, the values predicted by the Leveque equation (Figure 3A.1), for the range of the linear flow velocities below 1.5 cm/s, are slightly higher than the experimental results. This is because, the Leveque equation is valid for the velocity region in which the salt concentration profile across the DBL is not yet fully developed [25-27, 29, 37-39]. The concentration gradient across the DBL increases along the channel until it reaches a constant value. In such a way, the Leveque equation gives a mean limiting current density value over the considered region length. Therefore, a difference between estimated and experimental results will exist, if a fully developed concentration profile is achieved before the exit of the compartment channel. For the studied RED stack, with a channel length, L=16 cm, the Leveque equation is expected to be valid for linear flow velocity values above 2 cm/s (according to the range of validity of Eq. 3.2), which is indeed the behavior observed in Figure 3A.1.

APPENDIX 3B

Chronopotentiometry under over-limiting current density conditions

Figures 3B.1a and 3B.1b present chronopotentiometric curves, when an over-limiting current density was applied in the spacer-free RED stack, for NaCl solutions of 1 and 30 g/L, respectively. The objective of these experiments was, as referred in Section 3.3.3, to obtain the transition times required for calculation of the effective Na^+ transport number in the membrane for different NaCl solution concentrations (Table 3.2).

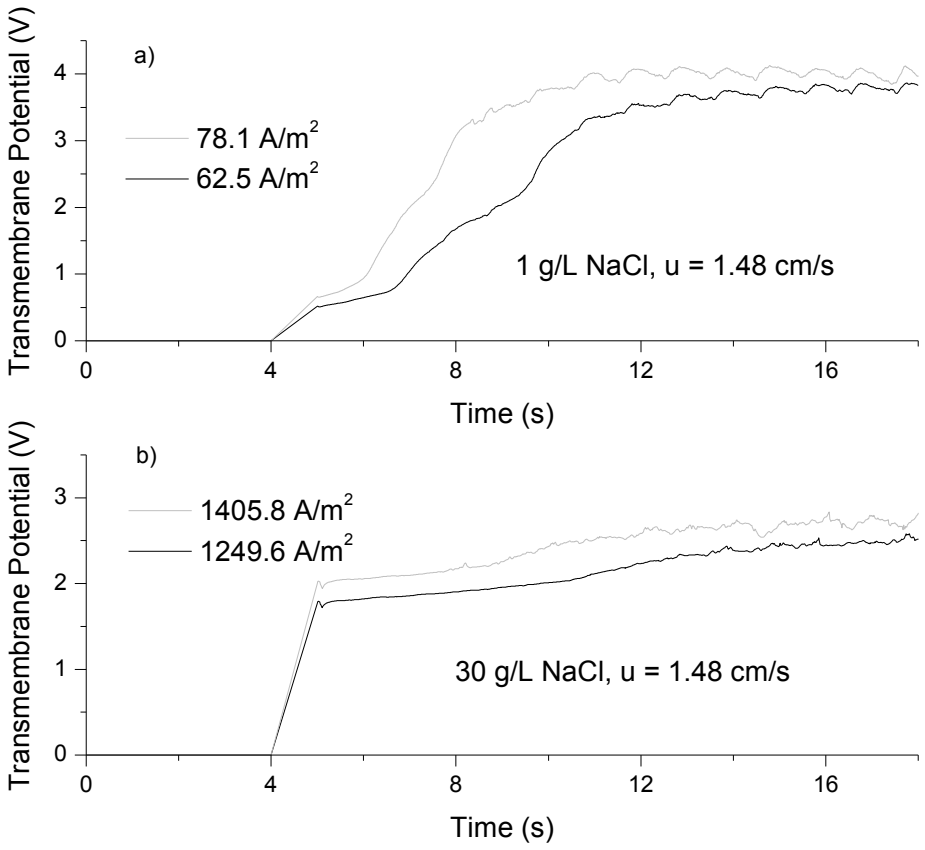

Figure 3B.1. Chronopotentiograms obtained in the over-limiting current density regime, over the central cation-exchange membrane in a two-cell pair, spacer-free RED stack, with a) 1 g/L NaCl solution and b) 30 g/L NaCl solution.

As it can be seen (Figure 3B.1), an increase in the applied current density leads to shorter transition times, as predicted by the Sand equation (Eq. 3.23). Also on the part of the curve at which the voltage drop levels off, some fluctuations can be observed, which have an appearance of an electric noise. The latter may indicate the presence of hydrodynamic instabilities in the DBL, which could result from vortices formation due to electroconvection induced by heterogeneities of the membrane surface [24, 26-27, 29, 36]. Electroconvection is more likely to occur in case of dilute saline solutions due to a higher thickness of the space charge region near the membrane surface [24, 26-27, 29], which is in accordance with the voltage oscillation observed in Figure 3B.1a, when a 1 g/L NaCl solution was used. The steady-state voltage oscillation in the case of a 30 g/L NaCl solution (Figure 3B.1b) could be a result of pulsatile flow provided by the peristaltic pumps used.

REFERENCES

[1] M. Turek, B. Bandura, Renewable energy by reverse electrodialysis, Desalination 205 (2007) 67-74.

[2] J.W. Post, H.V.M. Hamelers, C.J.N. Buisman, Energy recovery from controlled mixing salt and fresh water with a reverse electrodialysis system, Environ. Sci. Technol. 42 (2008) 5785–5790.

[3] B.E. Logan, M. Elimelech, Membrane-based processes for sustainable power generation using water, Nature 488 (2012) 313-319.

[4] G.Z. Ramon, B.J. Feinberg, E.M.V. Hoek, Membrane-based production of salinity-gradient power, Energy Environ. Sci. 4 (2011) 4423–4434.

[5] Y. Emami, S. Mehrangiz, A. Etemadi, A. Mostafazadeh, S. Darvishi, A brief review about salinity gradient energy, Int. J. of Smart Grid & Clean Energy 2 (2013) 295-300.

[6] D.A. Vermaas, M. Saakes, K. Nijmeijer, Doubled power density from salinity gradients at reduced intermembrane distance, Environ. Sci. Technol. 45 (2011) 7089–7095.

[7] D.A. Vermaas, M. Saakes, K. Nijmeijer, Power generation using profiled membranes in reverse electrodialysis, J. Membr. Sci. 385–386 (2011) 234–242.

[8] D.A. Vermaas, E. Guler, M. Saakes, K. Nijmeijer, Theoretical power density from salinity gradients using reverse electrodialysis, Energy Procedia 20 (2012) 170 – 184.

[9] E. Brauns, Salinity gradient power by reverse electrodialysis: effect of model parameters on electrical power output, Desalination 237 (2009) 378–391.

[10] D.A. Vermaas, M. Saakes, K. Nijmeijer, Early detection of preferential channeling in reverse electrodialysis, Electrochim. Acta 117 (2014) 9– 17.

[11] D.A. Vermaas, M. Saakes, K. Nijmeijer, Enhanced mixing in the diffusive boundary layer for energy generation in reverse electrodialysis, J. Membr. Sci. 453 (2014) 312–319.

[12] J. Veerman, M. Saakes, S.J. Metz, G.J. Harmsen, Reverse electrodialysis: performance of a stack with 50 cells on the mixing of sea and river water, J. Membr. Sci. 327 (2009) 136–144.

[13] R. W. Baker, Membrane Technology and Applications, Second edition, Wiley, Chichester, (2004) 411-415.

[14] P. Dlugolecki, P. Ogonowski, S.J. Metz, M. Saakes, K. Nijmeijer, M. Wessling, On the resistances of membrane, diffusion boundary layer and double layer in ion exchange membrane transport, J. Membr. Sci. 349 (2010) 369–379.

[15] H. Strathmann, Assessment of electrodialysis water desalination process costs, Proceedings of the International Conference on Desalination Costing, Limassol, Cyprus, 2004, pp. 32-54.

[16] K.S. Kim, W. Ryoo, M.S. Chun, G.Y. Chung, Simulation of enhanced power generation by reverse electrodialysis stack module in serial configuration, Desalination 318 (2013) 79–87.

[17] P. Dlugolecki, A. Gambier, K. Nijmeijer, M. Wessling, Practical potential of reverse electrodialysis as process for sustainable energy generation, Environ. Sci. Technol. 43 (2009) 6888–6894.

[18] P. Dlugolecki, B. Anet, S.J. Metz, K. Nijmeijer, M. Wessling, Transport limitations in ion exchange membranes at low salt concentrations, J. Membr. Sci. 346 (2010) 163–171.

[19] M. Tedesco, A. Cipollina, A. Tamburini, W. van Baak, G. Micale, Modelling the reverse electrodialysis process with seawater and concentrated brines, Desalin. Water Treat. 49 (2012) 404–424.

[20] S. Pawlowski, J.G. Crespo, S. Velizarov, Pressure drop in reverse electrodialysis: experimental and modeling studies for stacks with variable number of cell pairs, J. Membr. Sci. 462 (2014) 96–111.

[21] P. Dlugolecki, J. Dabrowska, K. Nijmeijer, M. Wessling, Ion conductive spacers for increased power generation in reverse electrodialysis, J. Membr. Sci. 347 (2010) 101–107.

[22] J.J. Krol, M. Wessling, H. Strathmann, Chronopotentiometry and overlimiting ion transport through monopolar ion exchange membranes, J. Membr. Sci. 162 (1999) 155-164.

[23] P. Sistat, G. Pourcelly, Chronopotentiometric response of an ion-exchange membrane in the underlimiting current-range. Transport phenomena within the diffusion layers, J. Membr. Sci. 123 (1997) 121-131.

[24] N. Pismenskaia, P. Sistat, P. Huguet, V. Nikonenko, G. Pourcelly, Chronopotentiometry applied to the study of ion transfer through anion exchange membranes, J. Membr. Sci. 228 (2004) 65–76.

[25] A. Kozmai, V. Nikonenko, N. Pismenskaya, O. Pryakhina, P. Sistat, G. Pourcelly, Diffusion layer thickness in a membrane system as determined from voltammetric and chronopotentiometric data, Russ. J. Electrochem. 46 (2010) 1383–1389.

[26] N. Pismenskaya, V. Nikonenko, E. Belova, G. Lopatkova, P. Sistat, G. Pourcelly, K. Larshe, Coupled convection of solution near the surface of ion exchange membranes in intensive current regimes, Russian Journal of Electrochemistry 43 (2007) 307–327.

[27] E. Belova, G. Lopatkova, N. Pismenskaya, V. Nikonenko, C. Larchet, G. Pourcelly, Effect of anion-exchange membrane surface properties on mechanisms of overlimiting mass transfer, J. Phys. Chem. B 2006, 110, 13458-13469.

[28] C. Larchet, S. Nouri, B. Auclair, L. Dammak, V. Nikonenko, Application of chronopotentiometry to determine the thickness of diffusion layer adjacent to an ion-exchange membrane under natural convection, Adv. Colloid Interface Sci. 139 (2008) 45–61.

[29] E. Volodina, N. Pismenskaya, V. Nikonenko, C. Larchet, G. Pourcelly, Ion transfer across ion-exchange membranes with homogeneous and heterogeneous surfaces, J. Colloid Interface Sci. 285 (2005) 247–258.

[30] C. Rodrigues, V. Geraldes, M. Pinho, V. Semiao, Mass-transfer entrance effects in narrow rectangular channels with ribbed walls or mesh-type spacers, Chem. Eng. Sci. 78 (2012) 38-45.

[31] J. Welty, Ch. Wicks, R. Wilson, G. Rorrer, Fundamentals of Momentum, Heat, and Mass Transfer, 5th edition, Wiley, Danvers, USA (2008), (305-307, 524-533, 542-545).

[32] M.C. Hatzell, B.E. Logan, Evaluation of flow fields on bubble removal and system performance in an ammonium bicarbonate reverse electrodialysis stack, J. Membr. Sci. 446 (2013) 449-455.

[33] J. Veerman, M. Saakes, S.J. Metz, G.J. Harmsen, Reverse electrodialysis: a validated process model for design and optimization, Chem. Eng. J. 166 (2011) 256–268.

[34] J. Veerman, M. Saakes, S.J. Metz, G.J. Harmsen, Electrical power from sea and river water by reverse electrodialysis: A first step from the laboratory to a real power plant, Environ.l Sci. Technol. 44 (2010) 9207–9212.

[35] D.A. Vermaas, J. Veerman, N. Yip, M. Elimelech, M. Saakes, K. Nijmeijer, High efficiency in energy generation from salinity gradients with reverse electrodialysis, Sustain. Chem. Eng. 1 (10) (2013) 1295-1302.

[36] J. Balster, M. H. Yildirim, D.F. Stamatialis, R. Ibanez, R.G.H. Lammertink, V. Jordan, M. Wessling, Morphology and microtopology of cation-exchange polymers and the origin of the overlimiting current, J. Phys. Chem. B 111 (2007) 2152-2165.

[37] N. Pismenskaya, N. Melnik, E. Nevakshenova, K. Nebavskaya, V. Nikonenko, Enhancing ion transfer in overlimiting electrodialysis of dilute solutions by modifying the surface of heterogeneous ion exchange membranes, Int. J. Chem. Eng. (2012) 1-11.

[38] P. Sistat, A. Kozmai, N. Pismenskaya, C. Larchet, G. Pourcelly, V. Nikonenko, Low-frequency impedance of an ion-exchange membrane system, Electrochimica Acta 53 (2008) 6380–6390.

[39] F. Li, W. Meindersma, A. B. Haan, T. Reith, Experimental validation of CFD mass transfer simulations in flat channels with non-woven net spacers, J. Membr. Sci. 232 (2004) 19–30.

[40] C. Larchet, V.I. Zabolotsky, N. Pismenskaya, V.V. Nikonenko, A. Tskhay, K. Tastanov, G. Pourcelly, Comparison of different ED stack conceptions when applied for drinking water production from brackish waters, Desalination 222 (2008) 489–496.

[41] M.S. Isaacson, A.A. Sonin, Sherwood number and friction factor correlations for electrodialysis systems, with application to process optimization, Ind. Eng. Chem. Process Des. Dev. 15 (1976) 313-321.

[42] R. Valerdi-Perez, J. Mengual, Current-voltage curves for an electrodialysis reversal pilot plant: determination of limiting currents, Desalination 141 (2001) 23-37.

[43] V. Geraldes, M.D. Afonso, Limiting current density in the electrodialysis of multi-ionic solutions, J. Membr. Sci. 360 (2010) 499–508.

[44] K. Bouzek, R. Chmelikova, M. Paidar, H. Bergmann, Study of mass transfer in a vertically moving particle bed electrode, J. Appl. Electrochem. 33 (2003) 205–215.

[45] E. Guler, W. Baak, M. Saakes, K. Nijmeijer, Monovalent-ion-selective membranes for reverse electrodialysis, J. Membr. Sci. 455 (2014) 254–270.

[46] F. Helfferich, Ion Exchange, Dover Publications, Inc., New York, 1995, pp. 326-327, 351, 408.

[47] V.V. Nikonenko, N.D. Pismenskaya, E.I. Belova, P. Sistat, P. Huguet, G. Pourcelly, C. Larchet, Intensive current transfer in membrane systems: Modelling, mechanisms and application in electrodialysis, Adv. Colloid Interface Sci. 160 (2010) 101–123.

[48] V.V. Nikonenko, A.V. Kovalenko, M.K. Urtenov, N.D. Pismenskaya, J. Han, P. Sistat, G. Pourcelly, Desalination at overlimiting currents: state-of-the-art and perspectives, Desalination 342 (2014) 85–106.

[49] F.Li, G.W.Meindersma, A.B.D.Haan, T.Reith, Novel spacers for mass transfer enhancement in membrane separations, J. Membr. Sci. 253 (2005) 1–12.

[50] C.P.Koutsou, S.G.Yiantsios, A.J.Karabelas, Numerical simulation of the flow in a plane-channel containing a periodic array of cylindrical turbulence promoters, J. Membr. Sci. 231 (2004) 81–90.

[51] A. Almeida, V. Geraldes, V. Semiao, Microflow hydrodynamics in slits: effects of the walls relative roughness and spacer inter-filaments distance, Chem.l Eng. Sci. 65 (2010) 3660-3670.

[52] R. Kodym, P. Panek, D. Snita, D. Tvrznık, K. Bouzek, Macrohomogeneous approach to a two-dimensional mathematical model of an industrial-scale electrodialysis unit, J. Appl. Electrochem. 42 (2012) 645–666.

[53] K. Bouzek, S. Moravcova, J. Schauer, L. Brozova, Z. Pientka, Heterogeneous ion-selective membranes: the influence of the inert matrix polymer on the membrane properties, J. Appl. Electrochem. 40 (2010) 1005–1018.

[54] J. Choi, S. Moon, Pore size characterization of cation-exchange membranes by chronopotentiometry using homologous amine ions, J. Membr. Sci. 191 (2001) 225–236.

[55] A.A. Moya, P. Sistat, Chronoamperometric response of ion-exchange membrane systems, J. Membr. Sci. 444 (2013) 412–419.

[56] A.H.Galama, D.A.Vermaas, J.Veerman, M.Saakes, H.H.M.Rijnaarts, J.W.Post, K. Nijmeijer, Membrane resistance: the effect of salinity gradients over a cation exchange membrane, J. Membr. Sci. 467 (2014) 279–291.

[57] O. Scialdone, A. Albanese, A. D'Angelo, A. Galia, C. Guarisco, Investigation of electrode material-redox couple systems for reverse electrodialysis processes. Part II: experiments in a stack with 10–50 cell pairs, J. Electroanal. Chem. 704 (2013) 1–9.

[58] M. Tedesco, A. Cipollina, A. Tamburini, I.D.L. Bogle, G. Micale, A simulation tool for analysis and design of reverse electrodialysis using concentrated brines, Chem. Eng. Res. Des., DOI: 10.1016/j.cherd.2014.05.009.

[59] A. Daniilidis, D. A. Vermaas, R. Herber, K. Nijmeijer, Experimentally obtainable energy from mixing river water, seawater or brines with reverse electrodialysis, Renew. Energy 64 (2014) 123-131.

[60] J.L.C. Santos, V. Geraldes, S. Velizarov, J.G. Crespo, Investigation of flow patterns and mass transfer in membrane module channels filled with flow-aligned spacers using computational fluid dynamics (CFD), J. Membr. Sci. 305 (2007) 103–117.

[61] F. Li, W. Meindersma, A. B. de Haan, T. Reith, Optimization of commercial net spacers in spiral wound membrane modules, J. Membr. Sci. 208 (2002) 289–302.

[62] R. Kodym, F. Vlasak, D. Snita, A. Cernin, K. Bouzek, Spatially two-dimensional mathematical model of the flow hydrodynamics in a channel filled with a net-like spacer, J. Membr. Sci. 368 (2011) 171–183.

Chapter

4

PRESSURE DROP IN REVERSE ELECTRODIALYSIS: EXPERIMENTAL AND MODELING STUDIES FOR STACKS WITH VARIABLE NUMBER OF CELL PAIRS

SUMMARY

Reverse electrodialysis (RED) is a sustainable technology for salinity gradient energy harvesting. In order to make the process economically competitive, it is desirable to operate it at the highest possible net power density, which depends on the RED stack geometry and on pressure drop along its pathways and, thus, on the energy spent for solutions pumping. The fluid flow in RED stacks generally occurs in rectangular compartment channels, equipped with spacers. The effects of spacers design and properties have been studied extensively in recent years. However, the other possible causes for in a RED stack and their relative impact on the process performance have not yet been systematically studied. In this study the partial pressure drops in (1) distribution ducts, (2) branches, (3) beams, (4) due to sudden section expansion between the beam and the compartment channel and (5) in the compartment channel were taken into consideration. A model for the total pressure drop inside a RED stack, with a parallel fluid flow distribution through the compartments, is proposed and experimentally validated for lab-scale RED stacks with sheet flow spacers and compared with an open channel (spacer-free) design. The importance of each partial pressure drop was then evaluated quantitatively through model simulations for industrial-scale stacks with an increasing number of cell pairs. It was found that the net power density decreases when the cell-pair number increases, since the partial pressure drop in the branches becomes dominant. Moreover, the possible reasons for a non-uniform fluid flow distribution are discussed, thus making the proposed model useful for planning and/or optimization of RED stacks design.

Published as: S. Pawlowski, J.G. Crespo, S. Velizarov, Pressure drop in reverse electrodialysis: experimental and modeling studies for stack with variable number of cell pairs, Journal of Membrane Science 462 (2014) 96-111.[1]

Graphical abstract:

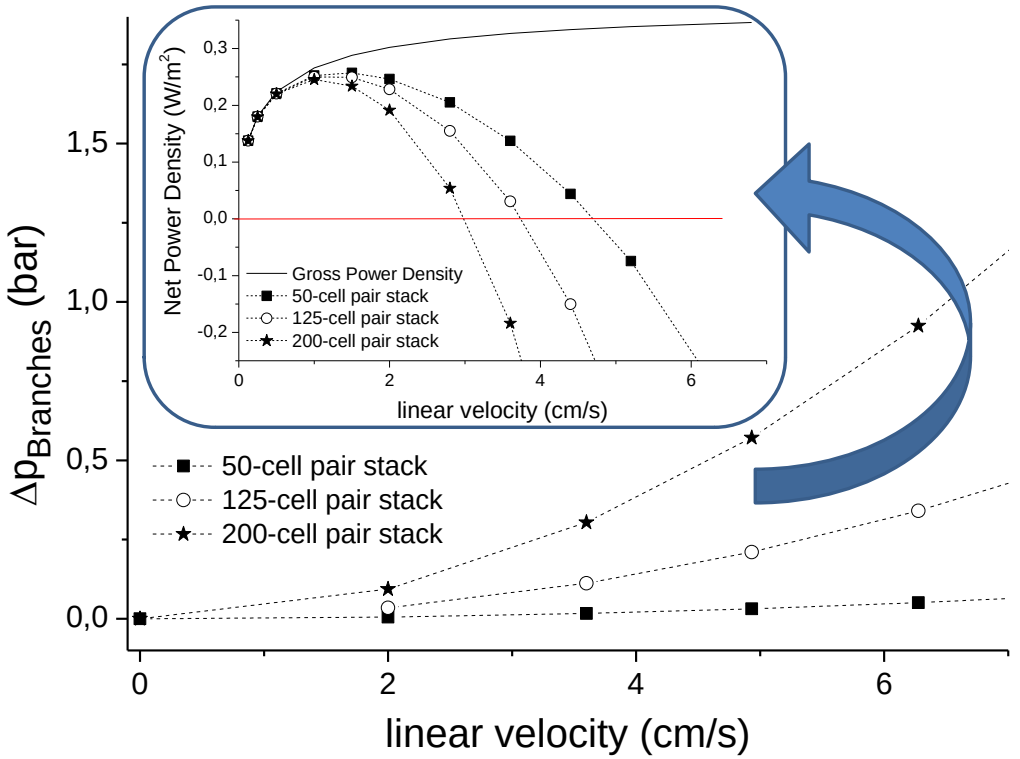

Highlights

- A mathematical model for pressure drop simulation inside RED stacks is proposed.
- Guidelines for planning and/or optimization of RED stacks are derived.
- For large-scale stacks, the partial pressure drop in the branches becomes dominant.
- At identical hydrodynamic conditions, net power density depends on cell-pair number.

Keywords: Pressure drop, Cell-pair number, Manifolds, Net power density

4.1. INTRODUCTION

Salinity gradient energy, first time described in 1954 [1], is classified as a renewable, sustainable and clean energy source [2-6]. It is based on an energy release, when two aqueous streams of different salinity are mixed. The process does not produce emissions which may interfere with the global climate change; the fuel cost is none; and via the continuous Earth's cycle of water (evaporation/precipitation), this source is non-periodic, thus a stable power supply can be guaranteed.

The chemical energy associated with solvation of salts can be quantified in terms of Gibbs' free energy. For example, the global power of salinity gradient energy due to rivers' discharge into the oceans has been estimated to be in the range from 1.4 TW to 2.6 TW [6-7]. However, at random mixing of the solutions, the system quickly reaches chemical equilibrium, without providing a sufficient time to capture the released energy [3]. To harvest a salinity gradient energy (through controlled mixing of aqueous streams of different salinity), several membrane-assisted technologies have been proposed so far: pressure retarded osmosis (PRO) [8-9], capacitive mixing (CAPMIX) [10-11] and reverse electrodialysis (RED) [12-14].

The advantage of RED is the direct conversion of chemical energy of salt solvation into electrical energy [15]. Through parallel flow compartments, formed by alternately arranged cation- and anion-exchange membranes, which are stacked between two electrodes, a concentrated and a dilute saline solutions are distributed, simultaneously. The resulting salinity gradient across the membranes leads to net movement of ions from the concentrated to the diluted saline solution. Ideally, perm-selective ion-exchange membranes would only allow the passage of the respective counter-ions, while excluding the flow of co-ions. Thus, the anions move through the anion-exchange membranes to the anode and the cations move through the cation-exchange membranes to the cathode. For electrical power generation, at the electrode compartments, a suitable redox couple converts the internal flux of ions into a flux of electrons via an external, conductive circuit connecting the anode and the cathode. In such a way, the power output of a RED stack depends on the potential difference, established between the two electrodes, and on the stack internal resistance.

It has been found that reduction in the RED stack channel's thickness and use of spacers can improve the fluid distribution [16], but increases the pressure drop [17-19]. Reducing the flow rates of the two aqueous streams allows for a better fluid flow distribution and lower pressure drop [16, 19], but decreases the gross power density [18-23]. Therefore for characterization of the energy obtainable in a RED stack, the net power density parameter is used, which is

estimated by subtracting the power spent for pumping from the gross power and normalized by the total membrane area [14, 24].

In an optimized RED system the power spent for pumping can consume up to 25 % of the total generated energy [25]. Even when a simplified stack geometry is considered, the demand for pumping power is significant compared to the generated energy, as shown by CFD studies [16, 26]. Therefore correct estimation of pressure drop in RED stacks is crucial, since it directly affects the net power density of the system.

The classical approach to study electrodialysis-related process has been to consider a single membrane pair as a repeating unit in the stack [27]. This approach does not take into account non-uniform fluid distribution inside the stack due to from the pressure variation inside the stack [27]. The Hagen-Poiseuille or Darcy-Weisbach equations have been generally used to calculate pressure drop in flow compartments assuming a fully developed, uniform flow [18, 28-30] and, therefore, equal pressure drop in all compartments. However, calculation of the net power density still depends on the experimental values of the pressure drop, as its theoretical values can be up to 20 times lower than the measured ones [18, 30]. For example, in a 50 cell-pair RED stack, 80 % of the experimentally determined pressure drop was found to be due to the contribution of the manifolds [25].

Moreover, the influence of the cell-pair number has been, so far, only studied experimentally in terms of the stacks' potential difference and internal electric resistance [22, 25-26, 31-32]. An almost linear dependence has been found with a slight deviation at higher cell-pair numbers, which was justified by ionic shortcut currents [31] or internal solutions leakages [26]. In case of a non-uniform fluid flow distribution through the compartments, simulated by CFD, the average gross power density was reduced by only 5 % [26]. In such a way, if the resistance offered by the electrodes' compartments can be neglected, the generated RED stack power can be normalized by the total working membrane area and, thus, the gross power density becomes independent of the cell-pair number.

Through analyzing the current state-of-the-art on the RED technology, it can be therefore concluded that no systematic research has been yet performed, relating the number of cell pairs in a RED stack with the resulting pressure drop and its effect on the net power density.

In the present study, the effect of the cell-pair number on the pressure drop was evaluated both experimentally and through dedicated mathematical modeling. The proposed model was

successfully validated with lab-scale RED stacks, composed by an increasing number of cell pairs with membranes separated either by sheet flow spacers or open (spacer-free) flow channels. Besides estimating the total RED stack pressure drop without significant deviations, the developed model provides guidelines for RED stack design, under non-uniform fluid distribution conditions. Since some of so far ignored partial pressure drops are taken into consideration, a new, and quantitative, perspective over the cell-pair number influence on the net power density achievable in the RED process is presented.

4.2. THEORETICAL PRESSURE DROP MODEL

The pressure drop in a RED stack depends on the solutions' flow rate and the geometry of the stack. Its estimation allows for determining the required power to pump the feed solutions, and therefore, to obtain the net power density. Figure 4.1 is a schematic representation of a possible plate-and-frame RED stack geometry with symmetrical design, in which the dilute and concentrated saline solutions flows are separated, through equal number of manifolds and compartment channels.

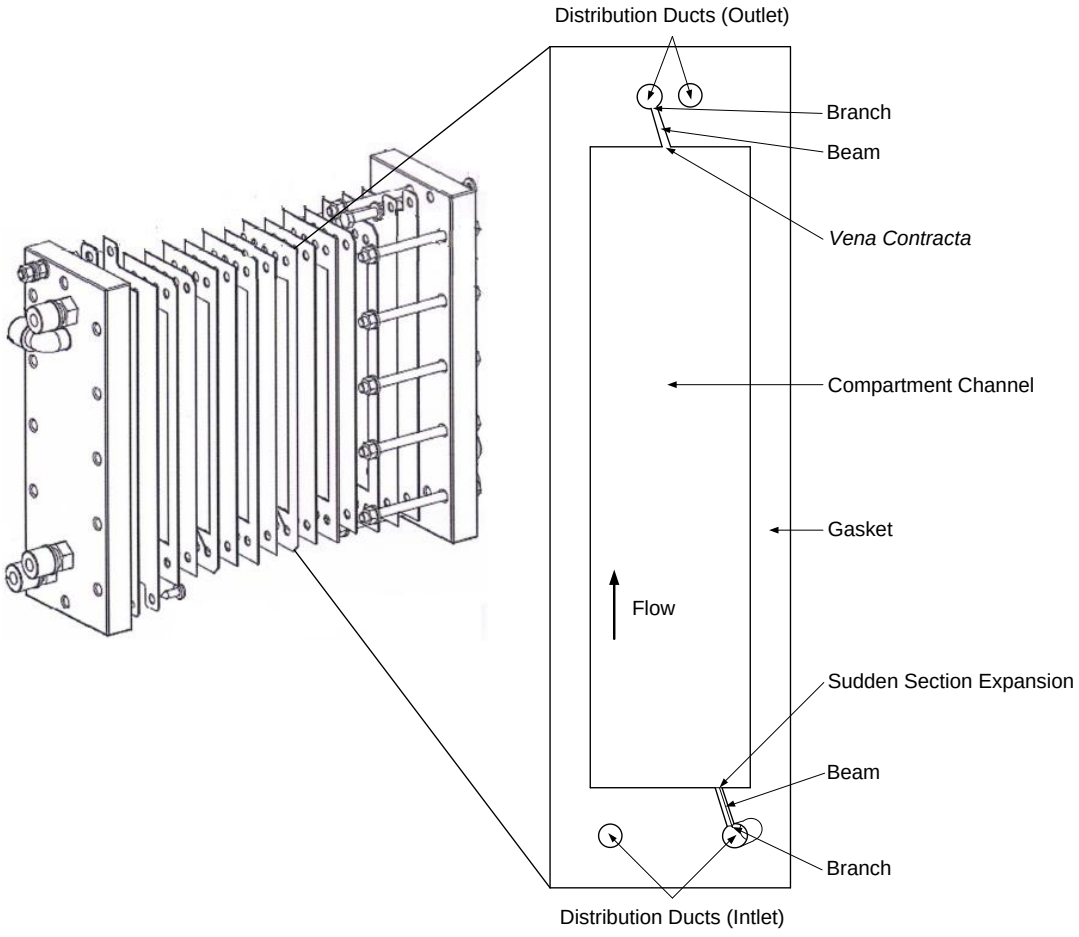

Figure 4.1. Schematic representation of the studied RED stack geometry. (Adapted from the Technical Documentation of Electrodialysis unit EDR-Z-MINI of MEGA a.s.)

The respective partial pressure drops in such a stack are:

- in the inlet and outlet distribution ducts,
- due to branches, associated with the compartment inlet and outlet, situated between the respective distribution duct and beam,
- in the connecting beams between the distribution ducts and a compartment channel,
- due to sudden section expansion between an inlet beam and a compartment channel,
- inside a compartment channel.

In lab-scale RED stacks, a uniform fluid flow and distribution has been usually considered [18, 28-30]. However, with an increasing cell-pair number, the probability of a non-uniform fluid flow distribution inside the system increases significantly [27].

In the present study, for the case of lab-scale stacks with small number of cell pairs, it was considered that the fluid distribution is uniform and that the linear flow velocity in the stack depends on the fluid position in the stack, the number of cell pairs (N), total inlet volumetric flow rate (Q) and the respective cross flow section. As the linear fluid flow velocity thus varies along its course through the stack, due to different cross-flow sections in the different constituent parts of the stack, the inlet volumetric flow rate (Q) is considered as the input variable for pressure drop calculations. The respective model equations are presented in Appendix 4A.

To predict the linear fluid flow velocity in for industrial-scale RED stacks, the flow distribution has been treated statistically and the frequency distribution (ξ) of the velocity ratio has been determined as follows [27, 33-36]:

$$\xi = \frac{u^* - \bar{u}}{\bar{u}} \qquad (4.1),$$

where u^* is the local real linear flow velocity in each compartment and $\bar{u}$ is the average linear velocity in the compartments, which is calculated as for the case of a uniform fluid distribution. It has been found experimentally that the mentioned frequency distribution obeys a normal distribution pattern characterized with a given standard deviation (σ) and a minimum linear velocity (u_{min}) equal to [33-36]:

$$u_{min} = \bar{u} \cdot (1 - 3 \cdot \sigma) \qquad (4.2)$$

Therefore the model described in Appendix 4A can be easily transformed for a case of a non-uniform fluid distribution inside the stack, if the linear flow velocity, explicitly or implicitly present, in equations 4A.7, 4A.12, 4A.14, 4A.16, 4A.18, 4A.19, 4A.20, 4A.21, 4A.23, 4A.25 and 4A.26, is transformed as follows:

$$u_{first\ compartment} = \bar{u} \cdot (1 + 3 \cdot \sigma) \tag{4.3}$$

4.3. EXPERIMENTAL

4.3.1. Lab-scale RED stack

An EDR-Z-Mini unit (MEGA a.s. – Czech Republic), equipped with AMH-PES and CMH-PES Ralex-type membranes was used as a RED stack to validate the model. Its geometry and mode of operation correspond to the drawings illustrated in Figures 4.1 and 4A.1. The Ralex heterogeneous ion-exchange membranes are less affected by water osmosis and co-ion transport phenomena [37], which have been identified as possible causes of non-ideal behavior of the membranes at low solution flow rates [38-39].

Each membrane has a working area of 64 cm^2. Twelve different stack arrangements were investigated. The number of cell pairs varied between one and six. The intermembrane distance in the compartments was equal to 0.8 mm, as the used spacers (with or without a spacer mesh) had that thickness. Two titan electrodes with a platinum layer closed the stack at the ends by pressing together the membranes and gaskets arrangement. The dimensions of the investigated RED stacks are summarized in Table 4.1.

Table 4.1. Dimensions of RED stacks used for model experimental validation.

Parameter	Lab-scale RED stack
N	1-6
h	0.8 mm
ε	0.775 or 1
L_{ch}	160 mm
w_{ch}	40 mm
w_b	1.5 mm
L_b	25 mm
r_d	3 mm
$\delta_{CEM} = \delta_{AEM}$	0.7 mm

4.3.2 Experimental measurement of pressure drop

The pure water at 20ºC (ρ = 998.2 kg/m^3 and μ = 0.100103 Pa.s) was used as the liquid fluid while the total stack pressure drop was measured. Two pressure transducers (Druck, PDCR 910, England) were mounted at the stack inlet and outlet. Through a LabVIEW data acquisition software, the pressure was registered every second during two minutes in each case. In such a way, the experimental pressure drops were obtained for the first node, as represented at Figure 4A.1. The investigated solution inlet flow rates were in the range of 0.28 to 4.88 cm^3/s, and the corresponding linear flow velocities in the compartments channels were calculated assuming a uniform fluid flow distribution, as the stacks had a small number of cell pairs (max. 6).

4.3.3 Model validation

The model equations were used to calculate the total stack pressure drop, through estimating and summing the partial pressure drops, and then compared with experimental pressure drop data. As the values of *K*s needed for calculation of the partial pressure drop in the branches are not tabulated for the lab-scale system geometry investigated (area ratio: S_2/S_3 = 0.042), the model was calibrated with experimental data for one cell pair stack.

The approach of parameters calibration with small stacks, followed by their validation with larger stacks has been successfully used for ionic shortcut currents modeling in RED stacks [31]. Furthermore, the utilization of pressure drop data for one cell pair stack, to calibrate the model, assures a uniform fluid flow distribution, since only one channel exists inside the stack for a given fluid flow. If a stack with more than one cell-pair would be used for model calibration, a possibility for a deviation from a uniform fluid distribution exists, which could lead to an overestimation of the K_{br} coefficient value.

The least-squares sum between model data and experimental pressure drop data was minimized (with a precision up to $1.0 \cdot 10^{-6}$ with Microsoft Office Excel Solver) through variation of the values of the model branches coefficients (*A*, *B* and *C*). These values (Table 4.2) were then used for computing of the partial pressure drop in the branches for experimentally investigated stack configurations.

Table 4.2. Branches coefficients obtained for model calibration with 1 cell pair lab-scale RED stack

Parameter	Lab-scale RED stack
A	-369.52
B	412.41
C	135.47

4.3.4 Model application

4.3.4.1 Interpretation of model physical meaning

In order to simulate the impacts of the partial pressure drops in large-scale RED units, the lab-scale stack with spacers, used in this study, was scaled-up to industrial size dimensions.

The dimensions of a virtual industrial RED stack (Table 4.3), were selected on the basis of the available information about industrial electrodialysis stacks: 100-500 cell pairs between the electrodes [4, 20, 40-41]; membrane area of 1-2 m^2 [20], intermembrane distance in the range 0.3 - 2.0 mm [40]. The ratio between compartment length and width, the section ratio of sudden expansion and the ratio between the distribution duct radius and beam length were maintained the same as in the lab-scale stack.

Table 4.3. Dimensions of hypothetical industrial RED stacks used for estimation of partial pressure drops contributions to the total pressure drop.

Parameter	"Industrial" RED stack
N	50, 100, 150, 200
h	0.8 mm
ε	0.775
L_{ch}	2000 mm
w_{ch}	500 mm
w_b	18.75 mm
L_b	52.125 mm
r_d	6.255 mm
$\delta_{CEM} = \delta_{AEM}$	0.7 mm

In order to select the value for the branch section ratio (the ratio between the cross-flow section of the beam and the distribution duct), a preliminary simulation was performed. It was found that when the branch section ratio increases (through a decrease in the duct radius) the branch coefficient (K_{br}) decreases; however, due to a smaller duct cross flow section, the linear flow velocity in the duct (u_3) increases (eq. 4A.13). Therefore the optimum branch section ratio for minimization of the pressure drop depends on how rapidly K_{br} decreases with an increase in the branch section. From available K_{br} values (for branch section ratios of 0.042, 0.122 and 0.34) [42], the lowest pressure drop is for a branch section ratio of 0.122 and therefore this value was used in the model simulations.

The average linear flow velocity in the simulations was set to be up to 10 cm/s, which is usually considered as the maximum value in case of electrodialysis, when sheet flow spacers are used as separators [4, 40]. A non-uniform fluid flow distribution was considered, with a standard deviation of 0.2, which represents the worst admissible case scenario for electrodialysis stacks [33-34].

4.3.4.2 Calculation of net power density

The influence of the pressure drop on the net power density was simulated in RED stacks similar to that described in Section 4.3.4.1, but with 3 inlets and 3 outlets (as in large-scale electrodialysis stacks of MEGA a.s. [27]) in order to decrease the pressure drop. Therefore the beam dimensions as well the duct diameter changed. The intermembrane distance was varied from 0.8 mm to 0.3 mm. Lower values of intermembrane distance were not possible for the selected branch section ratio (0.122), as the beam width would be higher than the half of the distribution duct perimeter. The dimensions of stacks are resumed in Table 4.4. A non-uniform fluid flow distribution was considered for pressure drop calculations, with a standard deviation of 0.2 in order to allow for a more straightforward comparison with the stack modeled in Section 4.3.4.1.

Table 4.4. Affected dimensions of hypothetical industrial RED stacks with a branch section ratio of 0.122, with 3 inlets and 3 outlets. The intermembrane distance (h) was varied between 0.8 mm and 0.3 mm. The other relevant dimensions are as presented in Table 4.3.

h (mm)	w_b (mm)	L_b (mm)	r_d (mm)
0.30	6.25	18.42	2.21
0.40	6.25	21.27	2.55
0.50	6.25	23.79	2.86
0.60	6.25	26.06	3.13
0.70	6.25	28.12	3.38
0.80	6.25	30.08	3.61

The fluid pressure drop in the stack represents an energy lost and therefore affects the obtained net power density in a RED stack. The power spent for pumping depends on the feed solution flow rate (Q) and the pressure drop (Δp_t) between the stack inlet and outlet:

$$P_{pumping} = 2 \cdot (\Delta p_t \cdot Q) \quad (4.4)$$

The factor 2 appears because two saline solutions (the dilute and the concentrated) are pumped, and their physical properties are similar as the differences in viscosity and density due to water salinity are insignificant (respectively, 7.56 % and 2.59 % for water salinity between 0 and 35 [43]). Certainly, if the difference in the salinity, and therefore in viscosity and density, of the two streams is high, or if the RED process is operated at a different flow velocity for each stream, the pressure drops for the diluted and concentrated pathways must be calculated separately. The energy required for pumping the electrode rinse solution is neglected, as it is commonly done in practical applications of electrodialysis [4], which stack geometry is similar to that of a RED stack.

The gross power density was calculated by the most recently available single membrane pair (SMP) model fed with the therein given typical specifications for a RED stack with spacers (R_{AEM} = R_{CEM} = 1 Ωcm^2, α = 0.97, β = 0.5, NaCl diluted and concentrated solutions concentrations: 0.017 M and 0.51 M respectively) [29]. R_{AEM} and R_{CEM} are the anion- and cation-exchange membrane resistance, respectively, α is the membrane permselectivity, and β is the shadow factor due to spacers "shadow" effect over the membranes. Furthermore, since the channel length was equal to 200 cm, local concentration gradients along the channel length have been considered, as indicated in this model [29].

The net power density can be therefore estimated by subtracting the power spent for pumping from the gross power density:

$$P_{net\ density} = P_{gross\ density} - \frac{P_{pumping}}{2 \cdot N \cdot A_m} \quad (4.5),$$

where A_m is the exposed area of one ion exchange membrane [18, 29].

4.4. RESULTS AND DISCUSSION

4.4.1 Pressure drop – experimental lab-scale data

Figures 4.2a and 4.2b show, respectively, the experimentally determined pressure drop between the inlet and outlet of the investigated lab-scale stack configurations with spacers and with open (spacer-free) channels, for flow rates ranging from 0.28 cm^3/s to 4.88 cm^3/s. In Figures 4.2c and 4.2d, the measured pressure drop is expressed as a function of linear flow velocity in the compartments' channels, calculated by eq. 4A.26.

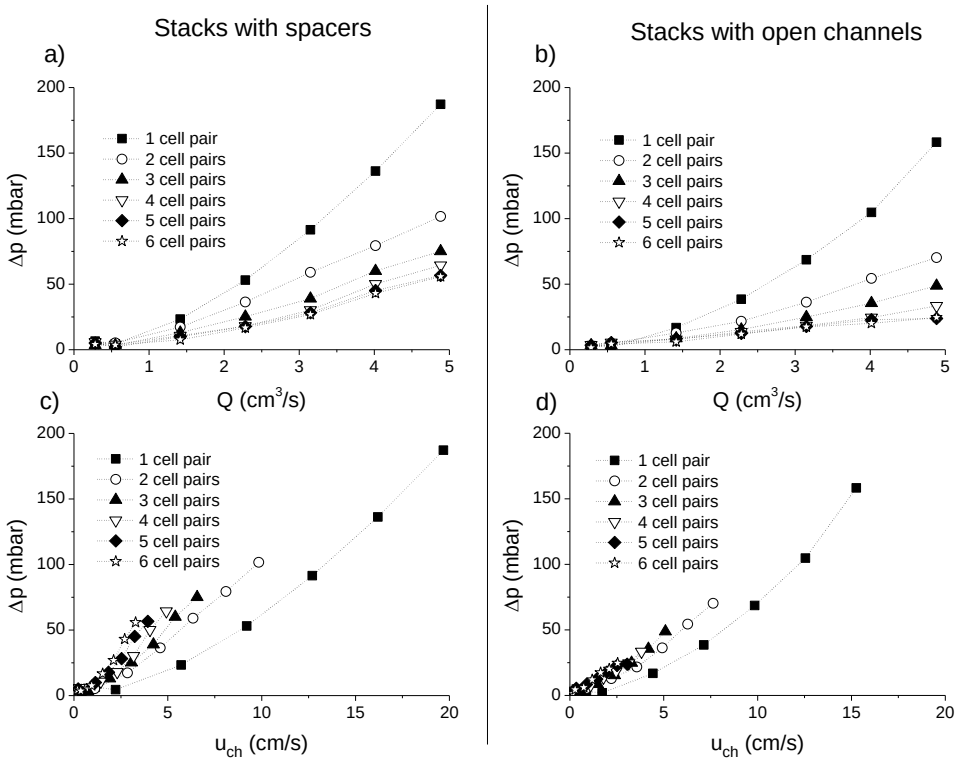

Figure 4.2. Experimental pressure drop in 1-6 cell pair RED stacks in function of the inlet volumetric flow rate (Q) or linear velocity inside the compartment (u_{ch}).

As expected, for the same cell-pair number and flow rate, the pressure drop in the stacks with spacers is higher (in average 1.55 times higher) than in stacks with open channels, as the presence of spacers, besides causing an additional hydraulic friction, increases the linear flow velocity.

An increase in the stack cell-pair number caused a decrease in the pressure drop for the same flow rate, as the linear flow velocity was reduced. However, this effect is not directly proportional, because the differences between the linear flow velocities become minor as the number of cell pairs increases. Also, as each new cell pair induces a need for longer ducts and new branches, a less uniform fluid flow distribution through the compartments is expected, which increases the pressure drop. Due to existence of partial pressure drops through the fluid route from the inlet toward the last compartment, the fluid energy is continuously lost. Therefore, as further away is a given compartment from the stack inlet, the lower will be the fluid pressure at the entrance of that compartment [42, 44]. Consequently, as the cell-pair number increases, the fluid flow rate in the first compartment is higher than the respective average flow rate value, and, thus, the total experimentally determined pressure drop becomes slightly higher than it would be the model prediction under ideal (uniform) fluid distribution conditions.

For the same linear flow velocities (Figures 4.2c and 4.2d), the pressure drop increased with the cell-pair number. As previously explained, a non-uniform fluid flow distribution more likely occurs at higher cell-pair number and thus it could cause a higher total pressure drop. Moreover, while the number of cell pairs increases, the inlet solution flow rate must rise to maintain constant the linear flow velocity inside the compartments; however, at the same time the cross flow section of the distribution duct remains constant. In result, the linear flow velocity in the distribution duct increases and therefore the pressure drops in the distribution ducts, and consequently in the branches, become higher. This behavior also indicates that, for the same linear flow velocity, the cell-pair number has an influence on the net power density.

4.4.2 Pressure drop – model adjustment

In Figures 4.3 and 4.4, the measured experimental pressure drops, in RED stacks with one to six cell pairs, are compared with the model predictions. As mentioned in Section 4.3.3, the values of the *A*, *B* and *C* parameters, presented in Table 4.2, and required for the branch coefficient (K_{br}) calculation, were computed from experimental data for a 1 cell-pair stack and then used in the model simulations.

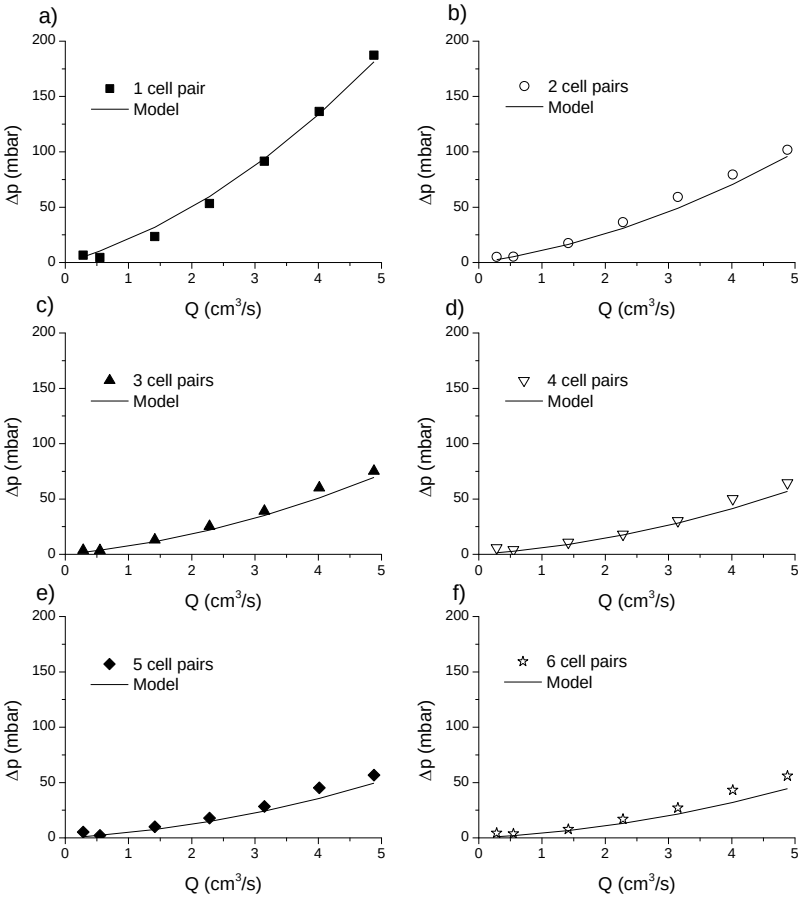

Figure 4.3. Model adjustment to experimental pressure drop data for 1-6 cell pair lab-scale RED stacks with sheet flow spacers inside the compartment channels.

The observed slight deviations of the model predictions from the experimental data in Figure 4.3, relatively to the data obtained for stacks with spacers with more than one cell pair are most probably due to deviation of the flow distribution from the uniformity condition assumed for lab-scale stacks. As the cell-pair number increases, a less uniform fluid flow distribution through the stack compartments occurs due to existence of pressure drops between each new compartment. Those pressure drops increase with increasing fluid flow rate. Thus, according to the piezometric head [42, 44], the flow in the first compartment is higher than in the last compartment. In such a way, the experimental pressure drop values are higher than those predicted by the model because the flow rate in the first compartment is higher than the assumed average value.

The model adjustment to pressure drop data for the stacks with spacers (Figure 4.3) resulted in a 25 % lower least-squares sum than in case of adjustment to pressure drop data of the stacks with open channels (Figure 4.4). The presence of spacers promotes turbulence and, therefore, a more uniform fluid flow distribution inside the compartments, but at the cost of a higher pressure drop inside the compartments (almost 8 times higher than in an open channels design, according to the model). This difference is due to a lower residence time of the solutions and a smaller hydraulic diameter caused by the presence of spacers. The spacer porosity affects the pressure drop in the compartments channel to the power - 4.2 (R^2 = 0.98 for ε between 0.1 and 1 with $\Delta\varepsilon$ = 0.1). Therefore, for example, a decrease in the spacer porosity from 0.8 to 0.4 would increase the pressure drop in the compartment channel almost 29 times.

The partial pressure drop due to sudden section expansion between the beam and the compartment channel is also influenced by the spacers. The degree of spacer porosity influence depends on the beam and compartment's width, but it is always higher than zero as a reduction of the cross flow section area in the compartment has a stronger impact than an increase in linear flow velocity in the compartments. In result of spacer presence, the section ratio between the compartment and the beam was reduced from 26.7 to 20.7. However, the beneficial aspect of spacers in the investigated lab-scale stack was modest as the reduction in pressure drop due to sudden expansion was only 2.25 % compared to a spacer-free stack design. In consequence, the spacers' presence had an overall harmful impact, due to their stronger contribution for an increase in the pressure drop inside the compartments.

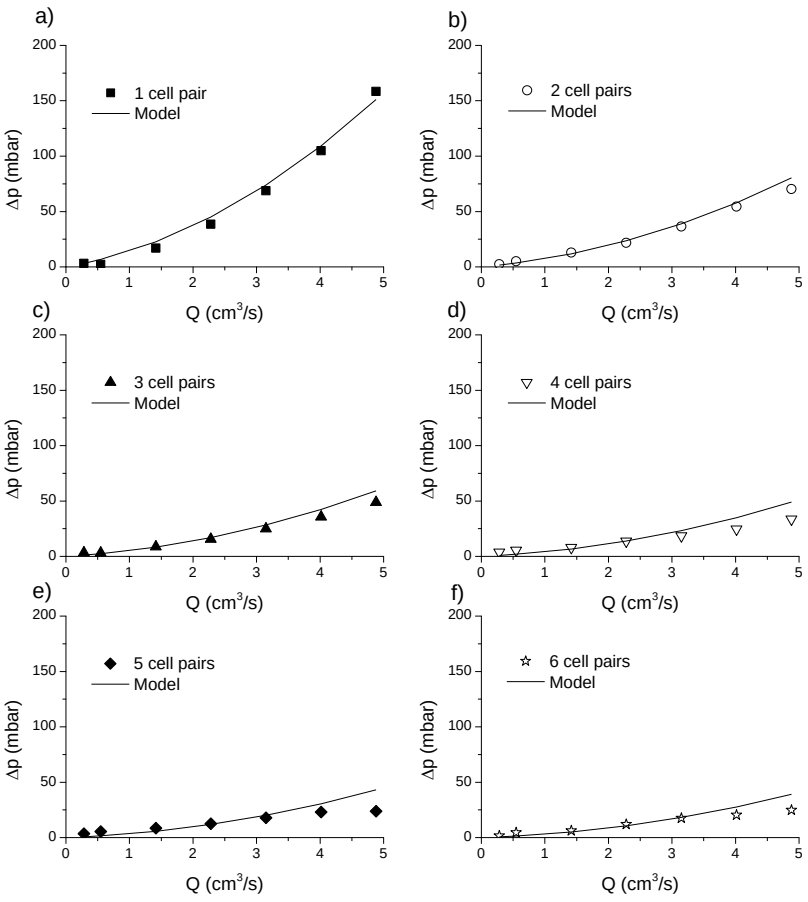

Figure 4.4. Model adjustment to experimental pressure drop data for 1-6 cell pair lab-scale RED stacks with open (spacer-free) compartment channels.

For spacer-free stacks (Figure 4.4) the model predicts slightly higher pressure drop values than the experimentally measured ones. This behavior is more accentuated at higher flow rates and in stacks with a higher number of cell-pairs. The intermembrane distance in the stacks with open channels is maintained by gasket situated on the membrane borders, which leaves all membrane area in contact with the solutions flow without any rigid support. Therefore in case of a non-uniform fluid flow distribution, which is favored at high linear velocities [16] or with increasing number of the compartments [42], a higher fluid flow rate in the first compartment could cause enlargement of the compartment thickness by exerting higher pressure on one of the membrane side. Such an increase of the intermembrane distance (*h*) would cause the measured pressure drop to be lower than the expected one, especially if the partial pressure drop inside the compartment channel is considered. The pressure drops at the distribution ducts, beams and branches can be also affected by varying the intermembrane distance and, under idealized conditions of perfectly uniform fluid flow distribution they are expected to be the same in the stacks with spacers and in the stacks with open channels, as nothing in their constitution differs between the stacks. From a practical viewpoint, if an open channel design is to be chosen, the

membranes must be thick and sturdy in order to prevent channels collapse [20]. Such properties are much more likely to be provided by heterogeneous ion-exchange membrane like the ones used in the present study.

Overall, the model predictions show a good adjustment to the experimental data, even despite of the assumption that the fluid flow is uniformly distributed. As the partial pressure drops in the duct and due to branches, which may cause a non-uniform fluid distribution, decrease while the fluid is distributed through the compartments, the differences in the flow rates between each new compartment vanish, which justifies the applicability of the model. While the pressure drop in the duct is clearly negligible (its contribution to the total pressure drop is always below 0.071 %), the pressure drop due to branches has a much higher impact (up to 74 % of total pressure drop in 6-cell pair spacer-less stack with fluid flow rate of 4.88 cm^3/s). As that partial pressure drop depends on the second power of the flow rate, the adjustment of the model is better at lower flow rates, when the pressure drop contribution due to branches is expected to be smaller, and therefore the hydrodynamic conditions are closer to a uniform fluid flow distribution through the compartments as assumed in the model.

To obtain an exact prediction of the pressure drop in lab-scale RED stacks with more than one cell pairs, a non-uniform fluid flow distribution should be considered. However, as successive approximations made case by case would be required [42], the advantages of a straightforward generalization to other geometries, cell-pair numbers, etc., allowed by the model, since all required parameters are accessible, would be lost.

4.4.3 Pressure drop - model physical meaning

Besides providing a value of the expected total pressure drop in a RED stack, the developed model can be used to identify the importance of each partial pressure drop inside the stack.

As it was found out for the studied lab-scale stack, a slightly non-uniform fluid flow distribution was already observable for stacks with just 4-5 cell pairs. Therefore the traditional approach of using a single cell pair as a repeating unit cannot be applied when the pressure drop is considered, especially in case of industrial-scale stacks, which are presumably composed by a relatively high number of cell pairs. The proposed model overcomes this limitation, since the influence of cell-pair number is included in all considered partial pressure drops. Furthermore, the used statistical approach for considering the fluid distribution through the stack compartments as non-uniform has been found to be valid in two different industrial electrodialyzers [27, 34].

Since in case of absence of any support in the channels of large RED stacks, a non-uniform fluid distribution can cause changes in the intermembrane distance, and eventually a channel may collapse; the intermembrane distance was simulated for the case with spacers.

The contribution of each partial pressure drop was analyzed for scaled-up stacks with a different number of cell pairs in function of the inlet flow rate (Figure 4.5) and the average linear flow velocity inside the compartments (and in the first compartment) (Figure 4.6).

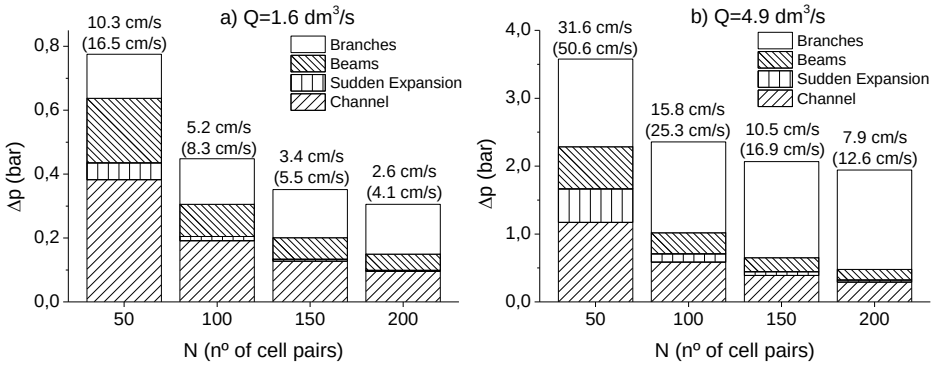

Figure 4.5. Partial pressure drop simulations for a 50-, 100-, 150- and 200- cell pair RED stack with industrial-scale dimensions for two constant inlet volumetric flow rates: (a) 1.6 dm^3/s and (b) 4.9 dm^3/s. Above each bar, the compartments' average linear flow velocity and between the parenthesis the linear flow velocity in the first compartment are indicated, respectively.

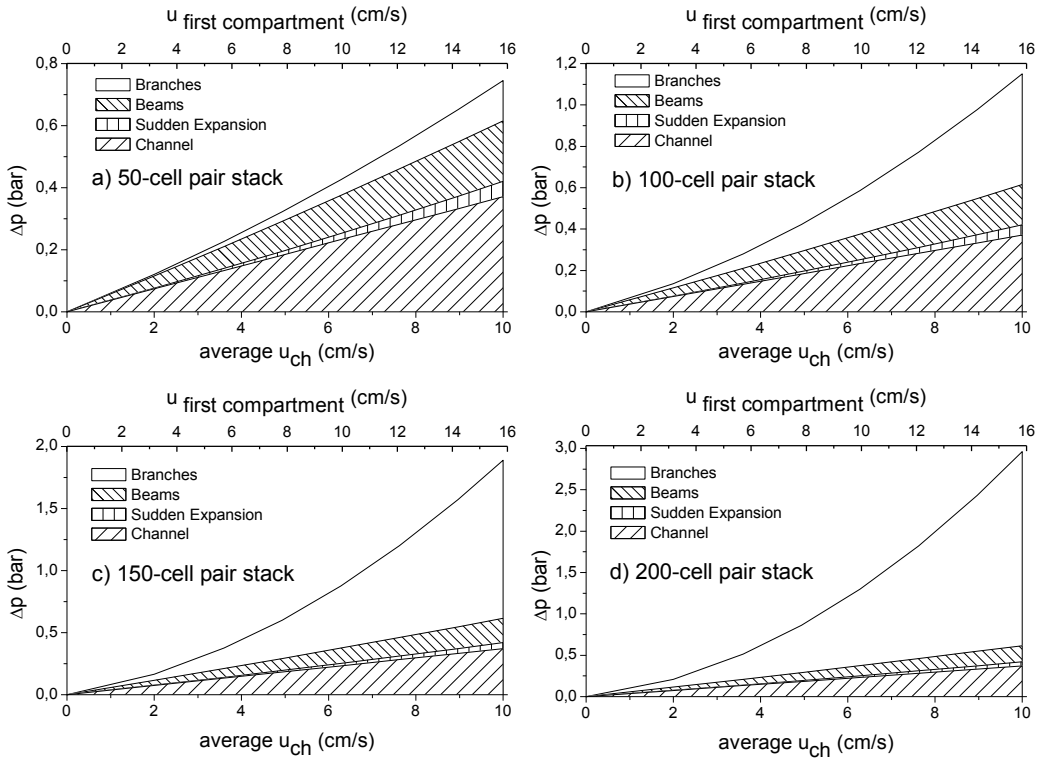

Figure 4.6. Partial pressure drops simulations for an average linear flow velocity of up to 10 cm/s (up to 16 cm/s considering the linear velocity in the first compartment) for: (a) 50-, (b) 100-, (c) 150- and (d) 200- cell pair RED stack with industrial-scale dimensions.

The flow rate (Figure 4.5) is the parameter that is important for determining the power generation, as it represents the quantity of ions available to be transported and therefore the amount of available energy to be harvested. For example, if the quantity of water is a limiting factor (which is pointed as the second major global concern, after the energy harvesting [45]), lower solution flow rates are required to ensure high power generation efficiency [30, 38]. On the other hand, the linear flow velocity inside the compartments (Figure 4.6) is one of the main parameters, determining the hydrodynamic conditions for ionic transport through the membranes [18, 20-23].

Increasing the values of both parameters always causes higher partial pressure drops, but as it can be seen, their respective contributions to the total pressure drop depend on the cell-pair number. The pressure drop in the distribution duct is not shown since its contribution to the total pressure drop was always lower than 0.045 % and can be therefore neglected. The dependence of the partial pressure drops on the power of the relevant parameters is summarized in Table 4.5, which can be used as a basis for a proper RED stack design in order to minimize its pressure drop.

Table 4.5. Parameters power influence on partial pressure drops.

Parameter	Channel	Sud. Exp.	Beam	Branch	D. Duct
Q	1	2	1	2	1
N	-1	-2	-1	-0.152[a] or 0.12[b]	-
h	-3	-2	(-)[c]	(-)[c]	(+)[d]
ε	-4.2[e]	(+)[c]	-	-	-
L_{ch}	1	-	-	-	-
w_{ch}	-1	(+)[c]	-	-	-
d_b	-	(-)[c]	-4	(-)[c]	-
w_b	-	(-)[c]	(-)[c]	(-)[c]	-
L_b	-	-	1	-	-
r_d	-	-	-	(+/-)[f]	-4

[a] For A, B, C from Table 4.2 and N between 2 and 102 with $\Delta N = 20$, with $R^2 = 0.95$.

[b] For tabulated K's for branch ratio of 0.122 [42] and N between 50 and 200 with $\Delta N = 50$, with $R^2 = 0.99$.

[c] Numerical value of power depends on the other parameters (the sign of the power is shown).

[d] $L_d = h + \delta_{CEM} + \delta_{AEM}$.

[e] For ε between 0.1 and 1 with $\Delta\varepsilon = 0.1$, with $R^2 = 0.98$.

[f] If K_{br} increases faster than u_3 decreases (Eq. 4A.13), while the r_d increases, the pressure drop increases; if not, the pressure drop decreases.

Considering partial pressure drops affected by the spacer's porosity, when the number of cell pairs increases, for the same flow rate (Figure 4.5), the pressure drop due to sudden expansion decreases faster (to power -2) than the pressure drop in the compartment's channel (to power -1). In such a way, the influence of the partial pressure drop in the compartments for RED stacks becomes more important with increasing number of cell pairs, and therefore it can be concluded that spacers with more open structure would be desirable. An increase in the solution's flow rate eventually would lead to the opposite conclusion, since the partial pressure drop due to sudden section expansion depends on power 2 of the flow rate, while the partial pressure drop in the compartment channel depends on power 1 of the flow rate.

In any case, the most important partial pressure drop, under the studied conditions, is located in the branches. This becomes more evident with increasing the flow rate/linear velocity. For example, in a 50-cell pair stack, in which 80 % of that stack pressure drop was due to manifolds, a parabolic curve showed a good adjustment between the pressure drop and the flow rate [25]. This is in agreement with our model predictions as the pressure drop in the branches depends on power 2 of the flow rate. At low flow rates, the pressure drop due to branches is less important; however, with increasing number of cell pairs, the partial pressure drop due to branches could become dominant at any flow rate, because the increase in the cell-pair number has the lowest beneficial influence on that partial pressure drop from all partial pressure drops (to power -0.152 for the lab-scale stack or to power 0.12 for the simulated industrial-scale stack). Also at the same linear velocities range, the pressure drop in the branches becomes dominant as the number of cell pairs increases because, beside that partial pressure drop and the pressure drop in the duct, all other partial pressure drops remain constant (Figure 4.6). This is also a reason for a non-uniform fluid flow distribution as, due to the pressure drop in the branches, the fluid energy is progressively reduced along the distribution duct as explained in Section 4.4.1.

4.4.4 Model application to different RED stack designs

There are other possible designs of the flow path, in which the fluid passes directly from the distribution duct to the channels [18, 22, 25, 31, 38, 46-47], or in which the beam has a geometrical form different from the rectangular one [17], as for example in the case of Eurodia electrodialysis stacks [48]. Since the model equations for each partial pressure drop are inter-independent, they can be modified according to the exact shape of a given RED stack. In any case, the problem of a non-uniform fluid distribution, and its increase with increasing the number of cell pairs, will exist independently of the shape of the spacer gasket. The pressure drop due to branches (of different shapes, with or without a beam) will eventually become

dominant with the increase of the number of cell pairs, for any RED stack geometry in which the fluid distribution is parallel (as shown in Figure 4A1).

For the case, in which the fluid passes directly from the distribution duct to the compartments channels, the partial pressure drop in the beam will be zero since the beam length is zero. In what concerns the pressure drop in the branches, the model required K_{br} coefficient can still be obtained as described in section 4.3.3.

In another possible configuration, the fluid can pass consecutively from one compartment to another, from the stack inlet to the stack outlet. In such a configuration, only one single pathway exists for each of the two streams, what could lead to a high pressure drop, since the linear flow velocity should be relatively high in order to provide a sufficient degree of mixing throughout the entire solution volume inside the stack. Also as the number of cell pairs increases, the maximum values of power, current density, and ion flux will decrease [49]. Therefore, in our understanding, such a design is less appropriate for the RED process, despite of being sometimes used in traditional electrodialysis.

4.4.5 Guidelines for pressure drop minimization inside RED stacks

As discussed in the previous sections, the pressure drop in RED stacks does not only affect the net power density of the system, in terms of energy spent for solutions pumping, but also influences the flow distribution. A non-uniform fluid distribution, also referred to as preferential channelling [50], can lead to an increase of the non-ohmic resistance. Moreover, in electrodialysis stacks, the membranes may suffer deterioration due to a rise in local temperature in zones with low linear flow velocity, as the current density in such zones may become over-limiting [27].

Therefore the performed analysis might be used for providing clues for a more adequate stack design and/or optimization in terms of minimizing its pressure drop. Possible strategies in this direction could be:

- Proper sizing of the cross flow section.
- Use of multiple stack inlets and outlets.
- Use of multiple beams connecting a distribution duct with a compartment channel.
- Providing a more opened spacer structure.

Sizing the cross flow section in order to provide the same hydraulic resistance in all pathways can provide a more uniform fluid flow distribution effect [51]. For example, progressive enlargement of the beam width in each new compartment, as further away it is situated from the stack inlet, would decrease the pressure drops in the beams, due to sudden expansion and in the branches (Table 4.5). This gain on fluid pressure could compensate the additional pressure drops that affect the fluid energy on the way to the compartments and, therefore, provide a more uniform fluid distribution through the compartments.

Another possibility is the use of a double inlet–double outlet configuration [16, 26] instead of the usually applied single inlet–single outlet stack configuration. In such a way, the fluid flow rate is divided and the fluid route becomes shorter, which combined could ensure lower pressure drops and therefore a more uniform fluid distribution through the stack compartments. However, such a symmetrical feeding configuration is technically more complex and expensive [16].

The same principle of fluid flow division could be applied to the beams. As the pressure drop in a beam depends on the cell-pair number to power -1, implementing multiple entrance and exit holes on the spacers' ends could reduce the pressure drop, besides promoting a more uniform flow distribution over the width of the compartments as it has been accomplished for fluid and gas distribution in a multi-hole distributor inside the header [52].

For an infinite number of beams, the situation will approximate to the case of a completely open passage from the distribution duct to the compartment channel, which is known as slot [53]. However, such distribution design may lead to a deformation of the ion-exchange membranes and to a consequent solution leakage [53]. A complete absence of the beams is another possibility, but as mentioned in the previous section, the proposed model can still be used, since the values of the relevant parameters could be determined by the methodology described in Section 4.3.3.

The final challenge is related with the design of the compartment channels. We will analyze this point separately in the next section since the channel's thickness has one of the strongest effects on pressure drop in the compartments (to power -3); however, in practice, the channel's thickness cannot be too large, as this will cause higher electric resistance in the compartments [18], especially in those fed with the solution of lower salinity [18, 20-21, 25].

Furthermore, a more opened spacer structure (the limit being a spacer-less configurations, ε=1) is preferable for pressure drop reduction in the compartments. This is consistent with previous studies demonstrating that mixing promoters are not effective within the flow velocity range adequate for power generation [19], their absence have a positive effect on the gross power generation, as the spacer "shadow" effect is removed [19, 22, 25, 47], and that the set-ups without spacers appear less sensitive to fouling [54]. Therefore it is desirable that such a design would be applied in large-scale stacks, if a uniform fluid distribution could be assured. Improvement of fluid distribution could also enable construction of stacks with higher nº of cell pairs, and, therefore, with shorter channels for the same total membrane area. Shorter channels means shorter residence time, lower non-ohmic resistance (due to smaller concentration gradient along the channel length), lower pressure drop in the channel, and, ultimately, higher net power density [18, 29, 55-56].

4.4.6 Power generation in large-scale RED stacks

So far it has been generally found that with increasing linear flow velocity in RED stacks, the power needed for pumping increases faster than the gross power density, which eventually results in negative net power densities [18, 25-26, 30, 38]. In Figure 4.7, the same behavior can be observed.

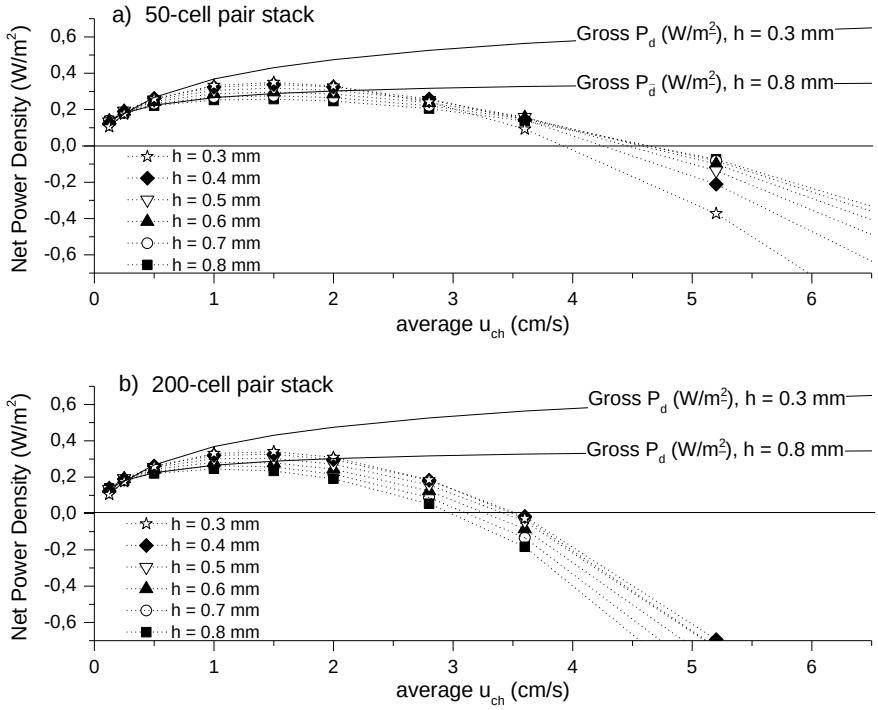

Figure 4.7. Model values for net power density for (a) 50- and (b) 200-cell pair stacks (with 3 inlets and 3 outlets; and with branch ratio of 0.122) in function of the compartments' average linear velocity. The values of gross power density, for two extreme intermembrane distances of 0.8 mm and 0.3 mm, are presented.

Besides this agreement with previous findings, our model prediction shows (Figure 4.7) that for the same linear flow velocity in the compartments and, therefore, for the same fluid dynamic conditions for the ionic transfer through the membranes, the net stack power decreases when the cell-pair number increases (from 50 cell pairs in Figure 4.7a to 200 cell pairs in Figure 4.7b). This is caused by an increase in the pressure drop with increasing the cell-pair number. At the end of Section 4.4.1, this effect was discussed qualitatively. Here the developed model shows quantitatively that the dependences on the power, of flow rate and cell-pair number, are both non-symmetrical in cases of partial pressure drops in the branches and in the distribution duct (Table 4.5). Physically, this is manifested by an increase of these partial pressure drops with increasing cell-pair number. Thus, the net power densities of identical stacks (providing the same gross power densities) decrease with an increasing number of cell pairs (Figure 4.7).

This behavior becomes more pronounced as the linear flow velocity increases. According to the developed model, for the same linear flow velocity, the partial pressure drop in the branches is the main cause for the pressure drop increase, when the number of cell pairs increases. Since the contribution of the partial pressure drop in the branches grows with the flow rate, the derived effect is more evident for a higher linear flow velocity.

At low flow rates (a condition which is more adequate for a positive net power generation) the impact of the cell-pair number is reduced, as the partial pressure drop in the branches becomes less important. Therefore it seems that using one large stack does not impair the obtainable net power density. In case of using several smaller stacks instead of one large stack, the additional costs of applying more electrodes could justify the use of the latter. However, performance of an economic study for each particular case is still advisable in order to compare the possible benefits and drawbacks of using multiple smaller stacks instead of one large stack.

As expected (Section 4.4.5), including more inlets and outlets in the stack reduces the partial pressure drops in the beams and due to sudden expansion (Figure 4.6a vs. Figure 4.8c and Figure 4.6d vs. Figure 4.8d), because of division of the total inlet volumetric flow into smaller streams disposed in parallel. As decreasing the pressure drop in the duct improves the fluid distribution, and multiple entrances into the compartments allow for a better fluid distribution inside them, it is expected that all partial pressure drops should decrease. This difference is not directly seen between the simulations as the standard deviation was maintained constant and equal to 0.2, in order to perform a more straightforward comparison between the modeled stacks. In practice, the standard deviation value will be lower in a stack with multiple inlets and outlets than in a stack with only one inlet and one outlet. Figure 4.8 shows what would be the

pressure drop for a lower linear flow velocity in the first compartment in case of a more uniform fluid flow distribution inside the stack.

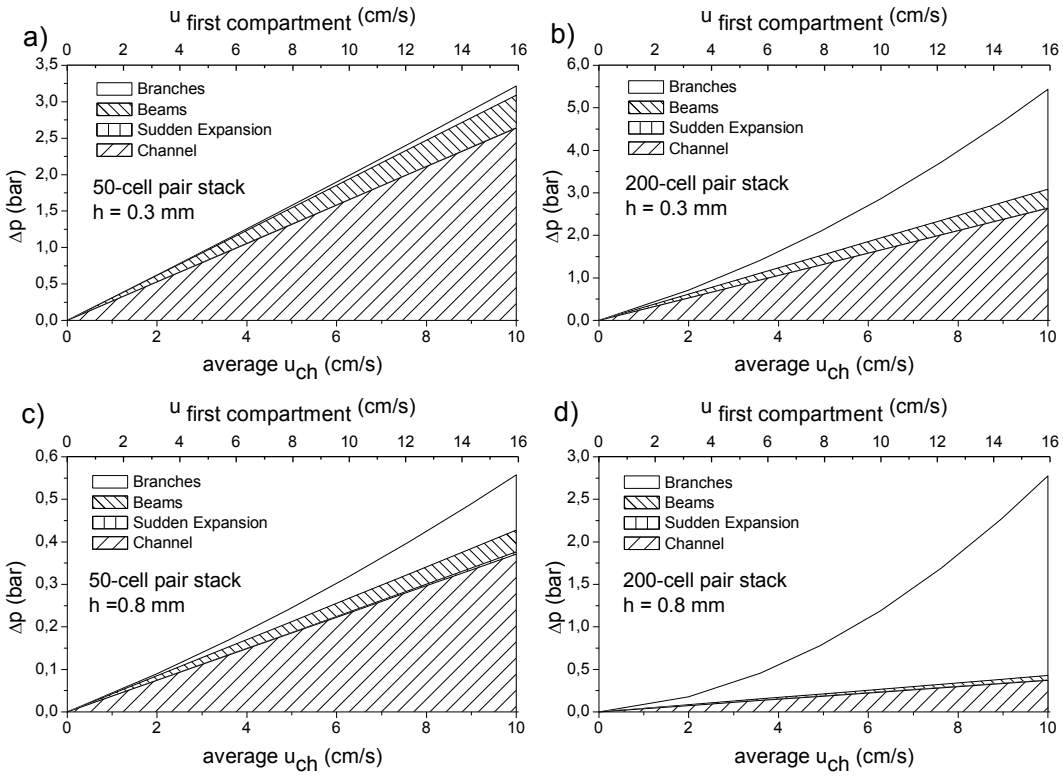

Figure 4.8. Model partial pressure drops for stacks (with 3 inlets and 3 outlets, and with a branch ratio of 0.122) represented in Figure 4.7: (a) 50-cell pair stack with intermembrane thickness of 0.3 mm, (b) 200-cell pair stack with intermembrane thickness of 0.3 mm, (c) 50-cell pair stack with intermembrane thickness of 0.8 mm and (d) 200-cell pair stack with intermembrane thickness of 0.8 mm.

Since the stack must have a large capacity in order to reduce the capital and operating costs per unit of inlet solution [27], and to generate a significant amount of power, the compartment length in a modeled large-scale situation was 20 times higher than in lab-scale stacks [18]. As the concentration gradient decreases along the compartments length, it is not surprising that a lower average value of the net power density has been obtained in our simulations (0.32 W/m^2 for h = 0.5 mm in a 50-cell pair industrial-scale stack) than the net power density value obtained experimentally (0.5 W/m^2 for h = 0.485 mm) in a 5-cell pair lab-scale stack [18].

Decreasing the intermembrane distance increases the pressure drop; however, in the investigated intermembrane range (0.8 - 0.3 mm), the reduction in compartment electrical resistance (especially of the diluted one [18, 22, 40, 46, 57]) is more important, and therefore the net power density increases with decreasing the compartment's thickness (Figure 4.7). An increase in net power density was already observed in experimental studies with lab-scale RED stacks, with intermembrane distance in the range of 0.485 mm to 0.060 mm, however, an optimum

intermembrane distance was found closely to 0.100 mm, as at a lower intermembrane thickness, the pressure drop increases to an extent that does not justify the gained decrease in the electric resistance [18]. Also even if the pressure drop is insignificant, at a very low linear fluid flow velocity, the resistance in narrow stack compartments could eventually become even higher than that in thicker ones [22], due to concentration polarization effects. In result, the salt concentration gradient across the membranes and the corresponding potential difference established between the electrodes decreases [22, 30], which reduces the stack power output.

The analysis of the partial pressure drop contributions of modeled stacks with a branch section ratio of 0.122 shows that with a decrease in the intermembrane distance, and at a smaller number of cell pairs, the dominant partial pressure drop becomes located in the compartments (Figure 4.8a). Moreover, since the gross power density reaches almost a plateau value for any compartment thickness and the pressure drop in a stack with a narrower intermembrane distance continues to increase more than in a stack with thicker compartments, the power density balance for thinner compartments becomes more negative than the one for thicker compartments as can be seen in Figure 4.7a for the case of 50-cell pair stacks.

The dominance of the partial pressure drop in the compartment channels can explain why the fluid distribution in a stack with narrow compartment channels was found to be more uniform [16], as the pressure drops causing the non-uniform fluid distribution (mainly the pressure drop in the branches) are insignificant in such stacks. Therefore in lab-scale stacks the design of the compartment channels becomes the most important task.

Curiously, under the previously mentioned experimental conditions (a low channel thickness and five cell pairs) [18], the measured pressure drop was by more than one order of magnitude higher than the theoretical predictions (in which only pressure drop in the compartments was considered). This is in contradiction with our findings based on simulations for a branch ratio of 0.122, presented in Figure 4.8, as it is expected that the pressure drop in the compartments would be the dominant one. However, values for intermembrane distance below 0.3 mm are physically possible if the beam width or the branch section ratio were smaller than those used in the simulation. Since in both cases the branch partial pressure drop increases, this could explain why the pressure drop in the compartment was not dominant in those lab-scale stacks.

In industrial-scale stacks, the pressure drop in the branch becomes more important with an increase in the cell-pair number. For example, in a 200-cell pair stack, with intermembrane distance of 0.8 mm (which is the intermembrane distance in an industrial-scale ED unit EDR-

III/500/0.8 of MEGA a.s. [27]), the partial pressure drop in the branches clearly becomes dominant for an average linear flow velocity higher than 2 cm/s. Also as the branch ratio was maintained constant, the partial pressure drop in the branch does not change when the intermembrane distance varies, since the cell-pair number and the linear velocity inside the channel are kept constant. Therefore for the case of 200-cell pair stacks (Figure 4.7b) the differences in net power density between stacks with different intermembrane distances depend more on the obtainable gross power density, which increases with decreasing the intermembrane distance. In such a way, the net power density for narrower intermembrane distances continues to be higher than in stacks with thicker compartments, as the fluid velocity increases (Figure 4.7b).

In terms of the calculated absolute total pressure drop values, the model predictions (Figures 4.8c and 4.8d) are also similar to the reported ones (0.2 - 2 bar) for industrial electrodialysis stacks operated in a linear flow velocity range from 2 cm/s to 10 cm/s [4, 27, 40]. Therefore the branch geometry and design must be carefully considered in RED stacks with high number of cell pairs, since besides strongly affecting the power spent for solutions pumping, it also affects the fluid distribution, which influences the pressure drop.

4.5.CONCLUSIONS

The presented mathematical model for pressure drop estimation inside a RED stack shows a very good agreement with experimentally obtained data, since it accounts for all significant partial pressure drops, and not just for the pressure drop in the stack channels. Through quantitative analysis of the impact of the RED stack dimension-related parameters on the respective partial pressure drops, the proposed model can provide indications about how the stack design could be planned and/or optimized in order to reduce a given partial pressure drop contribution.

The partial pressure drop in the distribution duct and, especially, the partial pressure drop in the branches were identified as the main causes of a non-uniform fluid flow distribution inside the investigated RED stack geometry. In result of a non-uniform fluid flow distribution, the partial pressure drops related to the beam, due to sudden expansion, and to the compartment channel can increase significantly. Moreover, for the same gross power density (granted by the same hydrodynamic conditions of ionic transport across the membranes), the net power density provided by the RED stack decreases with an increase in the cell-pair number, because the partial pressure drops in the distribution ducts and in the branches increase.

In lab-scale stacks, the pressure drop in the compartments has a dominant contribution, especially for narrow channels and low fluid flow rates. In such a way, a more open spacer structure would be desirable in order to decrease the pressure drop in the compartments.

Under conditions closer to those of large-scale stacks dimensions, the model simulations demonstrate quantitatively that the partial pressure drop in the branches becomes dominant, and, therefore, significant deviation from a uniform fluid distribution may exist. This effect becomes more pronounced as the cell-pair number and/or the fluid flow rate increases. Therefore, strategies for providing a more uniform fluid distribution through sizing the cross flow section, increasing the number of beam inlets/outlets to/from the flow compartment channels, or ensuring a proper selection of the branch section ratio are essential for an adequate RED stack design.

Finally, it should be noted that although the usefulness of the model developed was demonstrated on the example of a common RED stack design, the model could be also useful to compare this design with other existing or new ones, in order to identify their possible benefits and/or drawbacks. Moreover, the proposed methodology could be also applied to a mathematical description of the pressure drop and its minimization in other devices based on a plate-and-frame membrane configuration (*e.g.*, traditional electrodialysis, electrodeionization, Donnan dialysis, membrane fuel cells, etc.).

APPENDIX 4A

Pressure drop in the distribution ducts

Fluid distribution ducts are incorporated along the stack. From the inlet at the bottom of the stack, the solution flows through one duct towards the compartment channels, and in the top of the stack is collected by another duct and flows towards the outlet (Figure 4.1). For symmetrical and circular ducts, the pressure drop can be calculated by the Hagen-Poiseuille equation [42, 58]:

$$\Delta p = \frac{32 \cdot \mu \cdot u \cdot L}{d^2} \qquad (4A.1),$$

where u , L and d are respectively the linear fluid flow velocity, pipe length and pipe diameter, while μ is the fluid viscosity.

Along the duct (*y*), the flow is distributed or collected, through a series of beams to the parallel disposed compartments (Figure 4A.1). This causes a decrease or an increase in the flow rate along the duct.

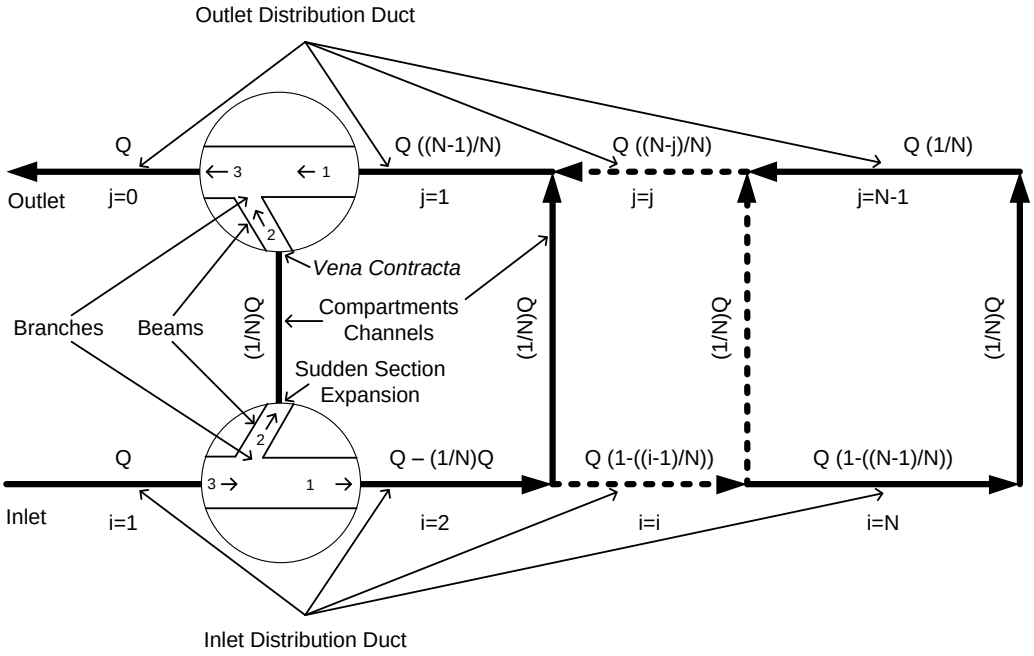

Figure 4A.1. Fluid distribution inside the RED stacks as considered by the model. The zoomed-in zones are relative to fluid distribution at separation (bottom) and junction (top) branches.

In case of a uniform fluid distribution, the fluid flow rate is equal in all compartments and therefore the flow rate in a given duct part between two successive beams ($Q_{d,y}$) depends on the inlet flow rate (Q), the cell-pair number (N) and the position inside the stack as follows:

$$Q_{d,y} = Q\left(1 - \frac{i-1}{N}\right), for\ i = 1, \dots, N \qquad (4A.2)$$

The respective pressure drop ($\Delta p_{d,y}$) thus becomes:

$$\Delta p_{d,y} = \frac{32 \cdot \mu \cdot Q_{d,y} \cdot L_{d,y}}{{d_d}^2 \cdot \pi \cdot r_d^2} \qquad (4A.3),$$

where r_d and d_d are the duct radius and diameter, respectively, and $L_{d,y}$ corresponds to the distance between the beams and is the sum of the thickness of one anion-exchange membrane, one cation-exchange membrane and one compartment channel.

The partial pressure drop due to ducts for the respective compartment therefore is:

$$\Delta p_d = 2 \cdot \Delta p_{d,y} \quad (4A.4)$$

The factor 2 appears due to the existence of two ducts for solution distribution: one at the stack bottom, to deliver solution to the compartments from the inlet; and second one, at the stack top, to collect solution from the compartments in direction of the outlet. In both ducts the respective solution flow rates are the same.

Pressure drop due to branches from the distribution ducts to the beams

The pressure drop in the junctions and separations (branches) is caused by shock and mixture of two streams with different velocities, as can be seen in Figure 4A1. The process is complex as it depends on the fluid velocity, changes in the stream direction and the branch geometry (for example the ratio between cross flow section of a beam and a duct) [42]. Therefore to describe the head loss (ΔH) in the junction empirical equations have been proposed [42, 51]:

$$\Delta H_{1.3} = \frac{K_{1.3} \cdot u_3^2}{2g} \quad (4A.5)$$

$$\Delta H_{2.3} = \frac{K_{2.3} \cdot u_3^2}{2g} \quad (4A.6),$$

from which it can be seen that both head losses depend on the squared fluid velocity after the junction (stream 3 in the upper magnified part of Figure 4A1). The g is the gravitational acceleration constant and the Ks are empirical tabulated coefficients depending on the system geometry [42, 51]. According to the K's sign, a pressure drop exists if the fluid flow is slowdown ($K > 0$) or energy is gained if the fluid flow is accelerated ($K < 0$).

The head losses in the separating branches, $\Delta H_{3.1}$ and $\Delta H_{3.2}$, depend respectively on $K_{3.1}$ and $K_{3.2}$, and both depend on the squared fluid velocity before the separation (stream 3 in lower magnified part of a Figure 4A1).

The values of Ks [42] are very well adjusted to:

$$K = a \cdot \left(\frac{Q_2}{Q_3}\right)^2 + b \cdot \left(\frac{Q_2}{Q_3}\right) + c \quad (4A.7)$$

for a given cross flow section ratio between pipe 2 (beam) and pipe 3 (duct), where a, b and c are fitting parameters. As all head loses depend on Q_3, which, in a stack with symmetrical and parallel channels design, is the same in the compartment separation and junction branches (both streams 3), it is possible to obtain the global head loss for a given compartment as follows:

$$K_{br} = K_{1.3} + K_{2.3} + K_{3.1} + K_{3.2} \quad (4A.8)$$

$$A = a_{1.3} + a_{2.3} + a_{3.1} + a_{3.2} \quad (4A.9)$$

$$B = b_{1.3} + b_{2.3} + b_{3.1} + b_{3.2} \quad (4A.10)$$

$$C = c_{1.3} + c_{2.3} + c_{3.1} + c_{3.2} \quad (4A.11)$$

$$K_{br} = A \cdot (\frac{Q_2}{Q_3})^2 + B \cdot \left(\frac{Q_2}{Q_3}\right) + C \quad (4A.12)$$

$$\Delta H_{br} = \frac{K_{br} \cdot u_3^2}{2g} \quad (4A.13),$$

where Q_2 is the flow rate in the compartment beam and *A*, *B* and *C* are constants, equal for all compartments, and depending only on the stack branch geometry. Knowing these constants, it is possible to calculate the pressure drop due to branches in the stack node. For a uniform fluid distribution, the respective equations are as follows:

$$\frac{Q_2}{Q_3} = \frac{1}{N-j} \; for \; j = 0, \dots, N-1 \quad (A.14)$$

$$Q_3 = Q \cdot \left(\frac{N-j}{N}\right) for \; j = 0, \dots, N-1 \quad (A.15)$$

$$\Delta p_{br} = \frac{9810}{2*9{,}81} \cdot \left[\left(\frac{Q}{\pi \cdot {r_d}^2}\frac{N-j}{N}\right)^2 \cdot \left(A \cdot \left(\frac{1}{N-j}\right)^2 + B \cdot \left(\frac{1}{N-j}\right) + C\right)\right] \quad (A.16)$$

As ΔH_{br} is in meters head, the respective value was multiplied by 9810 in order to convert the pressure drop units into Pascals.

Pressure drop in the beams

The beam is a junction connecting the distribution duct with the compartment channel. Different geometries and numbers of beams could exist. For a circular pipe, at a laminar flow regime, the Hagen-Poiseuille equation (eq. 4A.1) is applied to calculate the pressure drop [42, 58]. For rectangular channel geometry the mean hydraulic diameter (d_b) is defined as [58]:

$$d_b = \frac{2 \cdot h \cdot w_b}{h + w_b} \tag{4A.17}$$

and, therefore, the pressure drop in the beam becomes:

$$\Delta p_b = \frac{32 \cdot \mu \cdot u_b \cdot L_b}{{d_b}^2} \tag{4A.18}$$

with (if a uniform fluid distribution is considered):

$$u_b = \frac{Q}{\pi \cdot \frac{{d_b}^2}{4} \cdot N} \tag{4A.19},$$

where h is the intermembrane distance, w_b is the beam width and L_b is the sum of the lengths of the compartment two beams, as the inlet beam length may be not equal to the outlet beam length, while the other dimensions remain the same for both beams.

Pressure drop due to a sudden section expansion between a beam and a compartment channel

In a RED stack, the beam cross flow section is smaller than the cross flow section of the compartment channel. Due to this sudden section expansion, the fluid velocity reduces. Injection of fluid with a higher velocity from the beam to a fluid with lower velocity in the compartment channel causes turbulence. From the force balance, at laminar flow regime the pressure drop can be calculated by the Borda-Carnot equation [51, 58]:

$$\Delta p_{s.exp.} = \frac{\rho \cdot {u_{ch}}^2}{2} \left(\frac{A_{ch}}{A_b} - 1\right)^2 \tag{4A.20},$$

where u_{ch} is the linear flow velocity in the channel, A_{ch} is the channel cross flow section, A_b is the beam cross flow section and ρ is the fluid density. After replacing the section ratio by

compartment and rectangular beam dimensions, the pressure drop due to sudden expansion is calculated as follows:

$$\Delta p_{s.exp.} = \frac{\rho \cdot {u_{ch}}^2}{2} \left(\frac{h \cdot w_{ch} \cdot \varepsilon}{h \cdot w_b} - 1\right)^2 \quad (4A.21)$$

At the exit of the compartment channel the opposite situation exists: the so called *vena contracta*. When the fluid approaches the *vena contracta*, the pressure force is converted into kinetic energy and the fluid flow accelerates without forming any turbulence phenomena. In such a way, the pressure drop in this zone is generally small [58].

Pressure drop inside a compartment channel

The fluid flow in a plate-and-frame RED compartment channel is similar to a fluid flow between two parallel plates. If the width of the plates is much larger than the distance between them, the flow can be considered unidirectional and through a force balance, at a laminar flow regime, the following expression for the mean linear flow velocity in the channel (u_{ch}) is obtained [58]:

$$u_{ch} = \left(\frac{-\Delta p_{ch}}{L_{ch}}\right) \cdot \frac{h^2}{12 \cdot \mu} \quad (4A.22),$$

where L_{ch} is the compartment channel length and Δp_{ch} is the pressure drop in the compartment channel. To adapt this equation, which considers an open (spacer free) channel configuration, to conditions with spacers, eq. 4A.22 can be rewritten in the form of the well-known Darcy-Weisbach equation with a modified channel hydraulic diameter (d_{ch}) [29]:

$$\Delta p_{ch} = \frac{12 \cdot \mu \cdot L_{ch}^2}{\frac{1}{4} {d_{ch}}^2 \cdot t_{res}} \quad (4A.23)$$

$$d_{ch} = \frac{4 \cdot \varepsilon}{\frac{2}{h} + (1-\varepsilon) \cdot \frac{8}{h}} \quad (4A.24),$$

where t_{res} is solution residence time in the compartment channel and ε is the spacer porosity from the flow direction perspective, with:

$$t_{res} = \frac{L_{ch}}{u_{ch}} \quad (4A.25)$$

and (if a uniform fluid distribution is considered):

$$u_{ch} = \frac{Q}{w_{ch} \cdot h \cdot \varepsilon \cdot N} \quad (4A.26),$$

where, w_{ch} is the channel width.

Total pressure drop

From the fluid flow distribution pattern in the stack (Figure 4A.1), the total pressure drop between its inlet and outlet (Δp_t), can be more easily calculated from data for the first node as follows:

$$\Delta p_t = \Delta p_{d,i=1} + \Delta p_{br,j=0} + \Delta p_b + \Delta p_{s.exp.} + \Delta p_{ch} \quad (4A.27)$$

REFERENCES

[1] R.E. Pattle, Production of electric power by mixing fresh and salt water in the hydroelectric pile, Nature 174 (1954) 660.

[2] A.T. Jones, W. Finley, Recent developments in salinity gradient power, OCEANS 2003 Proceedings vol. 4, 2003, pp. 2284 – 2287.

[3] C.R. Merz, W.A. Moreno, M. Barger, S.M. Lipka, Salinity gradient power (SGP): a developmental roadmap covering existing generation technologies and recent investigative results into the feasibility of bipolar membrane-based salinity gradient power generation, Technol. Innov. 14 (2012) 249–275.

[4] H. Strathmann, Electrodialysis, a mature technology with a multitude of new applications, Desalination 264 (2010) 268–288.

[5] C. Murray, J. Blackledge, D. Kearney, The feasibility of salinity gradient technology for Ireland: an initial case study by the river Suir, J. Dev. Appl. Ocean. Eng. (2013) 1-11.

[6] Y. Emami, S. Mehrangiz, A. Etemadi, A. Mostafazadeh, S. Darvishi, A brief review about salinity gradient energy, Int. J. Smart Grid and Clean Energy 2 (2013) 295-300.

[7] G.Z. Ramon, B.J. Feinberg, E.M.V. Hoek, Membrane-based production of salinity-gradient power, Energy Environ. Sci. 4 (2011) 4423–4434.

[8] S. Loeb, Osmotic power-plants, Science 189 (4203) (1975) 654−655.

[9] A. Achilli, A.E. Childress, Pressure retarded osmosis: from the vision of Sidney Loeb to the first prototype installation – review, Desalination 261 (3) (2010) 205−211.

[10] F. La Mantia, M. Pasta, H.D. Deshazer , B.E. Logan, Y. Cui, Batteries for efficient energy extraction from a water salinity difference, Nano Lett. 11 (4) (2011) 1810–1813.

[11] D. Brogioli, R. Ziano, R.A. Rica, D. Salerno, O. Kozynchenko, H.V.M. Hamelerscd, F. Mantegazza, Exploiting the spontaneous potential of the electrodes used in the capacitive mixing technique for the extraction of energy from salinity difference, Energy Environ. Sci. 5 (2012) 9870-9880.

[12] J.N. Weinstein, F.B. Leitz, Electric power from differences in salinity: the dialytic battery, Science 191 (1976) 557–559.

[13] M. Turek, B. Bandura, Renewable energy by reverse electrodialysis, Desalination 205 (2007) 67-74.

[14] E. Brauns, Salinity gradient power by reverse electrodialysis: effect of model parameters on electrical power output, Desalination 237 (2009) 378–391.

[15] B.E. Logan and M. Elimelech, Membrane-based processes for sustainable power generation using water, Nature 488 (2012) 313-319.

[16] L. Gurreri, A. Tamburini, A. Cipollina, G. Micale, CFD analysis of the fluid flow behavior in a reverse electrodialysis stack, Desalt. Water Treat. 48 (2012) 390–403.

[17] A. Tamburini, G. La Barbera, A. Cipollina, M. Ciofalo, G. Micale, CFD simulation of channels for direct and reverse electrodialysis, Desalt. Water Treat. 48 (2012) 370–389.

[18] D.A. Vermaas, M. Saakes, K. Nijmeijer, Doubled power density from salinity gradients at reduced intermembrane distance, Environ. Sci. Technol. 45 (2011) 7089–7095.

[19] D.A. Vermaas, M. Saakes, K. Nijmeijer, Enhanced mixing in the diffusive boundary layer for energy generation in reverse electrodialysis, J. Membr. Sci. 453 (2014) 312-319.

[20] R.W. Baker, Membrane Technology and Applications, second edition, Wiley, Chichester (2004) 411-415.

[21] P. Dlugolecki, P. Ogonowski, S.J. Metz, M. Saakes, K. Nijmeijer, M. Wessling, On the resistances of membrane, diffusion boundary layer and double layer in ion exchange membrane transport, J. Membr. Sci. 349 (2010) 369–379.

[22] P. Dlugolecki, A. Gambier, K. Nijmeijer, M. Wessling, Practical potential of reverse electrodialysis as process for sustainable energy generation, Environ. Sci. Technol. 43 (2009) 6888–6894.

[23] P. Dlugolecki, B. Anet, S.J. Metz, K. Nijmeijer, M. Wessling, Transport limitations in ion exchange membranes at low salt concentrations, J. Membr. Sci. 346 (2010) 163–171.

[24] J. Jagur-Grodzinski, R. Kramer, Novel process for direct conversion of free energy of mixing into electric power, Ind. Eng. Chem. Process Des. Dev. 25 (1986) 443-449.

[25] J. Veerman, M. Saakes, S.J. Metz, G.J. Harmsen, Reverse electrodialysis: performance of a stack with 50 cells on the mixing of sea and river water, J. Membr. Sci. 327 (2009) 136–144.

[26] M. Tedesco, A. Cipollina, A. Tamburini, W. van Baak, G. Micale, Modelling the reverse electrodialysis process with seawater and concentrated brines, Desalt. Water Treat. 49 (2012) 404–424.

[27] R. Kodym, P. Panek, D. Snita, D. Tvrznık, K. Bouzek, Macrohomogeneous approach to a two-dimensional mathematical model of an industrial-scale electrodialysis unit, J. Appl. Electrochem. 42 (2012) 645–666.

[28] J. Veerman, M. Saakes, S.J. Metz, G.J. Harmsen, Reverse electrodialysis: a validated process model for design and optimization, Chem. Eng. J. 166 (2011) 256–268.

[29] D.A. Vermaas, E. Guler, M. Saakes, K. Nijmeijer, Theoretical power density from salinity gradients using reverse electrodialysis, Energy Proc. 20 (2012) 170 – 184.

[30] D.A. Vermaas, M. Saakes, K. Nijmeijer, Power generation using profiled membranes in reverse electrodialysis, J. Membr. Sci. 385–386 (2011) 234–242.

[31] J. Veerman, J.W. Post, M. Saakes, S.J. Metz, G.J. Harmsen, Reducing power losses caused by ionic shortcut currents in reverse electrodialysis stacks by a validated model, J. Membr. Sci. 310 (2008) 418–430.

[32] O. Scialdone, A. Albanese, A. D'Angelo, A. Galia, C. Guarisco, Investigation of electrode material – redox couple systems for reverse electrodialysis processes. Part II: Experiments in a stack with 10–50 cell pairs, J. Electroanal. Chem. 704 (2013) 1–9.

[33] Y. Tanaka, A computer simulation of feed and bleed ion exchange membrane electrodialysis for desalination of saline water, Desalination 254 (2010) 99–107.

[34] Y. Tanaka, Limiting current density of an ion-exchange membrane and of an electrodialyzer, J. Membr. Sci. 266 (2005) 6–17.

[35] Y. Tanaka, Current density distribution and limiting current density in ion-exchange membrane electrodialysis, J. Membr. Sci. 173 (2000) 179–190.

[36] Y. Tanaka, Ion-exchange membrane electrodialysis program and its application to multi-stage continuous saline water desalination, Desalination 301 (2012) 10–25.

[37] E. Güler, R. Elizen, D.A. Vermaas, M. Saakes, K. Nijmeijer, Performance-determining membrane properties in reverse electrodialysis, J. Membr. Sci. 446 (2013) 266–276.

[38] J. Veerman, M. Saakes, S.J. Metz, G.J. Harmsen, Electrical power from sea and river water by reverse electrodialysis: a first step from the laboratory to a real power plant, Environ. Sci. Technol. 44 (2010) 9207–9212.

[39] J. Veerman, R.M. de Jong, M. Saakes, S.J. Metz, G.J. Harmsen, Reverse electrodialysis: comparison of six commercial membrane pairs on the thermodynamic efficiency and power density, J. Membr. Sci. 343 (2009) 7–15.

[40] H. Strathmann, Assessment of electrodialysis water desalination process costs, Proceedings of the International Conference on Desalination Costing, Limassol, Cyprus, 204, pp. 32-54.

[41] M.C. Porter, Handbook of Industrial Membrane Technology, Noyes Publications, Westwood, New Jersey (1990) 487-490 (Reprint edition).

[42] A. Lencastre, Hidráulica geral, Edição do Autor, Lisboa, 1996 (pp. 45-46, 49-55, 138-139, 153-155, 492-493, 495).

[43] F. Webster, E.R. Cohen, D.R. Lide, G.L. Trigg, AIP Physics Desk Reference, Springer-Verlag, New York, 2003.

[44] R.H. Sabersky, A.J. Acosta, E.G. Hauptmann, E.M. Gates, Fluid flow: A first Course in Fluid Mechanics, fourth edition, Prentice Hall, Upper Saddle River (1999) 110-113.

[45] R.E. Smalley, Future global energy prosperity: the terawatt challenge, Mater. Res. Soc. Bull. 30 (2005) 412–417.

[46] J.W. Post, H.V.M. Hamelers, C.J.N. Buisman, Energy recovery from controlled mixing salt and fresh water with a reverse electrodialysis system, Environ. Sci. Technol. 42 (2008) 5785–5790.

[47] P. Dlugolecki, J. Dabrowska, K. Nijmeijer, M. Wessling, Ion conductive spacers for increased power generation in reverse electrodialysis, J. Membr. Sci. 347 (2010) 101–107.

[48] S. Judd, B. Jefferson, Membranes for Industrial Wastewater Recovery and Re-use, Elsevier, Kidlington, 2003 (pp. 58).

[49] K.S. Kim, W. Ryoo, M.S. Chun, G.Y. Chung, Simulation of enhanced power generation by reverse electrodialysis stack module in serial configuration, Desalination 318 (2013) 79–87.

[50] D.A. Vermaas, M. Saakes, K. Nijmeijer, Early detection of preferential channeling in reverse electrodialysis, Electrochim. Acta 117 (2014) 9– 17.

[51] Sulzer Pumps Ltd, Centrifugal Pump Handbook, third edition, Elsevier, Winterthur, 2010 (pp.162, 171-177).

[52] A. Marchitto, M. Fossa, G. Guglielmini, The effect of the flow direction inside the header on two-phase flow distribution in parallel vertical channels, Appl. Therm. Eng. 36 (2012) 245-251.

[53] Y. Tanaka, Ion Exchange Membranes: Fundamentals and Applications, Membrane Science and Technology Series 12, Elsevier, Amsterdam, 2007 (pp. 324).

[54] D.A. Vermaas, D. Kunteng, M. Saakes, K. Nijmeijer, Fouling in reverse electrodialysis under natural conditions, Water Res. 47 (3) (2013) 1289-1298.

[55] D.A. Vermaas, J. Veerman, N.Y. Yip, M. Elimelech, M. Saakes, K. Nijmeijer, High efficiency in energy generation from salinity gradients with reverse electrodialysis, Sustain. Chem. Eng. 1 (10) (2013) 1295–1302.

[56] M.C. Hatzell, B.E. Logan, Evaluation of flow fields on bubble removal and system performance in an ammonium bicarbonate reverse electrodialysis stack, J. Membr. Sci. 446 (2013) 449-455.

[57] J.W. Post, J. Veerman, H.V.M. Hamelers, G.J.W. Euverink, S.J. Metz, K. Nijmeijer, C.J.N. Buisman, Salinity-gradient power: evaluation of pressure-retarded osmosis and reverse electrodialysis, J. Membr. Sci. 288 (2007) 218–230.

[58] J.M. Coulson, J.F. Richardson, Tecnologia Química 1º Volume, 4ª Edição, Fundação Calouste Gulbenkian, Lisboa, 2004 (pp. 76-80, 86-90).

Chapter

5

COMPUTATIONAL FLUID DYNAMICS (CFD) ASSISTED ANALYSIS OF PROFILED MEMBRANES PERFORMANCE IN REVERSE ELECTRODIALYSIS

SUMMARY

Implementation of reverse electrodialysis (RED) is economically limited by the relatively high ion-exchange membranes price. Additionally, the shadow effect of non-conductive spacers reduces the membrane area available for counter-ion transport and increases the stack electric resistance. A promising alternative could be utilization of profiled membranes, since the reliefs formed on their surface keeps the membranes separated and provides channels for solutions flow. Herein, we have simulated, through computational fluid dynamics (CFD) tools, fluid behavior in channels formed by various profiled membranes. The highest net power density values were obtained for corrugations shape and arrangement in a form of chevrons due to the increase of the available membrane area and an excellent balance between enhancement of mass transfer and the increase of the pressure drop in the channel. When properly designed, corrugated membranes may offer a better performance even compared to the case of conductive spacers. The proposed membrane corrugation design in not limited to the RED application, and could be also extended to other electromembrane processes, such as electrodialysis and Donnan dialysis, in which high ionic mass transport rates are desirable at as low as possible energy costs.

Submitted as: S. Pawlowski, V. Geraldes, J.G. Crespo, S. Velizarov. Computational fluid dynamics (CFD) assisted analysis of profiled membranes performance in reverse electrodialysis, Journal of Membrane Science (2015).

Graphical abstract:

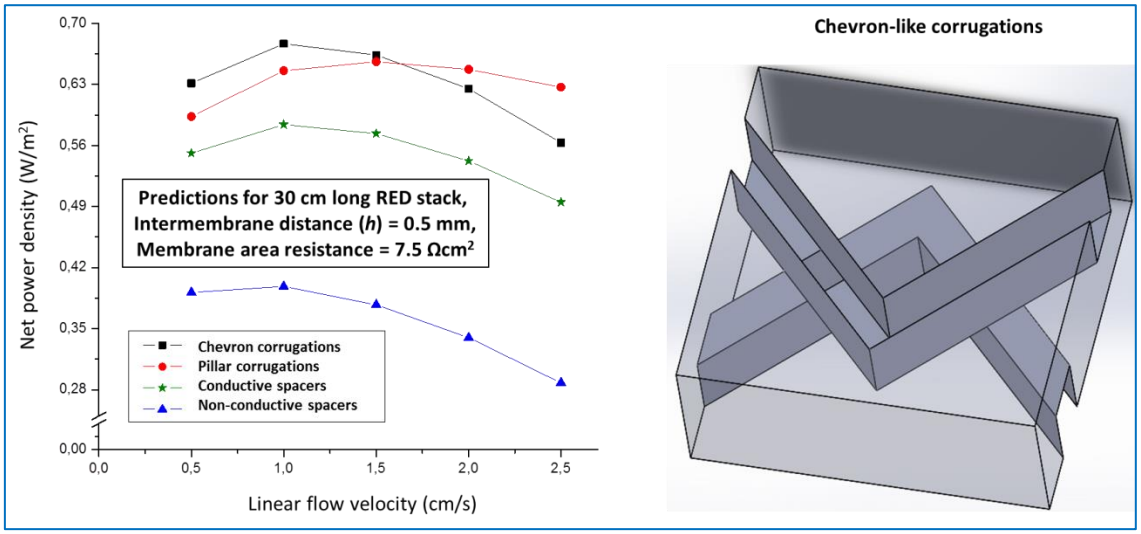

Highlights

- The obtainable net power density in RED has been modeled using CFD tools.
- Corrugations perpendicular to the fluid flow do not improve the fluid dynamics conditions.
- Chevron structures are found to be the most promising corrugation geometry.
- Profiled membranes perform better than conductive spacers.

Keywords: Profiled membranes, Chevron corrugations, Computational fluid dynamics (CFD), Net power density

5.1. INTRODUCTION

A potentially sustainable source of energy is the chemical energy associated with solvation of salts known as salinity gradient energy or blue energy. Mixing of two streams with different salt concentrations is spontaneous and releases energy (Gibbs free energy). Power generation from salinity gradients can be achieved by controlled mixing of concentrated and dilute electrolyte solutions in a reverse electrodialysis (RED) operation mode [1-4].

RED is an emerging technology, in which a number of alternating cation- and anion-exchange membranes are stacked between two electrodes (Figure 5.1). The mechanical support to create the flow channel compartments and maintain a constant distance between the membranes is usually assured by non-conductive spacers. The compartments are alternately fed with concentrated (e.g., sea water) and dilute (e.g., river water) saline solutions. In such a way, an electric potential difference is established between the electrodes and the cations and the anions migrate in opposite directions, toward the cathode and anode, respectively. This spontaneous ionic current is transformed into electron current at the electrode surfaces. In the electrode compartments, a solution containing, preferably, a homogeneous redox couple is recirculated.

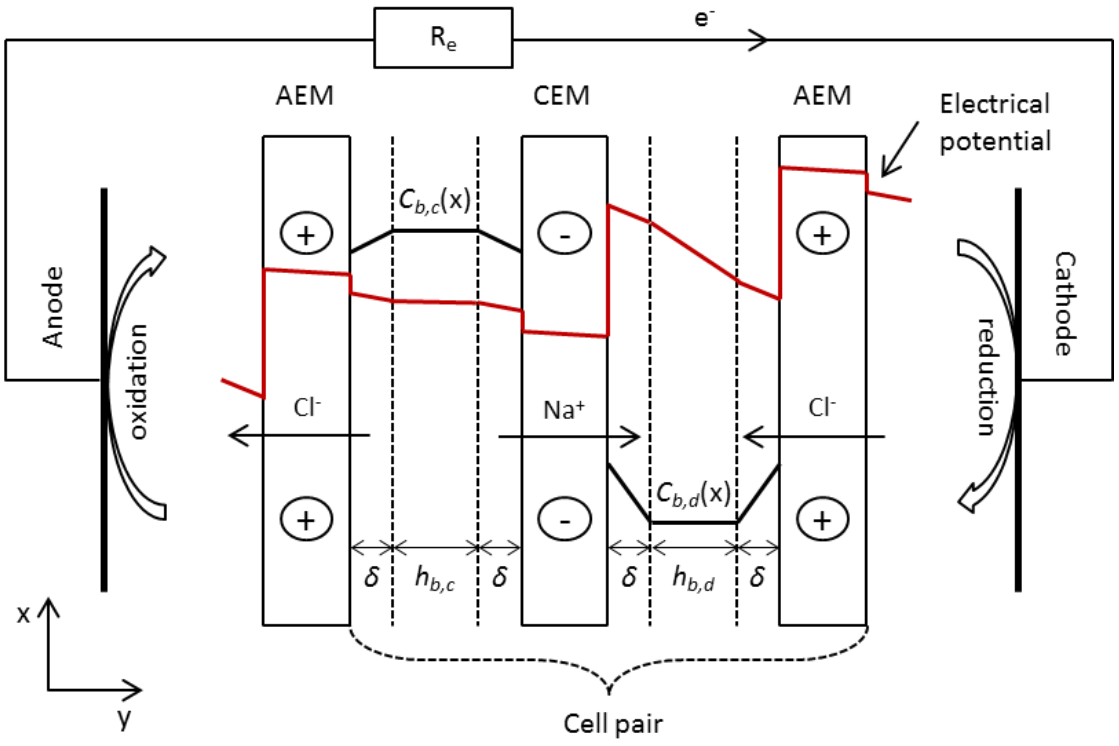

Figure 5.1. Schematic representation of concentration and electric potential profiles in the compartments of a reverse electrodialysis cell (CEM – cation-exchange membrane, AEM – anion-exchange membrane, Re – external load resistance).

The most appropriate engineering solution for RED optimization requires minimization of the stack internal electric resistance. This is due to the fact that the so-called "shadow" effect of non-conductive spacers over the membrane surface is one of the major contributions for increasing ohmic electric resistance, as the available area for counter-ion transport is significantly reduced [5-10]. For example, in lab-scale RED stacks, it was observed that the internal stack resistance dropped, in average to 67 % of its initial value, when the spacer' non-conductive parts, which taped 50 % of the available membrane area, were completely removed and the intermembrane distance was maintained only by the gasket [10]. The resistance value did not drop proportionally by 50 % since the spacer mesh absence decreased the fluid turbulence, and therefore led to formation of a thicker diffusion boundary layer (DBL).

Operation of a large-scale RED stack with empty channels could be, however, not feasible since such channels may easily collapse. A possible solution, in which the spacers are removed and the intermembrane distance is still maintained constant, even for large membrane areas, is the utilization of profiled membranes [10-11]. Profiled membranes, also known as corrugated membranes, provide channels for the feed streams, while the relief formed on their surfaces keeps the membranes separated [12-15]. Profiled membranes have been successfully used for filtration [15-19], gas permeation [20-21] and some electromembrane applications [22-24].

For power generation by reverse electrodialysis, the advantages of using profiled membranes, instead of non-conductive spacers, consists in a decreased internal electric resistance, an increased membrane effective area for counter-ion transport, a lower hydraulic friction (lower pressure drop) and reduced fouling [6-7, 12, 14, 22, 25-26]. Several profiled membrane geometries and configurations have been used with different success [7, 25]. For example, sub-corrugations perpendicular to the fluid flow did not proved to be beneficial as no additional mixing was observed and the non-ohmic resistance was mainly dominated by the fluid distribution [7] due to the existence of dead zones and preferential flow channeling [27].

So far, the best experimental results [25] and theoretical predictions [28] were obtained for corrugations with a round pillar structure as they enable a more uniform fluid distribution over the entire membrane surface area. However, within the linear flow velocity range ($Re < 3$) most appropriate for obtaining high net power density values, the concentration polarization in channels with profiled membranes was found to be higher compared to the cases in which the channels are empty or with spacers [28]. This may be related to the observation that the distance between the corrugations must be optimized in order to avoid formation of dead zones [29]. Therefore there is still a need to find new profile geometries that provide a better fluid

distribution, increase the effective membrane area available for ion transport and minimize concentration polarization effects.

The DBL thickness in RED stack can be calculated from experimental data (obtained through limiting current density and/or chronopotentiometric techniques) or by using available dimensionless mass-transfer correlations based on the film theory [10]. Utilization of mass-transfer correlations (sometimes even such obtained for convective-diffusive systems without any charge transfer) has been the common practice during the last decades for dimensioning electrodialysis stacks [30-33]. However, as these correlations are specific for a given channel geometry, for new geometries new correlations must be developed.

In case of laminar flow, which is common for RED channels, computational fluid dynamics (CFD) can estimate mass-transfer coefficients, as well as pressure drop, in a very accurate and reliable way [34]. Firstly, the flow patterns and concentration distribution inside the channels are obtained by solving the mass continuity and Navier-Stokes equations [34-38]. Then, the mass transfer coefficient is computed at the relevant interfaces, where interfacial mass transfer occurs [34-35].

In the present study, parameters such as available membrane area, pressure drop, and mass transfer coefficient, as well as flow entrance effects on mass transfer were considered. The effect of corrugations shape, height and spatial distribution was analyzed on the basis of the obtainable net power, which had been normalized by the flat membrane area before corrugated. More than twenty different corrugation shapes and arrangements were initially screened and compared by performing 2D simulations, for being faster and less demanding in terms of computational effort. Then, 3D simulations of more complex corrugations forms were performed. The highest net power density gain (by around 76 %) relatively to channels with non-conductive spacers was estimated for a corrugation in the form of chevrons, which use has not yet been reported for any membrane-based application.

5.2. MODELING

5.2.1. Strategy

Certainly, the most accurate approach to obtain mass transfer coefficient values in the DBLs would be to solve simultaneously the Navier-Stokes-Nernst-Planck-Poisson equations, which would yield the concentration and electric potential fields. However, due to the relatively small

contribution of the DBL resistances to the total electric resistance, applying such a complex approach appears unreasonable.

Therefore, at the membrane surface, the solute continuity equation was solved with a boundary condition of a constant solute concentration. With this approach, it was possible to decouple reasonably well the mass transfer coefficient from the variation of the solute flux along the channel. Another possibility would have been to perform simulations assuming a constant solute flux through the membranes or mixed boundary conditions of the Robin type [39]. The mass transfer coefficient value is slightly affected by the chosen boundary condition; however, for a laminar regime, the differences are lower than 20 % [40]. We also decoupled the computation of the solute concentration field from the velocity field, because the time scale of momentum transport was at least one order of magnitude lower compared to the time scale of mass transport.

The CFD simulations were performed using periodic inlet/outlet boundary conditions until the concentration distribution in the channel becomes quasi-periodic. In practice, this means that the channel has been divided into small sections with the same repetitive geometry, where the outlet boundary conditions of one section correspond to the inlet boundary conditions of the next section. In such a way, instead of simulating simultaneously the whole channel, the fluid behavior and concentration profiles are estimated section by section. The evolution of concentration distribution along the channel length can be followed since $x = u \cdot t$, where u is the linear flow velocity, x is the section distance from the channel entrance and t is the residence time required for a fluid element to reach that section. This approach significantly (by at least one order of magnitude) reduces the required computational time, and allows for simulating simultaneously different channel lengths, as was previously proven with a high confidence [34, 41].

Figure 5.2 presents the modelling strategy steps performed: CFD computing of the solute concentration distribution (Figure 5.2a), estimation of average diffusion boundary layer thickness (Figure 5.2b) and, finally, estimation of equivalent channel thickness (Figure 5.2c). These steps had the objective to normalize the estimated obtainable power by a nominal (flat) membrane area, in order to compare different corrugation designs. The nominal effective membrane area is in fact identical to the flat membrane area produced by membrane manufacturers.

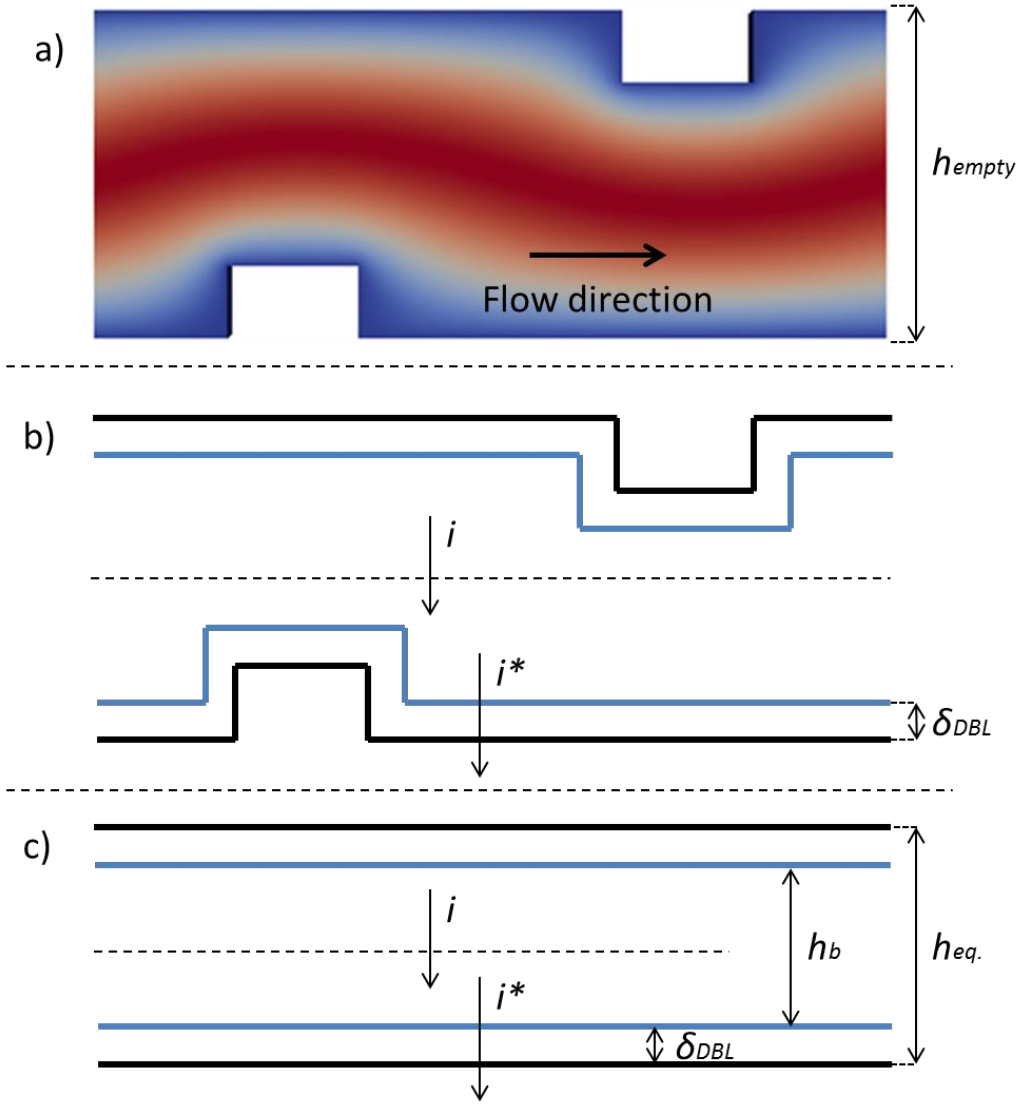

Figure 5.2. Scheme of the followed modeling strategy. a) Scheme of an obtained concentration distribution in a RED channel (Solute concentration decreases from red to blue color), b) Estimation of average diffusion boundary layer thickness (eqs. 5.10-5.11), c) Calculation of channel equivalent thickness (eq. 5.1).

The equivalent thickness of the channel formed by profiled membranes was calculated using the channel' porosity (ε):

$$h_{eq} = \varepsilon \cdot h_{empty} \quad (5.1),$$

where h_{empty} is the channel thickness without corrugations. The channel porosity was estimated taking into account the volume occupied by corrugations ($V_{corrugations}$) compared to the volume of the empty channel (V_{empty}) as follows:

$$\varepsilon = \frac{V_{empty} - V_{corrugations}}{V_{empty}} \quad (5.2).$$

Since in a river-sea system the main electric resistance of a RED stack is mainly offered by the dilute stream (river water) compartment [5, 10, 42-45], the net power density is strongly influenced by the membrane area offered by a given corrugation geometry. Therefore, for each simulation of a channel formed by profiled membranes, we simulated as well a channel composed by flat (non-profiled) membranes, separated by a distance equal to the equivalent channel thickness for the profiled membrane case.

Then, we defined a net power densities ratio (θ) between the value obtained for a channel with corrugations ($P_{net(profiled)}$) and for a flat channel with the equivalent height ($P_{net(flat)}$):

$$\theta = \frac{P_{net\,(profiled)}}{P_{net\,(flat)}} \tag{5.3}$$

Due to the same channel equivalent thickness in a stack with profiled and with flat membranes, and, thus, the same ohmic resistance for both stacks, the difference in net power density can be attributed to the effect of corrugations geometry on mass transfer and pressure drop. A θ ratio values above 1 means that the corrugations have led to an increase in mass transfer coefficient, which is higher in comparison of the increase in pressure drop. A θ ratio value below 1 means that the pressure drop increase is higher than the increase (if existing), in mass transfer coefficient.

5.2.2. Model

The main objective of the performed CFD simulations was to predict the mass transfer coefficient values. In order to decouple the prevision of diffusion boundary layer thickness from the charge transfer phenomena, the approach followed was based on a formalism assuming mass transfer in a binary salt (NaCl) aqueous solution system with permeable walls and without charge transfer [33].

In the performed CFD simulations, the considered governing equations for incompressible flow of a Newtonian fluid were the mass continuity and Navier-Stokes equations as follows [34-38]:

$$\nabla \boldsymbol{U} = 0 \tag{5.4}$$

$$\frac{\partial \rho U}{\partial t} + (u \cdot \nabla)\rho \boldsymbol{U} - \nabla \cdot (\mu \nabla \boldsymbol{U}) = -\nabla p \tag{5.5}$$

with $\boldsymbol{U}$ being the fluid velocity vector, ρ the fluid density, μ the dynamic viscosity and p the pressure. To restrict the computational domain to a single periodic segment of the channel, the pressure was decomposed by:

$$p = p^* + \beta \cdot x \quad (5.6),$$

where p^* is the periodic component of the pressure, β is the average pressure gradient in the channel and x is the local x-coordinate.

After obtaining the velocity and pressure fields at steady state, the solute mass concentration in the computed domain was calculated by solving the solute continuity equation:

$$\frac{\partial C}{\partial t} + \nabla \cdot (\boldsymbol{U}C) - \nabla \cdot (D\nabla C) = S \quad (5.7),$$

where D is solute mass diffusivity and S is given by

$$S = \frac{-D \iint_{A_m} \left(\frac{\partial C}{\partial y}\right)_m dA}{\iiint_V |U| C dV} \cdot |U| \cdot C \quad (5.8).$$

This field (S) represents a mass source, which is used to replace the mass transferred out of the periodic channel segment through a specified membrane area (A_m). Since each channel segment is divided in small control volumes and S depends on the position (x, y, z) inside the channel segment, in our approach, the solute is preferentially re-injected into regions with higher velocity and solute concentration, while the concentration close to membrane surface is almost not affected by such a numerical approach. In such a way, it is possible to solve the continuity equation for an element of fluid that enters in the channel and moves with the fluid average velocity.

The local mass transfer coefficient at each membrane point can be computed as follows:

$$k_{c,local} = \frac{1}{C_b - C_m}\left(-D\frac{\partial C}{\partial y}\right)_m \quad (5.9),$$

where, C_b and C_m are respectively solute concentration in the bulk and at membrane (m) surface. The DBL thickness was estimated according to the film model from the mass transfer coefficient (k_c) value [34-35]:

$$\delta_{DBL} = \frac{D}{k_c} \quad (5.10).$$

In order to obtain an average DBL thickness (Figure 5.2b), the average value of the mass transfer coefficient in the simulated domain was calculated by integration of the local mass transfer coefficient values over the total area of the walls of the channel segment area (*A*):

$$k_c(t) = \frac{1}{A}\int_A k_{c,local} dA \quad (5.11).$$

Knowing mass transfer coefficient values allows calculating the RED performance parameters using a relatively simple macroscopically based methodology. With some small differences, due to the different contexts of their applications, this approach has been followed in a number of studies [46-50]. Figure 5.1 shows a length fraction of a single RED cell with dilute and concentrated compartments formed by anion-exchange (AEM) and cation exchange (CEM) membranes. For ideally permselective membranes, only the respective counter-ions are transported from a concentrated to a dilute stream through the membranes (transport number in the membrane = 1). In such a way, the mass flux in the system is only of Coulombic nature [46-47, 51]. For model solutions of NaCl, the solute concentration in the bulk (C_b) along a channel can be obtained in the following way:

$$C_b(x + \Delta x) = C_b(x) \pm \frac{i(x)\cdot\Delta x}{F\cdot u\cdot h} \quad (5.12),$$

where *F* is Faraday constant, *u* is linear flow velocity *i* is the current density per flat membrane area, and *h* is channel thickness.

Since in RED the current density is much smaller than the limiting current density, the concentration profile in the DBL is linear and, therefore, the solute concentration on the membrane surface in the concentrated compartment ($C_{m(c)}$) can be obtained as follows [48, 52-54]:

$$C_{m(c)}(x) = C_{b(c)}(x)\cdot\left(1 - \frac{i^*(x)\cdot(T-t)\cdot\delta_{DBL}(x)}{D\cdot F\cdot C_{b(c)}(x)}\right) \quad (5.13),$$

where *D* is salt mass diffusivity, δ_{DBL} is diffusion boundary layer thickness and *T* and *t* are, respectively, the counter-ion transport number in the membrane and in the solution. Since the current has been previously normalized by the flat membrane area (A_{flat}), but at the membrane interface the current density (i^*) is smaller due to a larger available membrane area created by corrugations ($A_{profiled}$), $i^*(x)$ has been accounted as follows (Figure 5.2):

$$i^*(x) = \frac{i(x)\cdot A_{flat}}{A_{profiled}} \quad (5.14).$$

The concentration polarization close to both, AEM and CEM, surfaces was considered as the same [28, 55]. If the hydrodynamic conditions in the dilute and concentrated solutions channels are identical, and the solute mass diffusivity is considered equal in both compartments (for NaCl solutions within the range of 1-30 g/L the differences in mass diffusivity are less than 4 % [10]), the solute concentration on the membrane surface contacting the dilute solution becomes:

$$C_{m(d)}(x) = C_{b(d)}(x) + (C_{b(c)}(x) - C_{m(c)}(x)) \quad (5.15).$$

Using the extended Debye–Huckel equation to calculate the respective solution activities ($\gamma \cdot C$) [49], it becomes possible to calculate along the channel the open circuit voltage (*OCV*) across a cell pair:

$$OCV(x) = 2N \cdot \frac{R\cdot T}{F} \cdot \ln\left(\frac{\gamma_{m,c}(x)\cdot C_{m,c}(x)}{\gamma_{m,d}(x)\cdot C_{m,d}(x)}\right) \quad (5.16).$$

OCV is the RED driving force, R is the universal gas constant, T is the temperature, γ is the activity coefficient and N is the number of cell pairs.

The other important parameter is the RED stack internal resistance (R_i), which can be considered as a sum of ohmic and diffusion boundary layer resistances [7, 12-13, 27, 42, 46]. Due to variation of the solute concentration along the channel, the internal electric resistance correspondingly depends on the position along the channel. The ohmic resistance is composed by the sum of the resistances of cation-exchange (R_{CEM}), anion-exchange (R_{AEM}) membranes, bulk solutions resistances (h_b/κ_b) and electrodes (R_{el}):

$$R_{ohmic}(x) = N \cdot \left(\frac{R_{CEM}}{1-f} + \frac{R_{AEM}}{1-f} + \frac{h_{b,c}(x)}{\varepsilon\cdot\kappa_{b,c}(x)} + \frac{h_{b,d}(x)}{\varepsilon\cdot\kappa_{b,d}(x)}\right) + R_{el} \quad (5.17),$$

where κ is the solution conductivity, f is the fraction of membrane area covered by non-conductive spacers, ε is the spacers porosity (if present) and h_b corresponds to equivalent intermembrane distance not occupied by DBLs (Figure 5.2c). The electrodes resistance can be ignored if a big number of cell pairs is considered [47].

The resistance due to the DBL (R_{DBL}) can be accounted for as follows [10]:

$$R_{DBL}(x) = N \cdot \left(2\frac{\delta_{DBL}(x)}{\kappa_{DBL,c}(x)} + 2\frac{\delta_{DBL}(x)}{\kappa_{DBL,d}(x)}\right) \quad (5.18).$$

Since the solute concentration profile across the DBL is linear [48, 52-54], as the DBL solution conductivity we have considered an average value of the solutions conductivity in the bulk and on the membrane surface.

The gross power density (P_{gross}), when an external load resistance (R_e) is applied, can be obtained as follows:

$$P_{gross}(x) = i^2(x) \cdot R_e(x) \quad (5.19).$$

The value of $i(x)$ is adjusted by minimization of the least squares between the OCV values calculated by equations 5.16 and 5.20:

$$OCV\ (x) = i(x) \cdot (R_i(x) + R_e(x)) \quad (5.20).$$

The maximum value of gross power density, at 50 % efficiency of energy extraction, is achieved when the external load resistance has the same value as the internal stack resistance [5, 8, 43, 56-59]. For such a case:

$$P_{gross}(x) = \frac{OCV(x)^2}{4 \cdot R_i(x)} \quad (5.21).$$

In practical terms, this means that a stack with infinitely segmented electrodes is considered [43]. In order to obtain the value for a whole stack, it is necessary to integrate the local values along the channels length (L):

$$P_{gross(L)} = \frac{\int_0^{x=L} P_{gross}(x)dx}{L} \quad (5.22).$$

Thus, it becomes possible to calculate the net power density (P_{net}) of a RED stack, which consists in a trade-off between the generated (gross) power and the power consumed for pumping the solutions ($P_{pumping}$):

$$P_{net\ density} = P_{gross\ density} - \frac{P_{pumping}}{2 \cdot N \cdot A_{flat}} \quad (5.23).$$

The power spent for pumping depends on the feed solution flow rate (Q) and the total pressure drop (Δp_t) between the stack inlet and outlet [60]:

$$P_{pumping} = 2 \cdot (\Delta p_t \cdot Q) \quad (5.24).$$

The factor 2 appears because there are two saline solutions which are pumped, the dilute and the concentrated one. Based on previous studies [7, 12, 37, 60] we have considered for all simulated domains that the total pressure drop (Δp_t) in a RED stack is:

$$\Delta p_t = \Delta p_{channel} + 12 \cdot \Delta p_{10\ cm\ empty\ channel\ (h = 0.5\ mm)} \quad (5.25).$$

where the second term accounts for the partial pressure drop in manifolds. The second term in eq. 5.25 remains constant in all simulations, as the pressure drop in the manifolds does not depend on the working channels shape [60]. The important influence of manifolds on RED stack performance has been recognized [37, 60]; however, optimization of the manifolds system distribution is beyond the scope of the present study.

5.3. METHODOLOGY

5.3.1. CFD Numerical methods

The open-source OpenFOAM software package, version 2.3.0 [61], was used to simulate the flow patterns and mass transfer in a RED channel formed by two profiled membranes.

Equations 5.4-5.5 and 5.7 were solved by the transient pressure-implicit PIMPLE (merged PISO-SIMPLE) algorithm with 3 outer correctors for inter-equation coupling in the pressure-velocity system until the value of average velocity in the channel reached the specified goal while the value of β (eq. 5.6) was adjusted [61]. Time discretization was achieved by a second order backward Euler scheme and a 4th order Gauss scheme was used for spatial discretization of the solute continuity equation. The time step was lower than 1 ms in order to guarantee temporal accuracy and numerical stability. The simulations were processed on a four–node cluster (1.9 GHz CPU, 512 MB RAM/CPU) and the computational time varied from few hours up to a couple of days, depending on the simulated domain complexity. A preliminary mesh independence study was used to select the appropriate mesh for each case.

To draw all structures investigated by CFD, SolidWorks 2012 software was used to create *stl* files with the membrane design. The computational grid was generated from them by

blockMesh and *snappyHexMesh* OpenFOAM grid generation utilities. The created grid had a block-structure, in which a single block had an average volume of $4.0 \cdot 10^{-6}$ mm^3. Near the channel walls the grid was refined to resolve accurately the concentration boundary layers.

5.3.2. Channels shape

The net power density has been calculated for NaCl solutions of 1 and 30 g/L as inlet saline streams, for an average linear flow velocity inside the channel of 0.5 cm/s, 1.0 cm/s, 1.5 cm/s and 2.0 cm/s, respectively. The physical parameters used in the simulations are summarized in Table 5.1.

Table 5.1. Physical parameters used in simulations.

Parameter	Value
μ (NaCl)	0.00103 kg/(m·s)
ρ (NaCl)	998.2 (kg/m^3)
D_{NaCl}	$1.51 \cdot 10^{-9}$ (m^2/s)
$R_{CEM} = R_{AEM}$	7.5 (Ω·cm^2)
T	293.15 K
R	8.314 J/(mol·K)
F	96485.34 C/mol

The considered membrane area resistance is that of heterogeneous Ralex membranes [62], which, due to their relatively high thickness (~0.7 mm), are currently more suitable to be transformed into profiled membranes as they are mechanically rather stable. From a profiled membrane manufacturing point of view, the non-profiled membrane part should remain at least 0.2 mm thick in order to not start waving [25].

The initial simulations were done in two-dimensional space (2D), since it has been reported that the greatest mass transport improvement is reached for a flow directed at an angle of 90º to the corrugated membranes [18, 63], and that in channels with spacers, the flow structure is mainly determined by the spacer transverse filaments [34]. Given the simplicity of performing such simulations, twenty two different designs were initially compared (see, Supplementary material).

Since in such an arrangement the membranes reliefs must not touch each other, as this would obstruct the flow in the channel, a supporting frame is required to maintain the intermembrane

distance. Knowing that for existing profiled membranes the open area is of 83 % [7], we made an educated guess that this frame should cover 20 % of the membrane area.

The initial dimensions of the 2D simulated corrugations have been based on those of already existing profiled membranes, with corrugation width (w_c), height (h_c) and distance between corrugations (d_c) of 0.2 mm, 0.1 mm and 1 mm, respectively [7, 12, 25]. The channel thickness was chosen to be 0.5 mm. After identifying the most promising geometries, by comparing the net power densities ratio (θ), the corrugation height and the distance between two consecutive corrugations were optimized in terms of estimated net power density.

Based on the conclusions drawn from the 2D simulations results, 3D simulations were performed for two cases. The first one is known as "pillars" and has already been applied for power generation by RED [25, 28], while the second one has been inspired by staggered herringbone groves of fluidic mixing micro-devices [64-65]. For pillars, the dimensions are of the profiled membranes which were already fabricated [25], while for chevrons the dimensions were chosen in order to assure that the equivalent height of both structures is similar (0.411 and 0.417 mm for channels formed by pillars and chevrons, respectively).

Figure 5.3 shows the dimensions of a repetitive segment of the channel with chevron corrugations. This structure is similar to a design of a diamond-shape spacer, and therefore is expected to provide fully developed mass transfer conditions within the whole channel, even at low Reynolds numbers [66].

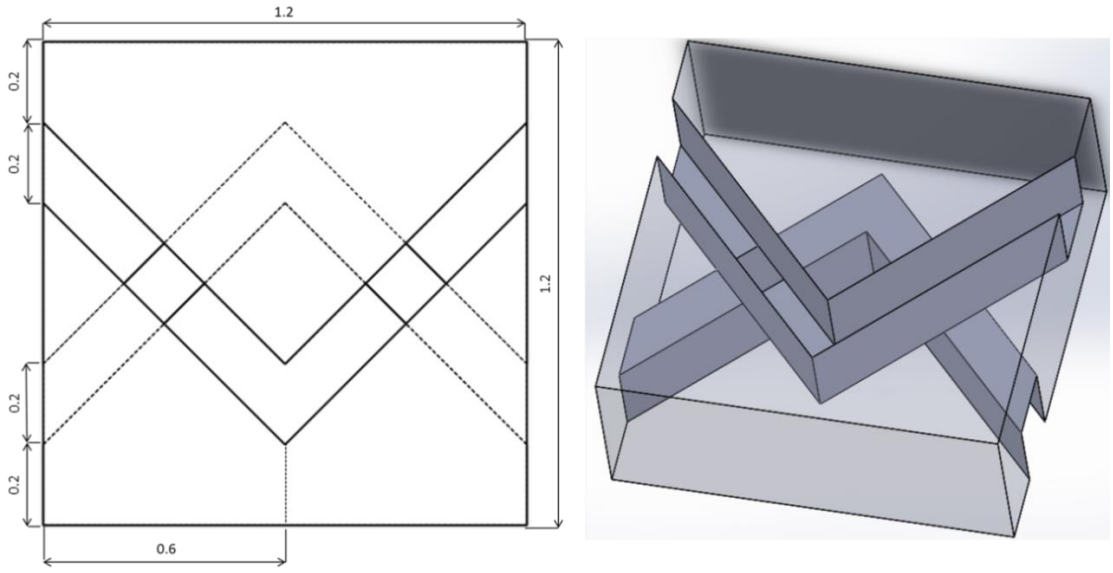

Figure 5.3. Dimensions of a repeated geometry segment of a channel with chevron corrugations used for CFD calculations.

Based on the mass transfer coefficient values obtained at the simulated linear flow velocities range, dimensionless empirical mass transfer correlations ($Sh = aRe^{b}Sc^{0.33}$) were obtained for pillar and chevron-like structures by adjusting the values of *a* and *b*: The Schmidt number (*Sc*) exponent is commonly set as 0.33 [30, 32, 40, 54] and was assumed as such herein. The Sherwood (*Sh*), Reynolds (*Re*) and Schmidt (*Sc*) numbers were calculated as follows:

$$Sh = \frac{k_c \cdot h_{eq.}}{D} \quad (5.26),$$

$$Re = \frac{\rho \cdot u \cdot h_{eq.}}{\mu} \quad (5.27),$$

$$Sc = \frac{\mu}{\rho \cdot D} \quad (5.28).$$

In order to compare the performance of the corrugations with non-conductive and conductive spacers, we calculated the net power density for such stacks, maintaining the same intermembrane distance and parameters values summarized in Table 5.1. The shadow effect of non-conductive spacers was assumed to be 50 % and both spacers porosities equal to 0.775 [60]. The mass transfer coefficient for channels with spacers was calculated by a previously developed and validated mass transfer correlation (Sh=0.29$Re^{0.5}Sc^{0.33}$) [10]. The pressure drop in the channel was obtained by the Darcy-Weisbach equation with a modified hydraulic diameter (d_{ch}), which accounts for the spacer influence on pressure drop [60]:

$$d_{ch} = \frac{4 \cdot \varepsilon}{\frac{2}{h} + (1-\varepsilon) \cdot \frac{8}{h}} \quad (5.29).$$

5.4. RESULTS AND DISCUSSION

5.4.1. 2D CFD simulations

As mentioned in Section 5.3.2, the available membrane area strongly affects the obtainable net power density. Therefore preliminary studies (see Supplementary material) were performed to find which corrugation geometries improve more significantly the obtainable net power density through their effects on mass transfer and on pressure drop.

A direct comparison of net power densities obtained with the studied corrugations shows that the highest net power density values were obtained for corrugations providing higher membrane surface area, even though pressure drop also increased in such cases. However, the highest

difference in net power density among the cases studied did not exceed 7 %, since the differences in available membrane area are actually small. The net power density shows to be sensitive to mass transfer coefficient and pressure drop values obtained by CFD, as for different corrugations, but with the same surface area, i.e., for the same equivalent channel height, the calculated net power density values were different between the cases, which opens space for corrugation shape optimization.

Since the distance between two consecutive corrugations and their height can be varied and, therefore, the membrane area could be increased for any of the studied corrugations, what is important to know is which geometry has the highest potential to increase the net power density due to its effect on mass transfer coefficient and on pressure drop. Therefore, we calculated the net power density ratios as defined by equation 5.3. The corrugation shapes more suitable for optimization are those with a higher ratio, since, in such cases, a corrugation increases more significantly the obtainable net power density only due to its shape. In this study, corrugations "A" and "C" presented the highest net power density ratios for mirror and diagonal arrangements, at linear flow velocities of 0.5 cm/s and 2.0 cm/s, respectively, and, therefore were the most promising structures to be investigated (see Supplementary material).

However, it was found, for both arrangements, that the only meaningful advantage of using transversal corrugation was a reduction of the spacer shadow effect comparatively to the design with non-conductive spacers. The optimal geometry based on θ (if the influence of the available membrane area on the ohmic resistance is ignored) tends to approximate to that of a flat (non-corrugated) membrane, as the trade-off between mass transfer increase and pressure drop increase is not favorable when the corrugations dimensions increase. A discussion on the 2D simulations results obtained can be found in Supplementary material.

5.4.2. Pillar and chevron corrugations (3D CFD simulations)

5.4.2.1 Mass transfer coefficients and pressure drop

Since 2D simulated corrugations did not promoted an effective fluid mixture close to membranes surfaces, more complex geometries must be investigated in order to induce transverse flow instabilities. Such structures require representation in a 3D space. Membrane corrugations in the form of pillars are one of the possibilities that have been already suggested for RED [25]. However, such corrugations can lead to creation of stagnant zones upstream to the structures. In these stagnant regions, particle deposition and biofilm formation may occur [28, 67]. 3D simulations performed by us for a pillar geometry (not shown) confirmed the existence of such stagnant regions upstream to the corrugation.

Therefore, inspired by microfluidic mixture devices [64-65], in which the flow is laminar, a herringbone type of corrugations was investigated. Since the herringbones grove depth strongly influences the mixing efficiency, while the flow attack angle does not [64-65], when groves exist on the two faces forming a channel, chaotic flows are induced and the mixing channel length is reduced [68]. Arrangement of symmetric herringbones on both faces of a channel is known as "chevrons" in the microfluidic devices related literature [69]. Herein, this type of corrugation was simulated for the first time in the context of a RED application.

Figure 5.4 presents the simulated mass transfer coefficient values of on the membrane surface for chevron channels at linear flow velocities of 0.5 cm/s and 2.0 cm/s when the solute concentration profile is fully developed.

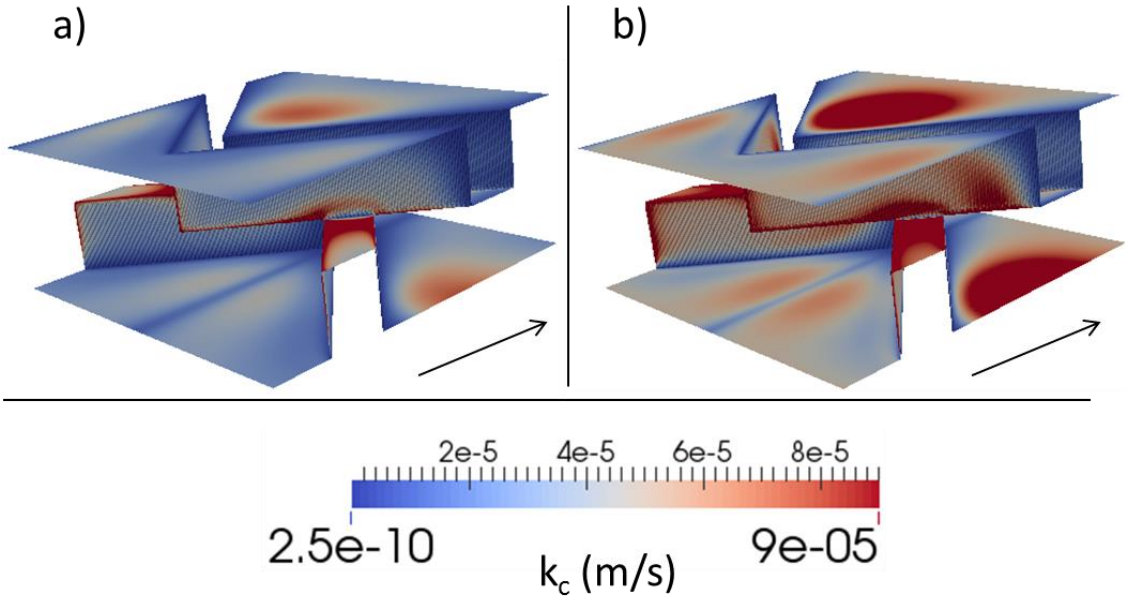

Figure 5.4. Maps of mass transfer coefficient in channels formed by membranes with chevron corrugations at two average linear flow rates: a) 0.5 cm/s, b) 2.0 cm/s.

As expected, the mass transfer coefficient values are lower at a lower linear flow velocity; however, in both cases the fluid flow distribution is similar. The main advantage of using the chevron design appears to be related to high local mass transfer coefficient values upstream to the chevron, where usually there are issues associated with flow dead zones. In this case, the only dead zone, which extends through the channel length, was found to be that located upstream to the chevron tip, and in such a way it occupies only a very small channel volume.

Figure 5.5 shows a comparison between pillar and chevron corrugations in terms of mass transfer coefficients and pressure drop within an identical linear flow velocity range.

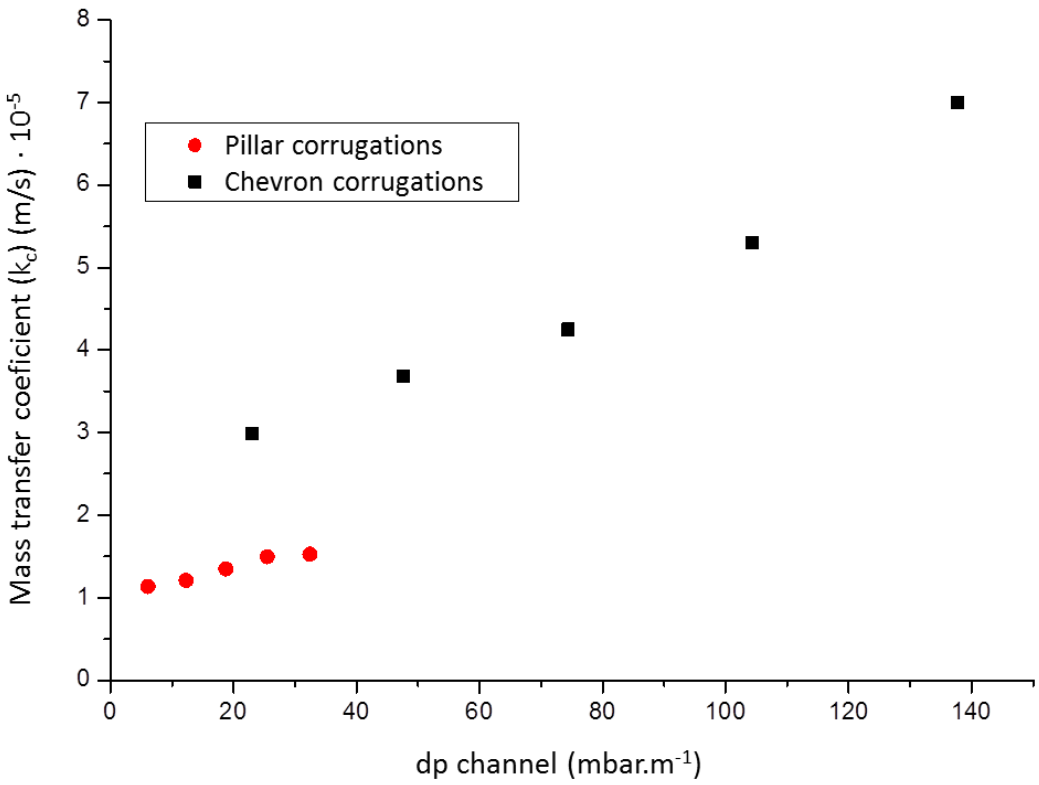

Figure 5.5. Representation of the average mass transfer coefficient at fully developed concentration profile in function of pressure drop for a linear flow velocity range between 0.5 cm/s and 2.5 cm/s.

Within the studied linear flow velocities range (0.5 cm/s – 2.5 cm/s), the mass transfer coefficient was found to be always higher for the design with chevron corrugations than for the design with pillars. The respective dimensionless empirical mass transfer correlations were:

- $Sh = 0.53 Re^{0.59} Sc^{0.33}$, for chevron corrugations, and

- $Sh = 0.30 Re^{0.20} Sc^{0.33}$, for pillar corrugations.

As it can be seen (Figure 5.5), for the same pressure drop, the mass transfer coefficient is higher for chevron corrugations, what could indicate that utilization of chevrons leads to a better fluid dynamics in the so formed channels. However, as a higher pressure drop was found at the same linear flow velocity for the chevron structures, the enhancement of mass transfer comes at an increased energy demand penalty, which may outweigh its benefits in terms of the power gained. Therefore a more detailed study on the obtainable net power densities is required.

5.4.2.2 Net power density

Figures 5.6a and 5.6b present the overall net power densities values for pillar and chevron structures, respectively, for channels with different lengths. In stacks with very short channels,

and therefore small membrane area, the net power density departs from negative values. That is caused by pressure drops in the stack flow distribution system (due to branches and in distribution ducts), which do not depend on channel length [60]. Therefore, when the power spent for pumping is normalized by the membrane area (eq. 5.23) it becomes much bigger than the obtained gross power density.

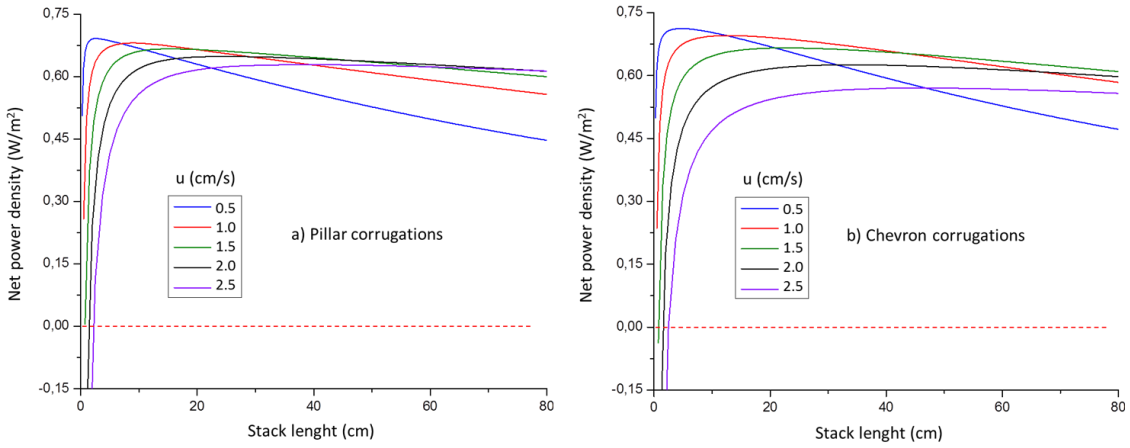

Figure 5.6. Simulated net power density (W/m^2) in stacks with a) pillar and b) chevron corrugations at different linear flow velocities (cm/s) for variable stacks' length.

As the channel length and the membrane area increase, the net power density becomes positive and reaches its maximum value. The decrease in the net power density afterwards is caused by a decrease in the potential difference along the channel, since the ions are transported from concentrated to dilute saline stream compartments (Appendix 5A). The maximal net power density values are higher for smaller linear flow velocities and smaller channels lengths since, for the same average potential difference, the pressure drop in the channels is smaller. As the channel length increases, the linear flow velocity must also increase, in order to keep the fluid residence time similar. The residence time for the maximal net power densities is not exactly the same for different velocities, as the flow entrance effects are more pronounced for higher velocities [10], which allows for utilization of longer channels than those expected from a direct proportionality between velocities. For example, for a chevron geometry, the optimum fluid residence time is 7.5 seconds for a linear flow velocity of 0.5 cm/s, and 13 seconds for a linear flow velocity of 2.0 cm/s.

In terms of obtainable net power density, the maximal values were higher for the chevron design up to a linear flow velocity of 1.5 cm/s. This means that chevron-like corrugations perform better than pillar corrugations since under the conditions more indicated for power generation, i.e. a stack with short channels, their utilization would generate more net power. Above 1.5 cm/s, the higher pressure drop caused by chevron-like corrugations limits their utilization.

One of the advantages of utilizing profiled membranes has been reported to be a pressure drop reduction comparatively to the case of using spacers (conductive and non-conductive) [12]. Nevertheless, since the simulations demonstrate that chevron structures performed better than pillar forms, which in turn were proven to be better than spacers [25], the higher pressure drop offered by chevron corrugations does not seem impeditive, if the linear velocity range (Table 5.2) is wisely chosen.

Table 5.2. Comparison of RED stacks with chevron and pillar corrugations and with conductive and non-conductive spacers.

u (cm/s)	Max. P_{net} Density (W/m^2)			k_c (m/s)·$10^{-5(*)}$			dp channel (mbar/m)		
	Pillar	Chevron	(Non) Conductive Spacer	Pillar	Chevron	w/ Spacer	Pillar	Chevron	w/ Spacer
0.5	0.69	0.71	(0.41) 0.58	1.14	2.99	1.30	6.08	23.07	14.47
1.0	0.68	0.70	(0.40) 0.59	1.21	3.68	1.83	12.31	47.56	28.94
1.5	0.67	0.67	(0.38) 0.57	1.35	4.25	2.25	18.76	74.44	43.40
2.0	0.65	0.63	(0.35) 0.55	1.49	5.30	2.60	25.48	104.32	57.87
2.5	0.63	0.57	(0.32) 0.52	1.53	7.00	2.90	32.45	137.68	72.34

(*) Values obtained for the region of a fully developed solute concentration profile (i.e. without flow entrance effects influence on mass transfer.

With the proposed chevron-like design, at a linear velocity range of 0.5 cm/s – 1.5 cm/s, the pressure drop is ~1.6 – 1.7 times higher comparatively to utilization of spacers, but also a higher increase in mass transfer coefficient (~2.3 – 1.9 x) is obtained. This may indicate that the energy spent for reducing the diffusion boundary layer thickness is applied where it is precisely needed (in the vicinity of the membrane surfaces), opposite to the case of spacers, which mainly promote bulk solution mixing. In such a way, chevron structures allow for a more significant increase in the mass transfer coefficient.

In section 5.2.1, the parameter θ was defined for comparing the performance of different corrugations in terms of obtainable net power density through dividing the net power density for a stack with corrugations/spacers by the net power density obtainable in a hypothetical stack with empty channels. The equivalent thickness of both channels was considered to be the same, what allows for excluding the influence of the ohmic resistance on the obtainable net power density and for comparing the effects of pressure drop and mass transfer coefficient. Figure 5.7 shows the value of this ratio for the simulated corrugations and spacers in function of linear flow velocity.

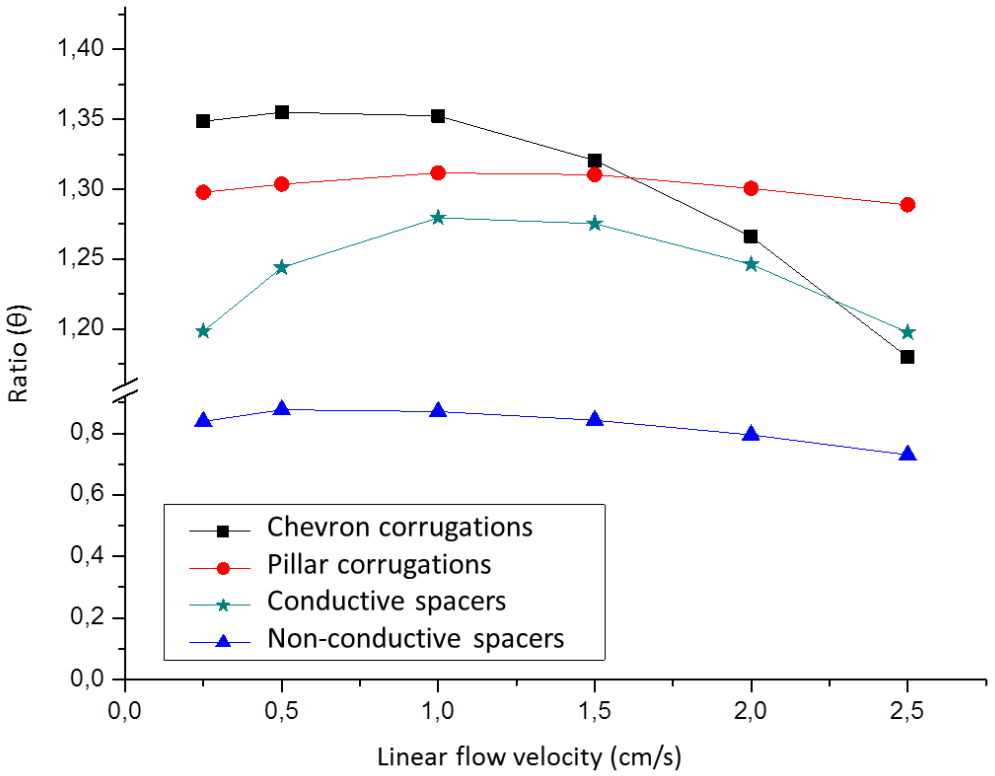

Figure 5.7. Comparison of net power density ratios (θ) between stacks with profiled membranes (Pillar and Chevron) and stacks with spacers (conductive and non-conductive).

As seen in Figure 5.7, the ratios are always higher than 1, except for a stack with non-conductive spacers. Moreover, the ratio for channels with corrugated membranes is higher than for a stack with conductive spacers. Also, since the values are higher than 1, this means that the shape of the corrugation had also improved the fluid dynamics, besides increasing the available membrane area, which it is an advantage relatively to corrugations which are perpendicular to the fluid flow.

The chevron corrugations proposed show that the highest improvement of stack performance and their highest efficiency is for linear velocities between 0.5 cm/s and 1.5 cm/s. For higher linear velocities, the use of chevron structures becomes less efficient. Curiously, since the chevron design is somehow similar to the design of a diamond-shape spacer, but with an advantage of a forced fluid transport upstream to the corrugations, the shape of the (θ) ratio curves for chevron and diamond-type spacers is very similar (Fig. 5.7).

It is also important to consider some practical issues when the choice of the corrugations and channels dimensions is done. As the final objective of RED is to take advantage of expected realizable global salinity gradient potential, due to rivers discharge, which is estimated to be close to 1 TW [4, 70], large membrane areas must be used. Despite the fact that shorter channels

allow for achievement of higher net power density values, from a practical point of view, utilization of longer channels and, therefore, higher linear flow velocities, could be more advisable. Under such conditions, for example for 30 cm long channels the optimum velocity for chevron configuration is around 1.0 cm/s, while for pillars is around 1.5 cm/s (Graphical abstract). Therefore, we anticipate that the developed chevron corrugations could improve the RED process economy by reducing the feed flowrate of saline solutions.

5.5. OUTLOOK

The results of this study support the idea that the use of non-conductive spacers, which increase the ohmic resistance and can create regions prone to fouling in their knits, should be avoided. Utilization of profiled membranes, with the proposed chevron corrugation shape, offers an appropriate trade-off between mass transfer and pressure drop, besides reducing the channels dead flow zones and increasing the available membrane area for ion transport. However, under currently realistic conditions for industrial-scale power generation, e.g., channels thickness of 0.5 mm (in order to avoid channels clogging) and chevron-like profiled membranes created from heterogeneous ion-exchange membranes (with a membrane area resistance of 7.5 Ωcm^2), the maximal expected net power density value (at a linear flow velocity of 0.5 cm/s) is 0.71 W/m^2.

Nevertheless, for chevron-like structures and the same parameters as in Table 5.1, but assuming a hypothetic profiled membrane area resistance of 1 Ωcm^2, the net power density values can be close to 1.15 W/m^2. If a free or cheap heat source could be found to increase the solutions temperature from 20ºC to 40ºC, the value of the net power density can additionally raise up to 1.3 W/m^2. Therefore, development of membranes with a low area electric resistance, but still thick enough to allow creating corrugations on their surfaces, is of an obvious interest. Even a higher increase in net power density could be achieved if, at the same time, the thickness of the channels can be also reduced. Based on the developed mass-transfer correlation, the obtainable net power density could be as high as 3.7 W/m^2 (at 20ºC) and 4.2 W/m^2 (at 40ºC) with chevron structures and the channel equivalent thickness of 0.1 mm. However, utilization of such thin channels will require extensive water pretreatment in order to remove possible foulants from the water streams, the cost of which is currently pointed out to be even higher than the solutions pumping associated costs [71]. Therefore, further studies are needed.

Also, as a general rule, it can be stated that channels should be as short as possible, in order to benefit from the flow entrance effect on mass transfer [10]. At the same time, the channels cannot be too short in order to avoid a situation, at which the power spent for solutions pumping

and required to overcome the partial pressure drops in the stack manifolds and branches (which are independent from the channel length) exceeds the generated power [60]. As the pressure drop in the manifolds becomes dominant when the channels are shorter, the feedwater distribution system becomes very important and should be optimized.

For designing new and improved feedwater distribution systems, CFD tools can be used, as the main objective passes through minimization of the pressure drop, which can be accounted for by the mass continuity and Navier-Stokes equations. An alternative to modification of the feedwater distribution system geometry could pass through changing the stack design from a plate-and-frame type to a tubular or a radial membrane arrangement. There are a number of designs explored in the field of heat exchangers and microfluidic devices, which may serve as sources of inspiration [72].

5.6. CONCLUSIONS

In the present work, we have simulated the net power density of RED stacks with different channel arrangement. Profiled membranes with corrugations perpendicular to flow as well as chevron and pillar structures were investigated in detail. The results were compared with the performance of RED stacks with conductive and non-conductive spacers.

Utilization of profiled membranes and conductive spacers present the already known advantage of eliminating the shadow effect when non-conductive spacers are used. In terms of fluid dynamic effects on net power density, perpendicular corrugations do not enhance the stack performance, but still lead to a net power density increase due to the increase of the available membrane area for counter-ion transport.

The chevron and pillar structures lead to higher performances, in terms of the fluid dynamics and net power density, than conductive spacers, which may be an indication that development and utilization of profiled membranes is advantageous. Also, in such a way, lower quantity of expensive and conductive material is used, since the membranes self-maintain the channel compartment thickness.

Simulations of chevron structures show the highest net power density values and the best compromise between mass transfer coefficient and pressure drop increase. Moreover, it is expected that due to the very specific fluid pathway, the channels with chevron corrugation will be less prone to fouling. Also, in order to grant a maximal net power density for a given stack length, the linear flow velocity is lower when chevron corrugations are applied, which, for

industrial size equipment, may represent economic advantages since smaller volumes of water must be pretreated.

The simulated chevron structures still need to be experimentally validated, as well as their geometry parameters should be optimized for RED application. Moreover, since we found that chevron structures do not only generate more power when used in RED stacks, but also represent the best compromise between mass transfer and pressure drop, they also should also be rather promising for other electromembrane processes.

APPENDIX 5A

The final goal of the performed simulation was to obtain the net power density values. In order to obtain these values, it was necessary to simulate the solute concentration profiles along the channel, and then to calculate the local electric potential difference and resistances values.

Herein, the case for channels with chevron structures for a linear flow velocity of 0.5 cm/s is presented. The respective curve for net power density can be seen in Figure 5.6b.

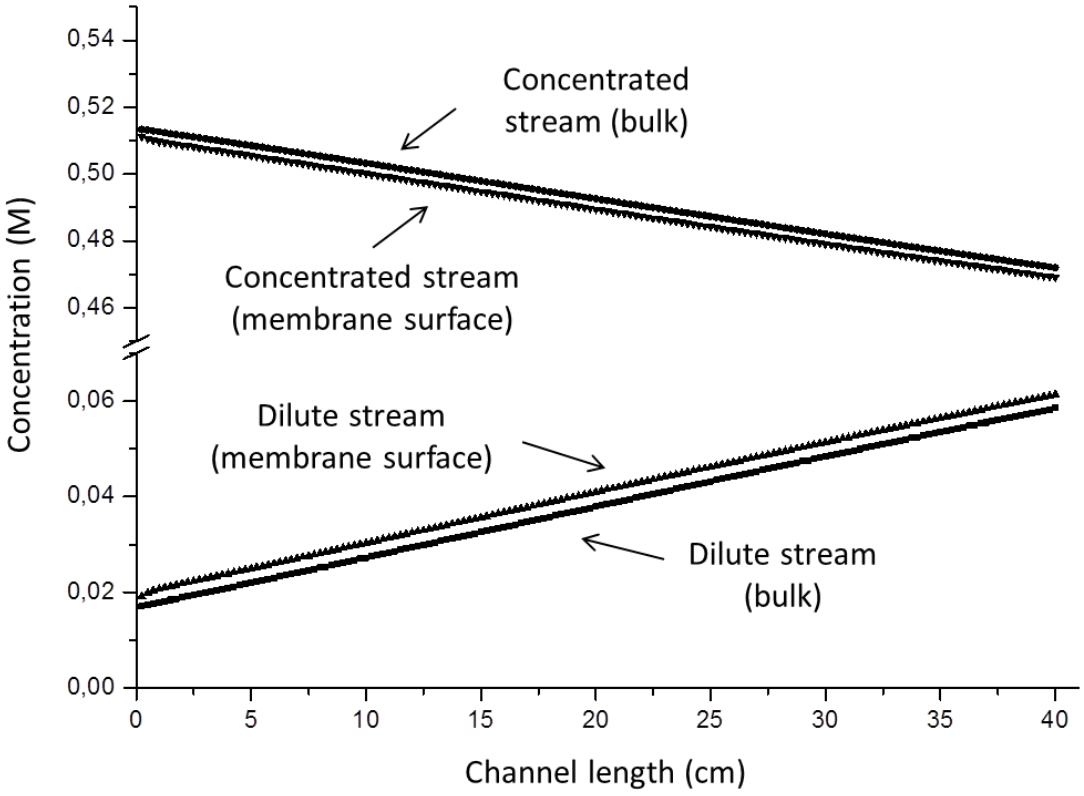

Figure 5A.1 Solute (NaCl) concentration profiles in dilute and concentrated streams channels in the bulk and on the membrane surfaces.

Figure 5A.1 shows the profile of solute concentrations in the dilute and concentrated channels. As can be seen, in the dilute saline stream compartment the concentration increases along the channel length, while in the concentrated saline stream compartment the opposite trend is observed. This is due to the transport of ions from the concentrated to the dilute solution compartment during the RED process.

Figure 5A.2 presents the values of the most significant resistances in a RED stack, besides the resistance of the membranes (set at 7.5 $\Omega.cm^2$).

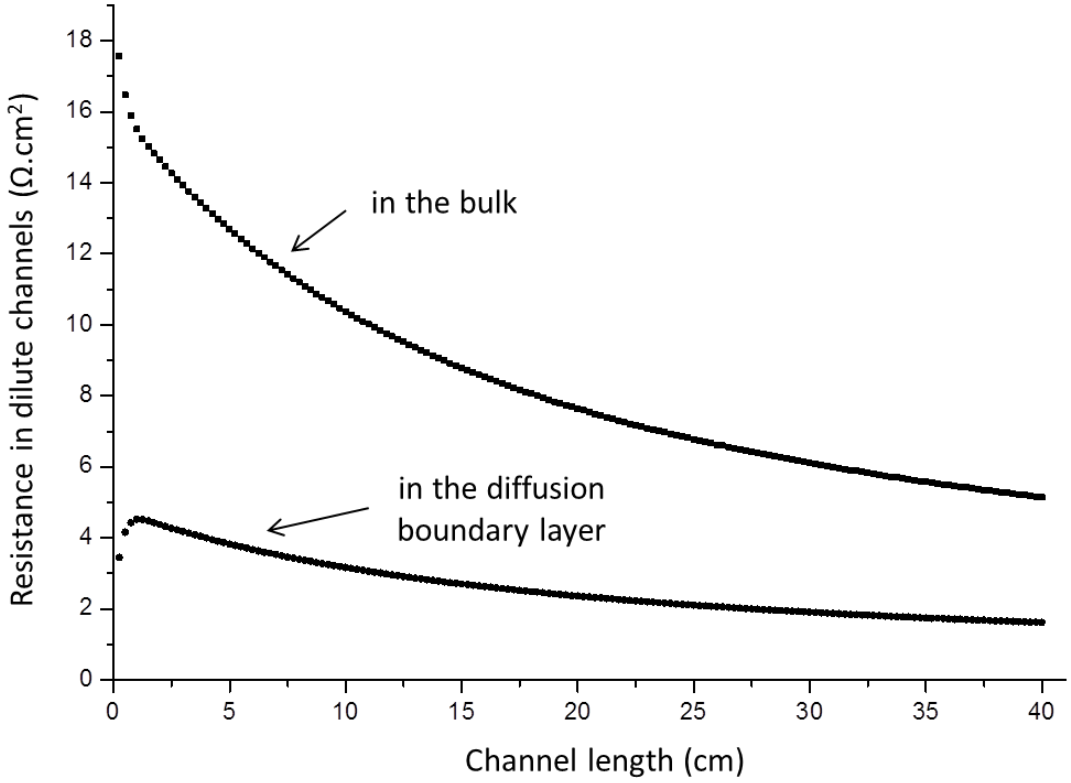

Figure 5A.2. Simulated local electric resistance values in RED stack channels with the dilute saline stream solution.

The resistance of the dilute saline stream in the bulk decreases along the channel length as the solution becomes more concentrated. For the liquid diffusion boundary layer, there are two effects observed. The DBL thickness increases until a channel length of 2 cm, what leads to an increase in the corresponding resistance, while after this point, since the thickness of DBL stabilizes, and the solute concentration within DBL increases, the DBL resistance starts to decreases. Just for comparison, the resistance in the concentrated compartment is never higher than 1.1 $\Omega.cm^2$ for the case shown.

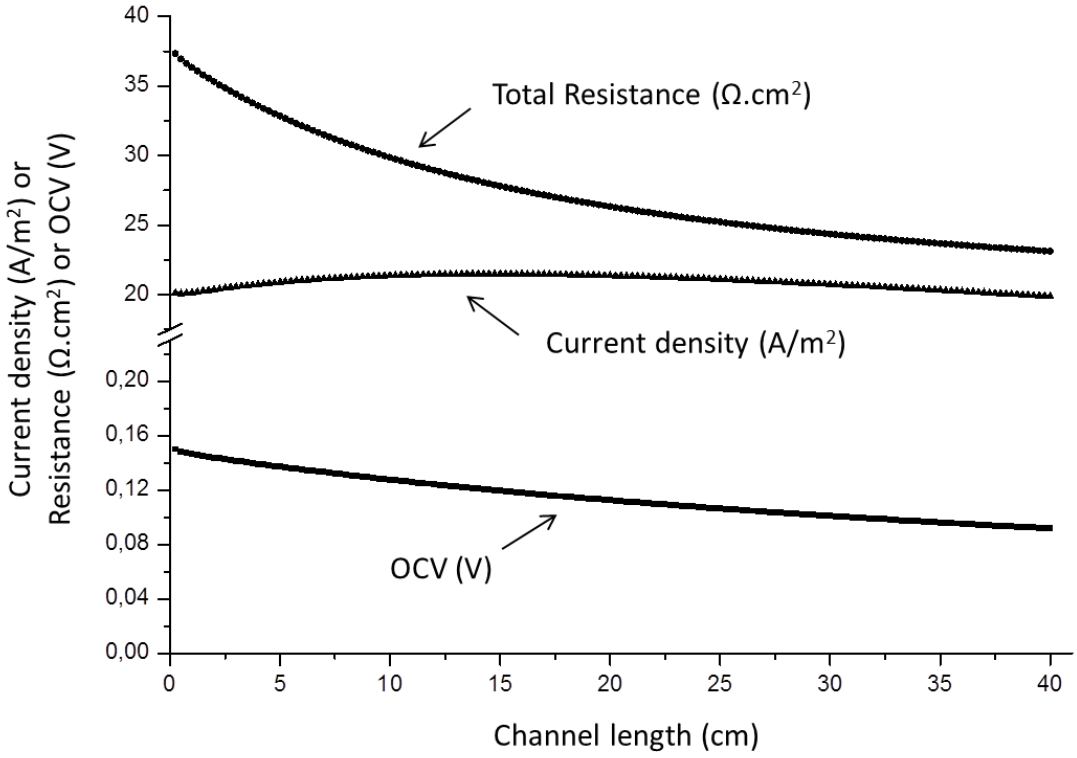

Figure 5A.3. Values of total electric resistance, current density and OCV along the channel length.

As expected, the OCV decreases along the channel length (Figure 5A.3) due to the reduction of solute concentration difference (Figure 5A.1). This decrease is higher close to channel entrance, when the DBL thickness is developing. The total resistance (i.e. the sum of resistances offered by the solutions, membranes and DBLs) decreases along the channel length as the dominant resistance (the dilute bulk solution resistance) has this tendency. Since the total resistance and OCV decrease along the channel length in a similar way, the current density remains almost constant at about 20 A/m^2.

SUPPLEMENTARY MATERIAL

Corrugation shapes studied by 2D simulations

Table 5SM.1 summarizes the investigated shapes of membrane surface corrugations. A flow channel is formed by two profiled membranes. The bottom membrane has corrugations as shown in Table 5SM.1, while the corrugations on the top membrane are symmetrical relatively to the X axis of the ones shown. The flow is from the right to the left. The corrugations may face each other (mirror arrangement) or may be located alternately on the bottom or top membrane along the channel (diagonal arrangement) (Figure 5SM.1).

Table 5SM.1. Corrugation shapes used in 2D CFD simulations and the respective net power density ratios (θ) at linear flow velocities of 0.5 cm/s and 2 cm/s. The highest obtained values of θ for both linear flow velocities are highlighted in bold.

Name	Corrugation shape	2 cm/s (Mirror)	2 cm/s (Diagonal)	0.5 cm/s (Mirror)	0.5 cm/s (Diagonal)
A		0.939	0.992	**1.016**	1.001
B		0.969	0.997	1.010	1.003
C		0.971	**0.998**	1.008	1.004
D		0.969	0.996	1.003	1.002
E		0.969	0.980	0.997	0.991
F		0.975	0.996	1.008	1.002
G		0.973	0.986	1.003	0.994
H	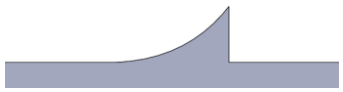	0.966	0.983	0.997	0.991
I		0.966	0.994	1.005	1.004
J	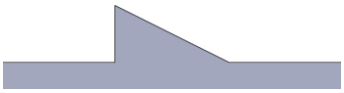	0.965	0.990	1.001	0.998
K	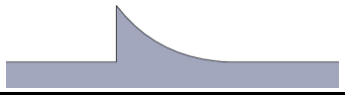	0.963	0.987	0.996	0.995

Table 5SM.1 presents the calculated θ ratio values for mirror and diagonal arrangements, respectively, using the corrugations dimensions as described in Section 5.3.2. At a linear flow velocity of 2 cm/s, the obtained θ ratio is higher for a diagonal arrangement for all cases. However, as the linear flow velocity decreases, it was observed that the mirror design eventually becomes preferable. This can be explained by the tortuous flow pathway in diagonal design, in which, even at high velocity, the solution is renewed close to all membrane surfaces. In mirror design, the fluid tends to flow preferably through the middle of the channel as the linear flow velocity increases.

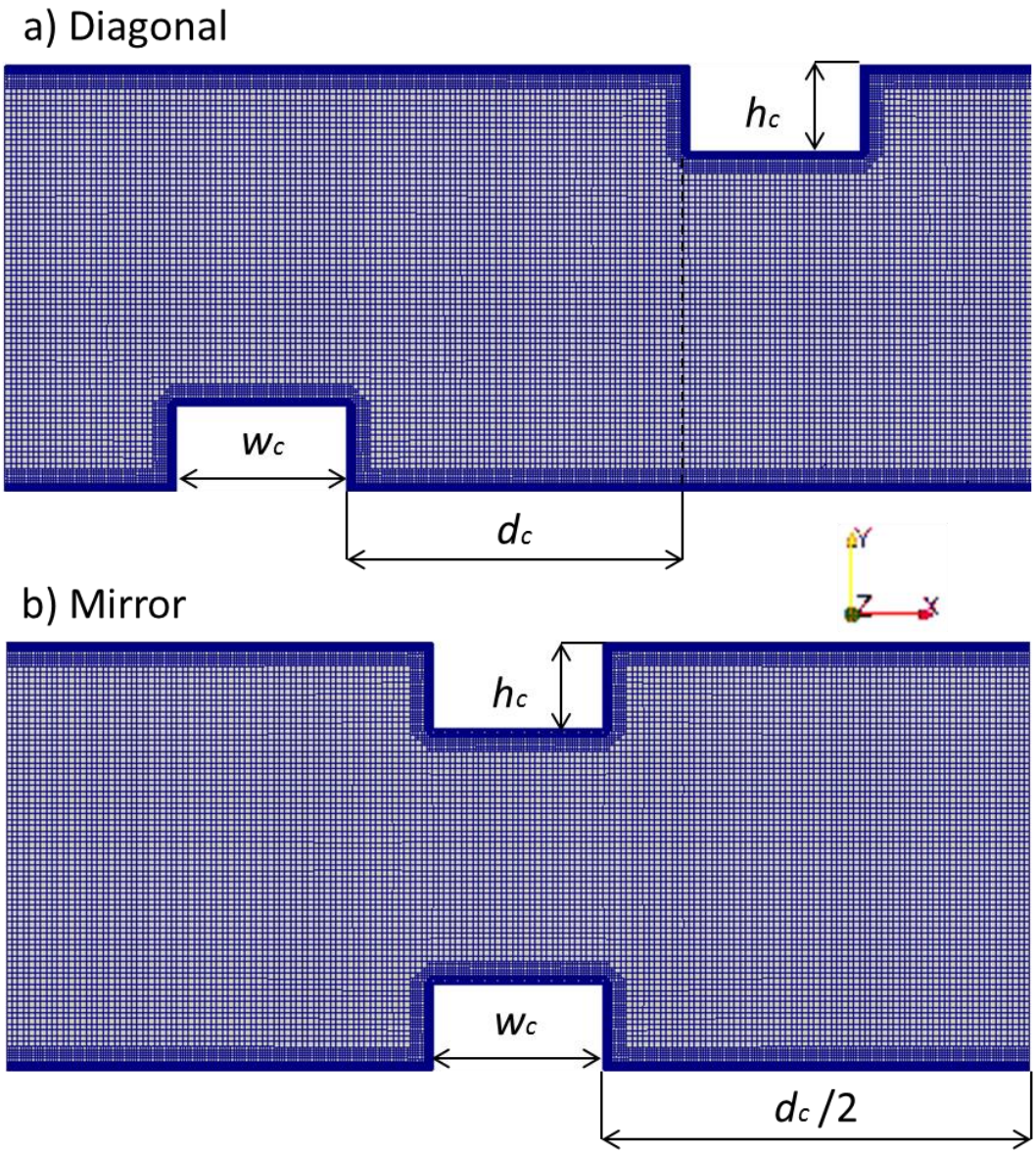

Figure 5SM.1. Examples of computational grids used for the CFD calculations at two arrangements of profiled membranes: a) diagonal, b) mirror (wc – corrugation width, hc – corrugation height, dc – distance between two consecutive corrugations).

Also it is possible to see that the presence of corrugations, with the initially defined dimensions, do not improve the channel performance ($\theta \leq 1$) relatively to an empty channel. The θ values increase with a decrease in linear flow velocity, but for such conditions only short channels can be used in order to grant a desirable residence time [46]. Obviously, as the channel length increases, the optimal linear flow velocity must also increase.

Optimization of most promising corrugation shapes studied in 2D CFD simulations

Diagonal arrangement:

Figure 5SM.2 shows the map of estimated net power density values for channel "C" in function of distance between two consecutive corrugations and its height. The average linear flow velocity in the channel is 2.0 cm/s.

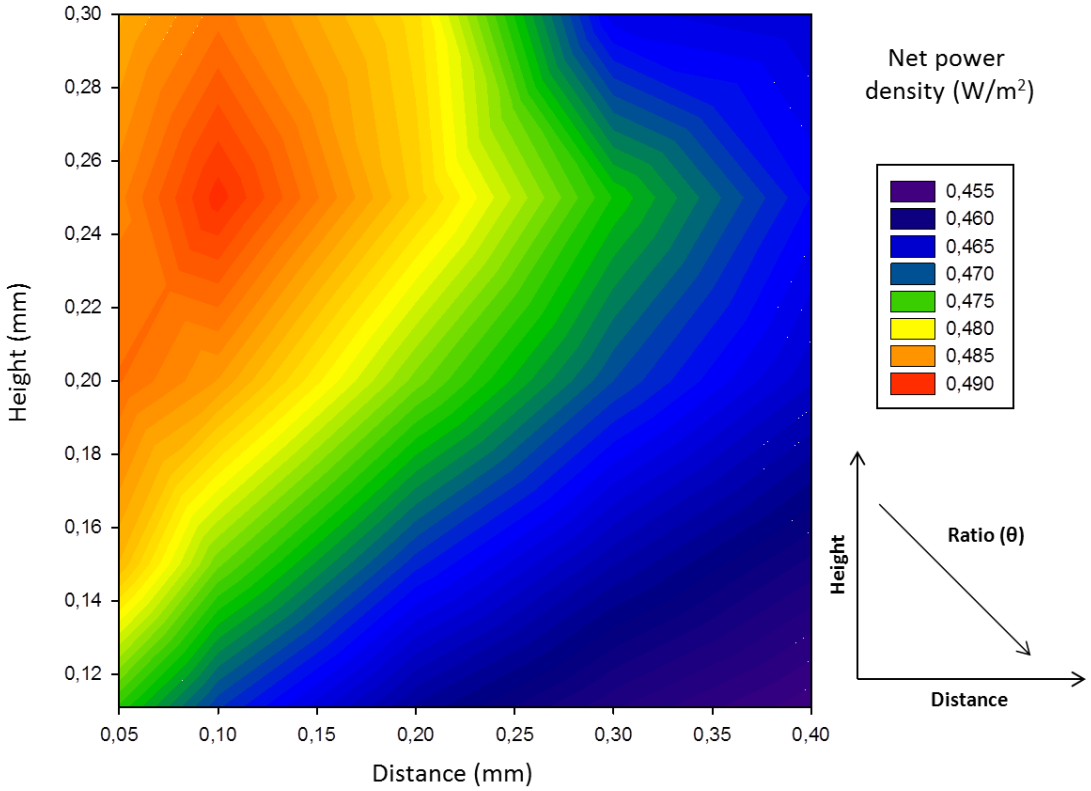

Figure 5SM.2. A net power density map for stacks with "C" corrugations, in diagonal arrangement, at an average linear flow velocity of 2.0 cm/s. The net power density value in a stack with flat (non-profiled) membranes and channel thickness corresponding to corrugations height and distance of 0.25 mm and 0.1 mm, is 0.514 W/m^2.

It is possible to observe that for each distance there is an optimal corrugation height, and for each height there is an optimal distance between the corrugation, and, together, it is possible to define optimal corrugations height and distribution, which are 0.25 mm and 0.10 mm, respectively. The net power density changes in a sharper way at bigger heights and lower inter-corrugations distances. Such behavior depends on the spatial evolution of pressure drop and mass transfer coefficient values, which are shown in Figure 5SM.3a and 5SM.3b, respectively.

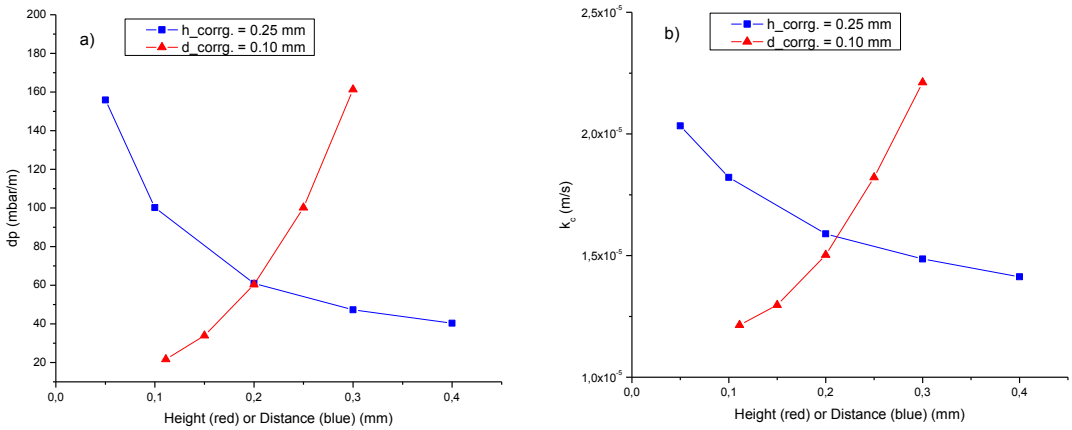

Figure 5SM.3. Normalized pressure drop (a) and mass transfer coefficient (b) in the channel with "C" corrugations, in a diagonal arrangement, at an average linear flow velocity of 2.0 cm/s. The blue line (with rectangular symbols) shows the variation of the investigated variable with distance between corrugations when the corrugations height is maintained constant (0.25 mm). The red line (with triangles) shows the variation of the investigated variable with corrugations height when the distance between corrugations is maintained constant (0.1 mm).

Figure 5SM.3a shows that the pressure drop increases by about 4 times when the distance between the corrugations decreases from 0.40 mm to 0.05 mm, while the corrugations height is maintained equal to 0.25 mm. However, that pressure drop increase is not uniform, and is more pronounced for lower distances between corrugations. If the distance between corrugations is maintained constant (0.1 mm), but the corrugations height is increased from 0.11 mm to 0.30 mm, the pressure drop increases almost 8 times. Again, this increase is not proportional as it is more pronounced for high corrugations' height. In such a way, at those regions in which the pressure drop strongly varies with any corrugation' dimensions alteration, the net power density values are also more affected.

Figure 5SM.3b demonstrates how the distance between corrugations and the corrugations height affect the average mass transfer coefficient. As expected, the mass transfer coefficient also increases when pressure drop increases since an increase in pressure drop is associated with an increase of laminar mixing, which is expected to enhance the mass transfer. However, the observed mass transfer coefficient increase is less than twice for both dimensions variation while, as mentioned previously, the pressure drop increase is about 8 times.

Observing the corrugations effect on both variables it is possible to understand the net power density evolution. An increase in corrugations height and a decrease in distance between corrugations, leads to an increase of mass transfer coefficient (and a net power density increase); however, there is a point where the pressure drop increase becomes the dominant effect on the process performance, which causes a decrease in the net power density.

Mirror arrangement:

Figure 5SM.4 shows the most important parameters for channel "A" in function of the distance between corrugations and their height. The average linear flow velocity in the channel is 0.5 cm/s.

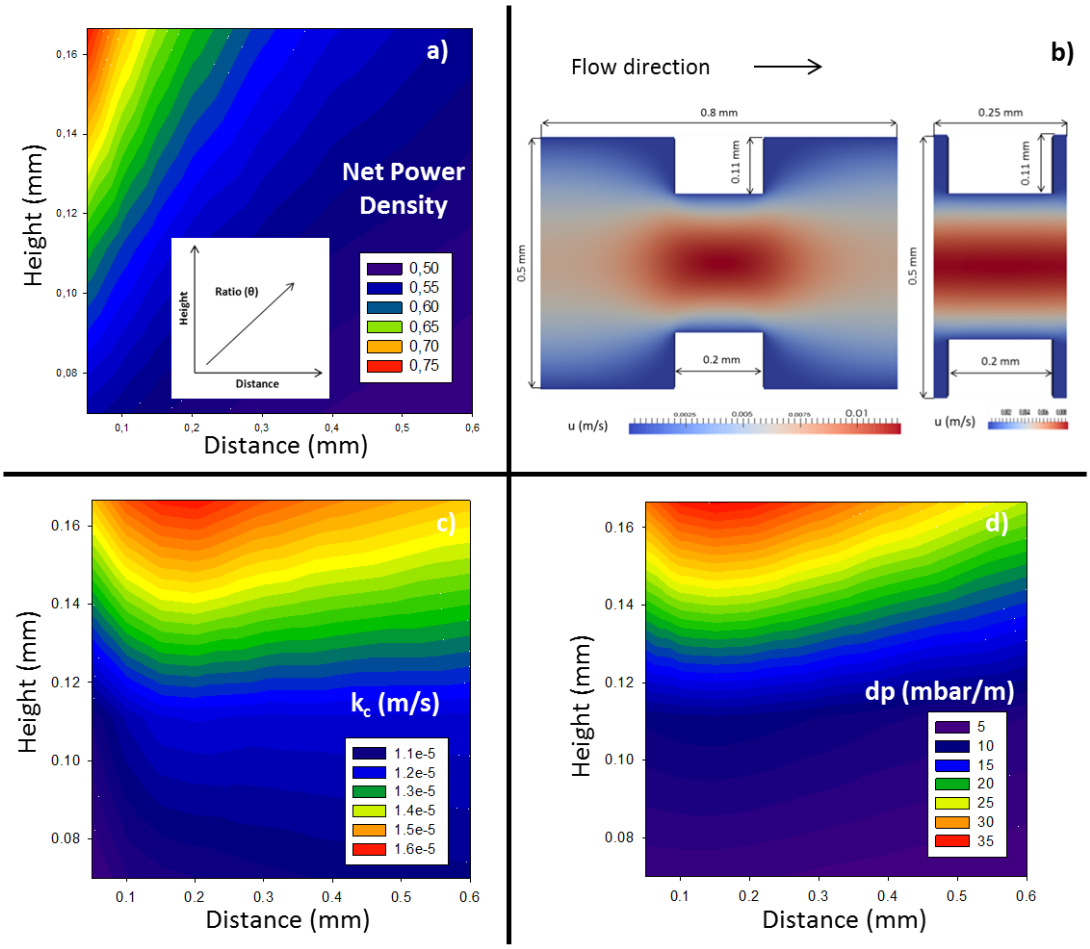

Figure 5SM.4. Maps of results for stacks with "A" corrugations, in mirror arrangement, at an average linear flow velocity of 0.5 cm/s: a) net power density values, b) velocity profiles for inter-corrugation distance of 0.6 mm and 0.05 mm, c) mass transfer coefficient values, d) normalized pressure drop values. The net power density value in a stack with flat (non-profiled) membranes and channel thickness corresponding to corrugations height and distance of 0.166 mm and 0.2 mm, is 0.599 W/m^2.

As can be seen, the net power density increases with increase of the corrugations height and with decrease of the distance between corrugations (Figure 5SM.4a). In such a way, the channel geometry tends to an empty channel with a very low height since, as the intermembrane distance decreases, the generated power densities are higher [42]. This is caused by reduction in the ohmic resistance in the compartments as well as due to a decrease in the diffusion boundary layer resistance, as predicted by the Leveque equation [10].

In terms of fluid dynamics, this is a somehow surprising result, since a small distance between the corrugations would be expected to lead to a creation of dead zones between them [7, 29]. In

Figure 5SM.4b, we present two extreme cases, for the lower and for the higher simulated distance between corrugations. Indeed, it is possible to see that at a smaller distance between corrugations, the solution does almost not flow in the "gap" between the corrugations.

Figures 5SM.4c and 5SM.4d show, respectively, how this affects the mass transfer coefficient and pressure drop values in the channel. Both parameters vary in a more pronounced way as the height of the corrugation increases, since this affects the flow pathway and leads to a stronger disruption of the flow. As the distance between corrugations decreases, the values of the two parameters increase, since the flow becomes more frequently disturbed, until the distance between corrugations becomes too short to allow solution renovation. In such a case, decreasing even more the distance between corrugations leads to a decrease in the mass transfer coefficient value, since the total membrane area becomes less efficiently used. The pressure drop also decreases, since the fluid flows mainly through the middle of the channel, and the corrugations do not cause perturbations of the flow.

For a mirror arrangement, the θ increases when corrugations height and distance between them increase. As the corrugations height increases this leads to a strangulation of the channel and, since the distance between two consecutive strangulations is high, the fluid may again expand through the whole channel. This behavior is very similar to the one typical for a *vena contracta* [60]. Since the fluid at a high velocity in the strangulation area shocks with comparatively stagnant fluid after a sudden section expansion, there exists fluid mixing [60, 73]. Despite this, the obtainable net power density values actually do not significantly increase since the increase in the membrane area available for ion transport is relatively small in such conditions.

REFERENCES

[1] M. Turek, B. Bandura, Renewable energy by reverse electrodialysis, Desalination 205 (2007) 67-74.

[2] J.W. Post, H.V.M. Hamelers, C.J.N. Buisman, Energy recovery from controlled mixing salt and fresh water with a reverse electrodialysis system, Environ. Sci. Technol. 42 (2008) 5785–5790.

[3] B.E. Logan and M. Elimelech, Membrane-based processes for sustainable power generation using water, Nature 488 (2012) 313-319.

[4] G.Z. Ramon, B.J. Feinberg, E.M.V. Hoek, Membrane-based production of salinity-gradient power, Energy Environ. Sci. 4 (2011) 4423–4434.

[5] J. Veerman, M. Saakes, S.J. Metz, G.J. Harmsen, Reverse electrodialysis: Performance of a stack with 50 cells on the mixing of sea and river water, J. Membr. Sci. 327 (2009) 136–144.

[6] J. Balster, D.F. Stamatialis, M. Wessling, Membrane with integrated spacer, J. Membr. Sci. 360 (2010) 185–189.

[7] D.A. Vermaas, M. Saakes, K. Nijmeijer, Enhanced mixing in the diffusive boundary layer for energy generation in reverse electrodialysis, J. Membr. Sci. 453 (2014) 312–319.

[8] P. Dlugolecki, A. Gambier, K. Nijmeijer, M. Wessling, Practical potential of reverse electrodialysis as process for sustainable energy generation, Environ. Sci. Technol. 43 (2009) 6888–6894.

[9] P. Dlugolecki, J. Dabrowska, K. Nijmeijer, M. Wessling, Ion conductive spacers for increased power generation in reverse electrodialysis, J. Membr. Sci. 347 (2010) 101–107.

[10] S. Pawlowski, P. Sistat, J.G. Crespo, S. Velizarov, Mass transfer in reverse electrodialysis: Flow entrance effects and diffusion boundary layer thickness, J. Membr. Sci. 471 (2014) 72–83.

[11] A. Daniilidis, D.A. Vermaas, R. Herber, K. Nijmeijer, Experimentally obtainable energy from mixing river water, seawater or brines with reverse electrodialysis, Renew. Energy 64 (2014) 123-131.

[12] D.A. Vermaas, M. Saakes, K. Nijmeijer, Power generation using profiled membranes in reverse electrodialysis, J. Membr. Sci. 385–386 (2011) 234–242.

[13] E. Brauns, Salinity gradient power by reverse electrodialysis: effect of model parameters on electrical power output, Desalination 237 (2009) 378–391.

[14] H. Strathmann, Electrodialysis, a mature technology with a multitude of new applications, Desalination 264 (2010) 268–288.

[15] I.G. Racz, J. Groot Wassink, R. Klaassen, Mass Transfer, Fluid flow and membrane properties in flat and corrugated plate hyperfiltration modules, Desalination 60 (1986) 213-222.

[16] L. Broussous, P. Schmitz, H. Boisson, E. Prouzet, A. Larbot, Hydrodynamic aspects of filtration antifouling by helically corrugated membranes, Chem. Eng. Sci. 55 (2000) 5049-5057.

[17] K. Scott, A.J. Mahmood, R.J. Jachuck, B. Hu, Intensified membrane filtration with corrugated membranes, J. Membr. Sci. 173 (2000) 1–16.

[18] K. Scott, R.J. Jachuck, D. Hall, Crossflow microfiltration of water-in-oil emulsions using corrugated membranes, Sep. Purif. Technol. 22-23 (2001) 431–441.

[19] P.Z. Culfaza, M. Wessling, R.G.H. Lammertink, Hollow fiber ultrafiltration membranes with microstructured inner skin, J. Membr. Sci. 369 (2011) 221–227.

[20] A.M. Peters, R.G.H. Lammertink, M. Wessling, Comparing flat and micro-patterned surfaces: Gas permeation and tensile stress measurements, J. Membr. Sci. 320 (2008) 173–178.

[21] A.M. Gronda, S. Buechel, E.L. Cussler, Mass transfer in corrugated membranes, J. Membr. Sci. 165 (2000) 177–187.

[22] C. Larchet, V.I. Zabolotsky, N. Pismenskaya, V.V. Nikonenko, A. Tskhay, K. Tastanov, G. Pourcelly, Comparison of different ED stack conceptions when applied for drinking water production from brackish waters, Desalination 222 (2008) 489–496.

[23] N. Tzanetakis, W.M. Taama, K. Scott, R.J.J. Jachuck, The effect of corrugated membranes on salt splitting, J. Appl. Electrochem. 33 (2003) 411–417.

[24] V.I. Vasileva, E.A. Goleva, Selective separation of sodium ions from a mixture with phenylalanine by Donnan dialysis with a profiled sulfogroup cation exchange membrane, Russ. J. Phys. Chem. A 87 (11) (2013) 1895–1901.

[25] E. Guler, R. Elizen, M. Saakes, K. Nijmeijer, Micro-structured membranes for electricity generation by reverse electrodialysis, J. Membr. Sci. 458 (2014)136–148.

[26] D.A. Vermaas, D. Kunteng, M. Saakes, K. Nijmeijer, Fouling in reverse electrodialysis under natural conditions, Water Res. 47 (2013) 1289-1298.

[27] D.A. Vermaas, M. Saakes, K. Nijmeijer, Early detection of preferential channeling in reverse electrodialysis, Electrochim. Acta 117 (2014) 9– 17.

[28] L. Gurreri, M. Ciofalo, A. Cipollina, A. Tamburini, W. Baak, G. Micale, CFD modelling of profiled-membrane channels for reverse electrodialysis, Desalination Water Treat., DOI: 10.1080/19443994.2014.940651.

[29] J. Balster, M.H. Yildirim, D.F. Stamatialis, R. Ibanez, R.G.H. Lammertink, V. Jordan, M. Wessling, Morphology and microtopology of cation-exchange polymers and the origin of the overlimiting current, J. Phys. Chem. B 111 (2007) 2152-2165.

[30] M.S. Isaacson, A.A. Sonin, Sherwood number and friction factor correlations for clectrodialysis systems, with application to process optimization, Ind. Eng. Chem. Process Des. Dev. 15 (1976) 313-321.

[31] H.J. Lee, H. Strathmann, S.H. Moon, Determination of the limiting current density in electro-dialysis desalination as an empirical function of linear velocity, Desalination 190 (2006) 43-50.

[32] V. Geraldes, M.D. Afonso, Limiting current density in the electrodialysis of multi-ionic solutions, J. Membr. Sci. 360 (2010) 499-508.

[33] J.G.D. Tadimeti, A. Chandra, S. Chattopadhyay S, Optimum concentrate stream concentration in CaCl2 removal from sugar solution using electrodialysis, J.Chem. Eng. Process Technol. 6 (2015) 1-13.

[34] J.L.C. Santos, V. Geraldes, S. Velizarov, J.G. Crespo, Investigation of flow patterns and mass transfer in membrane module channels filled with flow-aligned spacers using computational fluid dynamics (CFD), J. Membr. Sci. 305 (2007) 103–117.

[35] F. Li, W. Meindersma, A.B. de Haan, T. Reith, Optimization of commercial net spacers in spiral wound membrane modules, J. Membr. Sci. 208 (2002) 289–302.

[36] R. Kodym, F. Vlasak, D. Snita, A. Cernin, K. Bouzek, Spatially two-dimensional mathematical model of the flow hydrodynamics in a channel filled with a net-like spacer, J. Membr. Sci. 368 (2011) 171–183.

[37] L. Gurreri, A. Tamburini, A. Cipollina, G. Micale, CFD analysis of the fluid flow behavior in a reverse electrodialysis stack, Desalination Water Treat. 48 (2012) 390–403.

[38] A. Tamburini, G. Barbera, A. Cipollina, M. Ciofalo, G. Micale, CFD simulation of channels for direct and reverse electrodialysis, Desalination Water Treat. 48 (2012) 370–389.

[39] S.B. Beale, Use of streamwise periodic boundary conditions for problems in heat and mass transfer, J. Heat Transfer 129(4) (2006) 601-605.

[40] J. Welty, C. Wicks, R. Wilson, G. Rorrer, Fundamentals of momentum, heat, and mass transfer, 5th Edition, Wiley, Danvers – USA (2008), (pp. 305-307, 524-533, 542-545).

[41] L. Gurreri, A. Tamburini, A. Cipollina, G. Micale, M. Ciofalo, CFD prediction of concentration polarization phenomena in spacer-filled channels for Reverse Electrodialysis, J. Membr. Sci. 468 (2014) 133–148.

[42] D.A. Vermaas, M. Saakes, K. Nijmeijer, Doubled power density from salinity gradients at reduced intermembrane distance, Environ. Sci. Technol. 45 (2011) 7089–7095.

[43] J. Veerman, M. Saakes, S.J. Metz, G.J. Harmsen, Electrical power from sea and river water by reverse electrodialysis: A first step from the laboratory to a real power plant, Environ. Sci. Technol. 44 (2010) 9207–9212.

[44] P. Dlugolecki, P. Ogonowski, S.J. Metz, M. Saakes, K. Nijmeijer, M. Wessling, On the resistances of membrane, diffusion boundary layer and double layer in ion exchange membrane transport, J. Membr. Sci. 349 (2010) 369–379.

[45] R.W. Baker, Membrane technology and applications, Second edition, Wiley, Chichester, (2004) 411-415.

[46] D.A. Vermaas, E. Guler, M. Saakes, K. Nijmeijer, Theoretical power density from salinity gradients using reverse electrodialysis, Energy Proc. 20 (2012) 170 – 184.

[47] M. Tedesco , A. Cipollina , A Tamburini , W. van Baak, G. Micale, Modelling the reverse electrodialysis process with seawater and concentrated brines, Desalination Water Treat. 49 (2012) 404–424.

[48] A. Kozmai, V. Nikonenko, N. Pismenskaya, O. Pryakhina, P. Sistat, G. Pourcelly, Diffusion layer thickness in a membrane system as determined from voltammetric and chronopotentiometric data, Russ. J. Electrochem. 46 (2010) 1383–1389.

[49] J. Veerman, M. Saakes, S.J. Metz, G.J. Harmsen, Reverse electrodialysis: A validated process model for design and optimization, Chem. Eng. J. 166 (2011) 256–268.

[50] M. Tedesco, A. Cipollina, A. Tamburini, I.D.L. Bogle, G. Micale, A simulation tool for analysis and design of reverse electrodialysis using concentrated brines, Chem. Eng. Res. Des. 93 (2015) 441-456.

[51] D.A. Vermaas, J. Veerman, N. Yip, M. Elimelech, M. Saakes, K. Nijmeijer, High efficiency in energy generation from salinity gradients with reverse electrodialysis, Sustain. Chem.Eng. 1(10) (2013) 1295-1302.

[52] N. Pismenskaya, V. Nikonenko, E. Belova, G. Lopatkova, P. Sistat, G. Pourcelly, K. Larshe, Coupled convection of solution near the surface of ion exchange membranes in intensive current regimes, Russ. J. Electrochem. 43 (2007) 307–327.

[53] E. Belova, G. Lopatkova, N. Pismenskaya, V. Nikonenko, C. Larchet, G. Pourcelly, Effect of anion-exchange membrane surface properties on mechanisms of overlimiting mass transfer, J. Phys. Chem. B 2006, 110, 13458-13469.

[54] R. Valerdi-Perez, J. Mengual, Current-voltage curves for an electrodialysis reversal pilot plant: determination of limiting currents, Desalination 141 (2001) 23-37.

[55] H. Jeong, H. Kim, D. Kim, Numerical analysis of transport phenomena in reverse electrodialysis for system design and optimization, Energy 68 (2014) 229-237.

[56] J. Kim, S.J. Kim, D. Kim, Energy harvesting from salinity gradient by reverse electrodialysis with anodic alumina nanopores, Energy 51 (2013) 413-421.

[57] P. Dlugolecki, K. Nymeijer, S. Metz, M. Wessling, Current status of ion exchange membranes for power generation from salinity gradients, J. Membr. Sci. 319 (2008) 214–222.

[58] J. Veerman, J.W. Post, M. Saakes, S.J. Metz, G.J. Harmsen, Reducing power losses caused by ionic shortcut currents in reverse electrodialysis stacks by a validated model, J. Membr. Sci. 310 (2008) 418–430.

[59] J. Veerman, R.M. de Jong, M. Saakes, S.J. Metz, G.J. Harmsen, Reverse electrodialysis: Comparison of six commercial membrane pairs on the thermodynamic efficiency and power density, J. Membr. Sci. 343 (2009) 7–15.

[60] S. Pawlowski, J.G. Crespo, S. Velizarov, Pressure drop in reverse electrodialysis: Experimental and modeling studies for stacks with variable number of cell pairs, J. Membr. Sci. 462 (2014) 96–111.

[61] OpenFOAM, http://www.openfoam.org

[62] MEGA a.s., Division of electrodialysis technology, Straz pod Ralskem, Czech Republic, http://www.mega.cz

[63] K. Scott, J. Lobato, Mass transfer characteristics of cross-corrugated membranes, Desalination 146 (2002) 255-258.

[64] M. Ansari, K. Kim, Shape optimization of a micromixer with staggered herringbone groove, Chem. Eng. Sci. 62 (2007) 6687 – 6695.

[65] A.D. Stroock, S.K. Dertinger, A. Ajdari, I. Mezic, H.A. Stone, G.M. Whitesides, Chaotic mixer for microchannels. Science 295 (2002) 647–651.

[66] C. Rodrigues, V. Geraldes, M. Pinho, V. Semiao, Mass-transfer entrance effects in narrow rectangular channels with ribbed walls or mesh-type spacers, Chem. Eng. Sci. 78 (2012) 38-45.

[67] I. S. Ngene, R.G.H. Lammertink, M. Wessling, W.G.J. Van der Meer, Particle deposition and biofilm formation on microstructured membranes, J. Membr. Sci. 364 (2010) 43–51.

[68] D. Lin, F. He, Y. Liao, J. Lin, C. Liu, J. Song, Y. Cheng, Three-dimensional staggered herringbone mixer fabricated by femtosecond laser direct writing, J. Opt. 15 (2013) 1-5.

[69] D.R. Mott, P.B. Howell, J.P. Golden, C.R. Kaplan, F.S. Ligler, E.S. Oran, Toolbox for the design of optimized microfluidic components, Lab Chip 6 (2006) 540–549.

[70] J. Kuleszo, C. Kroeze, J.W. Post, B.M. Fekete, The potential of blue energy for reducing emissions of CO2 and non-CO2 greenhouse gases, J. Integr. Environ. Sci. 7 (S1) (2010) 89–96.

[71] A. Daniilidis, R. Herber, D.A. Vermaas, Upscale potential and financial feasibility of a reverse electrodialysis power plant, Appl. Energy 119 (2014) 257–265.

[72] D.A. Vermaas, PhD thesis, Energy generation from mixing salt water and fresh water, University of Twente, The Netherlands, 2013, pp. 239-241.

[73] Sulzer Pumps Ltd, Centrifugal Pump Handbook, third edition, Elsevier, Winterthur, 2010.

Chapter

6

2D FLUORESCENCE SPECTROSCOPY FOR MONITORING ION-EXCHANGE MEMBRANE BASED TECHNOLOGIES – REVERSE ELECTRODIALYSIS (RED)

SUMMARY

Reverse electrodialysis (RED) is one of the emerging, membrane-based technologies for harvesting salinity gradient energy. In RED process, fouling is an undesirable operation constraint since it leads to a decrease of the obtainable net power density due to increasing stack electric resistance and pressure drop. Therefore, early fouling detection is one of the main challenges for successful RED technology implementation. In the present study, two-dimensional (2D) fluorescence spectroscopy was used, for the first time, as a tool for fouling monitoring in RED. Fluorescence excitation-emission matrices (EEMs) of ion-exchange membrane surfaces and of natural aqueous streams were acquired during one month of a RED stack operation. Fouling evolvement on the ion-exchange membrane surfaces was successfully followed by 2D fluorescence spectroscopy and quantified using principal components analysis (PCA). Additionally, the efficiency of cleaning strategy was assessed by measuring the membrane fluorescence emission intensity before and after cleaning. The anion-exchange membrane (AEM) surface in contact with river water showed to be significantly affected due to fouling by humic compounds, which were found to cross through the membrane from the lower salinity (river water) to higher salinity (sea water) stream. The results obtained show that the combined approach of 2D fluorescence spectroscopy and PCA has a high potential for studying fouling in ion exchange membrane processes.

Submitted as: S. Pawlowski, C.F. Galinha, J.G. Crespo, S. Velizarov, 2D fluorescence spectroscopy for monitoring ion-exchange membrane based technologies – reverse electrodialysis (RED), Water Research (2015).

Graphical abstract:

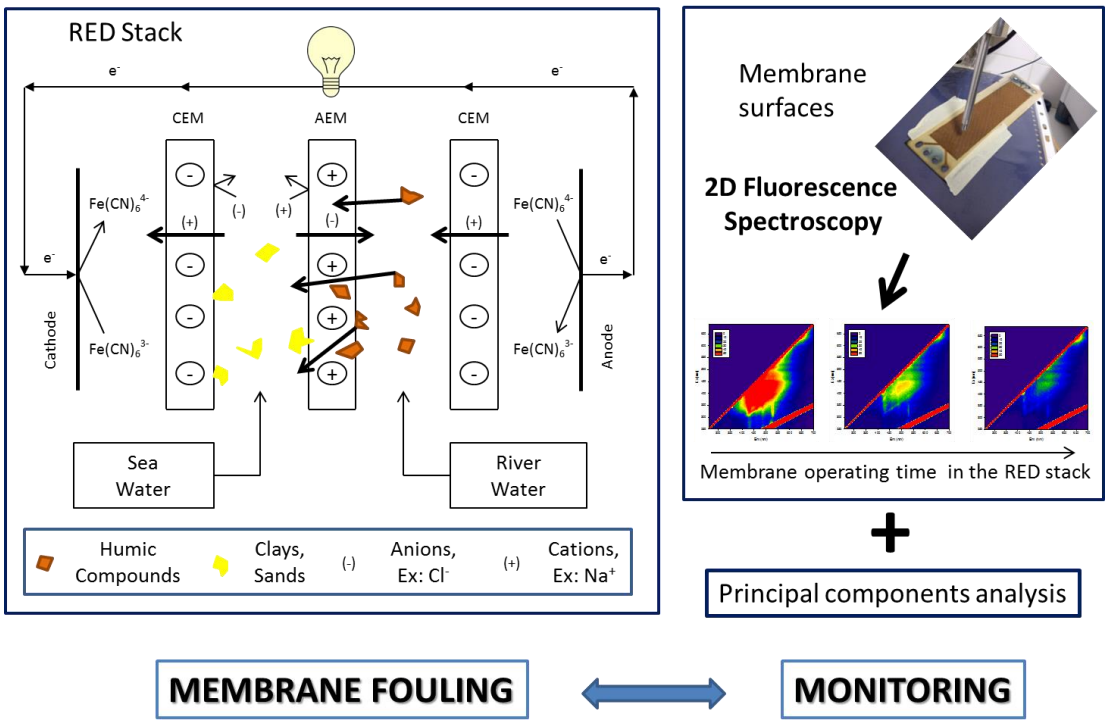

Highlights

- 2D fluorescence spectroscopy combined with PCA was used, successfully, for RED process monitoring.
- Cation- and anion-exchange membranes were clearly distinguished by 2D fluorescence spectroscopy.
- Fouling deposition on ion-exchange membrane surfaces was monitored along time.
- Efficiency of membrane cleaning was evaluated.
- Humic acids transport from dilute to concentrated compartment was detected.

Keywords: Monitoring of membrane fouling, Ion-exchange membranes, 2D fluorescence spectroscopy, Principal components analysis (PCA)

6.1. INTRODUCTION

During mixing of river water with sea water, energy associated to the chemical potential difference between these two water bodies is released. It is estimated that mixing of equal volumes (1 m^3) of river and sea waters, releases approximately 1.4 MJ of energy (~150 m of hydraulic head) [1], which has inspired the name "silent waterfalls" for rivers' mouths [2]. The expected power that can be generated due to worldwide rivers discharge, is close to 1 TW [2-3] and locally depends on the salinity difference between the two initial streams as well as on the solutions flow rate and molar volume of the brackish solution [1]. Since this energy source is completely renewable and sustainable [1-2], a reduction of greenhouse gas (GHG) emissions by around 8 Gt CO_2-eq/year, *i.e.* 24 % of GHG emissions related with the energy sector, would be achieved, if full potential of salinity gradient energy would be used [3].

To extract electrical energy from salinity gradient energy, the mixing of the two solutions must be controlled. In a reverse electrodialysis (RED) stack (Figure 6.1), the diluted and concentrated saline aqueous streams flow through an array of separated compartments formed by alternately arranged cation- and anion-exchange membranes, stacked between two electrodes. The ion-exchange membranes allow for transport of the respective counter-ions, while transport of co-ions is hindered due to the Donnan exclusion effect. The counter-ions, are transported from concentrated to dilute compartments, with cations and anions migrating toward the respective electrodes, at which, in order to maintain electro-neutrality, a redox couple solution is recirculated through the two electrode compartments. Thus, the chemical salinity gradient energy is converted into electrical energy, i.e. an electron flux through an external circuit connecting the two electrodes.

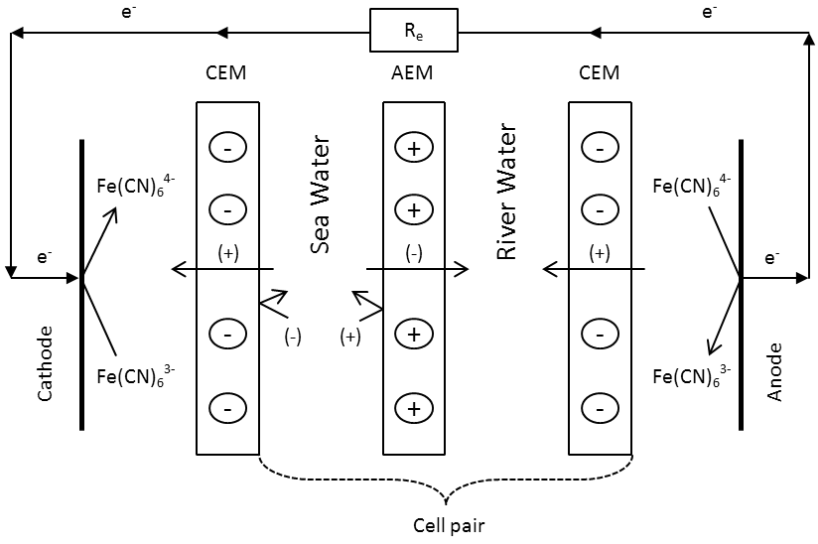

Figure 6.1. Schematic representation of RED principle (CEM – cation-exchange membrane, AEM – anion-exchange membrane, R_e – external load resistance).

The key elements for power generation in the RED process are, therefore, two saline water streams and the ion-exchange membranes. However, a conjugation of selective membranes and natural waters, with a significantly variable composition, may lead to fouling formation and, consequently, to a decrease in the power obtained [4]. At anion-exchange membrane (AEM) surfaces mainly remnants of diatoms, clay minerals and organic fouling deposition has been documented, while cation-exchange membranes (CEM) are more susceptible to scaling [5]. The main cause for a decreased power output in RED has been attributed to organic foulants, such as humic acids, as they can shield the fixed positively-charged groups of the anion-exchange membranes, thus lowering their selectivity and increasing their electric resistance [6]. Since most organic substances in natural water streams are negatively charged [7], fouling of anion-exchange membranes by organic compounds has been identified as the most important process limitation also in desalination of, for example, natural saline solutions by classical electrodialysis [8] and of an industrial NaCl streams with bipolar membranes [9]. In microbial desalination cells, the problem may become even more severe due to microbial growth supported by organic compounds transported across the AEM membrane, which, in such a way, suffers also from biofouling [10].

To reduce fouling in RED systems, two strategies have been presented so far: periodic feedwater reversal and air sparging [11]. Both strategies, at the moment of their application, reduce the power obtained; the salt concentration gradient becomes smaller during the feedwaters' switching periods, while air sparging has associated pumping energy costs [11]. Therefore the application of anti-fouling strategies must be wise and opportune in order to assure that the benefits of fouling removal overcome the associated power losses. For this reason, knowledge about fouling along the operating period of a RED stack is required.

Fouling formation and, especially, preferential channeling due to clogging, can be detected by monitoring the pressure drop [4]. However, the pressure drop is also affected by the solutions flow rate, the number of the compartments in the RED stack and a possible non-uniform fluid distribution caused by the design of the distribution channels [12-13]. Moreover, the pressure drop increases significantly only if a large channel volume is inaccessible for the flow [4], while the obtainable power density may been significantly decreased [5]. This power density decrease is mainly associated to an increase of the non-ohmic resistance, which can be followed by chronopotentiometric measurements [4]. The typical response time to establish the non-ohmic overpotential has been therefore used as an indicator for preferential channeling [4]. However the non-ohmic resistance, or its equivalent in terms of the diffusion boundary layer thickness, depends also on the position in the stack and in the channel [14-15]. At the channel entrance the non-ohmic resistance is lowest and then it increases along the channel length until the salt

concentration profiles across the boundary layers become fully developed [15]. Therefore, quantification of fouling by non-ohmic resistance can be affected by the liquid diffusion boundary layer thickness. Moreover, the very fouling formation could be non-uniform along the channel length.

More accurate analytical tools for fouling monitoring are needed. As the decrease in the obtained power density is, most likely, caused by organic fouling [5], and the aromatic organic matter contains natural fluorophores, fluorescence spectroscopy can be used for its detection [16]. Simultaneous variation of the excitation and emission wavelengths, i.e., two-dimensional (2D) fluorescence spectroscopy, results in an excitation-emission matrix (EEM) which can provide fast information about the composition of complex biological media [16]. The information contained in EEMs can give useful information to describe water quality [17-18] and, moreover, it already was successfully incorporated in hybrid (mechanistic + statistic) [19] and multivariate statistic [20] models for membrane bioreactors monitoring.

The present study explores new possible applications of 2D fluorescence spectroscopy as a valuable monitoring tool for ion-exchange membrane-based processes and, particularly, in RED. Two tests, with a RED stack fed with natural sea and river waters as concentrated and diluted saline streams, respectively, were performed, each within one month time period. A third, one day test, with a synthetic humic acids solution, was performed to investigate their possible membrane transport. Fluorescence EEMs of the ion-exchange membrane surfaces were acquired along the period of their utilization and after their cleaning. Fouling formation and evolution, as well as the membrane cleaning efficiency were then evaluated through principal component analysis (PCA) of the EEMs obtained. The same strategy was applied to assess samples of the two aqueous streams collected along the working periods, in order to identify possible time variable changes in their compositions.

6.2. MATERIALS AND METHODS

6.2.1. Reverse electrodialysis

For the three tests performed in this study, RED stacks composed of 3-cell pairs electrodialysis EDR-Z-Mini unit (MEGA a.s., Czech Republic), equipped with heterogeneous ion exchange membranes (Ralex), were used. The working channels dimensions were 4x16 cm (width and length) and the intermembrane distance (channel height) was kept constant by 0.8 mm thick polyethylene spacers. In the two first experiments, Atlantic Ocean water, collected in Fonte da Telha (Almada, Portugal), and Lisandro river water, taken in Cheleiros (Mafra, Portugal), were used respectively as concentrated and dilute saline streams. In the third experiment, synthetic

aqueous solutions were used; as dilute stream: 1.03 g/L NaCl solution with 40.4 mg/L of commercial humic acids (Fluka 53680) and, as concentrated stream: 31.0 g/L NaCl solution. The RED process was operated with recirculation of the two saline solutions, using flow rates ranging between 20-70 ml/min. Differential pressure sensors (Honeywell, model 24PCAFA6D) were used to measure pressure drop between the stack inlet and outlet, for each saline stream. In all experiments, samples of the two streams were periodically collected (once per day) for assessment of conductivity and 2D fluorescence spectroscopy.

The first experiment had a duration of 32 days, where 35 L of each, sea and river water, were continuously recirculated through the respective channels of the RED stack. The stack was operated without interruptions during the whole referred time period. EEMs of ion-exchange membrane surfaces were acquired before the start and immediately after the experiment end. The next step consisted in washing the membrane surfaces individually with deionized water. The washing waters were collected separately for the membrane surfaces in contact with the river water and in contact with the sea water. EEMs of the collected washing waters, as well as of the membrane surfaces after they had been cleaned with deionized water, were acquired. After this step, the stack was built up again, and its operating performance was followed during one day. After this period, the stack was opened and all membranes were chemically cleaned together in a 5 g/L NaOH aqueous solution for 10 minutes and then during 30 minutes in a 20 g/L citric acid aqueous solution. EEMs of the membranes surfaces after this chemical cleaning procedure were acquired and then the stack was build up again and its performance followed during more 3 days.

In the second experiment, 70 L of each, sea and river water, were recirculated during 34 days through the RED stack. For this specific experiment, virgin membranes were used. In this experiment, the stack was periodically opened (13 times in total) in order to acquire fluorescence EEMs of the membrane surfaces. After the experiment, the membrane surfaces were chemically cleaned as previously explained, but in this case each membrane surface was washed individually. The acid and basic washing solutions were then collected separately according to the treated membrane surfaces, and their TOC contents were analyzed using a total organic carbon analyzer (Shimadzu). After chemical cleaning, fluorescence EEMs of the membrane surfaces were acquired.

The third experiment had a complementary objective to confirm the excitation/emission regions corresponding to humic acids and following their possible transport across the membranes from the dilute to the concentrated saline stream. 500 ml of each synthetic model solution was

recirculated during 24 hours in the RED stack. During this period, 8 EEMs of each saline solution were acquired (6 samples in the first 6 hours and then after 21.5 and 24 hours, respectively).

The measurements of the electric parameters (potential difference and current) were performed with a Digital Multimeter (Kaito Electronics) in an OCV (open circuit voltage) mode. As the electrodes rinse solution, a solution of 0.1 M $K_4Fe(CN)_6$, 0.1 M $K_3Fe(CN)_6$ and 0.27 M NaCl was used. This solution was recirculated at a flow rate of 90 ml/min between the two electrode compartments. The experimental values of the RED stacks resistance were compared with the theoretical stack electric resistance (R_i) calculated by the following equation:

$$R_i = N \cdot \left(\frac{R_{CEM}}{1-\beta} + \frac{R_{AEM}}{1-\beta} + \frac{h_c}{\varepsilon^2 \kappa_c} + \frac{h_d}{\varepsilon^2 \kappa_d}\right) + R_{\Delta C} + R_{el} \quad (6.1),$$

where N is the number of cell-pairs (3 for the used stacks), R_{CEM} *and* R_{AEM} are, respectively, cation- and anion-exchange membranes resistances (8.5 Ωcm^2 for the membranes used), β is the spacers mask fraction (0.5 for the spacers used), $R_{\Delta C}$ accounts for the concentration change due to charge transport [21], R_{el} corresponds to the electrode compartments resistance (320 Ωcm^2 for the stacks used) and the term $h/\varepsilon^2\kappa$ is the solutions resistance in the concentrated ($_c$) and dilute ($_d$) compartments, where h is the compartment thickness (0.08 cm herein), κ is the solution conductivity (measured along the period of the stacks operation) and ε is the spacers porosity (0.8 for the spacers used). Since the theoretical model does not include any mathematical term for fouling influence, the theoretical electric resistance value does not account for fouling formation and development in the stack. Therefore, the ratio between the theoretical and experimental resistances can provide an indirect way of evaluating the impact fouling on the RED stack performance.

6.2.2. 2D fluorescence spectroscopy

2D fluorescence spectroscopy measurements result in excitation-emission matrices (EEMs), where each value of fluorescence emission intensity corresponds to a pair of excitation/emission wavelengths. EEMs were acquired with a fluorescence spectrophotometer Varian Cary Eclipse equipped with excitation and emission monochromators and coupled to an optical fiber bundle probe. The optical fiber bundle is constituted by a total of 294 randomized optical fibers (147 excitation and 147 emission) each with a diameter of 200 μm and a length of 2 m. Fluorescence EEMs were obtained at a scan speed of 12000 nm/min, excitation and emission slits of 10 and 5 nm, respectively, for membranes surfaces scanning, and excitation and emission slits of 20 and

20 nm, respectively, for aqueous solutions scanning. EEMs were generated in a range of 250 to 690 nm of excitation and 260 to 700 nm of emission, with an excitation wavelength incrementing step of 5 nm.

Fluorescence EEMs of the cation- and anion-exchange membrane surfaces in contact with river and sea waters were acquired in two predefined points; one close to the fluid flow entrance in the channel and the other close to the fluid flow exit from the channel. Each acquisition was performed twice and always the same region of the same membrane was scanned during all experiments. The optical fiber probe distance from the membrane surface was maintained constant (~ 1 cm) in all measurements. The optical probe and membrane surface were positioned with an angle of 45º in order to avoid an overlap of the excitation and emission light signals. For aqueous solutions, EEMs were acquired by immersing the optical probe in a stirred beaker, in order to avoid sedimentation of suspended solids. Identical stirring conditions were applied for all the samples.

For a better understanding of the results obtained, a mathematical data deconvolution was performed. The fluorescence EEMs were analyzed using principal component analysis (PCA), implemented with PARAFAC (parallel factor analysis) function using MATLAB (The MathWorks), which applicability has been demonstrated for the case of fluorescence spectra data treatment [22]. The objective of PCA is to substitute the initial representation of objects into a new Principal Component coordinate space with a reduced noise and lower dimensionality through decomposition of the data matrix, into a "structure" part (CP^T) plus a "noise" part (E). C is the scores matrix, and can be seen as the representation of the initial data in the new and reduced co-ordinate system, composed by the new components (Principal Components, PC). P^T is the loadings matrix that describes the 'distance' between the initial co-ordinate system and the PC system. The E matrix contains unexplained data variance, such as co-linearity and noise [18]. Herein, only the scores matrices will be shown, as in them the most relevant information from the original data is included.

6.3. RESULTS AND DISCUSSION

In the present work, several possible proof-of-concept applications of 2D fluorescence spectroscopy were investigated. First, the fouling deposition on the ion-exchange membrane surfaces was assessed (Section 6.3.2), then the membrane cleaning efficiency was evaluated (Section 6.3.3) and finally the mass transport of humic compounds between the streams was followed (Section 6.3.4).

Since in the present study, the used RED stacks have flow channels with a thickness of 0.8 mm and previous studies investigated fouling formation and channel clogging in RED stacks with a channel thickness of 0.23-0.24 mm [5, 11], an initial experiment (denominated as the first experiment in the materials and methods section), was performed in order to allow for comparison of the results obtained with the existing literature (Section 6.3.1).

6.3.1. Fouling effects on RED stack performance in a 32 days continuous experiment

Figure 6.2 shows the pressure drop data obtained for the dilute and concentrated circuits, divided by the respective stream flow rate at the moment of the pressure drop acquisition, as well as the normalized ratio between the measured and the expected electrical resistance. The pressure drop data were divided by the respective flow rate data in order to exclude possible influence of their variation on the pressure drop.

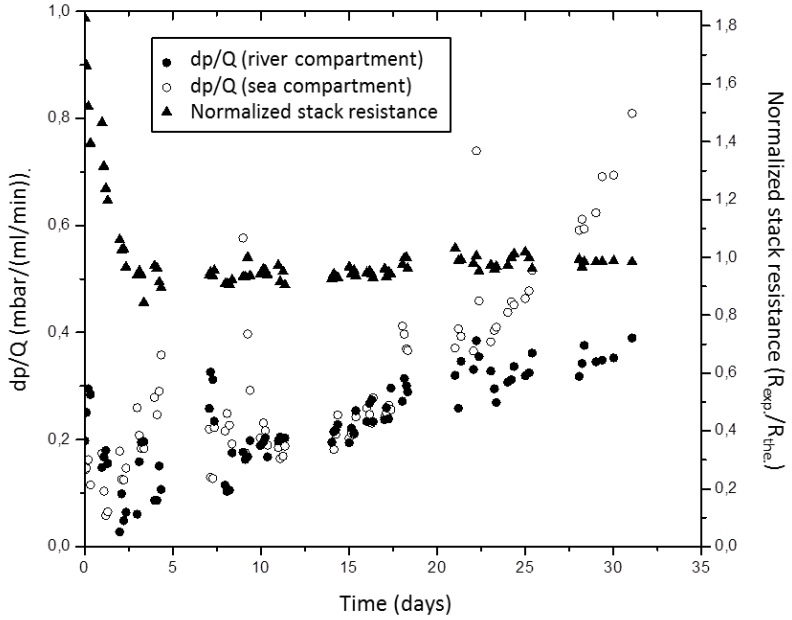

Figure 6.2. Variation of stack electric resistance and pressure drop / flow rate ratio in the sea and river compartment during the RED stack operation period in the 1st experiment.

As can be observed (Figure 6.2), in the dilute saline circuit (river water), the pressure drop increased slightly and with a linear progression during the 32 days of stack operation. Until the 22nd day of operation, in the concentrated circuit (sea water) the same behavior was observed. After that, an accentuated pressure drop increase started to occur in the concentrated circuit. At the end of the experiment, the pressure drop in the sea water circuit was more than two times higher than that measured in the river water circuit. When the stack was opened a thin layer of particles of a sand/clay texture was detected on the membrane surfaces. Nevertheless, this channel "obstruction" did not stop the sea water circulation and was easily removed by washing using the low pressure from a laboratory wash bottle or through manually rubbing the surface.

At the river water side, some occasional clay particles were also observed on the membrane surfaces, but in a much lower degree.

Nevertheless, pressure drop increased almost two and four times in river water and sea water circuits, respectively, between the start and the end of the RED stack operation. This is not as much as in the case of a stack with thinner channels (h= 230 μm), in which the pressure drop increased 15 times for the same period of the RED stack operation [11], however, since clogging by foulants, and eventual preferential flow channeling are less probable to occur as the thickness of the channel increases, the results are not unexpected.

In order to confirm fouling formation, the experimental stack electric resistance was compared with the theoretical electric resistance. In the beginning of this experiment, the experimental stack electric resistance was almost two times higher than the theoretical one, but after 3 days the expected and the measured resistances were almost equal and, therefore, the ratio between experimental and theoretical resistance approximated to value of 1 (Figure 6.2). The observed initial decrease of this ratio may be explained by progressive membrane swelling, as in the experiment start, the membranes were dryer compared to those in the end of the test. In such a way, the membrane electric resistance most probably was higher when the experiment start, and then decreasing to the expected calculated value. Moreover, during the beginning of the experiment, divalent ion transport from the dilute to concentrated stream may occur, at least until the Donnan equilibrium is approached [6]. Divalent ion transport can occur in the opposite direction of the monovalent ions transport from the concentrated to the dilute compartment, what causes a higher electric resistance than the predicted one. As the ions in the solutions approach Donnan equilibrium, the rate of transport of divalent ions decreases, and, thus, the experimental resistance approximates the calculated one.

After the initial period of three days, the resistances ratio started to increase slowly, showing that there is a resistance, not accounted for in the theoretical prediction, which can be most probably associated with fouling. Since organic fouling by aromatic substances is favored in membranes with low water content [7], the relatively slow increase of electric resistance registered in the experiment could be partially attributed to the high swelling degree of Ralex ion-exchange membranes [23]. Moreover the Ralex intrinsic membrane resistance is relatively high, which shadows the effect of the resistance caused by fouling. However, in order to develop adequate operating / cleaning strategies there is a need not only to detect indirectly possible fouling occurrence in the stack through pressure drop and/or electric resistance related parameters, but also to identify, which membrane surfaces are more affected and to follow the time evolvement of fouling development.

6.3.2. Fouling detection through 2D fluorescence spectroscopy

In order to access membrane fouling, a second experiment was performed. This experiment was operated during 34 days and the stack was periodically opened in order to analyze the membrane surfaces using 2D fluorescence spectroscopy. In this second experiment, the ratio between experimental and calculated resistance presented of a trend similar to the first experiment, while the pressure drop for both river and sea water compartments increased only slightly during operation (data not shown). However, it should be noticed that the periodical opening of the stack for observation of the membranes by 2D fluorescence, may disturb the fouling layer developed. It has been found that just an action of switching off and on of the pumps may reduce pressure drop, since occasional disturbances in water flow caused a reduction of the particulate and colloidal fouling accumulated in the system [5].

6.3.2.1. EEMs of ion-exchange membranes

The ion-exchange membrane surfaces, contacting the river and sea water circuits, were analyzed by 2D fluorescence spectroscopy. For each surface under investigation (AEM – river, AEM – sea, CEM – river, CEM – sea), fluorescence emission-excitation matrices (EEMs) were obtained in two different regions of the membrane: one close to the flow entrance into the respective channel and the other close to the flow exit from the channel. Figure 6.3 shows the fluorescence spectra of virgin membranes and the fluorescence spectra of the same membrane surface after being in contact with sea and river water, respectively, during 34 days of operation.

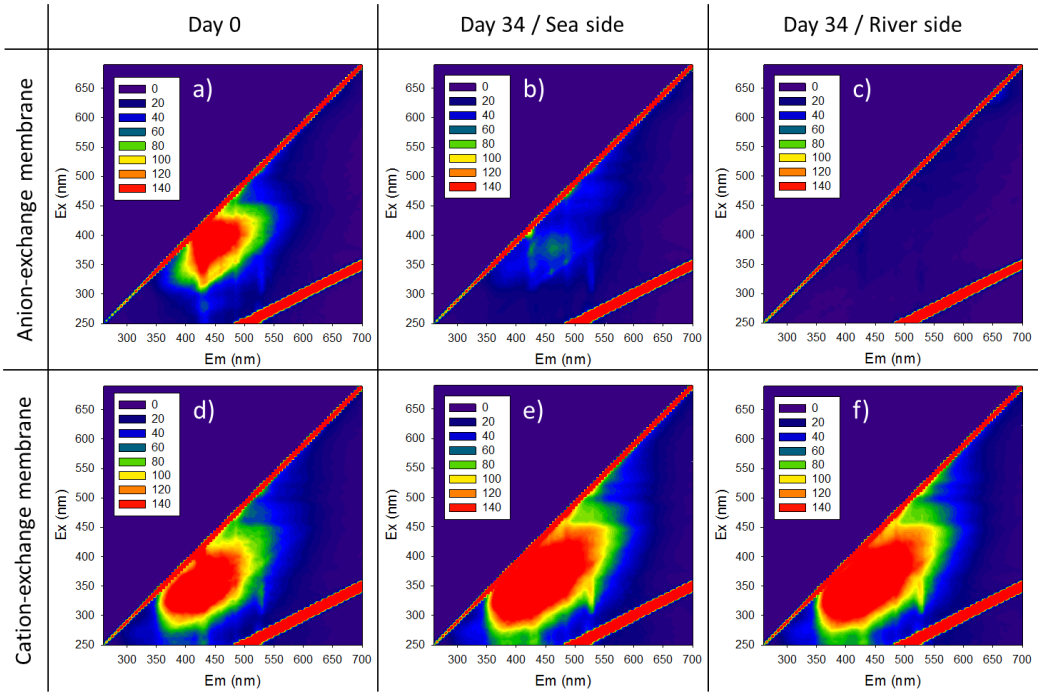

Figure 6.3. Fluorescence spectra of anion and cation-exchange membrane surface close to the fluid exit from the channel: (a and d) before utilization, (b and e) after 34 days in contact with sea water (2nd experiment), and (c and f) after 34 days in contact with river water (2nd experiment).

As can be clearly observed (Figure 6.3), the fluorescence spectra of the AEMs and CEMs are distinct before and during the whole period of their utilization. The spectra obtained for the CEMs show only a slight increase in the fluorescence emission intensity along the duration of the experiment, no matter if the CEM surface had been in contact with river water or with sea water. In contrast, the fluorescence spectra of the AEM surfaces showed a well-defined evolution, as their fluorescence emission intensity progressively decreased along the time of operation. The fluorescence emission intensity of the AEM surface in contact with river water showed a much more pronounced decrease than that of the surface in contact with sea water.

2D fluorescence spectroscopy can detect organic foulants containing fluorophores. However, since the ion-exchange membranes also have fluorescence (as it can be seen in Figure 6.3, day 0) and since some organic substances (e.g., humic compounds naturally present in surface waters) have a dark color, when deposited on membrane surfaces, the light emitted by the membrane surface may be partially absorbed by a layer of such type of fouling. Therefore, the fluorescence emission intensity, especially in the case of AEMs, decreased along time due to foulants deposition on the membrane surface. Moreover, the color of the AEM surface in contact with river water changed from a yellow to a brownish appearance, which supports the assumption of emission light interference.

The other membrane surfaces (both CEM surfaces and the AEM surface in contact with sea water) kept their appearance almost unchanged. This is in accordance with previous studies in which it was found that organic fouling, due to large negatively charged molecules such as humic compounds, affect more significantly the anion-exchange membranes [5-6]. Therefore the change of color to brown may indicate anion-exchange membrane fouling by humic compounds [5, 11].

The EEM acquisition position on the membrane surface (close to the flow entrance or exit in the channel) also influenced the fluorescence EEMs obtained (Figure 6.4).

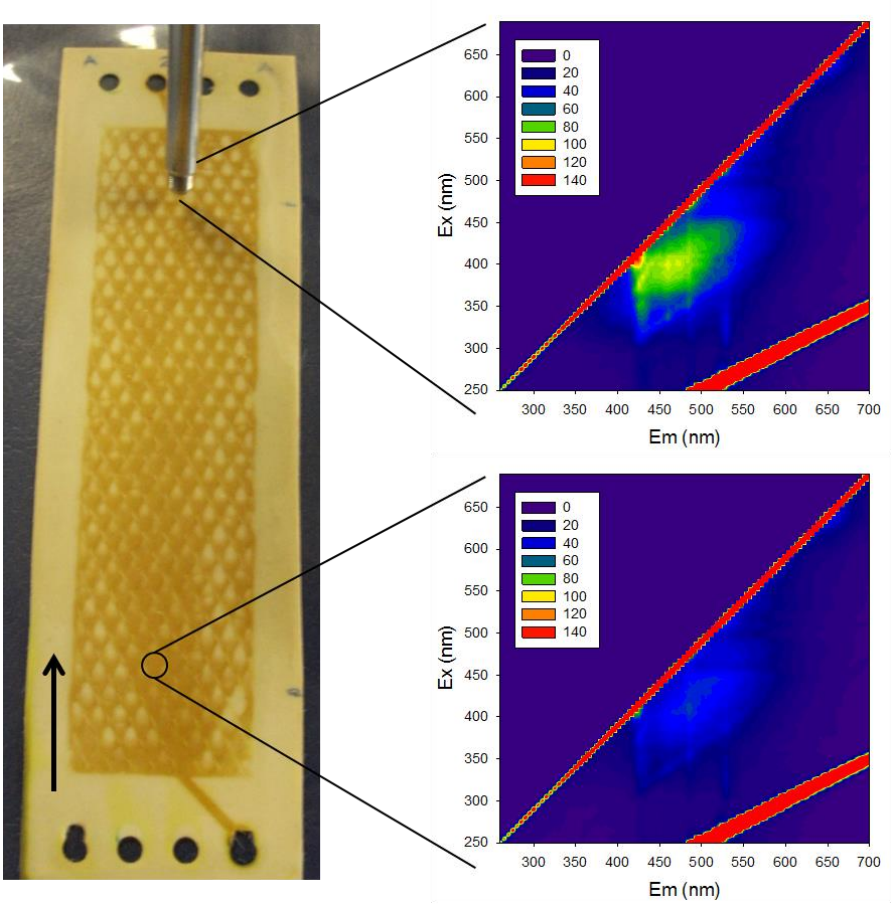

Figure 6.4. Photo of anion-exchange membrane surface in contact with river water after 1 day of operation in the 2nd experiment. The arrow indicates the flow direction. The bundle probe is visible in the photo. The EEMs as well as the regions of their acquisition are shown.

Close to the flow entrance in the channel, the membrane's color change is more pronounced (larger deposition of foulants on the membranes) than close to the flow exit. This could have been caused by lower linear flow velocity in the region adjacent to the flow entrance in the working channels (hydraulic shadows) [24], besides of the membrane area close to the flow entrance be the first one on which fouling may develop and accumulate. Therefore, the emission intensity was lower for the EEMs assessed at the flow entrance in the channel. It is also possible to observe clearly that the membrane color changed most significantly upstream to the spacers' filaments, as foulants accumulate preferentially at positions with a locally lower fluid flow velocity [4-5, 11].

A qualitative interpretation of the EEMs obtained by 2D fluorescence spectroscopy shows that fouling formation on ion-exchange membrane surfaces can be detected by this technique. Moreover, it is evident that, at different stages of foulants accumulation on the membrane surface, distinct EEMs are generated. However, a visual comparison between the EEMs is not straightforward, since 2D fluorescence spectroscopy generates a large amount of complex data

(in this study more than 4000 excitation-emission pairs had been obtained for each EEM), in which all possible quenching and/or inner filter effects are also included. Therefore, although much of information about the studied system is captured, its rationalization is only accessible through mathematical data treatment [16, 19].

Therefore, a principal components analysis (PCA) of the fluorescence EEMs obtained was performed. The PCA consisted on transforming the representation of the original EEMs data into a new principal components coordinate system in order to extract the relevant data (extract principal EEMs variations) and to remove noise.

6.3.2.2. PCA of EEMs of ion-exchange membranes

Figure 6.5 shows the correlations between the first 3 principal components (PCs) values obtained by PARAFAC for all fluorescence spectra of the membrane surfaces (scores plots).

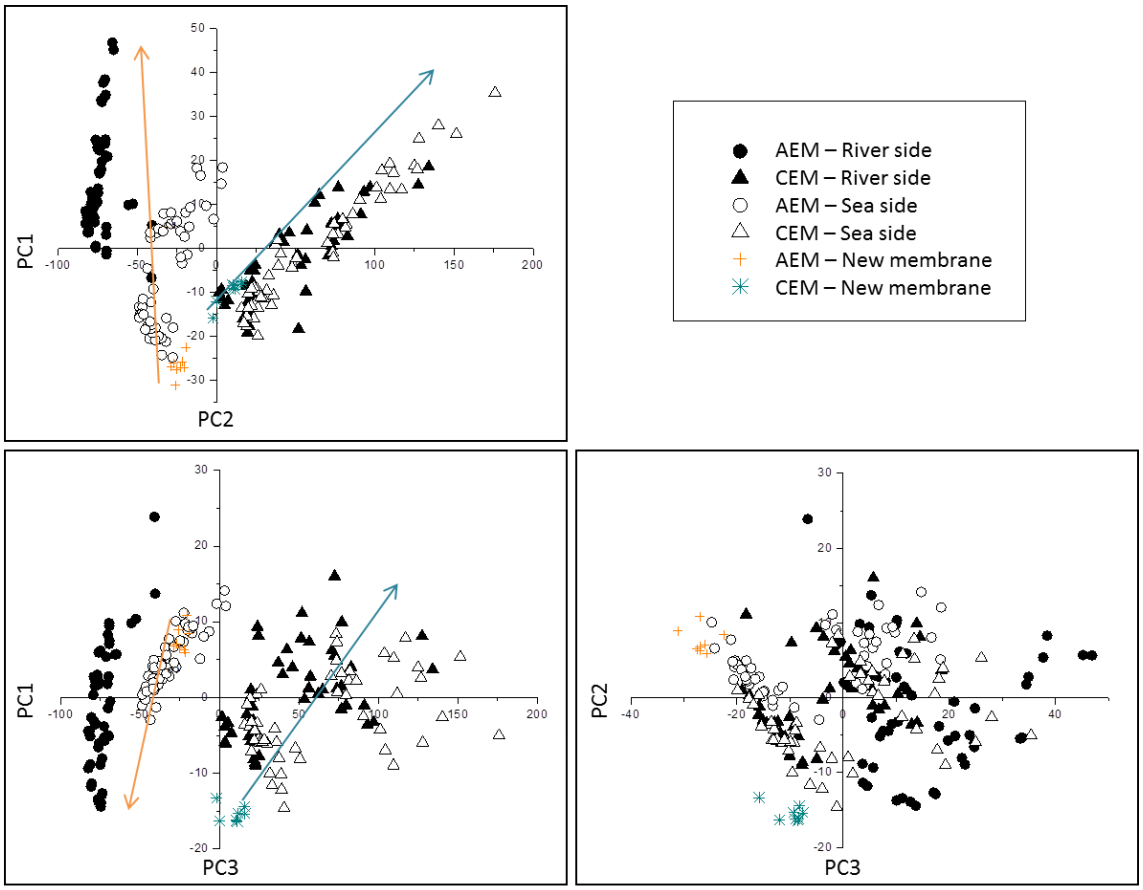

Figure 6.5. Scores plots: relation between the first 3 principal components (PCs) obtained by PCA of EEMs of all membrane surfaces acquired during the RED stack operation period in 2nd experiment. Arrows represents time line of the EEMs acquisition along the days (orange for AEMs and cyan for CEMs).

Each point in Figure 6.5 represents, one EEM, which was acquired for a given membrane surface in a known day of the experiment. For PC1 vs. PC2 and PC1 vs. PC3, the distance between the points relative to the new membranes and other points matches almost completely with the time line of the EEMs acquisition along the days, i.e. the points that are more distant from the point representing the EEM of a new membrane, correspond to EEMs taken closer to the end of the experiment. In section 6.3.3, examples of the behavior of fluorescence EEMs for the AEM and CEM surface in contact with river water are shown in more detail.

PC1 captured 88.99 % of variance, PC2 5.82 % and PC3 1.29 %, which totalizes 96.10 % of the total variance captured. It appears that the first principal component separates EEMs of AEMs from EEMs of CEMs, while the second and third principal components capture some of the variance associated with membrane surface modification along time. It is also possible to see that for the CEMs there was almost no difference between the membrane surfaces in contact with river water and with sea water, as the points are located close to each other. In contrast, the points representing EEMs of anion-exchange membrane surfaces in contact with sea water and with river water are clearly grouped separately. Since the points representing EEMs of the AEM surface in contact with river water are more distant from the points representing the EEMs of the new AEM surface (than the points representing EEMs of AEM surface in contact with the sea water) this suggest that the AEM surface in contact with river water was more affected by the operating conditions than the AEM surface in contact with sea water. Other important information, which can be taken from the principal component analysis, is that the EEMs of CEMs have significantly changed along time, which is not clear from a visual inspection of the obtained fluorescence spectra.

As presented in section 6.3.1, an increase of the pressure drop and of the stack electric resistance were observed during the period of RED stack operation. Both observations can be attributed to fouling formation. Through PCA it can be additionally recognized that the EEMs of membrane surfaces varied sequentially along time, and that this variation can be quantitatively described by values of the principal components. The results obtained can be valuable for the assessment of the role played by membrane fouling in the RED process performance. Moreover, the information about fouling, quantified by principal components, can be further used in mathematical models to correlate them with RED performance parameters.

6.3.3. Membrane cleaning

As exemplified in the previous section, 2D fluorescence spectroscopy can capture valuable information about the ion-exchange membranes' surface state. Since membrane cleaning has the

objective to recover the initial membrane state, 2D fluorescence spectroscopy was also herein used as a tool to evaluate the efficiency of membrane cleaning.

After the first experiment, the membranes were washed with deionized water and then chemical cleaning was performed. EEMs of membrane surfaces were acquired after each step. Figure 6.6 shows fluorescence spectra of the CEM surface close to the channel exit before the experiment (a), after being in contact with sea water during 32 days (b), after washing the membrane surface with deionized water (c) and after chemical washing of the same membrane surface (d). Only the data for this membrane surface are shown, since the fluorescence emission intensity variation was most clearly observed (a similar trend was observed for all membranes' surfaces).

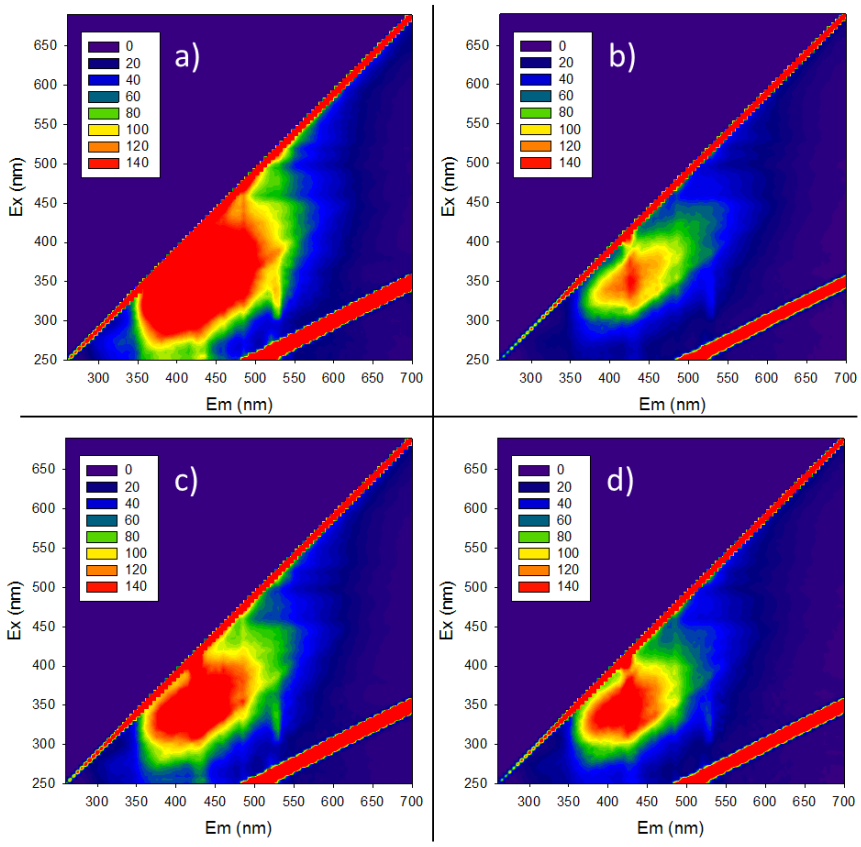

Figure 6.6. Fluorescence spectra of CEM surface close to the flow exit from the channel in contact with sea water used in 1st experiment: (a) before experiment, (b) after experiment, (c) after washing the membrane with water, (d) after membrane chemical cleaning.

In Figure 6.6, it can be seen that the highest fluorescence emission intensity was registered for the membrane surface before starting the experiment and the lowest one immediately after the end of the experiment. A very peculiar variation of fluorescence emission intensity, was however observed after washing the membrane surface. After washing with deionized water, the membrane recovered partially its initial fluorescence, although, not totally. The membrane color apparently did not change, although there was removal of clays from the membrane surface, as

described in Section 6.3.1. After chemical cleaning, the membrane fluorescence decreased, although it was still higher than that after the stack had been opened. The decrease of fluorescence emission intensity observed after chemical cleaning may be associated with degradation of charged sites and polymeric chains scission through chain radical oxidation [25].

Moreover, the ratio between experimental and expected resistances increased after chemical cleaning, as it can be seen in Table 6.1, which also shows that pressure drop has significantly decreased after first cleaning with deionized water and only slightly after the chemical cleaning. The registered pressure drop data can be most probably explained by removal of particulate/colloidal fouling with the first cleaning (using only water), since the pressure drop values are similar to the ones registered in the beginning of the experiment (Figure 6.2).

Table 6.1. Normalized pressure drop values in sea and river water compartment and ratio between experimental and predicted resistance on the last day of the 1st experiment, after washing the membranes with deionized water and after chemical cleaning.

	dp / Q in sea water circuit (mbar/ml.min^{-1})	**dp / Q in river water circuit (mbar/ml.min^{-1})**	**$R_{exp.}/R_{teor.}$**
Day 32	0.81 ± 0.12	0.39 ± 0.13	0.984
After cleaning with deionized water	0.18 ± 0.07	0.21 ± 0.03	0.988
After chemical cleaning	0.12 ± 0.01	0.17 ± 0.02	1.043

The washing deionized water was collected from the sea and river water compartments of the RED stack separately, and EEMs of these solutions were acquired. Figure 6.7a shows fluorescence spectra of the washing solution collected from the sea compartment and Figure 6.7b for the washing solution collected from the river compartment.

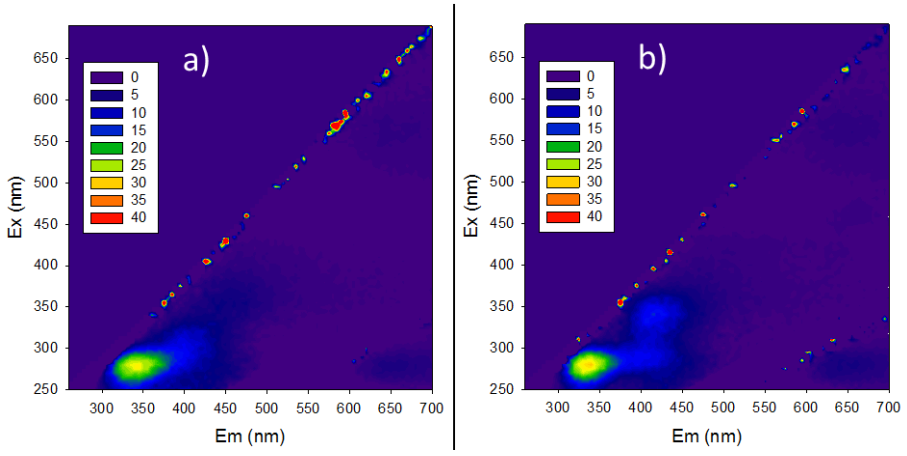

Figure 6.7. Fluorescence spectra of washing deionized water collected in the1st experiment from: (a) sea water compartment, (b) river water compartment.

For both washing waters collected, a characteristic peak for proteins (excitation/emission of 275/340 nm) [26] can be seen in the respective fluorescence spectra. In the presence of high amounts of humic acids, such visual detection of proteins in the fluorescence spectra can be impaired due to quenching effects [16]. Since the fluorescence emission intensity of the proteins peak is low, this may explain why it has not been observed in any fluorescence spectra of the membrane surfaces (due to quenching and interference effects with other compounds present and/or adsorbed at the membrane surfaces, such as for example humic compounds). In the washing water collected in the river compartment, a small peak characteristic to humic acids [26] is also visible (excitation/emission of 340/410 nm). The presence of humic compounds in the washing water collected from the river compartment and its absence in the washing water collected from the sea compartment is not unexpected, as humic acid adsorption has been mainly observed on the AEM surface in contact with river water, as previously mentioned in section 6.3.2.1.

In order to better understand the effect of chemical cleaning, the membranes were washed only by chemical cleaning after the second experiment and the acid and base cleaning solutions were collected separately for each washed membrane surface and analyzed in terms of the total organic carbon (TOC). The solutions collected were visually transparent and the amounts of organic and inorganic carbon detected by a TOC analysis were nearly zero (data not shown). Therefore, the chemical cleaning either did not remove organic matter from the membrane surfaces, or the quantity of the removed organic compounds in the washing solutions was too small to be detected.

Additionally, after chemical cleaning the color of the membranes did not change when submitted to visual inspection. However, the fluorescence emission intensity increased for all membrane surfaces after chemical cleaning. A higher increase in fluorescence emission intensity was observed for the CEMs than for AEMs. The lowest fluorescence emission intensity increase was found for the AEM surface in contact with river water.

Although, despite of apparently the chemical cleaning of AEM surface in contact with river water had no significant effect on that membrane surface fluorescence, by principal component analysis it was possible to identify differences before and after chemical cleaning of the membrane surface (Figure 6.8).

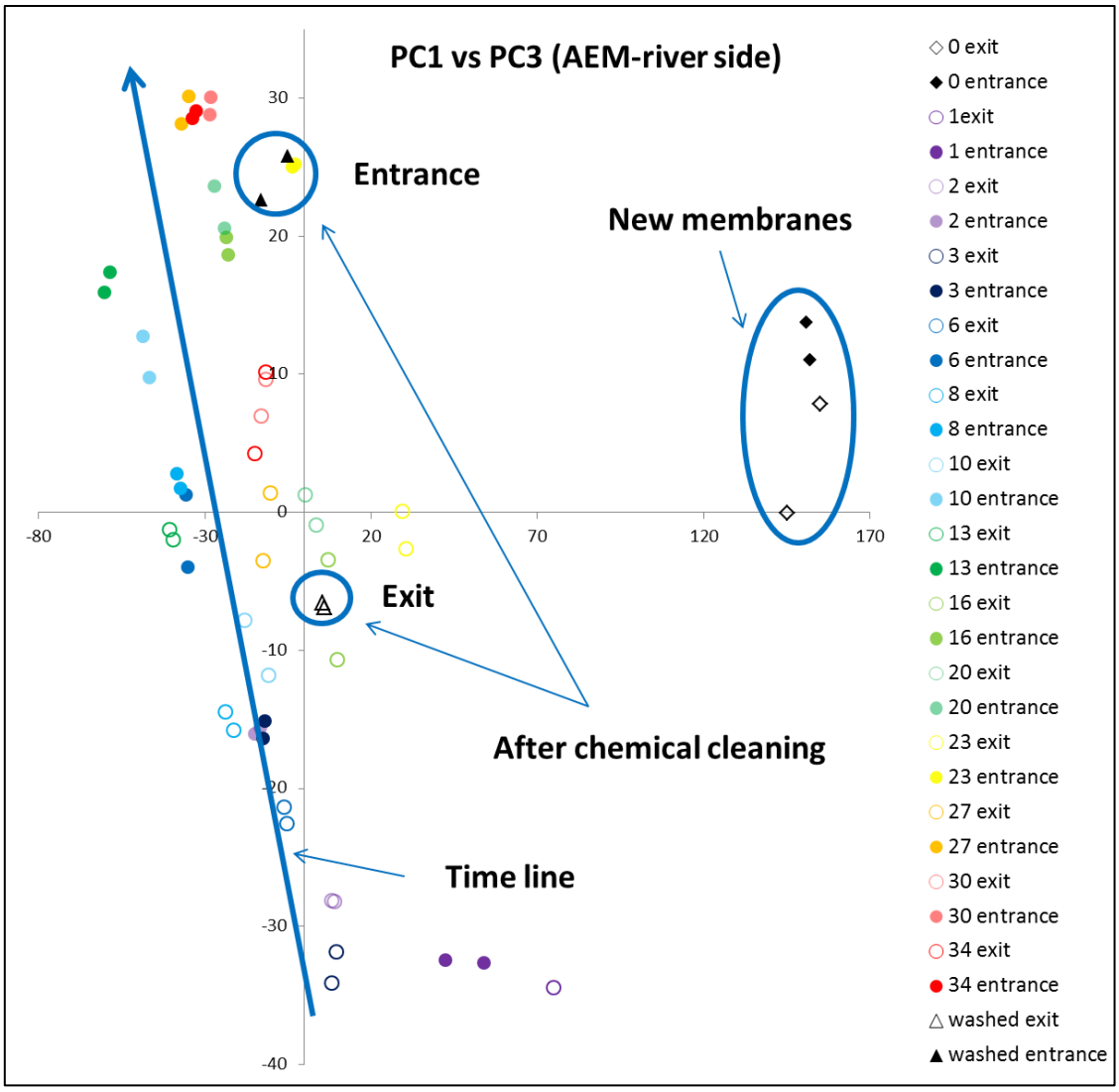

Figure 6.8. Scores plot for PC1 and PC3 obtained by PCA of all EEMs of AEM surface in contact with river water during the stack operation in the 2nd experiment. Open and closed symbols are respectively for EEMs acquired on membrane surface close to fluid exit and entrance into the channel. In the legend, the numbers represent for how many days the stack has been operated before the EEM acquisition, and the term "washed" refers to the EEM acquired after membrane chemical cleaning.

Figure 6.8 shows the relation between first and third principal components obtained by PCA of the EEMs of AEM surfaces in contact with river water, only. Therefore, the principal components values and the percentage of variance captured (PC1-64.62 %, PC2-18.96 %, PC3-9.22 %) are different from the PCA data presented in Figure 6.5. In Figure 6.8, it can be seen that the points representing fluorescence EEMs of new, virgin membranes are distant (isolated) from all other points. This means that fluorescence EEMs of the new membranes are very different from the EEMs of membranes after use. It is also possible to observe that the points representing the fluorescence EEMs acquired along time are disposed sequentially. Therefore, a time line trend exists. Moreover, the highest change in membrane color, i.e. foulants deposition, observed close to flow entrance in the channel (as shown in Figure 6.4), was also captured by

PCA, as the points relative to the EEMs acquired at the channel entrance are more distant from the start of the time line. The points representing fluorescence EEMs acquired for the AEM surface close to the flow exit appear closer to each other on the time line, since this membrane surface region was less affected by fouling.

Since the points representing the EEMs of membrane surfaces are disposed according to a time line in Figure 6.8, the zone in which the point representing the EEMs of the cleaned membrane surface appears, may indicate how well the membrane has recovered its initial state after chemical cleaning. Therefore, for the AEM surface in contact with river water, the fluorescence EEMs of cleaned surface closer to the channel exit is similar to the EEMs acquired on day 16, while the EEMs acquired closer to the fluid entrance in the channel, have similarities with the EEMs acquired on days 20-23.

Similar analysis of fluorescence EEMs, in terms of principal components, has been performed for all other membrane surfaces (for the sake of simplicity, the data for membrane surfaces contacting sea water are not shown, nevertheless they could also be used, to demonstrate this 2D fluorescence spectroscopy application). For the AEM in contact with sea water, the points representing EEMs after chemical cleaning were close to the points representing EEMs acquired on days 27-30. Therefore, based on PCA, chemical cleaning was more effective for the membrane surface in contact with river water, as the points representing EEMs after chemical cleaning were closer to EEMs acquired earlier than in case of membrane surface in contact with sea water. These results emphasize the importance of mathematical analysis of the fluorescence data, since a higher increase in fluorescence emission intensity after the chemical cleaning was observed for the membrane surface in contact with sea water than with river water, which could give an erroneous idea that chemical cleaning was more effective for the membrane surface in contact with sea water.

For the CEMs, the points representing fluorescence EEMs after chemical cleaning were located in a different area of the points representing all other acquired EEMs and, therefore, it is not possible to conclude to which day state, the chemical cleaning has restored the CEM surfaces. Figure 6.9 shows an example of such a situation for the CEM surface contacting the river water. Herein, it was chosen to show the relation between second and third principal components, since for different membrane surfaces, the combinations of PCs that are more illustrative could be different, as obviously the captured variance depends of what sample is the object of PCA.

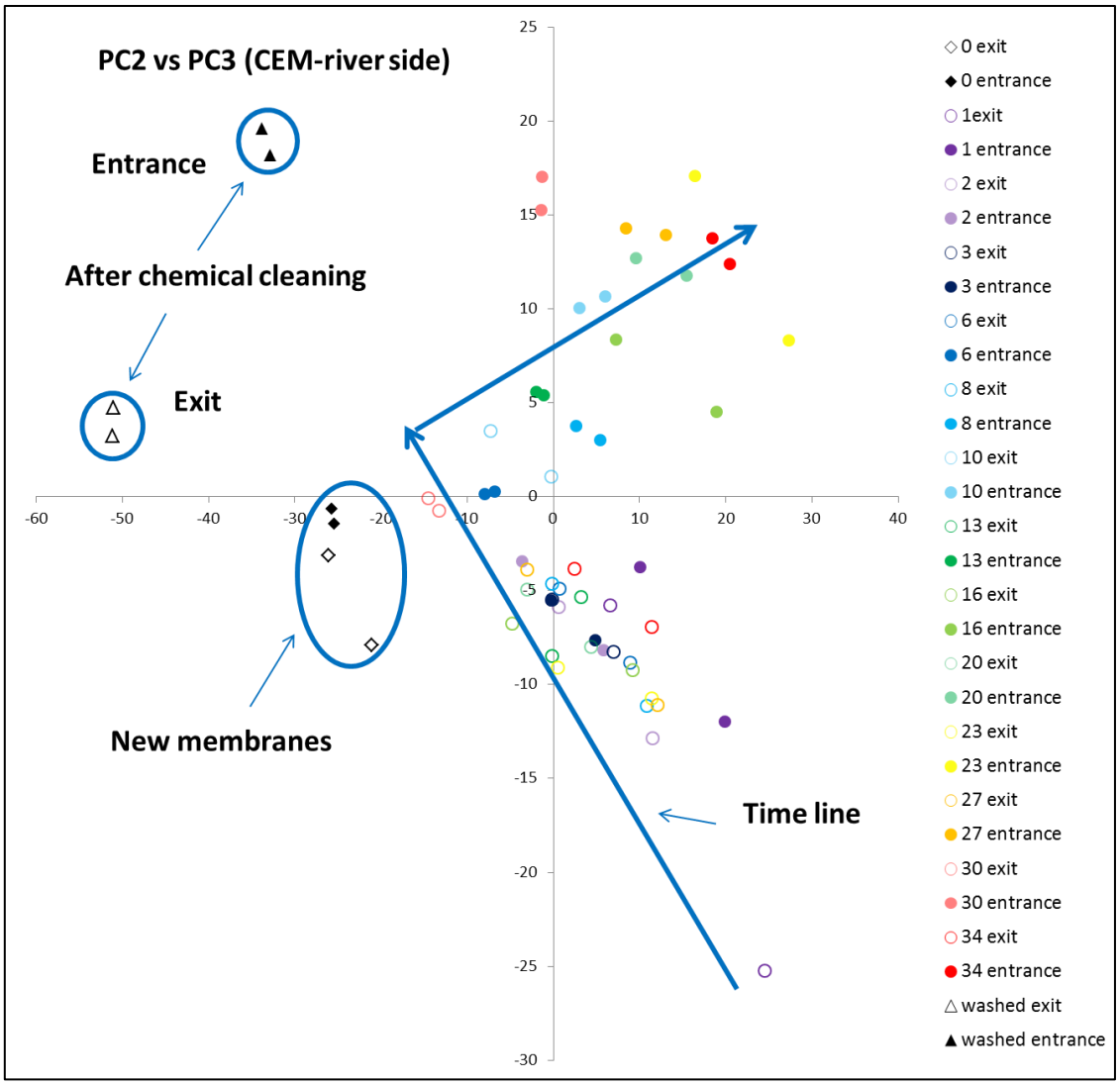

Figure 6.9. Scores plot for PC2 and PC3 obtained by PCA of all EEMs of CEM surface in contact with river water during the stack operation in the 2nd experiment. Open and closed symbols are respectively for EEMs acquired on membrane surface close to fluid exit and entrance into the channel. In the legend, the numbers represent for how many days the stack has been operated before the EEM acquisition, and the term "washed" refers to the EEM acquired after membrane chemical cleaning.

For the PCA of EEMs of CEM surface in contact with river water, the variance captured by the first three principal components was: PC1-86.08 %, PC2-6.71 % and PC3-2.23 %. As in Figure 6.8, for the AEM surface contacting the river water, in Figure 6.9 it is possible to see that the points representing the EEMs of new (virgin) CEM are separated from all other points corresponding to the EEMs of CEM surface acquired during the period of the RED stack operation. The points are distributed sequentially along a time line and the difference between EEMs acquired close to flow entrance or exit continues to exist as in the previous example. The only difference is that the points corresponding to EEMs acquired after chemical cleaning are located in a completely different region than all other points.

In the first experiment, an increase in fluorescence emission intensity was observed when the CEMs were washed with water, mainly due to removal of colloids from the membrane surface. However, after chemical cleaning their fluorescence emission intensity decreased. In this second experiment, only chemical cleaning was applied, and thus an increase in fluorescence emission intensity, compared to that before chemical cleaning, was observed. However, the PCA analysis (Figure 6.9) suggest that chemical cleaning induced some structural changes in the CEM morphology, since no similarities with the EEMs acquired before chemical cleaning were found. The fluorescence emission intensity increase can therefore be due to removal of colloids, which was also achieved by washing with deionized water alone, as observed in the first experiment.

For ion-exchange membranes, chemical cleaning is usually recommended by manufactures if the membranes are to be used for treatment of highly nutritious media, in which microorganisms may cause spoilage or deposition of particulate and colloidal matter [25]. Therefore, in view of the results obtained in the present study, a dedicated chemical cleaning strategy for the membranes used in RED should be developed in function of the saline streams compositions used, in order to minimize membrane damage.

6.3.4. 2D fluorescence spectroscopy of aqueous streams

Monitoring of the aqueous streams used in RED can be also achieved through 2D fluorescence spectroscopy. During both experiments, with natural sea and river waters used, as concentrated and dilute saline streams, respectively, liquid samples were collected during the operating period and their fluorescence EEMs acquired. Figure 6.10 shows the fluorescence spectra of the sea and river water at the beginning and in the end of the 2nd experiment (the results for the 1st experiment were similar). Therefore, only the results of the second experiment are shown and discussed in Figure 6.10. Additionally, in each fluorescence spectra of Figure 6.10, an inset is shown. These insets are the fluorescence spectra obtained in the 3rd experiment, in which synthetic solutions were used in order to confirm the accuracy of the conclusions taken from the results obtained in the two first experiments.

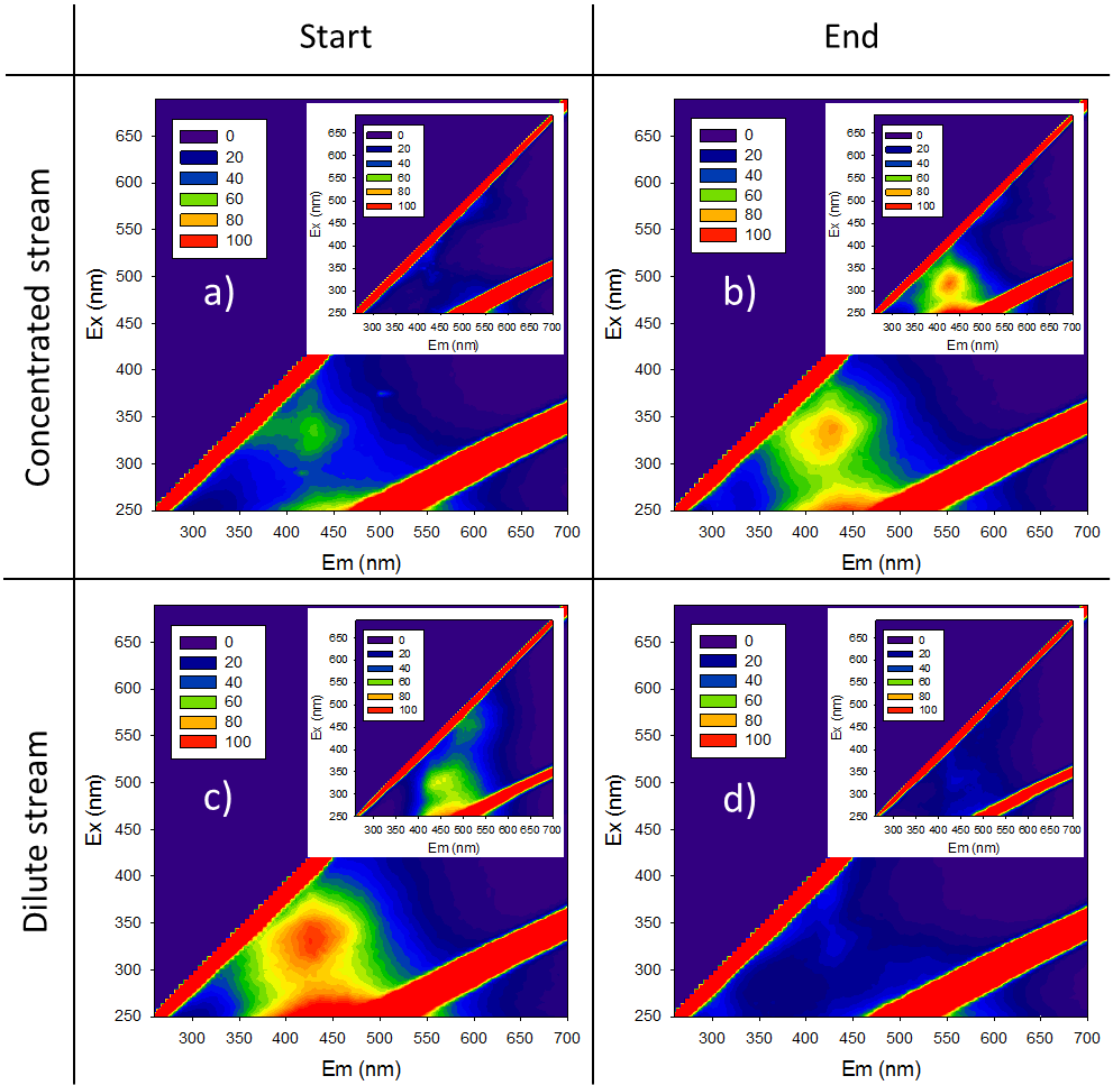

Figure 6.10. Fluorescence spectra of natural water streams at the beginning and in the end of the 2nd experiment. The insets show the fluorescence spectra of synthetic saline aqueous streams in the beginning and in the end of the 3rd experiment.

As can be seen, there is a variation of fluorescence emission intensity in the region corresponding to humic compounds (Figure 6.10). At first, the humic compounds peak is clearly present in the river water, while in the sea water the corresponding peak is not visible. During the RED stack operation, the intensity of the humic peak in the river water decreased, while in the sea water it increased. This result suggests the transport of humic compounds from the river water to the sea water compartment across the membrane. Since the charge of humic acids at the operating pH (between 7.0 and 8.5) is negative, some humic compounds may have been transported through the anion-exchange membrane. This hypothesis seemed to be supported by visual observation of the AEMs in contact with the river water, as their surface color changes during the stack operating time, from yellowish to a dark brown appearance, as described in Section 6.3.2.1.

The transport of small anionic organic compounds such as acetate through AEMs has been commonly observed [27]; however, humic compounds have been mostly found to be adsorbed on AEM surfaces [8]. In order to investigate, if transport of humic compounds was possible through the anion-exchange membrane used in the present study, a complementary experiment with 40 mg/l commercial humic acids dissolved in a 1 g/L NaCl solution, as "river water", and with a 31 g/L NaCl solution, as "sea water", was performed. Ralex membranes, which had been used in this study, may be of a particular interest for the RED process since, due to their relatively high thickness (~0.7 mm), are more suitable to be used for production of profiled membranes. Since in such a configuration, the intermembrane distance is only maintained by profiled membranes, they should be mechanically stable and, from a membrane manufacturing point of view, the membrane non-profiled part should be at least 0.2 mm thick in order to not wave [28].

As shown in Figure 6.10 (insets), in the beginning of this test, the humic acids peak only appears in the dilute water sample. Then, during the period of stack operation (24 hours), fluorescence EEMs of water samples were acquired and the samples returned to the respective vessels. It was seen that progressively the fluorescence emission intensity in the region of humic acids peak decreased in the dilute saline water and started to appear increasingly in the concentrated saline water, which suggests a transport of humic compounds from the river compartment to the sea compartment. This may be explained by heterogeneous ion-exchange membranes inherently contain defects in their interior [29], which could allow the penetration of humic compounds.

When comparing the fluorescence spectra of natural and synthetic solutions of dilute saline samples in the beginning of the experiments (Figure 6.10), they appear to be very different in the region of the humic acids peak (possibly due to the different composition of natural humic compounds present in the river water and of the commercial humic acids used to make the synthetic solution). However, the fluorescence spectra of both (natural and synthetic) concentrated saline water samples in the end of the experiments look similar. Also, the natural samples, as well as the synthetic sea water (even in the end) were visually transparent, while the synthetic river water was always brown. This may mean that although the initial composition of humic compounds present in the natural river water has been different from the one available commercially and used to prepare the synthetic solution, similar humic compounds have been transported from the dilute to the concentrated stream.

In order to compare the fluorescence responses of the aqueous streams used in the three experiments, PCA of all fluorescence EEMs (natural river and sea water samples from experiments one and two, as well from the experiment with synthetic waters) was performed. As previously explained, similar PC values mean that two points are statistically similar. Figure 6.11 presents the first three PCs obtained (scores plots) with an indication of the EEMs acquisition time sequence.

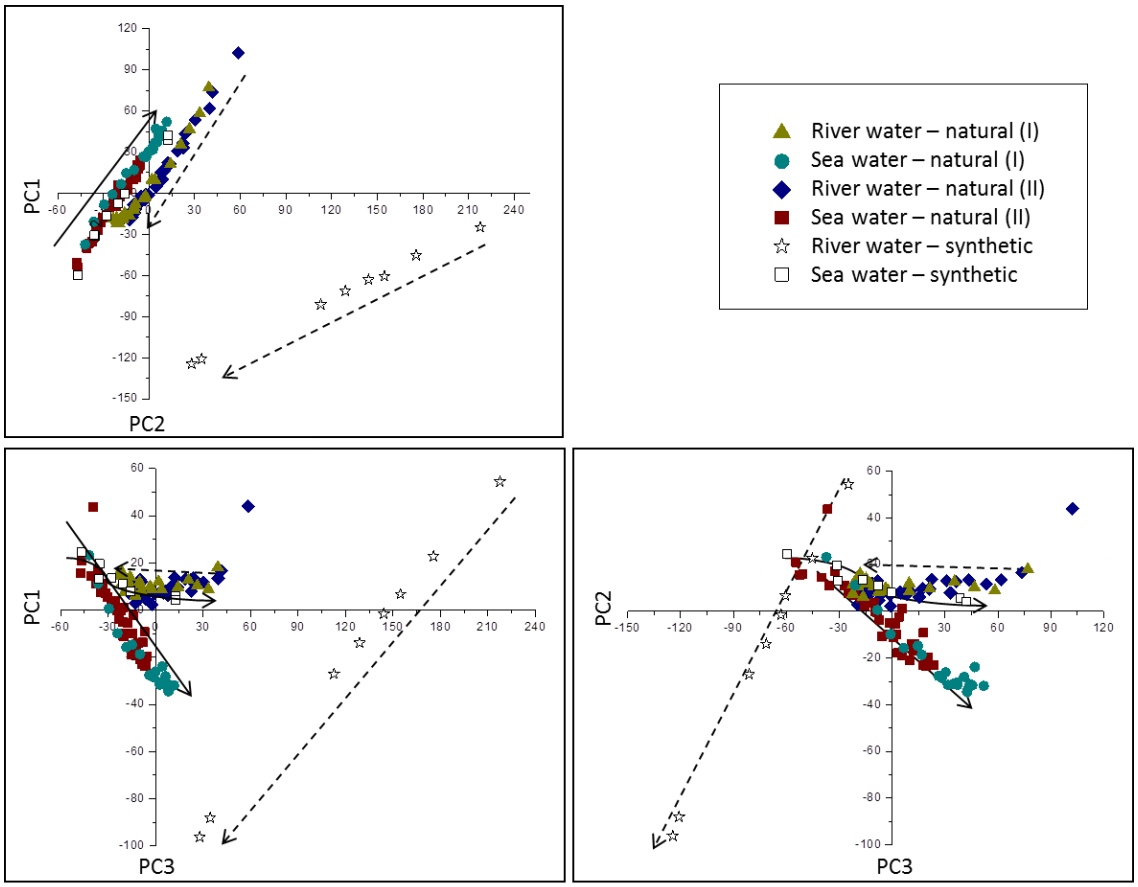

Figure 6.11. Scores plots of the first 3 principal components obtained through PCA of the fluorescence EEMs of the aqueous streams collected for all experiments (1st experiment – natural water (I), 2nd experiment – natural water (II), 3rd experiment – synthetic solution). Dash line is the time line of EEMs acquisition of dilute streams fluorescence. Continuous line is time line of EEMs acquisition of concentrated streams fluorescence.

The total variance captured by the first three components was 80.77 % (PC1-40.54 %, PC2-29.72 %, PC3-10.52 %). As can be seen, the synthetic river water is clearly different from all other water streams, which can be explained by different composition of the commercial humic acids compared with those present in the natural river water used in the present study. The synthetic sea water initially is very similar to the natural sea water, but with time begins to present more similarities with the initial natural river water (see PC1vsPC3 and PC2vsPC3 plots in Figure 6.11). These similarities may suggest that the humic compounds, which are transported from the river water compartment to the sea water compartment, are similar for the

experiments using real and synthetic river water, independently of the initial humic compounds composition in the working solutions.

When looking to the PCs of the natural samples (Figure 6.11), it is possible to see that the distance between the points decreases over time (samples were taken with an average frequency of about 24 hours), which may indicate that in the beginning of the experiments the transport of humic acids was faster, and then slowing down over time. This result is not unexpected since the driving force of charge transport in RED stacks is the concentration gradient and, initially, the humic compounds concentration was higher in the river water. Additionally, the composition of the solutions used in the 1st experiment seems to have changed more significantly than in the 2nd experiment. Since the initial waters were collected in the same time and the other operating parameters, such as flow rates, were similar for both experiments, this difference can be explained by the smaller water volumes used (35 L of each river and sea water) in the 1st experiment comparatively to the 2nd experiment (70 L), i.e. faster equilibration in the case of the 1st experiment occurred.

Based on the results obtained, the humic compounds due to their high molecular mass may have increased the resistance, through their partial retention in the membrane and also due to their transport from the dilute to the concentrated water compartment. There is a need to further investigate the transport of humic compounds from dilute to concentrated streams when natural saline waters are used to generate power in RED stacks.

6.4. CONCLUSIONS

In this study, the use of 2D fluorescence spectroscopy as a monitoring tool in Reverse Electrodialysis was investigated. Fluorescence EEMs of anion and cation-exchange membranes were different and changed along the period of membrane utilization, since the membranes were affected by fouling. 2D fluorescence spectroscopy, given its sensibility and amount of information captured, allows in such a way for monitoring the development of fouling on ion-exchange membrane surfaces and to detect which regions are more affected.

The membrane cleaning efficiency was also assessed and evaluated by 2D fluorescence spectroscopy combined with a PCA analysis. For RED systems, the cleaning strategy commonly used for ion-exchange membranes may require further revision and study since, despite the need for clogging removal from the channels, the chemical treatment leads to the ion-exchange membrane damage. This conclusion based on 2D fluorescence spectroscopy is supported by the observed increase of electrical resistance after chemical cleaning. 2D

fluorescence spectroscopy allowed also for the detection and following the transport of humic acids from the dilute to the concentrated compartment, which may negatively affect the RED stack performance.

Moreover, since fluorescence data can be quantified and relevant information may be extracted through PCA, it may be possible to use florescence data in correlations with performance parameters of RED process, e.g. net power density or electric resistance. 2D fluorescence spectroscopy proved to be fast (less than 5 minutes to acquire a complete spectrum), reproducible and it is potentially non-invasive. An ideal solution should pass through incorporation of fluorescence probes inside the working channels for online monitoring, which represents still a technological challenge.

REFERENCES

[1] D.A. Vermaas, J. Veerman, N.Y. Yip, M. Elimelech, M. Saakes, K. Nijmeijer, High efficiency in energy generation from salinity gradients with reverse electrodialysis, Sustain. Chem. Eng. 1(10) (2013) 1295-1302.

[2] G.Z. Ramon, B.J. Feinberg, E.M.V. Hoek, Membrane-based production of salinity-gradient power, Energy Environ. Sci. 4 (2011) 4423–4434.

[3] J. Kuleszo, C. Kroeze, J.W. Post, B.M. Fekete, The potential of blue energy for reducing emissions of CO2 and non-CO2 greenhouse gases, J. Integr. Environ. Sci. 7 (S1) (2010) 89–96.

[4] D.A. Vermaas, M. Saakes, K. Nijmeijer, Early detection of preferential channeling in reverse electrodialysis, Electrochim. Acta 117 (2014) 9– 17.

[5] D.A. Vermaas, D. Kunteng, M. Saakes, K. Nijmeijer, Fouling in reverse electrodialysis under natural conditions, Water Res. 47 (2013) 1289-1298.

[6] D.A. Vermaas, J. Veerman, M. Saakes, K. Nijmeijer, Influence of multivalent ions on renewable energy generation in reverse electrodialysis, Energy Environ. Sci. 7 (2014) 1434-1445.

[7] N. Tanaka, M. Nagase, M. Higa, Organic fouling behavior of commercially available hydrocarbon-based anion-exchange membranes by various organic-fouling substances, Desalination 296 (2012) 81–86.

[8] H. Lee, J. Choi, J. Cho, S. Moon, Characterization of anion exchange membranes fouled with humate during electrodialysis, J. Membr. Sci. 203 (2002) 115–126.

[9] K. Ghyselbrecht, A. Silva, B. Van der Bruggen, K. Boussu, B. Meesschaert, L. Pinoy, Desalination feasibility study of an industrial NaCl stream by bipolar membrane electrodialysis, J. Environ. Manag. 140 (2014) 69-75.

[10] Q. Ping, B. Cohen, C. Dosoretz, Z. He, Long-term investigation of fouling of cation and anion exchange membranes in microbial desalination cells, Desalination 325 (2013) 48–55.

[11] D.A. Vermaas, D. Kunteng, J. Veerman, M. Saakes, K. Nijmeijer, Periodic feedwater reversal and air sparging as antifouling strategies in reverse electrodialysis, Environ. Sci. Technol. 48 (2014) 3065−3073.

[12] S. Pawlowski, J.G. Crespo, S. Velizarov, Pressure drop in reverse electrodialysis: Experimental and modeling studies for stacks with variable number of cell pairs, J. Membr. Sci. 462 (2014) 96–111.

[13] L. Gurreri, A. Tamburini, A. Cipollina, G. Micale, CFD analysis of the fluid flow behavior in a reverse electrodialysis stack, Desalination Water Treat. 48:1-3 (2012) 390-403.

[14] L. Gurreri, A. Tamburini, A. Cipollina, G. Micale, M. Ciofalo, CFD prediction of concentration polarization phenomena in spacer-filled channels for reverse electrodialysis, J. Membr. Sci. 468 (2014) 133–148.

[15] S. Pawlowski, P. Sistat, J.G. Crespo, S. Velizarov, Mass transfer in reverse electrodialysis: Flow entrance effects and diffusion boundary layer thickness, J. Membr. Sci. 471 (2014) 72–83.

[16] C.F. Galinha, G. Carvalho, C.A.M. Portugal, G. Guglielmi, M.A.M. Reis, J.G. Crespo, Two-dimensional fluorescence as a fingerprinting tool for monitoring wastewater treatment systems, J. Chem. Technol. Biotechnol. 86 (2011) 985–992.

[17] C.F. Galinha, G. Carvalho, C.A.M. Portugal, G. Guglielmi, R. Oliveira, J.G. Crespo, M.A.M. Reis, Real-time monitoring of membrane bioreactors with 2D-fluorescence data and statistically based models, Water Sci. Technol. 63 (2011) 1381-1388.

[18] M. Pons, S. Le Bonte, O. Potier, Spectral analysis and fingerprinting for biomedia characterisation, J. Biotechnol. 113 (2004) 211–230.

[19] C.F. Galinha, G. Carvalho, C.A.M. Portugal, G. Guglielmi, M.A.M. Reis, J.G. Crespo, Multivariate statistically-based modelling of a membrane bioreactor for wastewater treatment using 2D fluorescence monitoring data, Water Res. 46 (2012) 3623-3636.

[20] C.F. Galinha, G. Guglielmi, G. Carvalho, C.A.M. Portugal, J.G. Crespo, M.A.M. Reis, Development of a hybrid model strategy for monitoring membrane bioreactors, J. Biotechnol. 164 (2013) 386– 395.

[21] D.A. Vermaas, E. Guler, M. Saakes, K. Nijmeijer, Theoretical power density from salinity gradients using reverse electrodialysis, Energy Proc. 20 (2012) 170 – 184.

[22] R. Bro, PARAFAC. Tutorial and applications. Chemometr. Intell. Lab. Syst. 38 (1997) 149-171.

[23] P. Dlugolecki, K. Nijmeijer, S.J. Metz, M. Wessling, Current status of ion exchange membranes for power generation from salinity gradients, J. Membr. Sci. 319 (2008) 214–222.

[24] R. Kodym, F. Vlasak, D. Snita, A. Cernin, K. Bouzek, Spatially two-dimensional mathematical model of the flow hydrodynamics in a channel filled with a net-like spacer, J. Membr. Sci. 368 (2011) 171–183.

[25] W. Garcia-Vasquez, R.Ghalloussi, L.Dammak, C.Larchet, V.Nikonenko, D.Grande, Structure and properties of heterogeneous and homogeneous ion-exchange membranes subjected to ageing in sodium hypochlorite, J. Membr. Sci. 452 (2014) 104–116.

[26] J.N. Louvet, B. Homeky, M. Casellas, M.N. Pons, C. Dagot, Monitoring of slaughterhouse wastewater biodegradation in a SBR using fluorescence and UV–Visible absorbance, Chemosphere 91 (2013) 648–655.

[27] J. Kim, S. Cheng, S. Oh, B. Logan, Power generation using different cation, anion, and ultrafiltration membranes in microbial fuel cells, Environ. Sci. Technol. 41 (2007) 1004-1009.

[28] E. Guler, R. Elizen, M. Saakes, K. Nijmeijer, Micro-structured membranes for electricity generation by reverse electrodialysis, J. Membr. Sci. 458 (2014)136–148.

[29] M. Asraf-Snir, J. Gilron, Y. Oren, Gypsum scaling on anion exchange membranes during Donnan Exchange, J. Membr. Sci. 455 (2014) 384–391.

Chapter

7

PREDICTION OF REVERSE ELECTRODIALYSIS PERFORMANCE BY INCLUSION OF 2D FLUORESCENCE SPECTROSCOPY DATA INTO MULTIVARIATE STATISTICAL MODELS

SUMMARY

The power density obtainable by a reverse electrodialysis (RED) stack decreases along its operating period due to fouling; however this effect is not accounted for by the so far proposed mechanistic models. In Chapter 6, it has been demonstrated that 2D fluorescence spectroscopy can capture important information regarding the RED performance, including the time evolvement of ion-exchange membrane fouling. Moreover, since the 2D fluorescence data can be compressed through parallel factor analysis (PARAFAC) into few principal components (PCs), the latter can be successfully included in multivariate statistical models. In this work, such multivariate statistical modeling was performed, by using the projection to latent structure (PLS) approach, to predict four RED stack performance parameters: pressure drop in river and sea waters circuits, stack electric resistance and net power density. Several PLS models were developed, with and without 2D fluorescence data as models inputs. It was found that inclusion of fluorescence data considerably improved the models fitting, because the otherwise missing information about the dynamic state of ion-exchange membranes was added. Additionally, the coefficients of the optimized models revealed important contributions of some of the input parameters to the predicted outputs and allowed to mathematically confirm the qualitative observations that fouling of anion-exchange membranes facing river water is the main factor affecting the RED stack performance. This work confirms the applicability of 2D fluorescence spectroscopy for monitoring of fouling in RED stacks and demonstrates the ability of simple, statistically based models to follow RED performance.

Submitted as: S. Pawlowski, C.F. Galinha, J.G. Crespo, S. Velizarov, Prediction of reverse electrodialysis performance by inclusion of 2D fluorescence spectroscopy data into multivariate statistical models, Separation and Purification Technology (2015).

Graphical abstract:

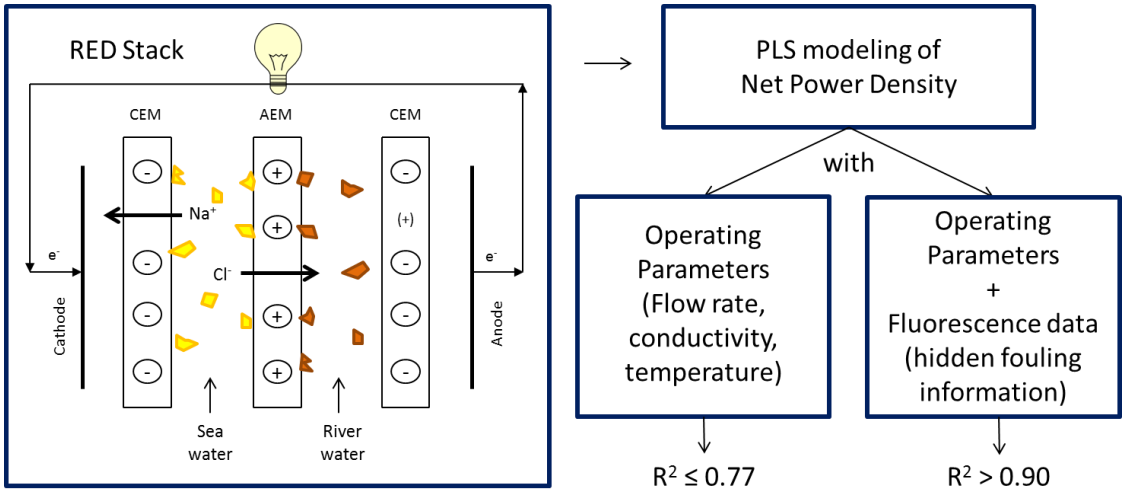

Highlights

- Statistically-based multivariate models were developed for reverse electrodialysis.
- PLS modeling was used to predict net power density, electric resistance and pressure drop.
- 2D fluorescence spectroscopy was used to capture information about fouling.
- 2D fluorescence data, after PARAFAC compression, were incorporated in PLS models.
- Inclusion of fluorescence data significantly improved the PLS models fitting.

Keywords: Ion-exchange membranes, 2D fluorescence spectroscopy, Fouling Monitoring, PLS modeling

7.1. INTRODUCTION

Reverse electrodialysis (RED) is a promising, ion-exchange membrane-based technology for sustainable power generation from salinity gradients, such as those existing in estuaries, where a dilute saline stream (river water) mixes with a concentrated saline stream (sea water) [1]. In a RED stack, the saline streams are separated by alternately arranged cation- and anion-exchange membranes, through each, the respective counter-ions pass from the concentrated to the dilute stream. Therefore, the anions and the cations migrate in opposite directions, toward the anode and cathode, at which the salinity gradient energy is converted into electrical energy by an appropriate redox couple solution.

The most important parameter determining a RED stack performance is the net power density, which accounts for the trade-off between the power density generated by the stack and the power density spent for pumping the solutions [2]. When natural water streams are used, transport of multivalent ions from dilute to concentrated saline stream [3-4] and fouling in RED stack channels [5-6] may cause a significant decrease in the obtained power density. However, while the influence of multivalent ions on potential difference and electric resistance can be reasonably well predicted [7], the fouling effects on stack electric resistance and pressure drop are not accounted for by the so far proposed RED mechanistic models [8-12]. Such a mechanistic approach could hardly be applied in a straightforward and simple manner, when there is a lack of fundamental knowledge of the system behavior (e.g. fouling development) [13].

Recently, we found out that fluorescence excitation-emission matrices (EEMs) of ion-exchange membrane surfaces, acquired during 34 days of RED stack operation with natural river and sea water streams, showed a progressive change over time [14]. This evolution was associated with adsorption of humic compounds on anion-exchange membrane surfaces and with sands and clay deposition on cation-exchange membrane surfaces. Additionally 2D fluorescence spectroscopy allowed for evaluating the membrane cleaning strategy efficiency and detecting transport of humic compounds from the river to the sea water stream. Therefore, it was concluded that 2D fluorescence spectroscopy could be eventually (after reduction of fluorescence probe dimensions and its incorporation in working channels) a valuable monitoring tool for assessment of fouling on ion-exchange membrane surfaces. Finally, since the data captured by EEMs could be deconvoluted by parallel factor analysis (PARAFAC) into few principal components (PCs), it was proposed to use this information in multivariate statistical models for prediction of relevant RED stack performance parameters.

Multivariate statistical models have been successfully applied to correlate large sets of data in membrane bioreactors (including performance parameters and the information captured by 2D fluorescence spectroscopy), extract hidden information and disclose unobvious relationships between variables [15]. Such mathematical models can be obtained through projection to latent structures (PLS) modeling, which is a linear regression method that maximizes the covariance between the input matrix X and the output performance parameters in matrix Y. PLS models generate reduced orthogonal factors (latent variables), by decomposing iteratively both the X and Y matrices, in order to explain the maximum variance in the output variables [16]. PLS models handle well with co-linearity between variables, data noise and missing data. The output in PLS model is described by linear correlations of the multiple inputs:

$$y = a \cdot x_1 + b \cdot x_2 + c \cdot x_3 + \ldots \quad (7.1),$$

where a, b, and c are the regression coefficients and x_1, x_2, and x_3 are the useful predictors to describe the modeled output. In case of unsatisfactory model fitting, there is a possibility to make the models more complex. The inputs can be manipulated by making them quadratic or by multiplying different inputs [17-18].

In this study, PLS modeling was performed in order to model pressure drop, electric resistance and net power density of a RED stack operated during 34 days with natural river and sea water as saline streams. EEMs of the ion-exchange membrane surfaces were periodically acquired. PLS model fitting with and without fluorescence data as inputs was carried out and compared.

7.2. MATERIALS AND METHODS

7.2.1. Reverse Electrodialysis

A 3-cell pairs electrodialysis EDR-Z-Mini unit (MEGA a.s., Czech Republic), equipped with virgin heterogeneous ion exchange membranes (Ralex), was used as RED stack. Previously, it was found that cation- and anion-exchange membranes can be clearly distinguished by 2D fluorescence spectroscopy due to their different fluorescence spectra. Furthermore, after principal component analysis of all obtained spectra, it was possible to follow fouling evolvement on the membrane surfaces [14].

The working channels dimensions were 4x16 cm (width and length) and the intermembrane distance (channel height) was kept constant by 0.8 mm polyethylene spacers. 70 L of Atlantic Ocean water, collected in Almada (Fonte da Telha), and 70 L of Lisandro river water, taken

from Mafra (Cheleiros), were stored in semitransparent vessels, without stirring, pre-filtration or any other pretreatment steps, at a room temperature. The mentioned solutions were used as concentrated and dilute saline streams, respectively, and were recirculated, at flow rates ranging between 17-85 ml/min, during 34 days through the RED stack. Differential pressure sensors (Honeywell, model 24PCAFA6D) were used to measure pressure drop between stack inlet and outlet, for each saline stream. No external potential difference was applied, and the potential difference (OCV) was measured with a Digital Multimeter (Kaito Electronics). As electrodes redox pair solution, a 0.1 M $K_4Fe(CN)_6$ / 0.1 M $K_3Fe(CN)_6$ in 0.27 M NaCl aqueous solution was used. This solution was recirculated at a flow rate of 90 ml/min between the two electrode compartments. The total RED stack electric resistance was calculated by Ohm´s law from experimental potential difference and current intensity data. The stack was periodically opened (13 times in total) after 1, 2, 3, 6, 8, 10, 13, 16, 20, 23, 27, 30 and 34 days of operation, in order to acquire fluorescence EEMs of the membranes' surfaces. Before each stack opening, the solutions flow rate, conductivity and temperature were measured, except for the first day, when EEMs of membrane surfaces were obtained before building the stack, and all mentioned measurements were performed immediately after the start of the experiment. Therefore, in total, operating and performance data were collected 14 times. For each time, the obtainable stack net power density ($P_{net\ \ density}$) was calculated from the trade-off between gross power density ($P_{gross\ density}$) obtained in the stack and the power spent for pumping the solutions ($P_{pumping}$):

$$P_{net\ density} = P_{gross\ density} - \frac{P_{pumping}}{2 \cdot N \cdot A_m} \quad (7.2),$$

where A_m is the area of one membrane and N is the number of cell pairs [11, 19]. The power spent for pumping the river and the sea water streams can be obtained as follows [2]:

$$P_{pumping} = \Delta p_{river} \cdot Q_{river} + \Delta p_{sea} \cdot Q_{sea} \quad (7.3),$$

where Q is the feed solution flow rate and Δp is the pressure drop between the stack inlet and outlet for each solution water circuit. The gross power generated by a RED stack depends of the potential difference established between the electrodes (OCV – open circuit voltage), the stack internal resistance (R_i) and the external load resistance. If internal and external resistances have equal values (in practice this presupposes the use of infinitely segmented electrodes), the obtainable gross power density reaches its maximum value and can be calculated as follows [20]:

$$P_{gross\ density} = \frac{OCV^2}{4 \cdot R_i} \quad (7.4).$$

7.2.2. 2D fluorescence spectroscopy

2D fluorescence spectroscopy measurements result in excitation-emission matrices (EEMs) where each value of fluorescence emission intensity corresponds to each pair of excitation/emission wavelengths. EEMs were acquired with a fluorescence spectrophotometer (Varian Cary Eclipse) equipped with excitation and emission monochromators and coupled to an optical fibre bundle probe, constituted by a total of 294 randomized optical fibres (147 excitation and 147 emission) each with a diameter of 200 μm and a length of 2 m. Fluorescence EEMs were obtained using the scan speed of 12000 nm/min and excitation and emission slits of 10 and 5 nm, respectively. EEMs were generated in a range of 250 to 690 nm (excitation) and 260 to 700 nm (emission), with an excitation wavelength incrementing step of 5 nm.

Fluorescence EEMs of the cation- and anion-exchange membranes' surfaces in contact with river and sea waters were acquired in two predefined regions: one close to the fluid flow entrance of the channel and the other close to the flow exit from the channel. Each acquisition was performed twice and the same points were scanned during all trials. In such a way, for the 14 sets of collected operating data 4 EEMs of each membrane surfaces were obtained. The optical fibre probe distance from the membrane surface was maintained constant (1 cm) in all measurements. The excitation light angle with membrane surface is 45º in order to avoid overlap of excitation and emission light.

An EEM is composed by more than 4 thousand useful (for excitation wavelengths > emission wavelengths) fluorescence intensity values, one for each pair of excitation/emission wavelengths. Each EEM was converted in the one line with 4005 columns, one column for each fluorescence emission light intensity of the corresponding excitation/emission wavelength pair. For each membrane surface, AEM surface contacting with river water, AEM surface contacting with sea water, CEM surface contacting with river water and CEM surface contacting with sea water the obtained EEMs for the corresponding membrane surface were grouped together in one matrix, with the number of lines corresponding to the number of acquired EEMs for each membrane surface (56 in total) and 4005 columns. In such a way, four sets of EEMs were created, each one relative to the respective membrane surface. To reduce the dimension and the number of variables to introduce in the mathematical models, each data matrix was vectorised and compacted. Compression was done to decrease the number of variables, co-linearity and noise. The PARAFAC (parallel factor analysis), tool which is a decomposition method of multi-way data (such as EEMs) that can be considered an extension of the well-known principal

component analysis (PCA) [21], was used. PARAFAC was applied separately, using 8 principal components, for each membrane surfaces EEMs set, which corresponded to > 99.9 % of variance captured in each case.

7.2.3. Development of PLS models

Multivariate statistically-based models were developed to correlate the operating data (solutions' flow rates, conductivities and temperature) and the fluorescence data with four relevant RED stack performance parameters (pressure drop in the sea water and river water circuits, electric resistance and net power density).

Mathematical models were obtained through projection to latent structures (PLS) modeling. All experimental data used in PLS models were previously normalized by subtracting from each value the average of the experimental data of the respective variable and dividing by the respective standard deviation. With this procedure all variables are fed to the model with comparable weights, regardless of the units used for each variable. The regression coefficients of each model obtained are, therefore, relative to normalized data and can be compared between them.

Three groups of sampling events (observed data) were used to obtain PLS models. The 1st group contained values of all observed data and the 2nd group consisted of all observed data except for the data obtained in the first day of the experiment. In the 3rd group, the variation of observations' values was used as inputs, i.e., to predict the output value at observation (n+1), the value of the difference between input value at observation (n+1) and input value at the previous observation (n) was used.

For each mentioned group, models with two different kinds of inputs were developed: 1- with only operating data or 2 – with, simultaneously, fluorescence and operating data. In case when the fluorescence was one of the inputs, 1st group of sampling events was constituted by 56 observations and the 2nd and 3rd group had 52 observations. If only operating data were used, the number of observations was 14 and 13, respectively for 1st and for 2nd and 3rd groups of sampling events.

Sampling events which contained fluorescence data were divided randomly into two sets: training (75 % of observations) and validation (25 % of observations). The distribution of data for each set was verified in order to assure that the validation set was representative of the training set, i.e. avoiding extrapolation on the forecast by validation values. The same training

and validation sets were used to develop the models for an output to allow direct comparison of the different models. For the case of sampling event constituted only by operating data, all available data were used in the training set, and the validation set was not created due to the reduced sampling dimension.

The selection of the number of latent variables of each PLS regression and model optimization was performed based on the lowest root mean square error of cross-validation (RMSECV). This parameter translates the error of the training set established through cross-validation, and was calculated using the following equation:

$$RMSECV = \sqrt{\frac{\sum_{i=1}^{N}(\ddot{y}_i - y_i)^2}{N}} \quad (7.5),$$

where y_i is the experimental value at the i event, $\ddot{y}_i$ is the predicted value for the i event using the model obtained with N-i events, and N is the number of sampling events in the training set.

However, not all parameters available to be used as inputs are necessarily correlated with the target outputs. Therefore, three different mathematical methods were used for elimination of not useful inputs: iterative stepwise elimination (ISE) [22]; stepwise elimination [23], and the Martens uncertainty test [24] using the jackknife standard deviations [25]. This procedure aims improving models' fitting and reduce their complexity, and results in PLS models, which are more robust. PLS models were implemented in Matlab using the n-way tool box [26].

7.3. RESULTS AND DISCUSSION

7.3.1. Reverse Electrodialysis

7.3.1.1. Operating data

The RED stack was operated during 34 days, using natural river and sea waters as the dilute and concentrated saline streams, respectively. As operating parameters the solutions' flow rate, conductivity and temperature were considered, while pressure drop in the river water compartment, pressure drop in the sea water compartment, the stack electric resistance and the obtainable net power density were the performance (output) parameters. The operating and performance data are presented in Figure 7.1.

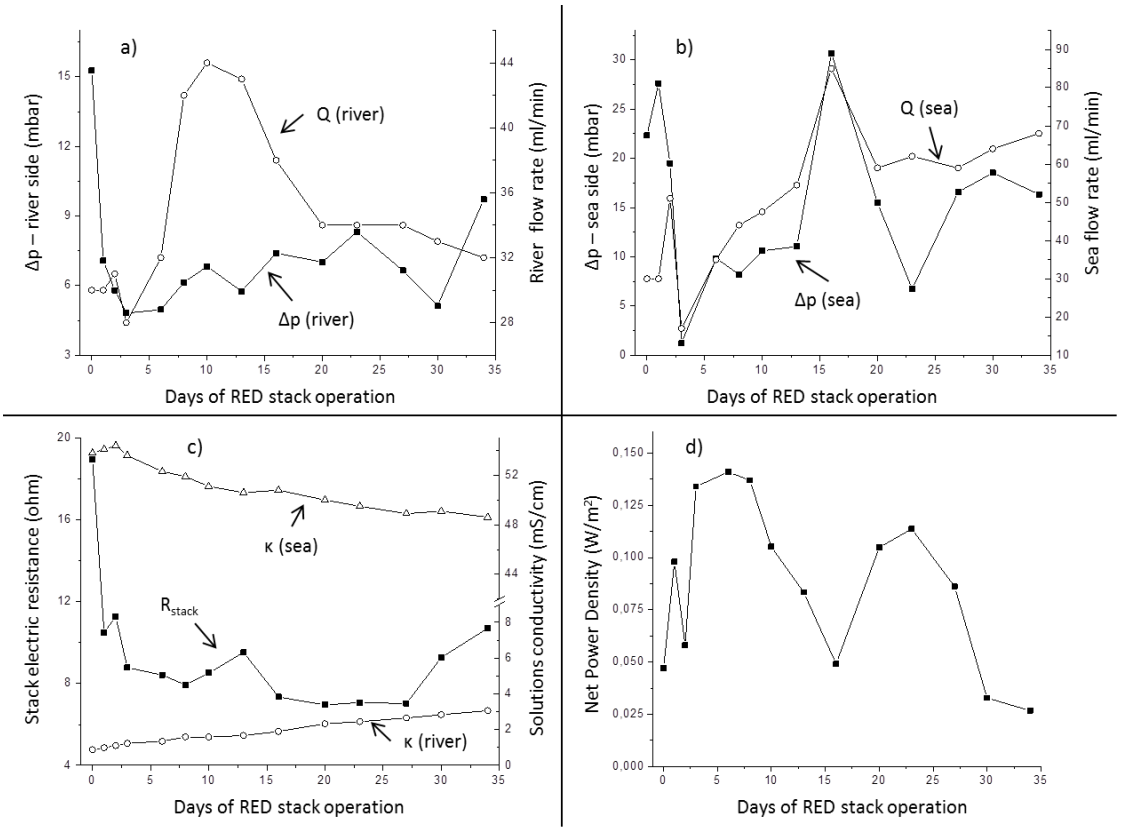

Figure 7.1. Variation of a) river stream flow rate and pressure drop in the river circuit, b) sea stream flow rate and pressure drop in the sea circuit, c) stack electric resistance and river and sea water streams conductivity and d) net power density, in the RED stack during its operation period (34 days).

As can be seen (Figure 7.1), the performance parameters varied during the stack operating period, mostly due to the randomly imposed solutions flow rate after reassembling RED stack. However, when the resistance values were compared with the theoretically expected resistance (as in [5]), the ratio between experimental and theoretical resistance showed a linear increase (data not shown) that indicates a fouling formation, which is not accounted for by theoretical mechanistic models.

The flow rate of both streams was varied randomly within the range of 17 to 85 ml/min. With exception of the first two days, the flow rates in the river and in the sea compartment were always different. This choice of flow rate varying conditions was to assure that the multivariate models could capture separately the influence of each flow rate on the performance parameters. The imposed variations were essential for obtaining PLS models calibrated for a wide values range of performance parameters. If, for example, the RED stack had been operated with no operating parameters variation, after few days, a linear increase of the pressure drops and of stack electric resistance and a linear decrease in net power density would have been expected to be observed [5]. Moreover, a linear model output variation can be easily modeled by any operating parameter (input), which varies also linearly, being it physically related or not with

the output, that evidently could result in models with excellent fitting, but lacking a physical reality meaning. The range of operating and stack performance parameters used in the PLS models as inputs and outputs is summarized in Table 7.1.

Table 7.1. Range of operating data of both saline streams (Sea and River water streams) and the performance parameters of a RED stack operated during 34 days and the range of the same observations, but after excluding the observations for the 1st day.

Parameters	Unit	Range (All observations)	Range (Without 1st day' observations)
Flow rate (Sea)	ml/min	17-85	the same
Flow rate (River)	ml/min	28-44	the same
Conductivity (Sea)	mS/cm	48.6-54.4	the same
Conductivity (River)	mS/cm	0.873-3.06	0.986-3.06
Temperature (Average)	ºC	24.2-26.8	the same
Pressure drop (Sea)	mbar	1.2-30.7	the same
Pressure drop (River)	mbar	4.8-15.3	4.8-9.71
Stack electric resistance	ohm	6.95-18.97	6.95-11.27
Net power density	W/m^2	0.027-0.14	the same

Table 7.1 presents the range of values for two time intervals: for all operation days and for all operation days excluding the first day, during which the main alterations in the RED stack performance have been reported to occur [6]. In the beginning of the experiment, the ion-exchange membranes were new (virgin) and therefore had never previously experienced any fouling. Also, there is always an initial period, in which the membranes come to equilibrium with the working solutions. Therefore, the values of the stack electric resistance and pressure drop in the river compartment for the first day of operation were almost two times higher than the values registered in the following days.

7.3.1.2. 2D fluorescence spectroscopy data

During the stack operation, the stack was opened periodically to assess the membrane surfaces by 2D fluorescence spectroscopy. Figure 7.2 shows representative fluorescence spectra of the anion-exchange membrane surface in contact with river water. It was chosen to present herein those spectra, because it was seen that the main fouling was located on that membrane surface [14].

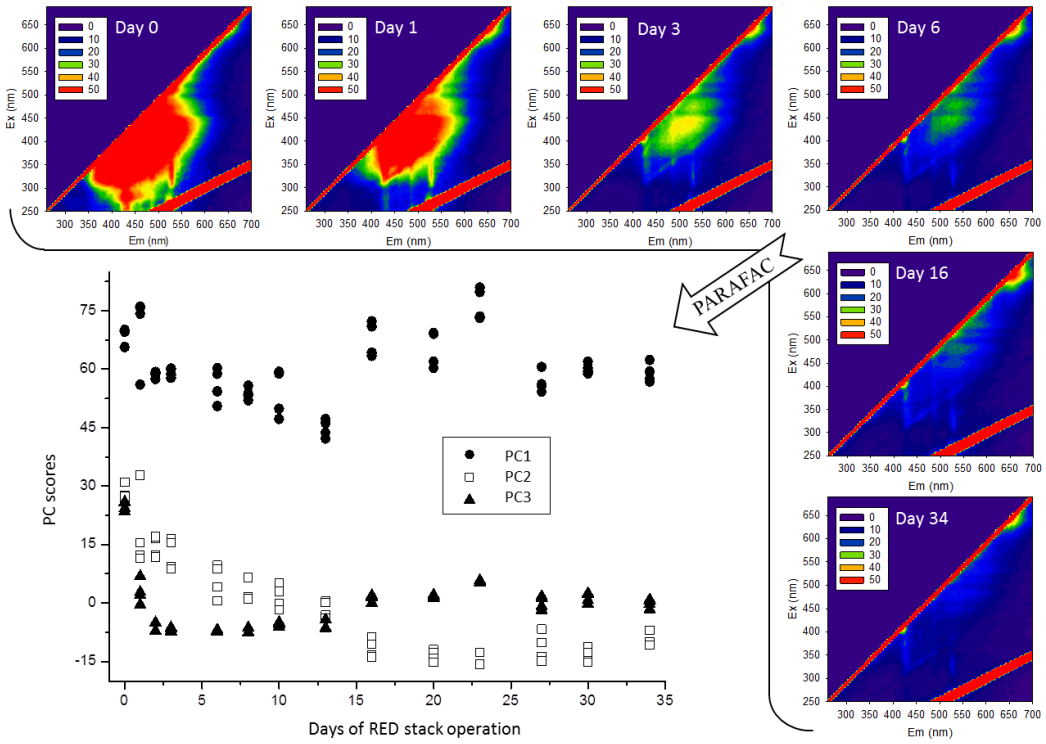

Figure 7.2. Representative fluorescence spectra of anion-exchange membrane surface close to the fluid exit from the channel, after 0, 1, 3, 6, 16 and 34 days in contact with river water and scores of first three principal components (PCs) obtained by PARAFAC of EEMs of all anion-exchange membrane surfaces in contact with river water acquired during the RED stack operation period (34 days).

Briefly, each fluorescence spectra represents intensity of the emitted light (herein between 0 – dark blue and 50 – red) in function of emission light wavelength (axe of x's) and excitation light wavelength (axe of y's). In this specific case, it is possible to observe that the virgin membrane (day 0) had the higher fluorescence intensity of the emission light, which decreased along time. Since the foulants (such as humic organic compounds) have a dark brownish color, the light emitted by the membrane surface is partially absorbed by the fouling layer, causing the observed fluorescence emission decrease along time. For CEMs, such clear visual evolution, as herein presented for AEM, was not seen. But, with mathematical tools, such as parallel factor analysis (PARAFAC), the main variations of EEMs along time, even if visually not perceptive, can be extrapolated in form of PCs. Therefore, the main conclusion in our previous work [14], was that fluorescence EEMs (herein represented as fluorescence spectra) are able to capture information and follow the fouling evolvement for the two types of ion-exchange membranes and for both of their surfaces (in contact with river and sea water) [14]. Scores of the first three principal components (PCs) obtained by PARAFAC of fluorescence EEMs of the AEM surfaces in contact with river water, acquired during the RED stack operation period (34 days) are also presented in Figure 7.2. Some of them, as well as others not shown in Figure 7.2, were used as inputs in the obtained PLS models (selection of those inputs is discussed in detail in section 7.3.2.3).

7.3.2. PLS modeling

PLS modeling was used to predict four RED stack performance parameters (models' outputs): pressure drop in the river compartment, pressure drop in the sea compartment, stack electric resistance and the obtainable net power density.

Various multivariate statistical PLS models were developed to predict each output independently from the others, using as inputs the principal components (PC) of EEMs of membrane surfaces obtained by 2D fluorescence spectroscopy and/or a set of operating process data (saline streams flow rate, conductivity and temperature). From the possible inputs set, only few were chosen (by mathematic methods for input elimination) to be used as inputs in PLS models, because the selection of useful inputs results in a general improvement of fitting, as well as it reduces the complexity of models [15].

Table 7.2 presents the statistical parameters of the selected PLS models. An ideal slope and R^2 for training and validation sets should be equal to 1 and the best models should have the lowest RMSECV values (as the RMSECV represents the error in the prediction of the training set of outputs).

Two data sets were used: only operating data ("no 2DFS") or operating and 2D fluorescence spectroscopy data together ("with 2DFS"). This step has an objective to see if inclusion of fluorescence data will improve the models fitting due to inclusion of the information relative to fouling on membrane surfaces. For each output prediction 3 kinds of models were developed: "All days" (Section 7.3.2.1), "Without 1st day" (Section 7.3.2.2) and "Delta" (Section 7.3.2.3).

"All days" models were obtained using the observations acquired in all days, including those obtained in the first day of experiment. Just to remember: the data values in the first day were quite different from the rest of the data. Since "All days" models with fluorescence data included had an excellent fitting, a question about if such a good models fitting is not influenced by those data from the first day of operation arises. Therefore, the data from the first day were eliminated, and new models were derived ("Without 1st day"). Two approaches were followed: exactly the same inputs found for the "All days" models were used and only the inputs' regression coefficients were recalibrated ("Recal."), or a new inputs' selection was performed ("New"). Finally, the influence of process history on output prediction was tested ("Delta" models). With this approach, it was tested if it is possible to accurately predict outputs by using information from previous days.

Table 7.2. Statistical parameters for the selected PLS models. In the models, as inputs were used: the data obtained by 2D fluorescence spectroscopy (2DFS) together with operating parameters (with 2DFS) or only the data of operating parameters (no 2DFS). "(Recal.)" means that the same inputs as in the model "All days – with 2DFS" were used and only the inputs regression coefficients were recalibrated. "(New)" stands for a model found independently from previous models. "All days" means that observations from all days were used, "Without 1st day" means that the observations from the 1st day were excluded, and "Delta" means that variation of the data was used as models inputs. RMSEP and RMSECV have the same units as the predicted outputs.

Outputs	Model #	Description	Inputs	LV used in PLS	Variance (%)	RMSEP	RMSECV	R^2 train.	R^2 valid.	Slope train.	Slope valid.
Pressure drop in river circuit (mbar)	1[a]	All days – no 2DFS	2	2	32	2.29		0.32		1.00	
	2[a]	All days – with 2DFS	6	6	94	0.60	0.71	0.94	0.95	1.00	1.03
	3	Without 1st day - no 2DFS	2	2	11	1.32		0.11		1.00	
	4	Without 1st day – with 2DFS (Recal.)	6	5	83	0.71	0.65	0.83	0.72	1.00	0.94
	5[b]	Without 1st day – with 2DFS (New)	8	7	90	0.42	0.91	0.90	0.91	1.00	1.09
	6	Delta – no 2DFS	3	1	21	1.24		0.21		1.00	
	7[c]	Delta – with 2DFS	8	8	88	0.60	0.61	0.88	0.80	1.00	0.98
Pressure drop in sea circuit (mbar)	8[a]	All days – no 2DFS	2	2	30	7.10		0.30		1.00	
	9[a]	All days – with 2DFS	4	4	73	4.39	4.44	0.73	0.71	1.00	0.90
	10	Without 1st day - no 2DFS	2	2	33	7.12		0.33		1.00	
	11[b]	Without 1st day – with 2DFS (Recal.)	4	4	72	4.50	4.68	0.72	0.71	1.00	0.88
	12	Without 1st day – with 2DFS (New)	The same as the previous model								
	13	Delta – no 2DFS	3	2	25	7.29		0.25		1.00	
	14[c]	Delta – with 2DFS	8	8	72	4.54	4.98	0.72	0.69	1.00	0.86

RED stack electric resistance (ohm)	15[a]	All days – no 2DFS	5	4	57	2.13		0.57		1.00	
	16[a]	All days – with 2DFS	7	3	95	0.73	0.81	0.95	0.95	1.00	1.09
	17	Without 1st day - no 2DFS	5	5	67	0.93		0.67		1.00	
	18	Without 1st day – with 2DFS (Recal.)	7	7	79	0.64	0.86	0.79	0.81	1.00	1.13
	19[b]	Without 1st day – with 2DFS (New)	7	5	83	0.51	0.70	0.83	0.87	1.00	1.06
	20	Delta – no 2DFS	5	3	59	1.00		0.59		1.00	
	21[d]	Delta – with 2DFS	7	7	93	0.33	0.45	0.93	0.95	1.00	1.05
RED stack net power density (W/m^2)	22[a]	All days – no 2DFS	4	4	60	0.025		0.60		1.00	
	23[a]	All days – with 2DFS	7	7	89	0.013	0.015	0.89	0.89	1.00	0.90
	24	Without 1st day - no 2DFS	4	4	72	0.021		0.72		1.00	
	25[b]	Without 1st day – with 2DFS (Recal.)	7	6	89	0.013	0.015	0.89	0.89	1.00	0.90
	26	Without 1st day – with 2DFS (New)	The same as the previous model								
	27	Delta – no 2DFS	4	3	77	0.019		0.77		1.00	
	28[d]	Delta – with 2DFS	7	7	92	0.012	0.013	0.92	0.91	1.00	1.05

[a], [b], [c], and [d] – Models represented in Figures 7.3, 7.4, 7.5 and 7.6, respectively.

Figures 7.3-7.6 presents, graphically, some of the results for the optimized models summarized in Table 7.2. The observed data were plotted against predicted data and the confidence intervals for PLS predictions were defined as two times the standard deviation of the output experimental data. A possible interpretation of the selected inputs utility for the output prediction, is discussed in more detail for the case of the optimized models (Figures 7.5 and 7.6), where the normalized regression coefficients for each input are also shown. However, it is not always possible to draw a mechanistic interpretation related with the system's behavior if the regression coefficient of an input shows a very high standard deviation, meaning that, although that input is essential for the output prediction, the positive or negative correlation obtained may have or not a mechanistic interpretation [15].

7.3.2.1. PLS modeling using data from all days ("All days" models)

As mentioned in Section 7.2.1, the RED stack was periodically opened in order to assess the membrane surfaces by 2D fluorescence spectroscopy and before opening the stack, the two streams conductivity and temperature, pressure drop in river and sea water circuit, the potential difference between the electrodes (open circuit voltage) and the current intensity were measured. From these values, the stack electrical resistance and net power density were calculated. The only exception was for the first day, when the performance parameters were immediately measured after the experiment had started, but the EEMs of membrane surfaces were acquired before, when they were still virgin.

Therefore, special attention is herein given to the measurements performed in the first day of the experiment. It was observed that the values of electric resistance and pressure drop in river compartment were much higher (almost twice) when the experiment started, compared with the values obtained for the stack after one day of operation. Moreover, due to the formation of fouling, the EEMs of membrane surfaces before operation were very different from the EEMs obtained for the membranes after they had been used (Figure 7.2).

Figure 7.3 shows the fitting of models #2 (pressure drop in the river circuit), #9 (pressure drop in the sea circuit), #16 (stack electric resistance) and #23 (net power density), when all observations were used and 2D fluorescence spectroscopy data was included in the inputs. For each output prediction, an inset with the fitting of the model is shown, in which only operating parameters were used for the respective output prediction (models #1, #8, #15 and #22, correspondingly, in a), b), c) and d)).

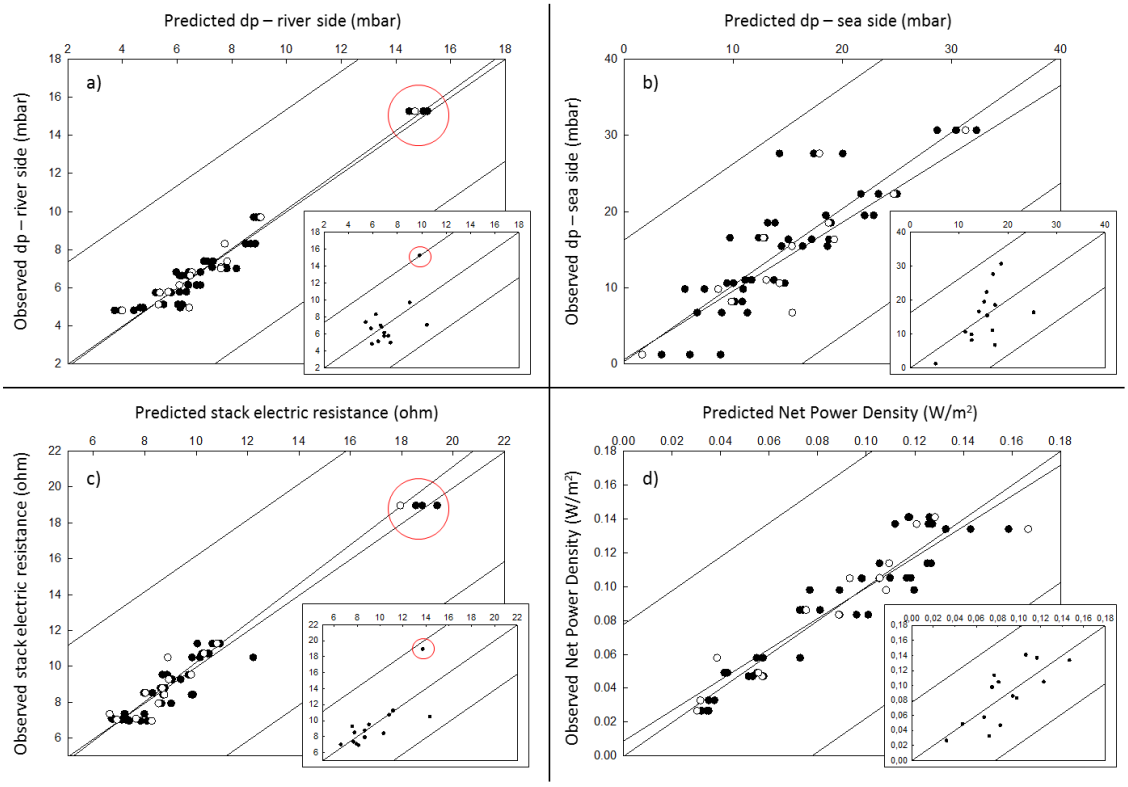

Figure 7.3. PLS models with operating and fluorescence data for all days used directly as inputs for prediction of: a) pressure drop in river circuit (model #2), b) pressure drop in sea circuit (model #9), c) stack electric resistance (model #16) and d) net power density (model #23). Closed circles represent training data and open circles represent validation data. In each figure, an inset with the PLS model, developed with only operating parameters used as inputs, is shown for the prediction of the same output (Models #1, #8, #15 and #22, respectively). The red circle shows the outputs obtained in the 1st day.

As previously mentioned, for pressure drop in the river compartment and for stack electric resistance, the measurements obtained in the beginning of the experiment (featured with red circle) were clearly out of the range of all other measurements. When only operating data were used as inputs, the data corresponding to that measurement were not well described by the model (i.e. outliers). This happens because the operating parameters during the first day had values similar and inside the range used in the following days. Therefore the operating parameters do not allow for describing how the membrane status was different during that particulate day.

Similarly, despite the fact that there were no clear outliers, the results of model fitting for pressure drop in the sea circuit (Figure 7.3b (inset)) show almost a vertically aligned distribution of points. This means that the values of predicted pressure drops in sea circuit were similar, although the observed pressure drop data had a broader range of values and dispersion. Despite the sea water flow rate variation showed a very similar trend to the variation of the pressure drop in the sea water circuit (Figure 7.1b) the model was not able to accurately predict this

output because no information about fouling was included. Moreover, the absence of a validation set for models with only operating parameters used as inputs may hide an overfitting, meaning that the models fitting may be even lower if validation set would be used as well for outputs prediction instead of the training set alone.

As it can be seen (Figure 7.3), for models in which the 2D fluorescence spectroscopy data obtained were included, the models' fitting improved considerable. There are no outliers, data are less dispersed and the predicted values match almost perfectly with the experimental data values. Such a good model fitting can be explained through an increase of captured variance. The data which were captured by 2D fluorescence spectroscopy bring to the model an important information associated to fouling and evolvement of the membrane surface status, in addition to the information provided by the imposed operating parameters.

With the exception of the pressure drop in the sea water circuit, the best models showed R^2 of training and validation sets equal to or above 0.90. This result is considered as an excellent adjustment. For pressure drop in the sea compartment, the R^2 values were 0.73 and 0.71 for the training and the validation set, respectively. The lower accuracy of prediction of this output may be associated with the periodical stack opening and the fouling characteristics in the sea compartment. While in the river compartment fouling was mostly caused by organic matter (rich in humic compounds) deposition on the AEM surface, in the sea compartment a significant accumulation of sands and clays was clearly visible [14]. Therefore the pressure drop in the sea compartment increased faster and reached higher values than those registered in the river compartment. However, when the stack is opened, the layer of sands and clays is always partially removed. Therefore, the EEMs captured a cleaner state of membrane surfaces compared to the moment before the stack opening, at which the pressure drop was measured. Also, since the pressure drop is measured for the whole circuit, i.e. including the manifolds, clays and sands may have also accumulate in the manifolds, which regions were not accessed by 2D fluorescence spectroscopy.

7.3.2.2. Verification of models fitting by removal of the first day data ("Without the 1st day" models)

Since the measurements for the first day were clearly different, it was decided to investigate the impact of removing these initial observations. The objective was to investigate if the good "All days" models' fitting for pressure drop in the river circuit and for stack electric resistance was indeed due to the inclusion of the fluorescence data or if such a good fitting was caused by those outputs high values difference between the first and other days. Also, it gives the opportunity to

verify if it is possible to obtain a good output prediction during the fouling development, i.e. when fouling on the membrane surfaces was already formed.

Relatively to the models where only operating data were used, for both pressure drop predictions, R^2 with and without 1st day, was always below 0.33. However, when the observation for the first day was removed, the R^2 of the models for prediction of stack electric resistance and net power density increased from 0.57 (#15) to 0.67 (#17) and from 0.60 (#22) to 0.72 (#24), respectively (Table 7.2). Since the membrane state was very different when the trial started, the R^2 increased, as expected, when the point from the first day was removed.

Relatively to the models fitting with both, operating and fluorescence data as inputs, removing the observations from the first day allowed to confirm that models' R^2 continued to be above 0.90, and that the previously found high R^2 values did not result from a good model fit to the observations from the first day. Figure 7.4 shows the best models with both, operating and fluorescence data as inputs, for pressure drop in the river circuit (#5), pressure drop in the sea circuit (#11), stack electric resistance (#19) and net power density (#25).

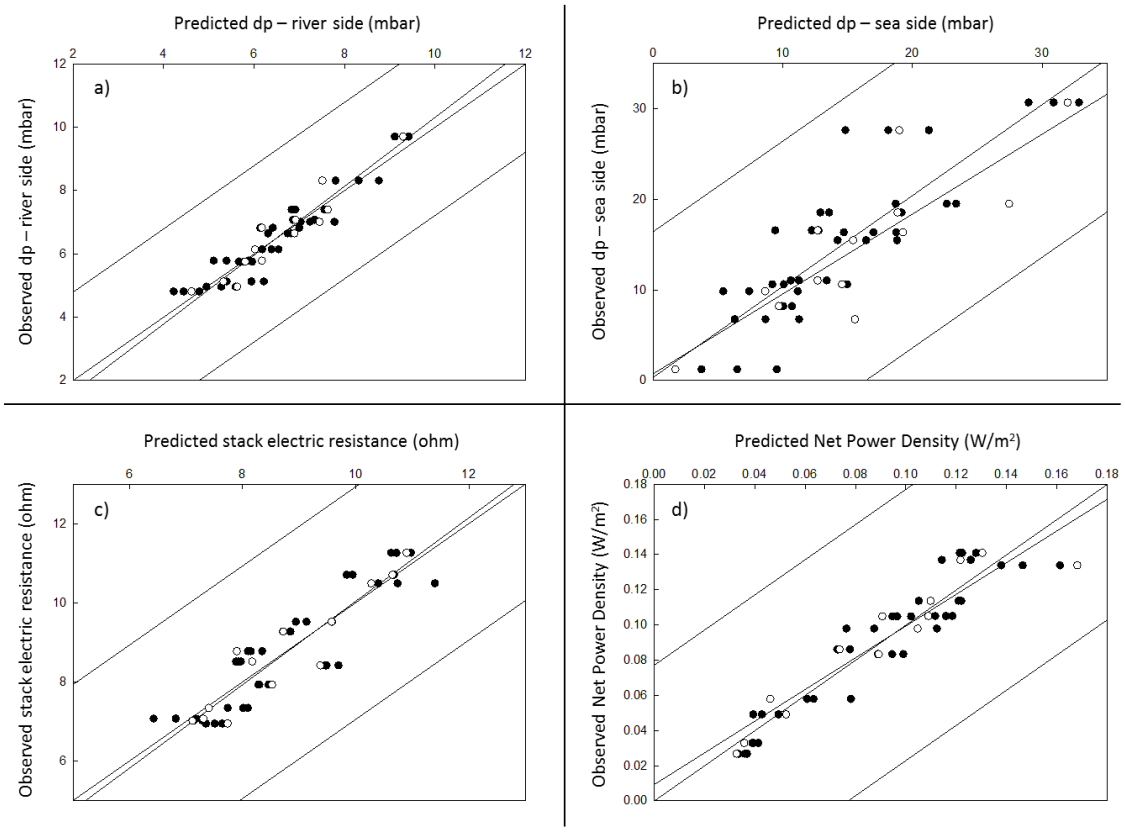

Figure 7.4. PLS models with operating and fluorescence data for all days, except for the 1st day of stack operation, used directly as inputs for prediction of: a) pressure drop in river circuit (model #5), b) pressure drop in sea circuit (model #11), c) stack electric resistance (model #19) and d) net power density (model #25). Closed circles represent training data and open circles represent validation data.

For the net power density and the pressure drop in the sea circuit, exclusion of the data from the first day almost did not alter the models statistical parameters presented in Table 7.2. Also, it was found that the best model for those two outputs, considers the same inputs as the model in which all observations were used. For the prediction of the pressure drop in the river compartment and of the stack electric resistance, the recalibrated models: #4 and #18, respectively, were not the best ones, even despite their relatively satisfactory R^2 (around 0.80). Since the overall database was more significantly affected by removal of the measurements from the first day, as the range of the outputs values changed, incorporation of other inputs was necessary to improve the models fitting ((#5 – Figure 7.4a and #19 - Figure 7.4c). For pressure drop in the river circuit, for example, different principal components of fluorescence EEMs were used in the new model. For the stack electric resistance, an accurate prediction was achieved after alteration of some PCs and inclusion of the flow rates of both streams as model inputs.

7.3.2.3. Influence of process history in output prediction ("Delta" models)

For models developed without including fluorescence data, the effect of this approach (which consisted in utilization of inputs variations instead of directly using the inputs values) was found to be not useful since the operating parameters were varied randomly and, therefore, their variations between performance parameters acquisition were artificial, and not caused by the time evolvement of the RED stack performance due to fouling.

Relatively to the models where both, fluorescence and operating data were used as inputs, the 3rd kind models were found to be the best ones. For prediction of both circuits pressure drops (Figure 7.5) the fitting kept the same accuracy level, as in the previously shown models, while for prediction of stack electric resistance and net power density (Figure 7.6) even better fittings were obtained.

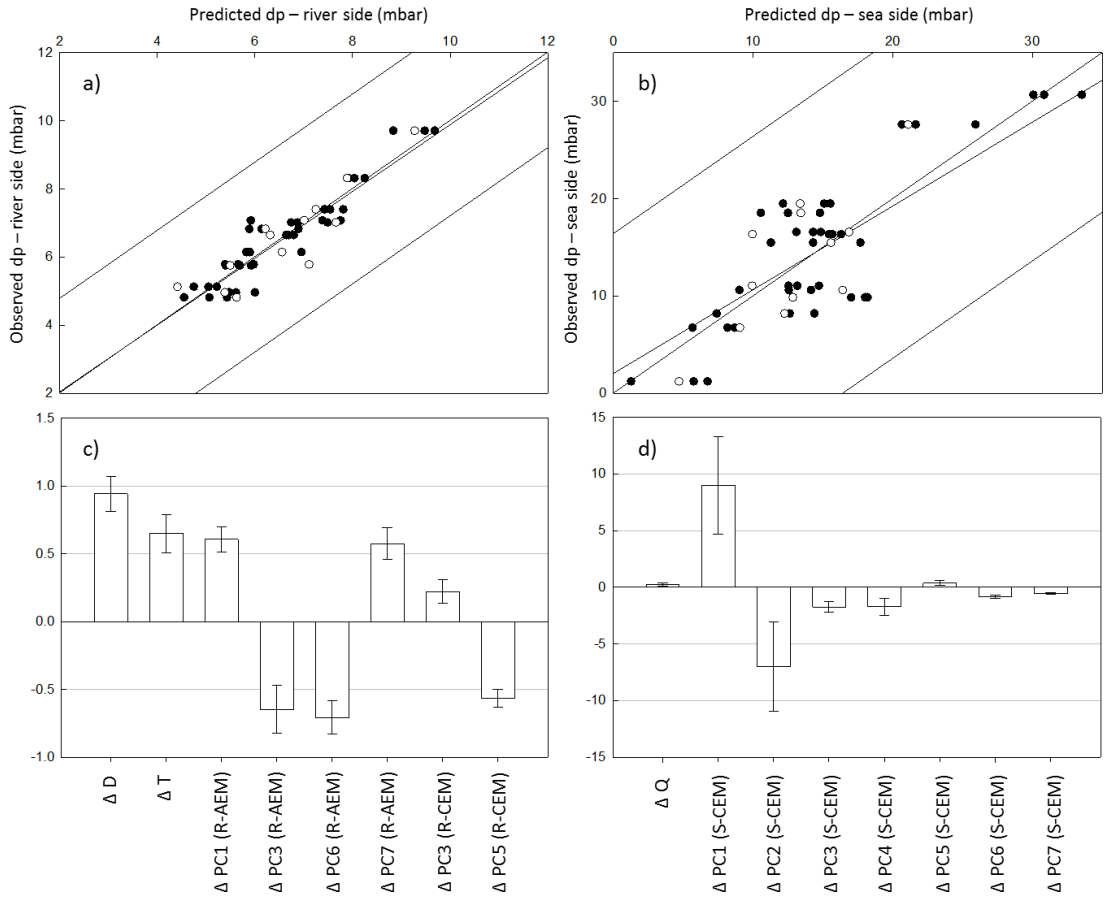

Figure 7.5. Fitting and inputs regression coefficients of PLS models (#7 and #14) predicting pressure drop in the river water circuit (Figures 7.5a and 7.5c) and pressure drop in the sea water circuit (Figures 7.5b and 7.5d). Closed circles represent training data and open circles represent validation data. The regression coefficients are normalized. "ΔD" stands for the days difference between measurements, T is temperature, Q is flow rate, R and S mean river and sea water, AEM and CEM are anion and cation-exchange membrane surface, respectively.

Pressure drop in river water circuit was successfully modeled by 8 inputs (Figure 7.5a and 7.5c), each one with a very similar contribution (similar regression coefficient values of each input). Six of the inputs are related to fluorescence data, four describing EEMs of AEM surface in contact with river water and two describing EEMs of CEM surface in contact with river water. A predominance (and slightly higher regression coefficients) of inputs associated to the state of AEM is not surprising, since the main fouling in the river compartment is correlated to the transport of humic acids and/or other organic compounds adsorption on the AEM surface. However, the absence of the river water flow rate as one of the inputs was surprising. This may have been due to a capability of fluorescence data to indirectly capture this information by, for example, a possible relation between the membrane fouling and the water residence time in the compartments. Another possibility is that variation of the flow rate during the RED stack operating period (Table 7.1) could had been too small to cause significant variations in the pressure drop.

For prediction of the pressure drop in the sea water circuit, 8 inputs were also necessary (Figure 7.5b and 7.5d). However, their regression coefficients standard deviations are considerable and therefore, a mechanistic interpretation may not be accurate. Despite of this, the chosen inputs could be relatively easily explained. The sea water flow rate is one of the inputs, most probably due to its high variation in the performed study (Table 7.1). All other inputs are associated with EEMs of CEM in contact with sea water. The fouling in the sea compartment was mainly due to large particles such as clays and sands. Moreover it has been reported that scaling is usually the main issue affecting CEMs [2].

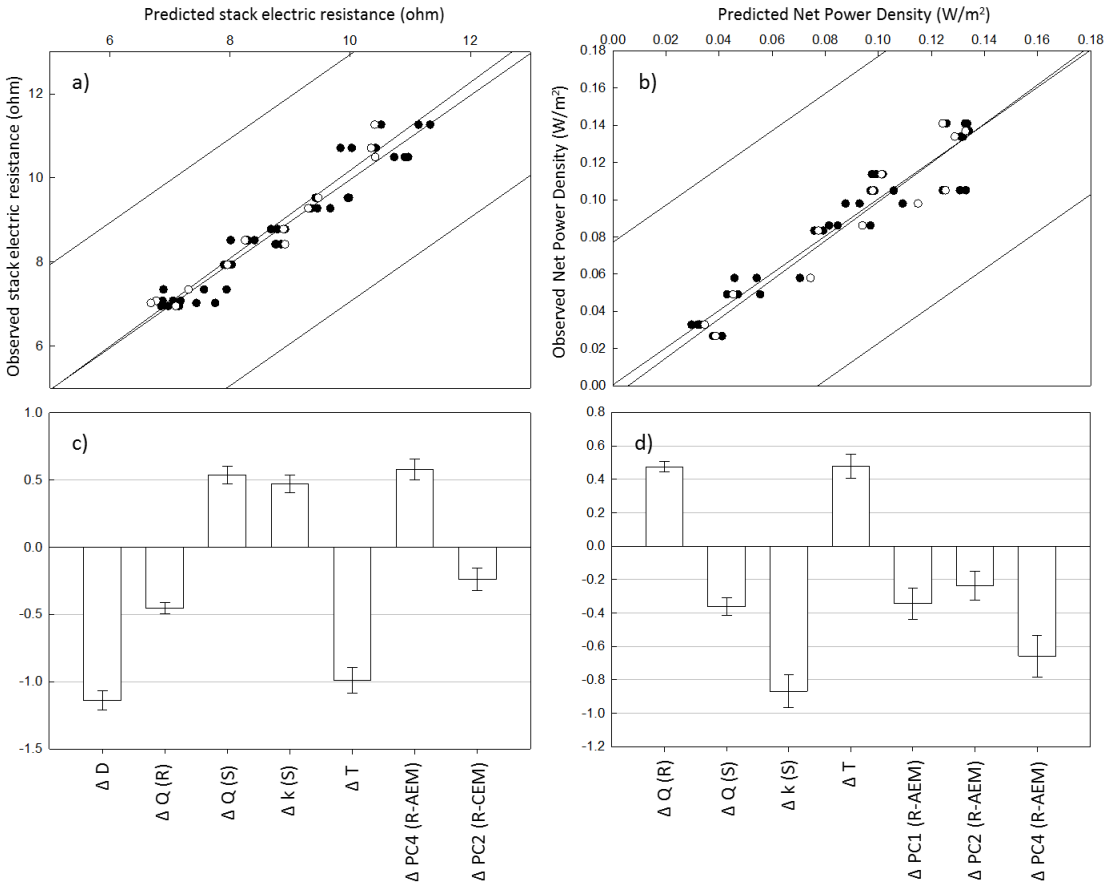

Figure 7.6. Fitting and inputs regression coefficients of PLS models (#21 and #28) predicting stack electric resistance (Figures 7.6a and 7.6c) and net power density (Figures 7.6b and 7.6d). Closed circles represent training data and open circles represent validation data. The regression coefficients are normalized. "ΔD" stands for the days difference between measurements, T is temperature, Q is flow rate, k is conductivity, R and S mean river and sea water, AEM and CEM are anion and cation-exchange membrane surface, respectively.

For prediction of the stack electric resistance (Figure 7.6a and 7.6c) and net power density (Figure 7.6b and 7.6d), 7 inputs were necessary. Five of the inputs were common for both outputs prediction. The standard deviations of the regression coefficients are very small what shows that the models are robust. Curiously, the signs of regression coefficients of all inputs which were selected for both, stack electric resistance and net power density prediction, are

opposite in the mentioned models (#21 and #28). Therefore, if in the model for stack electric resistance the input regression coefficient was positive, in the model for net power density prediction, the regression coefficient of the same input was negative. It was mentioned previously that even if the PLS models can predict very well the outputs, it does not mean that there is necessarily a plausible mechanistic interpretation, which could be attributed to the selected inputs. Herein, however, the found opposite signs, and therefore, an opposite contribution of each input for the stack electric resistance and for the net power density seemed reasonable from a mechanistic viewpoint. This behavior may be explained by influence of the stack electric resistance on the net power density. If the stack electric resistance increases, the obtainable net power density decreases, and vice-verse, so if an input causes an increase of the stack electric resistance, it leads to a decrease of the net power density, as shown by the sign of inputs regression coefficients.

From the operating parameters, flow rates of both streams were found to influence both outputs (stack electric resistance and net power density), however, only the conductivity of the sea water seemed to be necessary, as the conductivity of the river water was not included in the models. Obviously, in mechanistic terms, river water conductivity is an extremely important parameter as it affects the potential difference over the membranes, as well as the main ohmic resistance is usually located in the dilute compartment [27]. However, since in the present study, the water streams were recirculated, the conductivity of the sea water decreased along time, while during the same period the conductivity of the river water increased (Figure 7.1c). Therefore, both conductivities are correlated and only one of them was sufficient to predict the outputs.

Finally the fluorescence data used as models inputs, for stack electric resistance and net power density, were those for the membrane surfaces contacting the river compartment. However, as previously explained, this does not necessarily mean that fouling in the sea compartment did not influence the stack performance. It must be pointed out that despite of few inputs related with fluorescence in the models predicting these two outputs, they were essential for obtaining a good model fitting, since the R^2 values increased from 0.59 (model #20) to 0.95 (model #21) relatively to the stack electric resistance prediction and from 0.77 (model #27) to 0.91 (model #28) for the net power density prediction.

7.4. CONCLUSIONS

Multivariate statistical modeling showed a very good potential for predicting the most important RED stack performance parameters, such as pressure drop in the river and sea water circuits, electric resistance and net power density, when 2D fluorescence spectroscopy data are one of the models' input.

2D fluorescence spectroscopy was found to capture relevant information about membrane surface status which, during a RED stack operation, is affected by fouling. Through parallel factor analysis, the information contained in the fluorescence spectra obtained can be quantitatively extracted in the form of principal components. Incorporation of principal components scores of fluorescence EEMs of membrane surfaces, together with relevant operating data, as inputs in the PLS models, proved to be an appropriate strategy to improve the fitting ($R^2 > 0.90$) and prediction of relevant RED stack performance parameters. Moreover, it was proved that it is possible to predict well the RED stack performance parameters during fouling development.

Utilization of only operating parameters such as solutions' flow rate, conductivity and temperature, could give relatively good estimations for the output parameters, if the membrane status does not changed significantly. However, if during the period of RED stack operation, phenomena such as fouling significantly alter the membranes properties, models including only operating parameters are not able to capture all system alterations and performance (output values).

For the currently available fluorescence bundle probe dimensions it is necessary to open the stack in order to access the membrane surfaces. Nevertheless, this is a technical limitation which, with the current progress of nanotechnologies and minimizing the probe dimensions, eventually could be solved in future. However, an alternative could pass through using a dedicated fouling monitoring cell located externally to a RED stack. Additionally, given the EMMs data set full of information, the latter opens the possibility of a future identification of the type of fouling. Finally, although 2D fluorescence spectroscopy allows for following the deposition of foulants on the membrane surfaces and for predicting RED stack performance parameters, it still remains to be investigated when antifouling procedures should be applied based, for example, on a specific PC value or its sudden variation.

REFERENCES

[1] G.Z. Ramon, B.J. Feinberg, E.M.V. Hoek, Membrane-based production of salinity-gradient power, Energy Environ. Sci. 4 (2011) 4423–4434.

[2] S. Pawlowski, J.G. Crespo, S. Velizarov, Pressure drop in reverse electrodialysis: Experimental and modeling studies for stacks with variable number of cell pairs, J. Membr. Sci. 462 (2014) 96–111.

[3] J.W. Post, H.V.M. Hamelers, C.J.N. Buisman, Influence of multivalent ions on power production from mixing salt and fresh water with a reverse electrodialysis system, J. Membr. Sci. 330 (2009) 65–72.

[4] D.A. Vermaas, J. Veerman, M. Saakes, K. Nijmeijer, Influence of multivalent ions on renewable energy generation in reverse electrodialysis, Energy Environ. Sci. 7 (2014) 1434-1445.

[5] D.A. Vermaas, D. Kunteng, M. Saakes, K. Nijmeijer, Fouling in reverse electrodialysis under natural conditions, Water Res. 47 (2013) 1289-1298.

[6] D.A. Vermaas, D. Kunteng, J. Veerman, M. Saakes, K. Nijmeijer, Periodic feedwater reversal and air sparging as antifouling strategies in reverse electrodialysis, Environ. Sci. Technol. 48 (2014) 3065−3073.

[7] J.G. Hong, W. Zhang, J. Luo, Y. Chen, Modeling of power generation from the mixing of simulated saline and freshwater with a reverse electrodialysis system: The effect of monovalent and multivalent ions, Appl. Energy 110 (2013) 244–251.

[8] E. Brauns, Salinity gradient power by reverse electrodialysis: effect of model parameters on electrical power output, Desalination 237 (2009) 378–391.

[9] J. Veerman, M. Saakes, S.J. Metz, G.J. Harmsen, Reverse electrodialysis: a validated process model for design and optimization, Chem. Eng. J. 166 (2011) 256–268.

[10] M. Tedesco, A. Cipollina, A. Tamburini, W. van Baak, G. Micale, Modelling the reverse electrodialysis process with seawater and concentrated brines, Desalin. Water Treat. 49 (2012) 404–424.

[11] D.A. Vermaas, E. Guler, M. Saakes, K. Nijmeijer, Theoretical power density from salinity gradients using reverse electrodialysis, Energy Proc. 20 (2012) 170 – 184.

[12] M. Tedesco, A. Cipollina, A. Tamburini, I.D.L. Bogle, G. Micale, A simulation tool for analysis and design of reverse electrodialysis using concentrated brines, Chem. Eng. Res. Design 93 (2015) 441–456.

[13] M. Dalmau, N. Atanasova, S. Gabarron, I. Rodriguez-Roda, J. Comas, Comparison of a deterministic and a data driven model to describe MBR fouling, Chem. Eng. J. 260 (2015) 300–308.

[14] S. Pawlowski, C.F. Galinha, J.G. Crespo, S. Velizarov, 2D fluorescence spectroscopy for monitoring ion-exchange membrane based technologies - reverse electrodialysis (RED), submitted to Water Research.

[15] C.F. Galinha, G. Carvalho, C.A.M. Portugal, G. Guglielmi, M.A.M. Reis, J.G. Crespo, Multivariate statistically-based modelling of a membrane bioreactor for wastewater treatment using 2D fluorescence monitoring data, Water Res. 46 (2012) 3623-3636.

[16] C.F. Galinha, G. Carvalho, C.A.M. Portugal, G. Guglielmi, R. Oliveira, J.G. Crespo, M.A.M. Reis, Real-time monitoring of membrane bioreactors with 2D-fluorescence data and statistically based models, Water Sci. Technol. 63 (2011) 1381-1388.

[17] S. Sanches, C.F. Galinha, M.T. Barreto Crespo, V.J. Pereira, J.G. Crespo, Assessment of phenomena underlying the removal of micropollutants during water treatment by nanofiltration using multivariate statistical analysis, Sep. Purif. Technol. 118 (2013) 377–386.

[18] B. Santos, C.F. Galinha, J.G. Crespo, M. Santos, S. Velizarov, Prediction of polar oil and grease contamination levels in refinery wastewater through multivariate statistical modeling, Sep. Purif. Technol. 119 (2013) 51–57.

[19] D.A. Vermaas, M. Saakes, K. Nijmeijer, Doubled power density from salinity gradients at reduced intermembrane distance, Environ. Sci. Technol. 45 (2011) 7089–7095.

[20] J. Veerman, M. Saakes, S.J. Metz, G.J. Harmsen, Electrical power from sea and river water by reverse electrodialysis: A first step from the laboratory to a real power plant, Environ. Sci. Technol. 44 (2010) 9207–9212.

[21] R. Bro, PARAFAC. Tutorial and applications. Chemometr. Intell. Lab. Syst. 38 (1997) 149-171.

[22] R. Boggia, M. Forina, P. Fossa, L. Mosti, Chemometric study and validation strategies in the structure-activity relationships of new cardiotonic agents, Quant. Struct. Act. Rel. 16 (1997) 201–213.

[23] T.P. Ryan, Modern Regression Methods, John Wiley & Sons, Inc., 1997.

[24] M. Forina, S. Lanteri, M.C.C. Oliveros, C.P. Millan, Selection of useful predictors in multivariate calibration, Anal. Bioanal. Chem. 380 (2004) 397–418.

[25] C. Duchesne, J.F. MacGregor, Jackknife and bootstrap methods in the identification of dynamic models, J. Process Contr. 11 (2001) 553–564.

[26] C.A. Andersson, R. Bro, The N-way toolbox for MATLAB, Chemometr. Intell. Lab. 52 (2000) 1–4.

[27] S. Pawlowski, P. Sistat, J.G. Crespo, S. Velizarov, Mass transfer in reverse electrodialysis: Flow entrance effects and diffusion boundary layer thickness, J. Membr. Sci. 471 (2014) 72–83.

Chapter

8

CONCLUSIONS AND FUTURE WORK

8.1. FINAL OVERVIEW

This PhD thesis was dedicated to exploring the potential of reverse electrodialysis (RED) as a sustainable technology for power generation through performing experimental and theoretical modeling studies. The thesis explored some of the most relevant aspects of the RED process: Mass transfer and fluid dynamics (Chapters 3-5) and Fouling (Chapters 6-7).

The studies were further focused on describing and understanding the effects of the related mass transfer (Chapter 3) and pressure drop (Chapter 4) phenomena, which conclusions were then used as support for profiled membrane design using the computational fluid dynamics (CFD) approach (Chapter 5).

It was found that utilization of the diffusion relaxation zone of chronopotentiograms allows for an accurate estimation of diffusion boundary layer (DBL) thickness under RED operating conditions even for large and inhomogeneous ion-exchange membrane surfaces. Moreover, chronopotentiometry proved to be a simple, fast (not requiring more than 300 s) and accurate electrochemical tool. Spacers presence in the channels reduced the DBL thickness between 25 % and 60 % for the applied solutions flow rate range, however, the ohmic resistance duplicated comparatively to empty channels. Also, based on the adjustment between estimated DBL thickness and its prediction by available empirical correlations (Leveque equation for empty channels and Sh=f(Re, Sc) correlation for channels with spacers), it was demonstrated that flow entrance effects on mass transfer could favor power generation in RED stacks. Therefore designing stacks with short flow channels will be beneficial from a mass transfer viewpoint.

However, for short channels, in order to grant a sufficiently large total membrane area, a high number of channels (cell-pairs) should be used in a RED stack. It was found, based on a proposed and successfully validated mathematical model for pressure drop simulation, that in RED stacks with many cell-pairs the main pressure drop is no longer associated with the pressure drop in the channels, as the pressure drops in the manifolds and branches become dominant. Moreover, the partial pressure drop in the branches was identified as the main cause of a non-uniform fluid flow distribution inside a RED stack. In such a way, when the gross power density is maintained constant, the net power density provided by the RED stack decreases when the number of cell-pairs increases, because the partial pressure drops in the distribution ducts and in the branches increase. Also it has been observed that in the investigated RED stack geometry the total pressure drop was in average 1.55 times higher when the spacers were incorporated in the channels in comparison with the same stack with empty channels.

In spite that the investigated lab-scale RED stack empty channels geometry showed lower ohmic resistance and pressure drop comparatively to channels with spacers, for industrial-scale utilization of empty channels may not be viable since the channels may easily collapse. Therefore, utilization of profiled membranes, which self-maintain the channel compartment thickness, seems rather promising, as the spacers' shadow effect is eliminated in such a stack configuration. Previous findings, regarding flow entrance effects on mass transfer and importance of other partial pressure drop besides the pressure drop in the channels, were included in the estimation of the obtainable net power density in RED stacks, based on computation fluid dynamics (CFD) modeling of fluid behavior in channels formed by different corrugated membranes. Herein, proposed chevron structures were found to be the most promising corrugation geometry, with a performance even better than conductive spacers, and an increase of 75 % in the obtainable net power density comparatively to the one obtained in channels with non-conductive spacers. For industrial size equipment, chevron corrugations may represent economic advantages since smaller volumes of saline solutions will be needed, as lower linear flow velocities will be required for obtaining the desired net power density values. Besides, the best compromise between mass transfer coefficient and pressure drop increase was found to exist for chevron corrugations, which means that net power density improvement offered by chevron corrugations is not only due to increase of the available membrane area, but is also caused by an improved fluid dynamics. Moreover, as the linear flow velocity upstream to the corrugations is high due to the created specific fluid pathway and dead zones are almost not present, it may be anticipated that channels with chevron corrugation design will be also less prone to fouling.

Fouling is an undesirable phenomenon in RED, since it leads to a decrease of the obtainable net power density due to increasing stack electric resistance and pressure drop. In this thesis, the fouling detection studies were focused on utilization of 2D fluorescence spectroscopy as a monitoring tool for assessment of fouling on ion-exchange membrane surfaces (Chapter 6) and on use of information captured by 2D fluorescence spectroscopy for prediction of relevant RED stack performance parameters, by multivariate statistical models (Chapter 7).

It was found that cation- and anion-exchange membranes can be clearly distinguished by 2D fluorescence spectroscopy and that the obtained fluorescence spectra of membrane surfaces change during a RED process operation due to accumulation of foulants on the membrane surfaces. The 2D fluorescence spectroscopy data obtained can be quantified by parallel factor analysis (PARAFAC) into few principal components (PCs). In such a way, the fouling deposition on membrane surfaces can not only be detected, but also monitored over time. The AEM surface in contact with river water was the one most affected by fouling, mostly by humic compounds present in river water. Additionally, the transport of these organic substances from river to sea water was followed by 2D fluorescence spectroscopy. Moreover, it was possible to evaluate the membrane cleaning efficiency, as the PCs obtained before and after cleaning of the membrane surfaces can be compared. Based on the fact that 2D fluorescence spectroscopy captures information about fouling, which can be compressed and mathematically deconvoluted, it was proposed to use this information in multivariate statistical models for prediction of relevant RED stack performance parameters.

Statistically-based multivariate models were thus developed to predict net power density, electric resistance and pressure drop in RED. Firstly, only operating parameters such as solutions' flow rate, conductivity and temperature were used as inputs and a relatively good estimation of the output parameters was obtained. However, if phenomena such as fouling significantly alter the membranes properties, models with only operating parameters were found to be not able to capture all system alterations and outputs variation. Inclusion of fluorescence data, after PARAFAC compression, as inputs significantly improved the PLS models fitting ($R^2 > 0.90$), since the information about fouling was included in the model. 2D fluorescence spectroscopy proved therefore to be a powerful analytical tool providing an important process related information about fouling, which could be used for system performance description/prediction purposes.

Based on results obtained in this thesis, it can be concluded that the channels should be as short as possible, in order to benefit from the flow entrance effect on mass transfer, but at the same time not too short in order to the avoid a situation at which the power spent for solution pumping and required to overtake the partial pressure drops in manifolds and branches (both independent from channel length), exceeds the generated power. Implementing strategies for providing a more uniform fluid distribution such as a proper sizing the cross flow section, increasing the number of beam inlets/outlets to/from the flow compartment channels, or ensuring a proper selection of the branch format are therefore essential for an adequate RED stack design. Such steps may decrease the values of the mentioned partial pressure drops and avoid creation of lower linear flow velocity zones, where fouling is more likely to occur. Channels design must tend to eliminate the use of non-conductive spacers, which increase the ohmic resistance and in their knits create regions prone to fouling. Utilization of profiled membranes, with the proposed chevron corrugation shape, offers an appropriate trade-off between mass transfer and pressure drop, besides reducing the channels dead zones and increasing the available membrane area for ion transport. In order to monitor fouling, 2D fluorescence spectroscopy can be a powerful tool to do it, as well as it can be successfully applied to evaluate the effects of membrane cleaning and to follow transport of fluorophore-containing organic foulants across the membranes. Moreover, fluorescence spectra can be acquired in few minutes, at chosen zones, where, for example, fouling occurs more frequently. Finally, it was found out that multivariate statistical modeling shows a very good potential for predicting the most important RED stack performance parameters, such as pressure drop, electric resistance and net power density, when 2D fluorescence spectroscopy data is one of the models' inputs. These models can be continuously updated and improved with a new data.

However, under realistic conditions, *e.g.*, channels thickness of 0.5 mm and chevron-like profiled membranes created from flat heterogeneous ion-exchange membranes (with 7.5 Ωcm^2 of membrane area resistance), the maximal expected net power density value is around 0.71 W/m^2. If the membrane area resistance could be decreased to half of the above-mentioned value, the obtainable net power density could become close to 0.89 W/m^2. The current costs of flat heterogeneous ion-exchange membranes (without the cost of making them profiled) is commonly in the range of 50 €/m^2 to 70 €/m^2. Therefore both, the obtainable net power density and the current heterogeneous ion-exchange membrane prices values, are still far away from 2.7 W/m^2 and 4.3 €/m^2, respectively, at which the cost of generated electricity has been considered to be competitive with other energy sources as mentioned in section 1.3. Also, although the amount of salinity gradient energy due to rivers discharge to Oceans is theoretically capable of providing the half of the World current electricity demand, it supposes that all rivers flows would pass through RED stacks, which does not seem realistic. Therefore,

in my understanding, utilization of RED for a massive, worldwide electricity generation is very unlikely. Nevertheless, in local small stations, where the access to different saline streams and conditions to create a salinity gradient already exists, there is a clear possibility to generate electricity by RED since, as discussed throughout the Thesis, in smaller stacks the generated power could be higher than in large stacks as the total pressure drop is smaller, the manifold structure is reduced and the channels could be shorter. The advantages of smaller devices may also suggest that RED could have a brighter future if applied for energy recovery or as "engines"/power source of nanoscale sized devices.

Nevertheless, recently (on November 26, 2014), a RED pilot plant (50 kW of capacity) was inaugurated at the Afsluitdijk (The Netherlands) by Fujifilm, REDstack B.V and the Wetsus consortium. Therefore, the RED technology has crossed the line between being only a promising idea explored in scientific laboratories and has become a tangible way of generating power. This fact brings a hope that the results obtained, the conclusions drawn and the suggested guidelines for planning and/or optimization of RED stacks, as well as the RED monitoring tools developed during this PhD project, could be useful for the studied process. Moreover, it should be noted that although this Thesis was focused on the RED process, its conclusions can be often extended to other devices based on a plate-and-frame membrane configuration (e.g., traditional electrodialysis, electrodeionization, Donnan dialysis, membrane fuel cells).

8.2. SUGGESTIONS FOR FUTURE RESEARCH

Although the results obtained throughout this PhD project represent one more step forward, in the mathematical modeling, experimental validation and monitoring tools development, for practical implementation of the RED process, the following recommendations for future work could be proposed.

Firstly, the feedwater distribution system, i.e. the design of the manifolds and the connection between the distribution ducts and stack flow channels, i.e. the branches, should be improved. It had been found that pressure drop in these regions can strongly affect the RED stack performance, especially if the flow rate and number of cell-pairs increase. Decrease of this pressure drop could allow for using shorter channels, and therefore obtaining a higher net power density. For designing new and improved feedwater distribution systems, CFD tools can be used, as the main objective passes through minimization of the pressure drop, which can be accounted for by mass continuity and Navier-Stokes equations.

An alternative to modification of the feedwater distribution system geometry could pass through changing the stack design from a plate-and-frame type to tubular or radial membrane arrangement. There are numerous possibilities in the field of heat exchangers and microfluidic systems that may serve as an inspiration.

A geometry of a microfluidic mixture device served precisely as an inspiration for the proposed chevron corrugation shape of profiled membranes to be used in a RED stack. These simulated chevron structures still need to be experimentally validated and the performance of RED stacks with different types of profiled membranes compared. Moreover, the chevron corrugation geometry parameters should be optimized for the RED application, first using CFD and then experimentally, as herein only one set of possible dimensions was used.

Furthermore, since the main electric resistance is usually located in the dilute stream compartment, the possibility of using different corrugations' design and/or compartments' thickness for dilute and concentrated channels could be explored. The alternative of using seawater and brines as dilute and concentrated stream, respectively, does not seem as a promising strategy to reduce the electric resistance of the dilute compartment, due to the risk of a decreased potential difference because of lower concentration difference and weaken Donnan co-ion exclusion. Besides, such saline streams are much less abundant than river water and sea water. Also, fouling / scaling issues could become more severe if brines are used through increasing the pressure drop.

Also ion-exchange membranes, which are so far more suitable (thick) for creation of corrugations on their surfaces are heterogeneous and with a relatively high membrane area resistance (≈ 7.5 Ωcm^2) comparatively to the existing thin homogeneous ion-exchange membranes (≈ 1.0 Ωcm^2). Therefore, the development of membranes with low area resistance, but thick enough to allow creating corrugations on their surfaces, would be of interest.

Regarding the monitoring of fouling, 2D fluorescence spectroscopy can be a very useful tool, but with the current dimensions of the bundle fluorescence probe, it is necessary to open the stack in order to access the membrane surfaces. However, 2D fluorescence spectroscopy can become potentially a non-invasive and online monitoring technique, if it would be possible to incorporate the fluorescence probes inside the working channels. This still remains a technological challenge.

Moreover, under the conditions used in the present PhD project it was found that cleaning the channels with water or with acid and base solutions (chemical cleaning) had similar efficiency on reducing the pressure drop; however, when chemical cleaning was applied, the membranes' electric resistance increased. Therefore, for RED systems, the cleaning strategy commonly applied for ion-exchange membranes used in classical ED may require further investigation and possible revision. Also, although 2D fluorescence spectroscopy allows for following the deposition of foulants on the membrane surfaces and for prediction of RED stack performance parameters, it still remains to be investigated when, and what antifouling strategies should be applied. Finally, since feedwaters may need to be pretreated, for example to remove humic compounds from river water, or sand particles from sea water, feasibility studies, considering the additional costs associated with such pre-treatment, should be performed in the future.